



# MID-AMERICA TRANSPORTATION CENTER

Report # MATC-MS&T: 133-1

Final Report  
WBS:25-1121-0005-133-1

UNIVERSITY OF  
**Nebraska**  
Lincoln

THE UNIVERSITY  
OF IOWA

THE UNIVERSITY OF  
**KU** KANSAS

MISSOURI  
**S&T**

LINCOLN  
UNIVERSITY  
MISSOURI



UNIVERSITY OF  
**Nebraska**  
Omaha

University of Nebraska  
Medical Center

**KU** MEDICAL  
CENTER  
The University of Kansas

## Behavior and Repair of Corroded Steel H-Piles Phase I (Axial Behavior)

**Mohamed A. ElGawady, Ph.D.**

Professor

Department of Civil, Architectural, &  
Environmental Engineering  
Missouri University of Science and  
Technology

**Mohanad M. Abdulazeez**

Ph.D. Candidate

**Amro Ramadan**

Ph.D. Student

**Binod Sherstha**

Ph.D. Student

**Ahmed Gheni, Ph.D.**

Postdoctoral Fellow

**Eslam Gomaa**

Ph.D. Student

**Yasser Darwish**

Ph.D. Student

MISSOURI  
**S&T**

2019

A Cooperative Research Project sponsored by  
U.S. Department of Transportation- Office of the Assistant  
Secretary for Research and Technology

The contents of this report reflect the views of the authors, who are responsible for the facts and the accuracy of the information presented herein. This document is disseminated in the interest of information exchange. The report is funded, partially or entirely, by a grant from the U.S. Department of Transportation's University Transportation Centers Program. However, the U.S. Government assumes no liability for the contents or use thereof.

MATC

## **Behavior and Repair of Corroded Steel H-Piles Phase I (Axial Behavior)**

Mohamed A. ElGawady, Ph.D.  
Professor  
Department of Civil, Architectural, &  
Environmental Engineering  
Missouri University of Science and  
Technology

Mohanad M. Abulazeez,  
Ph.D. Candidate  
Department of Civil, Architectural &  
Environmental Engineering  
Missouri University of Science and  
Technology

Amro Ramadan,  
Ph.D. Student  
Department of Civil, Architectural &  
Environmental Engineering  
Missouri University of Science and  
Technology

Binod Sherstha,  
Ph.D. Student  
Department of Civil, Architectural &  
Environmental Engineering  
Missouri University of Science and  
Technology

Ahmed Gheni, Ph.D.  
Postdoctoral Fellow  
Department of Civil, Architectural &  
Environmental Engineering  
Missouri University of Science and  
Technology

Eslam Gomaa,  
Ph.D. Student  
Department of Civil, Architectural &  
Environmental Engineering  
Missouri University of Science and  
Technology

Yasser Darwish,  
Ph.D. Student  
Department of Civil, Architectural &  
Environmental Engineering  
Missouri University of Science and  
Technology

A Report on Research Sponsored by

Mid-America Transportation Center

University of Nebraska-Lincoln

May 2019

# **TECHNICAL REPORT DOCUMENTATION PAGE.**

1. Report No.: 25-1121-0005-133-1		2. Government Accession No.:		3. Recipient's Catalog No.:	
4. Title and Subtitle:  Behavior and Repair of Corroded Steel H-Piles Phase I (Axial Behavior)				5. Report Date: May 2019	
				6. Performing Organization Code:	
7. Author(s): Mohanad M. Abdulazeez, Amro Ramadan, Binod Sherstha, Ahmed Ghani, Eslam Gomaa, Yasser Darwish, and Mohamed A. ElGawady				8. Performing Organization Report No.: 25-1121-0005-133-1	
9. Performing Organization Name and Address: Mid-America Transportation Center 2200 Vine St. PO Box 830851 Lincoln, NE 68583-0851				10. Work Unit No.:	
				11. Contract or Grant No.: 69A3551747107	
12. Sponsoring Agency Name and Address:  Missouri University of Science and Technology 300 W 13 <sup>th</sup> St Rolla, MO 65409				13. Type of Report and Period Covered: Final Report	
				14. Sponsoring Agency Code: MATC TRB RiP No. 91994-8	
15. Supplementary Notes: The investigation was conducted in cooperation with the U. S. Department of Transportation, Federal Highway Administration.					
16. Abstract: This report summarizes the details of an experimental work and finite element modeling that were conducted to evaluate: 1) the remaining axial capacity of steel H-piles having different corrosion severity and extension levels, and 2) the performance of repaired corroded steel H-piles. The research consisted of 32 short steel H-piles (10 × 42) encased in different types of concrete including conventional concrete, high strength concrete, high-early strength concrete, and geopolymer concrete. Different embedment lengths and shear studs were used. Thirteen long steel H-piles (10 × 42) were milled to represent the loss of cross-sectional area associated with corrosion and tested under concentric and eccentric axial loads. Different corrosion levels and patterns were considered. According to the obtained and observed results from the test, the axial capacity of the concentrically loaded corroded H-piles decreases as the corrosion severity increases. Both the FEMs and experimental work showed that the buckling load is more susceptible to corrosion in the flanges. The length of the corroded region had no effect on the axial load capacity. Increasing the concrete compressive strength increased the bond strength. Furthermore, implementing different concrete jackets types was successful in producing compressive strengths similar to those of the conventional concrete. Using the CFRP jackets without headed studs slightly increased the bond stress between the concrete jackets and steel piles. Using headed studs and CFRP jackets increased the bond strength between the jackets and steel piles by a range of 580% to 1,130%, compared to the reference specimen. Using headed studs considerably increased the bond strength between the concrete jackets and steel piles.					
17. Key Words: Steel H-piles, Geopolymer concrete, CFRP, Corrosion, LS-DYNA				18. Distribution Statement: No restrictions. This document is available to the public through National Technical Information Center, Springfield, Virginia 22161.	
19. Security Classification (of this report): Unclassified.		20. Security Classification (of this page): Unclassified.		21. No of Pages: 189	
				22. Price:	

## Table of Contents

Executive Summary .....	xi
Acknowledgements .....	x
Table of Contents .....	iii
Chapter 1 Introduction .....	1
1.1 Layout of the report .....	9
Chapter 2 Finite Element Modeling.....	10
2.1 Introduction.....	10
2.2 FE Model Calibration .....	10
2.3 Results and Discussion .....	15
2.4 Effects of Eccentricity on the Corroded Piles.....	18
2.5 Model Validation .....	21
Chapter 3 Experimental Testing of Corroded Piles Under Concentric and Eccentric Loads .....	37
3.1 Introduction.....	37
3.2 Existing Design Specifications .....	37
3.3 Test Specimens .....	41
3.4 Test Setup and Loading Protocol.....	48
3.5 Instrumentation .....	50
3.6 Results and Discussion .....	53
Chapter 4 Bond Behavior of Steel Bridge H-Pile Columns Encased In Concrete Jacket .....	62
4.1 Introduction.....	62
4.2 Experimental Program .....	63
4.3 Results and Discussion .....	74
Chapter 5 Interfacial Shear Strength of Steel H-Piles Encased in Concrete Filled Cfrp Jackets .	86
5.1 Introduction.....	86
5.2 Experimental Program .....	86
5.3 Results and Discussion .....	97
Chapter 6 Experimental Testing and Finite Element Analyses of Retrofitted Full-Scale Steel H-Piles.....	120
6.1 Experimental Work.....	120
6.2 Materials .....	120
6.3 Fabrication and Installation of the Repair System.....	124
6.4 Instrumentation .....	127
6.5 Piles Testing.....	128
6.6 Results and Discussion .....	129
6.7 FE Modeling .....	130
Chapter 7 Conclusions .....	143
References .....	147



## List of Figures

Figure 1.1 Corrosion of H-piles in I-70/I-270 interchange in St. Louis. ....	1
Figure 1.2 Corroded steel column.....	2
Figure 1.3 An example of the strength of a pile for a given web thickness reduction (Dawood et al. 2017). ....	3
Figure 1.4 Retrofitting using bolted steel channels (GDOT 2012).....	5
Figure 1.5 Concrete encasement retrofitting method (ODOT 2008).....	6
Figure 1.6 FRP jacket retrofitting types (Dawood et al. 2017).....	7
Figure 2.1 Three-dimensional (3D) view of the simulated H-pile.....	12
Figure 2.2 Vertical and horizontal constraints for the loading plates. ....	13
Figure 2.3 Mesh size for FE model of pile 0/0. ....	14
Figure 2.4 Experimental (Belarbi and Dawood 2015) versus FEMs for specimens: (a) 0/0, ( b) 0/20, (c) 20/40, (d) 40/60, and (e) 80/60.....	16
Figure 2.5 Comparison between the modes of failure of the experimental and finite element models: (a) 0/0, (b) 0/20, (c) 20/40, (d) 40/60 and (e) 80/60.....	17
Figure 2.6 Three-dimensional (3D) view of simulated H-piles with different eccentricity: (a) $e=0$ mm; (b) $e=50$ mm; (c) $e=100$ mm; (d) $e=150$ mm. ....	19
Figure 2.7 Effect of eccentricity of load about minor axis on capacity of: (a) Pile (0-0);(b) Pile (0-20); (c) Pile (40-20); (d) Pile (40-60); (e) Pile (80-60).....	20
Figure 2.8 Residual axial capacity with eccentric loads. ....	21
Figure 2.9 Boundary conditions for the H-piles. ....	22
Figure 2.10 Deformed shape of corroded piles.....	25
Figure 2.11 Axial load vs axial shortening of corroded piles having 50% reduction in the thickness of: (a) flanges with different reductions in the thickness of web (b) web with different reductions in the thickness of flange. ....	25
Figure 2.12 Reductions in the axial load capacity due to different reductions in the web and flanges. ....	26
Figure 2.13 Undeformed and deformed shapes of the corroded piles in groups C and D.....	29
Figure 2.14 Axial load vs axial shortening of corroded piles having different corroded lengths: (a) piles with reduction of 70% in the thickness of web and 50% in the thickness of flanges, and (b) piles with reduction of 0% in the thickness of web and 50% in the thickness of flanges. ....	30
Figure 2.15 Reductions in the axial load capacity due to different reductions in the corroded section lengths. ....	30
Figure 2.16 Axial load vs axial shortening of corroded piles having different corroded section locations and a reduction of: (a) 50% in the thickness of web and 70% in the flanges, (b) 70% in the thickness of web and 50% in the flanges, and (c) 0% in the thickness of web and 50% in the flanges. ....	32
Figure 2.17 Undeformed and deformed shapes of the corroded piles in groups E, F, and G.....	33
Figure 2.18 Mesh generation and sizes of the voids in the webs.....	34
Figure 2.19 Mesh generation and sizes of the cuts in the flanges.....	35
Figure 2.20 Axial load vs axial shortening of corroded piles having different sizes for the cut in the: (a) Web with fixed cut size in the flanges, and (b) Flanges with fixed void size in the web. ....	36
Figure 2.21 Reductions in the axial load capacity due to different void and cut sizes in the pile.....	36
Figure 3.1 Effective width method (AISI, 2012).....	39

Figure 3.2 Reduction details of the investigated piles: (a) W70-F00, (b) W00-F50, (c) W70-F50, (d) W70-F50/0, (e) W70V-F50, (f) W70-F50C, (g) W70V-F50C, (h) W70-F50-6.....	44
Figure 3.3 Test setup: (a) drawing, and (b) picture.....	49
Figure 3.4 Loading instruments: (a) hydraulic jack, and (b) rail track with rolling cylinders.....	49
Figure 3.5 Swivel plates (a) maximum rotation, and (b) installed in the setup. ....	50
Figure 3.6 Eccentricity of the swivel with the pile. ....	50
Figure 3.7 Layout of the SPs.....	51
Figure 3.8 Installation of strain gauges on H-pile: (a) Type 1, and (b) Type 2. ....	52
Figure 3.9 Installation of strain gauges on post-tensioned bar. ....	53
Figure 3.10 Axial force-Axial shortening relation: (a) W00-F00, (b) W70-F00, (c) W00-F50, (d) W70-F50, (e) W70-F50/0, (f) W70V-F50, (g) W70-F50C, (h) W70V-F50C, (i) W70-F50-6 , (j) W70V-F50C-10%, (k) W70V-F50C-30%, (l) W70-F50-10%. ....	55
Figure 3.11 Failure during the experimental vs. FEMs (a) W00-F00 , (b) W70-F00, (c) W00-F50, (d) W70-F50, and (e) W70-F50/0.....	58
Figure 3.12 Failure during the experimental vs FEMs (a) W70V-F50 , (b) W70-F50C, (c) W70V-F50C, (d) W70-F50-6in. ....	59
Figure 3.13 Correlation between experimental to analytical axial capacity and remaining cross-sectional area.....	61
Figure 4.1 Test specimen layout. ....	64
Figure 4.2 Steel tubes average stress-strain curve (a) flange, and (b) web.....	65
Figure 4.3 Particle size distribution of the coarse and fine aggregates. (Note: CA: coarse aggregate) .....	66
Figure 4.4 H-pile repair (a) assembly, (b) section 1-1, (c) section 2-2, (d) Sonotube installation, and (e) the assembly ready for concrete placement.....	69
Figure 4.5 Instrumentation: (a) strain gauges mounted on the steel H-pile, (b) two LVDTs on each pile, (c, d, and e) strain gauges layout for $L_{CE}$ =254, 508, 762 mm (10, 20, and 30 in.). ....	70
Figure 4.6 Concrete encasement procedure (a) placing, (b) vibrating, and (c) finalizing. ....	72
Figure 4.7 Geopolymer concrete curing process (a) GA, and (b and c) GT.....	73
Figure 4.8 Concrete encased steel H-pile columns under push-out test (a) test layout, (b) $L_{CE}$ = 254 mm (10 in.), (c) $L_{CE}$ = 508 mm (20 in.), and (d) $L_{CE}$ = 762 mm (30 in.). ....	74
Figure 4.9 Concrete encasement crack patterns with different embedment length ( $L_{CE}$ ) of 254, 508, 762 mm (10, 20, and 30 in.) (a-c) CC, (d-f) HES, (g-i) GA, and (j-l) GT.....	76
Figure 4.10 Concrete encasement – steel H-pile contact area condition (a) $L_{CE}$ =254 mm (10 in.), (b) $L_{CE}$ =508 mm (20 in.). ....	77
Figure 4.11 Typical bond stress ( $\tau$ ) versus slip curve .....	78
Figure 4.12 Bond stress versus slip of the tested H-pile columns encased with concrete (a) CC, (b) HES, (c) GA, and (d) GT. ....	79
Figure 4.13 Bond strength ratio of the tested composite columns.....	80
Figure 4.14 Passive film formation (a) GA specimen ( $L_{CE}$ =508 mm (20 in.)), (b) closer view... ..	81
Figure 4.15 Bond strength versus $f'_c$ : (a) absolute, and (b) normalized values. ....	82
Figure 4.16 Strain distribution along 254 mm (10 in.) embedded length ( $L_{CE}$ ) of different concrete encasement (a) CC, (b) HES, (c) GA, and (d) GT.....	83
Figure 4.17 Strain distribution along 508 mm (20 in.) embedded length ( $L_{CE}$ ) of different concrete encasement (a) CC, (b) HES, and (c) GT. ....	84
Figure 4.18 Strain distribution along 762 mm (30 in.) embedded length ( $L_{CE}$ ) of different concrete encasement (a) CC, (b) HES, and (c) GA. ....	85

Figure 5.1 Test specimens (a) RS, (b) repaired with studs on the web and CFRP, (c) repaired with studs on the flanges and CFRP. ....	87
Figure 5.2 Average steel pile stress-strain curves. ....	89
Figure 5.3 Tested CFRP coupon results. ....	91
Figure 5.4 HS attached to web and flanges of the steel pile. ....	92
Figure 5.5 CFRP wrapping process. ....	94
Figure 5.6 Concrete encasement: (a) placement, (b) vibrating, and (c) finalizing. ....	94
Figure 5.7 Test instrumentation (a) strain gauges layout, mounted on the steel H-piles and the CFRP jacket, (b) strain gauges covered with mastic rubber protection, (c) two LVDTs set up on each steel H-pile flanges sides. ....	96
Figure 5.8 Push-out test setup: (a) layout, and (b) specimen during the test. ....	97
Figure 5.9 Failure modes of the test specimens. ....	101
Figure 5.10 Bond stress-slip model. ....	103
Figure 5.11 Bond stress ( $\tau$ ) vs. axial displacement. ....	106
Figure 5.12 Residual strength of the tested specimens. ....	107
Figure 5.13 Headed stud conditions (a and b) $d_a=25.4$ mm (1 in.), (c and d) $d_a=19$ mm (0.75 in.), (e and f) $d_a=12.5$ mm (0.5 in.). ....	109
Figure 5.14 Bond strength ratio vs. $A_{hs}$ . ....	109
Figure 5.15 Axial force vs. displacement with shear resistance ( $P_{u(hs)}$ ) of the HS. ....	114
Figure 5.16 CFRP failure mode (a) C6 (1P-8HS-1W), (b) C7 (2P-4HS-1W), (c) C8 (2P-8HS-1W). ....	116
Figure 5.17 CR versus (a) bond stress ratio, and (b) 8HS specimen experimental axial load ( $P_{exp}$ )–to –yield load ( $P_y$ ) ....	117
Figure 5.18 Strain vs. CE length ( $L_{CE}$ ) for the tested specimens. ....	119
Figure 6.1 All threaded bars and heavy-duty nuts used as HSs. ....	121
Figure 6.2 Distributions of the HSs in the three H-piles: (a) R-1, (b) R-2, and (3) R-3. ....	121
Figure 6.3 Longitudinal reinforcement in the repair region: (a) closed bar profile, (b) distributions of rebars, and (c) reinforcement cage. ....	122
Figure 6.4 ASTM tests: (a) Slump flow, (b) Passing ability using J-ring, and (c) L-box. ....	124
Figure 6.5 (a) Magnetic drill used to drill holes for the HSs, and (b) general distribution for studs. ....	125
Figure 6.6 Specimens after CFRP Installation. ....	126
Figure 6.7 Strain gauges distribution on the flanges and web of H-pile. ....	127
Figure 6.8 Strain gauges distribution on the CFRP cross-section (a) Cross section (b) longitudinal direction. ....	128
Figure 6.9 String potentiometer vertical and horizontal measurements. ....	128
Figure 6.10 Experimental axial load vs. displacement curves (a) R1, (b) R2, and (c) R3. ....	130
Figure 6.11 FE of the repaired piles and HSs layout of (a) R-1, (b) R-2, and (c) R-3. ....	132
Figure 6.12 FE modeling: (a) 3D view of the repaired steel pile, (b) steel H-pile, (c) CFRP tube, (d) concrete filling, and (e) steel rebar. ....	133
Figure 6.13 Axial load vs. displacement curves (a) R1, (b) R2, and (c) R3. ....	137
Figure 6.14 Failure modes of the simulated repaired pile R1 (a) exp., (b) FE whole system, (c) Exp. steel pile localized buckling, (d) FE steel pile localized buckling, and (e) concrete encasement stress concentration. ....	139
Figure 6.15 Stress concentration at the tips of flanges on the concrete encasement. ....	140
Figure 6.16 Failure modes of the simulated repaired pile R3 (a and c) exp., (b and d) FE. ....	141

Figure 6.17 Failure modes of the simulated repaired pile R2 (a) exp., (b and c) FE.....	142
Figure A.1 Deformation profile with respect to the pile length: (a) Horizontal profile, (b) Vertical profile.....	154
Figure A.2 Axial shortening-steel strains in different position of pile: (a) 9in from edge,(b) 57.5in from edge, (c) 60in. from edge, (d) 62.5in. from edge, (e) 111in. from edge. FN: Flange north FS: Flange south WW: Web west WE: Web east .....	155
Figure A.3 Deformation profile with respect to the pile length: (a) Horizontal profile, (b) Vertical profile.....	155
Figure A.4 Axial shortening-steel strains in different position of pile: (a) 6in from edge, (b) 53in. from edge, (c) 55in. from edge, (d) 57.5in. from edge, (f) 60in. from edge, (e) 62.5 from edge, and (g) 114in. from edge .....	156
Figure A.5 Deformation profile with respect to the pile length: (a) Horizontal profile, (b) Vertical profile.....	157
Figure A.6 Axial shortening-steel strains in different position of pile: (a) 6in from edge,(b) 51in from edge, (c) 53in. from edge, (d) 55in. from edge, (e) 57.5in. from edge, (f) 60in. from edge, (g) 62.5 from edge, and (h) 114in. from edge .....	158
Figure A.7 Deformation profile with respect to the pile length: (a) Horizontal profile, (b) Vertical profile.....	158
Figure A.8 Axial shortening-steel strains in different position of pile: (a) 6in from edge, (b) 53in. from edge, (c) 55in. from edge, (d) 57.5in. from edge, (f) 60in. from edge, (e) 62.5 from edge, and (g) 114in. from edge .....	159
Figure A.9 Deformation profile with respect to the pile length: (a) Horizontal profile, (b) Vertical profile.....	159
Figure A.10 Axial shortening-steel strains in different position of pile: (a) 6in from edge, (b) 53in. from edge, (c) 55in. from edge, (d) 57.5in. from edge, (f) 60in. from edge, (e) 62.5 from edge, and (g) 114in. from edge .....	160
Figure A.11 Deformation profile with respect to the pile length: (a) Horizontal profile, (b) Vertical profile.....	161
Figure A.12 Axial shortening-steel strains in different position of pile: (a) 6in from edge, (b) 53in. from edge, (c) 55in. from edge, (d) 57.5in. from edge, (f) 60in. from edge, (e) 62.5 from edge, and (g) 114in. from edge .....	162
Figure A.13 Deformation profile with respect to the pile length: (a) Horizontal profile, (b) Vertical profile.....	162
Figure A.14 Axial shortening-steel strains in different position of pile: (a) 6in from edge, (b) 53in. from edge, (c) 55in. from edge, (d) 57.5in. from edge, (f) 60in. from edge, (e) 62.5 from edge, and (g) 114in. from edge .....	163
Figure A.15 Deformation profile with respect to the pile length: (a) Horizontal profile, (b) Vertical profile.....	164
Figure A.16 Axial shortening-steel strains in different position of pile: (a) 6in from edge, (b) 53in. from edge, (c) 55in. from edge, (d) 57.5in. from edge, (f) 60in. from edge, (e) 62.5 from edge, and (g) 114in. from edge .....	165
Figure A.17 Deformation profile with respect to the pile length: (a) Horizontal profile, (b) Vertical profile.....	165
Figure A.18 Axial shortening-steel strains in different position of pile: (a) 6in from edge, (b) 53in. from edge, (c) 55in. from edge, (d) 57.5in. from edge, (f) 60in. from edge, (e) 62.5 from edge, and (g) 114in. from edge .....	166

Figure A.19 Deformation profile with respect to the pile length: (a) Horizontal profile, (b) Vertical profile.....	167
Figure A.20 Axial shortening-steel strains in different position of pile: (a) 6in from edge, (b) 53in. from edge, (c) 55in. from edge, (d) 57.5in. from edge, (f) 60in. from edge, (e) 62.5 from edge, and (g) 114in. from edge .....	168
Figure A.21 Deformation profile with respect to the pile length: (a) Horizontal profile, (b) Vertical profile.....	168
Figure A.22 Axial shortening-steel strains in different position of pile: (a) 6in from edge, (b) 53in. from edge, (c) 55in. from edge, (d) 57.5in. from edge, (f) 60in. from edge, (e) 62.5 from edge, and (g) 114in. from edge .....	170
Figure A.23 Deformation profile with respect to the pile length: (a) Horizontal profile, (b) Vertical profile.....	170
Figure A.24 Axial shortening-steel strains in different position of pile: (a) 6in from edge, (b) 53in. from edge, (c) 55in. from edge, (d) 57.5in. from edge, (f) 60in. from edge, (e) 62.5 from edge, and (g) 114in. from edge .....	171
Figure B.1 Steel H-pile cleaning and strain gauges attaching .....	172
Figure B.2 Form working .....	173
Figure B.3 GT curing chamber manufacturing.....	174
Figure B.4 Specimens concrete mixing and Amb. curing .....	175
Figure B.5 CFRP jacket (Fabric) works .....	176
Figure B.6 CFRP jacket (Laminate) works.....	177
Figure B.7 CFRP jacket + HS specimen concrete placing .....	178
Figure B.8 Specimen push-out testing.....	179
Figure B.9 Stacking of the piles for storing .....	182
Figure B.10 Milling the flanges to the reduced thickness .....	182
Figure B.11 Milling the webs to the reduced thickness.....	183
Figure B.12 Cleaning and painting the specimen with white water based paint .....	183
Figure B.13 Trimming the rough edges of the specimens .....	184
Figure B.14 Attaching strain gauges to the expected points of failure .....	184
Figure B.15 Installing the specimen in the testing setup .....	185
Figure B.16 Local position of failure: (a) W00-F00, (b) W70-F00,.....	186
Figure B.17 Local position of failure: (a) W70-F50, (b) W70-F50/0.....	186
Figure B.18 Local position of failure: (a) W70V-F50, (b) W70-F50C .....	187
Figure B.19 Local position of failure: (a) W70V-F50C, (b) W70-F50-6in.....	187
Figure B.20 Addition of stiffeners at the location of loading (a) stiffeners pattern (b) position of the stiffeners.....	188
Figure B.21 Calibration of the used instrumentations (a) bolt of swivel plate (b) hydraulic jacks.....	188
Figure B.22 Rail system for the loading beam (a) bottom track and roller (b) top roller.....	189

## List of Tables

Table 2.1 Summary of the Investigated Piles and Their Experimental Results (Modified from Shi and Dawood 2015).....	10
Table 2.2 Summary of Validated FE Results against the Experimental Results .....	17
Table 2.3 Failure Loads with Different Load Eccentricities.....	19
Table 2.4 Summary of the Investigated Parameters for the FEMs .....	23
Table 2.5 Summary of the Investigated FEMs for Corrosion Extension.....	27
Table 2.6 Summary of the Investigated FEMs for Corrosion Location .....	31
Table 2.7 Summary of the Investigated FEMs for Web Voids.....	34
Table 2.8 Summary of the Investigated FEMs for Flange Cuts .....	35
Table 3.1 Summary of the Test Specimens .....	45
Table 3.2 Actual Dimensions of the Tested Piles .....	46
Table 3.3 Sectional Properties at Minimum Cross Section based on the Measured Dimensions for Concentrically loaded Specimens .....	47
Table 3.4 Summary of the Results for the Tested Piles.....	56
Table 3.5 Evaluating the axial capacity of the tested specimens using existing design specifications .....	61
Table 4.1 Parametric Study .....	63
Table 4.2 Mechanical Properties of Steel H-Pile Flange and Web.....	64
Table 4.3 Chemical Composition of FAs by XRF.....	66
Table 4.4 Mix Design of CC, HES, and Geopolymer Concrete Mixtures.....	67
Table 4.5 Specimen Geometrical Properties.....	68
Table 4.6 Test Results of the Push-Out Tests of Concrete Encased H-Pile Columns .....	75
Table 5.1 Parametric Study of the Tested Specimens.....	88
Table 5.2 Mechanical Properties of Steel H-pile Flange and Web.....	89
Table 5.3 Mix Design of the Conventional Concrete (CC) Mixture .....	90
Table 5.4 Measured Mechanical Properties of CFRP.....	90
Table 5.5 Mechanical Properties of the Epoxy Resins per Manufacturers' Data .....	91
Table 5.6 Specimen Geometrical Properties.....	92
Table 5.7 Test Results of the Investigated Specimens.....	98
Table 5.8 Shear Resistance ( $P_{u(hs)}$ ) Results of the Investigated Specimens .....	111
Table 5.9 CFRP Jacket Hoop Strain Gauges Readings at Peak Strength .....	117
Table 6.1 Mixture Used for the Concrete .....	123
Table 6.2 Arrangement of HSs in Different Test Specimens .....	125
Table 6.3 Mechanical Properties of the Headed Stud Elements .....	135
Table 6.4 Mechanical Properties of the Steel Rebar Elements.....	135

## Acknowledgements

The authors would like to acknowledge the many individuals and organizations that made this research project possible. The authors wish to extend a very sincere thank you to the Mid-America Transportation Center (MATC) which provided valuable match funding from the United States Department of Transportation through RITA. The authors would like also to extend their appreciation to Missouri Department of Natural Resources (MoDNR), Missouri Department of Transportation. In addition to their financial support, the authors appreciate MoDOT's vision and commitment to innovative concepts and pushing the boundaries of current practice.

The authors would also like to thank the companies that provided material contributions necessary for the successful completion of this project, including Skyline Steel and QuakeWrap Inc.

Finally, the authors would like to thank Missouri S&T for their valuable contributions to the research. The authors also appreciate the tireless staff of the Department of Civil, Architectural, and Environmental Engineering and the Center for Infrastructure Engineering Studies. Their assistance both inside and out of the various laboratories was invaluable to the successful completion of this project.

## Executive Summary

This report summarizes the details of an experimental work and finite element modeling that were conducted to evaluate: 1) the remaining axial capacity of steel H-piles having different corrosion severity and extension levels, and 2) the performance of repaired corroded steel H-piles. The research consisted of 32 short steel H-piles ( $10 \times 42$ ) encased in different types of concrete including conventional concrete, high strength concrete, high-early strength concrete, and geopolymer concrete. Different embedment lengths and shear studs were used. Thirteen long steel H-piles ( $10 \times 42$ ) were milled to represent the loss of cross-sectional area associated with corrosion and tested under concentric and eccentric axial loads. Different corrosion levels and patterns were considered.

This report includes seven chapters. Chapter 1 presents an overview of the problem and existing solutions. Chapter 2 presents different finite element models that were calibrated versus data from the literature. Then, the developed models were used to predict the performance of full-scale H-piles having different corrosion scenarios. Chapter 3 presents an experimental work to assess the load carrying capacity of corroded piles subjected to concentric and eccentric axial loads. Chapter 4 presents the results of H-piles embedded in concrete jackets. The concrete was made of either conventional concrete, high early strength concrete, or geopolymer concrete. Different embedment lengths were investigated as well. Chapter 5 presents pushout testing of H-piles embedded into concrete-filled FRP jackets. Different types of FRP jackets, confinement ratios, and head stud stiffness's were investigated. Chapter 6 presents the results of analytical and experimental work on H-piles repaired using FRP jackets. Chapter 7 summarizes the main conclusions and findings of the research project.



According to the obtained and observed results from the test, the axial capacity of the concentrically loaded corroded H-piles decreases as the corrosion severity increases. Both the FEMs and experimental work showed that the buckling load is more susceptible to corrosion in the flanges. The length of the corroded region had no effect on the axial load capacity. Increasing the concrete compressive strength increased the bond strength. Furthermore, implementing different concrete jackets types was successful in producing compressive strengths similar to those of the conventional concrete. Using the CFRP jackets without headed studs slightly increased the bond stress between the concrete jackets and steel piles. Using headed studs and CFRP jackets increased the bond strength between the jackets and steel piles by a range of 580% to 1,130%, compared to the reference specimen. Using headed studs considerably increased the bond strength between the concrete jackets and steel piles.

## Chapter 1 Introduction

Stakeholders, including bridge owners, departments of transportation engineers, and researchers, have been working for years to develop reliable and efficient ways to maintain and prolong the life of bridges across the United States. For example, the Missouri Department of Transportation (MoDOT) is responsible for maintaining nearly 10,400 bridges on the state system. These bridges have an average age of 46 years, and most of them were designed to last 50 years. Furthermore, Missouri is the 4<sup>th</sup> highest state in terms of deficient bridges, with 3,222 deficient bridges (FHWA 2015). Many of these were constructed using steel H-piles as substructures. Steel H-piles carry a large amount of loads while occupying a relatively small area.

Inspection of many of these bridges revealed severe localized corrosion damage due to aggressive environmental conditions or repetitive dry-wet cycles in a variable level of water table (figs. 1.1 and 1.2). Therefore, there is an urgent need to repair these piles using new techniques that have longer durability and require less maintenance during the extended service lifetime of the bridge.



**Figure 1.1** Corrosion of H-piles in I-70/I-270 interchange in St. Louis.



**Figure 1.2** Corroded steel column.

Pile corrosion can be classified into minor, moderate, or major based on the remaining capacity of the pile (Fig. 1.3). Minor damage is defined when the yield strength of the corroded section of the pile is higher than the original design load of the pile. Thus, the pile requires only stiffening sufficient to prevent local and global buckling in order for a remediation measure to be effective. Both moderate and major damages are characterized as the yield strength of the corroded section of a pile being smaller than the original design load of the pile. The pile would require load sharing repair or an alternative load path to reach the design capacity.

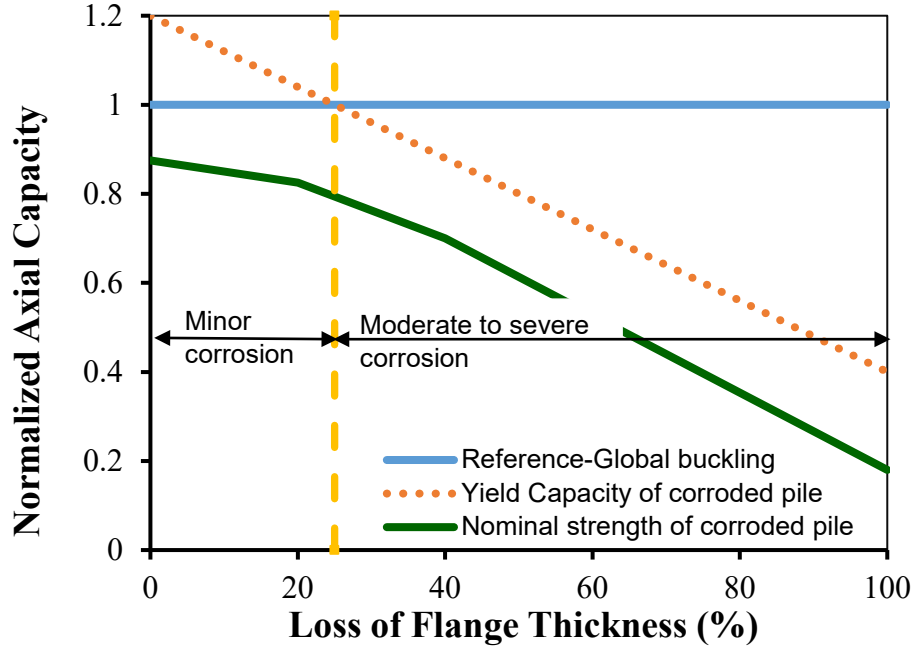


**Figure 1.3** An example of the strength of a pile for a given web thickness reduction (Dawood et al. 2017).

Researchers used experimental, analytical, and numerical methods to accurately estimate the residual capacity of corroded members having different steel sections (Beaulieu et al. 2010; Kayser and Nowak 1989; Paik et al. 2003; Sarveswaran et al. 1998; Shi et al. 2014). A corrosion model was developed for steel girder bridges, which took into account the location and rate of corrosion (Kayser and Nowak 1989). Sarveswaran et al. (1998) evaluated the structural safety of corroded steel structures by applying the theory of structural reliability. The model predicts an interval of residual capacity based on an estimate of the remaining thickness of the member (Sarveswaran et al. 1998). Paik et al. (2003) developed a simple design formula to predict the ultimate compressive capacity of a plate with pit corrosion based on experiments and numerical analysis. Beaulieu et al. (2010) evaluated the axial compressive strength of corroded steel angles that were used in transmission towers (Beaulieu et al. 2010). These studies revealed that the current codes did not accurately predict the capacity of corroded members.

A non-linear finite element analyses on panels with various locations and sizes of pitting corrosion was conducted (Ok et al. 2007) to investigate the effects of localized corrosion on the axial capacity of unstiffened plates. The results indicated that increasing the length, width, or depth of pit corrosion reduced the capacity of the plates, although the plate slenderness did not significantly influence the capacity (Ok et al. 2007).

Shi (2014) carried out an analytical study on the axial assessment of corroded steel sections W4×13 with the baseline model validated against experiments on the same sections by Karagah et al. (2013) (Karagah and Dawood 2013). The analytical study varied in location, configuration, and severity of deterioration to evaluate the sensitivity of axial capacity to the various parameters. It was determined that flange deterioration was the single factor that most significantly affected the remaining axial capacity of the pile. It was also established that the location of the deterioration along the pile did not have a significant effect on the axial capacity.

By knowing what capacity still remains, an appropriate retrofit can be applied to a pile. Many repair techniques have been implemented by DOTs for strengthening and ensuring the integrity of corroded steel H-pile columns. Retrofitting involves steel channels bolted or welded (fig. 1.4) to the exterior of the flange across the damaged area of the pile were used by IADOT (Wipf et al. 2003), GDOT (Georgia Department of Transportation 2012), WisDOT (Wan et al. 2013), and Department of the Army (1991). This type of repairing would only serve as a temporary repair because of its susceptibility to continued corrosion (Stauffer 2016).

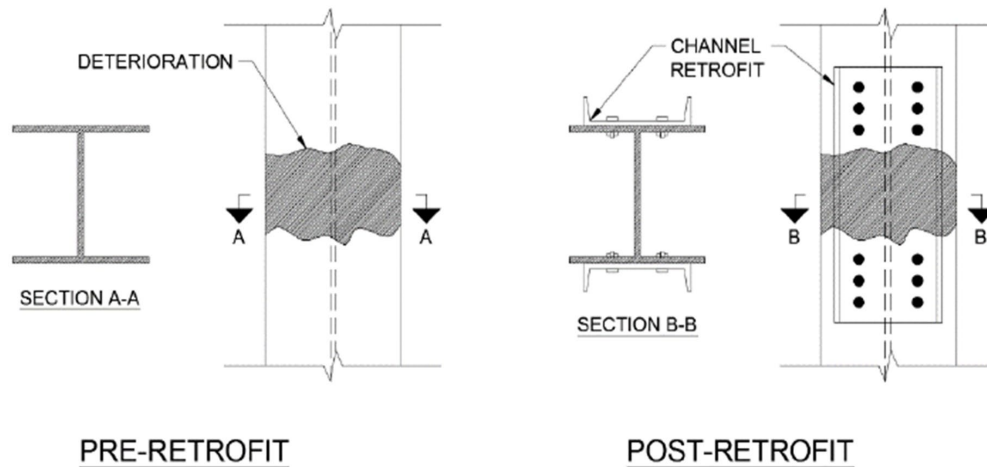


**Figure 1.4** Retrofitting using bolted steel channels (GDOT 2012).

Another repair technique included the application of a concrete jacket (fig. 1.5) to corroded steel members to avert the corrosion and increase the strength. It was considered one of the most cost effective and easy to implement retrofit techniques (Soliman et al. 2013). The form can remain in place as part of the jacket or be removed, leaving the concrete on the retrofitted piling (Army and Air Force 1994; Georgia Department of Transportation 2012; Wipf et al. 2003). In some cases, reinforcement can be embedded into the concrete to add sufficient strength and to compensate for the loss of the weak axis bending stiffness (Dawood et al. 2017). This method of retrofitting provides continuous bracing along the deteriorated section, but also inhibits monitoring the condition of the steel after the retrofit is made (Florida Department of Transportation 2011).



**Figure 1.5** Concrete encasement retrofitting method (ODOT 2008).

For severely corroded H-piles, the concrete encasement works as an alternative load path for the applied axial load. Hence, the concrete jacket needs to extend beyond the corroded section and embedment length. Successful transfer of load from steel through the embedment length to the concrete depends on the bond strength between the concrete and steel interface. When the interfacial shear stress between two materials exceeds the bond strength, bond failure and severe slip occurs. A good understanding of the bond behavior of the concrete and steel is, therefore, pertinent for the retrofit of corroded steel pile. Furthermore, concrete with recycled or byproduct constituents such as geopolymer concrete or concrete including recycled aggregate can be used for the repair in order to reduce its carbon footprint (Dahou et al. 2016; Doguparti 2015; Jaffar et al. 2016). However, few studies have been conducted to investigate the bond strength of the geopolymer concrete.

Another option to repair corroded piles includes the use of concrete-filled fiber-reinforced polymer (FRP) jackets. FRP jackets have been used worldwide for retrofitting a large number of deteriorated reinforced concrete and steel bridge columns, and are considered one of

the most efficient and reliable methods available to remedy structural element deterioration. In the case of column repair, the procedure including wrapping the built-up section with an FRP jacket and filling the jacket with grout or expansive concrete. Using the expansive lightweight concrete allows the FRP jacket to provide active confinement to the steel columns, and hence increases the bond strength and the load capacity of the retrofitted columns (Liu et al. 2005; Vijay et al. 2016). While FRP jacketing of concrete columns is a well-established technique, there has been substantially less research conducted to investigate the effectiveness of this method to retrofit steel piles (fig. 1.6). Moreover, the concrete and FRP tube restrain the steel section, so their susceptibility to buckling is greatly reduced (Karimi et al. 2011; Teng and Yu 2015).

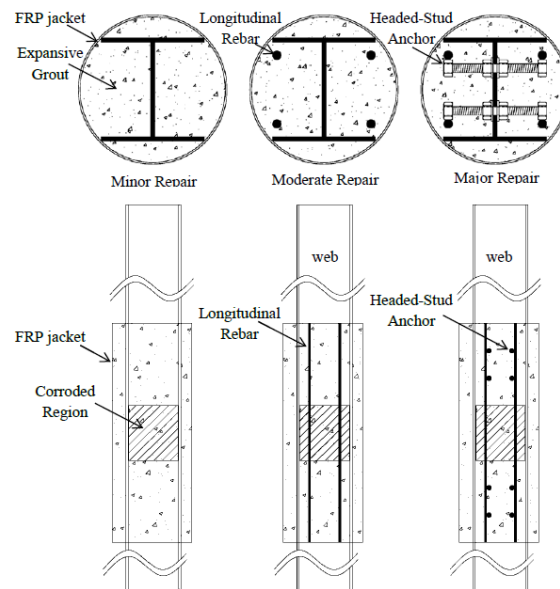


**Figure 1.6** FRP jacket retrofitting types (Dawood et al. 2017).



To improve the load transfer between the FRP jacketing and existing steel structural element, shear studs may be used (Alenezi et al. 2015; Vijay et al. 2016). Headed steel studs are subjected to flexural and axial forces in resisting the interfacial shear forces between the existing column and FRP jacketing. Consequently, the force transfers to the concrete-filled FRP jackets depending on the strength and stiffness of the studs, concrete, and FRP jacket.

Limited research has been conducted to investigate the composite action of steel columns having shear connectors embedded in concrete encasement confined by FRP jackets (Dawood et al. 2017; Vijay et al. 2016). It was concluded that the force transfer between concrete and steel increased with the use of shear connectors as they provide mechanical anchorage, and their use was highly recommended. Using headed-stud anchors reduced the amplitude of the pile-localized deformations within the corroded region and the axial shortening of the piles as well as the slip at the steel-concrete interface. Moreover, after bond failure, the anchors were able to transfer the shear forces from the steel pile to the concrete encasement. The hoop strain in the FRP jackets of the piles that were retrofitted with headed-stud anchors was also lower than the hoop strain in the FRP jackets of those piles that were retrofitted without anchors (Dawood et al. 2017; Vijay et al. 2016).

The bond between a concrete jacket and steel is commonly determined using a push-out test (Grzeszykowski and Szmigiera 2017; Pecce and Ceroni 2010; Zheng et al. 2016). Different parameters such as concrete compressive strength, presence of steel reinforcement, and the interface conditions were investigated. It was concluded that the bond strength depends on interface roughness and the compressive strength of concrete. Moreover, the application of load on steel sections does not change the residual bond strength. However, studying the effect of different FRP retrofitting system parameters such as confinement ratio, cross-sectional

configuration, and diameter, different headed studs' sizes in a retrofit system are still very limited.

### 1.1 Layout of the report

This report includes seven chapters. Chapter 1 presents an overview of the problem and existing solutions. Chapter 2 presents different finite element models that were calibrated versus data from the literature. Then, the developed models were used to predict the performance of full-scale H-piles having different corrosion scenarios. Chapter 3 presents experimental work to assess the load carrying capacity of corroded piles subjected to concentric and eccentric axial loads. Chapter 4 presents the results of H-piles embedded in concrete jackets. The concrete was made of either conventional concrete, high early strength concrete, or geopolymer concrete. Different embedment lengths were investigated as well. Chapter 5 presents push-out testing of H-piles embedded into concrete-filled FRP jackets. Different types of FRP jackets, confinement ratios, and head stud stiffness's were investigated. Chapter 6 presents the results of analytical and experimental work on H-piles repaired using FRP jackets. Chapter 7 summarizes the main conclusions and findings of the research project.

## Chapter 2 Finite Element Modeling

### 2.1 Introduction

This chapter presents nonlinear finite element models (FEMs) of steel H-piles that were subjected to axial loads. The FEMs were validated against the experimental results gathered from five steel H-piles tested by Shi et al. (2015). The main parameter in this set of data was the severity of the corrosion of the investigated piles. The developed FEMs were used to conduct a numerical parametric study investigating the severity of corrosion in the form of corrosion location, extension, and form. The FEMs were developed using Ls-Dyna R9 solver (Ls-Dyna 971 Manual).

### 2.2 FE Model Calibration

Five piles having pin-pin boundaries were investigated during an experimental work (Shi, 2015) and simulated during this chapter. This included a reference pile and four corroded piles. The corrosion was simulated using a reduction in the thickness of the web, ranging from 20% to 80%, and/or the flange, ranging from 20% to 60% (table 2.1). The piles designation consisted of two numbers: the first one representing the reduction in the web followed by a backslash and the second one representing the reduction in the flanges.

**Table 2.1** Summary of the Investigated Piles and Their Experimental Results (Modified from Shi and Dawood 2015)

Pile designation	Loss of cross section (%)	Axial capacity (kN)	Loss of axial capacity (%)	Failure mode
0/0	0.0	2771	0.0	GB
0/20	3.1	2688	3.0	GB
20/40	32.7	1936	30.1	FLB
40/60	48.2	1481	46.6	FLB,WLB
80/60	67.9	811	70.7	FLB,WLB

Note: GB = global buckling; FLB = flange local buckling; WLB = web local buckling

### *2.2.1 Geometry*

A typical pile height, measured from the top of the lower loading plate to the bottom of the upper loading plate, was 4750 mm (187 in.). Steel 310 x 79 (12 x 53) H-piles with cross sectional dimensions of 306 mm (12.03 in.) in width and 299 mm (11.75 in.) in length were modeled (fig. 2.1). Each loading plate was 400 x 400 x 100 mm (15.75 x 15.75 x 4 in.). A 100 mm (4 in.) diameter, 400 mm (15.75 in.) long loading cylinder was used at each end.

Each FE model had 5,248 elements and 6,840 nodes. The loading plates and cylinders were modeled using solid elements with an average length of 50 mm (2 in.) and constant-stress one-point quadrature integration to reduce the computational time and increase the model stability. A reduced integration element may suffer from the hourglass effect, which was controlled by selecting sufficiently fine mesh. Furthermore, LS-DYNA has several readily available algorithms to inhibit hourglass mode. The Type 5 algorithm, with an hourglass coefficient of 0.03, was used during the course of this study. The hourglass energy for each model was investigated, and it represented less than 10% of the peak internal energy. The deformed shapes of each investigated model were also carefully investigated for any spurious hourglass-type deformations to ensure that the adopted measures were adequate to avoid the hourglass effect. In addition, specimen 0/0, which represents the reference specimen, was analyzed using two different FEMs having reduced and full integration elements. Both models yielded similar results; however, the full integration FEM used more analysis time. The H-pile cross section was modeled using a fully integrated shell element type 16 with an average size of 50 mm (2 in.).

Surface-to-surface contact elements were used to simulate the interface between the loading plate and pile. This type of contact considers slip and separation that occurs between

master and slave contact pairs. Node-to-surface contact elements were used between the loading cylinder and the pile. The coefficient of friction for all of the contact elements was taken as 0.6.

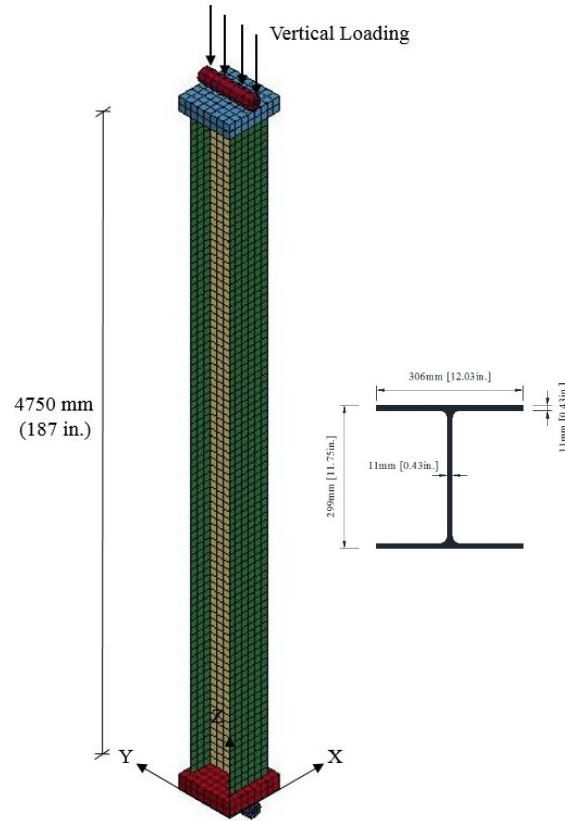


**Figure 2.1** Three-dimensional (3D) view of the simulated H-pile.

### *2.2.2 Loading and Boundary Conditions*

All piles were subjected to displacement-controlled concentric axial compressive load until the FEMs could not proceed any further due to numerical instability, which was designated as failure of the investigated pile.

A loading plate and cylinder were used at each end of each investigated pile, which replicated the pin-pin boundary conditions used during the experimental work. The plate ensured the uniform distribution of the applied axial load on the sections of the piles (fig. 2.1). The

loading plates had no constraints, while the displacements of the loading cylinders were constrained in the Y- and X-directions (fig. 2.2). Furthermore, displacement in the Z-direction of the bottom-loading cylinder was constrained. It should be noted that using the loading cylinder triggered buckling around the weak axis while precluding buckling around the strong axes.

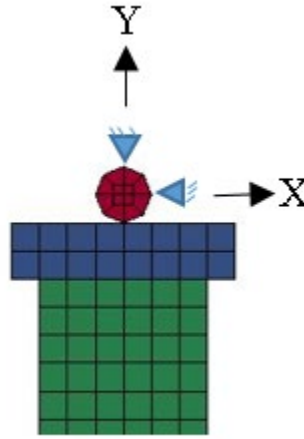


**Figure 2.2** Vertical and horizontal constraints for the loading plates.

### 2.2.3 Material and Element Types

#### 2.2.3.1 H-pile

An elastoplastic constitutive model, 003-plastic\_kinematic, readily available in Ls-Dyna, was adopted to model the webs and flanges of the piles. This model requires the following three material parameters for the used steel to be fully defined: (1) the elastic modulus,  $E$ , (2) the steel's yield stress, and (3) Poisson's ratio,  $\nu$ . The elastic modulus and the yield stress of the flanges were 196.0 GPa (28427ksi) and 360.0 MPa (52.2ksi), respectively, while those for the webs were 221.0 GPa (32053ksi) and 418.0 MPa (60.6ksi), respectively. Both the webs and flanges used a Poisson's ratio  $\nu$  value of 0.3.

### 2.2.3.2 Loading Plates and Cylinders

The loading plates and cylinders were modeled using an isotropic material, 001-elastic. The following three parameters are required to fully define this material model: (1) density, (2)  $E$ , and (3) Poisson's ratio  $\nu$ . The mass density,  $E$ , and  $\nu$  used during this study were  $7.83 \times 10^{-6}$   $\text{Kg/mm}^3$  (0.32 lb. /in<sup>3</sup>.), 500 GPa (72520 ksi), and 0.3 respectively. The loading was applied as an axial compressive load that was applied to all the nodes at the top of the upper cylinder until failure occurred.

### 2.2.4 Sensitivity Analyses

A sensitivity study was conducted to determine the effects of the mesh size on the results. Element sizes of 25, 50, 100, 150 mm (1, 2, 4, and 6 in.) were used for the meshing of the shell elements in pile 0/0. The results indicated that there was a small variation in the strength of the piles due to changing the mesh size (fig 2.3). Considering the accuracy of the results and computational time, a mesh size of 50 mm (2 in.) was used during the remaining course of this study.

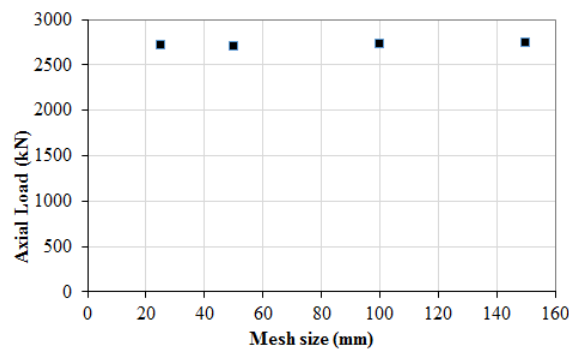
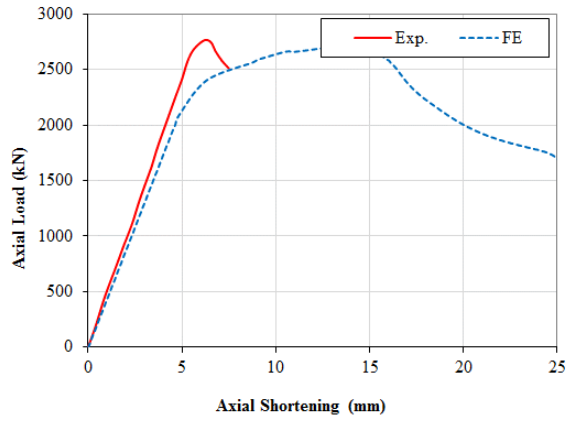


**Figure 2.3** Mesh size for FE model of pile 0/0.

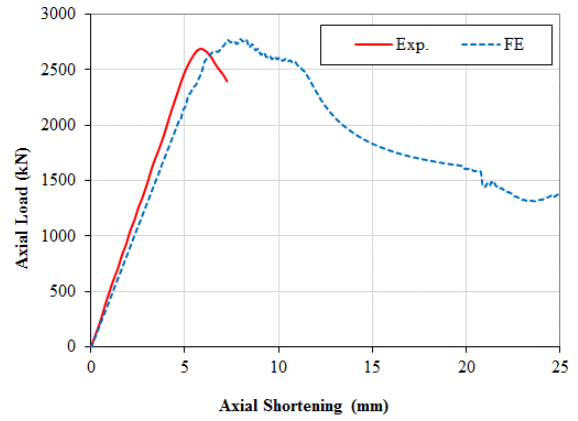
### 2.3 Results and Discussion

The FE models were able to capture the test specimens' behavior in terms of initial stiffness and peak load with an error ranging from 0.4% to 10%. The FEMs were not biased in terms of peak loads, as it overestimated the strengths of two specimens and under estimated the strength of three specimens. The FEMs predicted quite well the modes of failure (fig. 2.4). The FEMs and experimental testing showed that all piles reached their yielding loads, which was followed by either global buckling in the case of piles 0/0 and 0/20 (fig. 2.5 (a, b)), or local buckling in the flange or web, depending on the thickness of the corroded section (fig. 2.5 (c, d, e)).

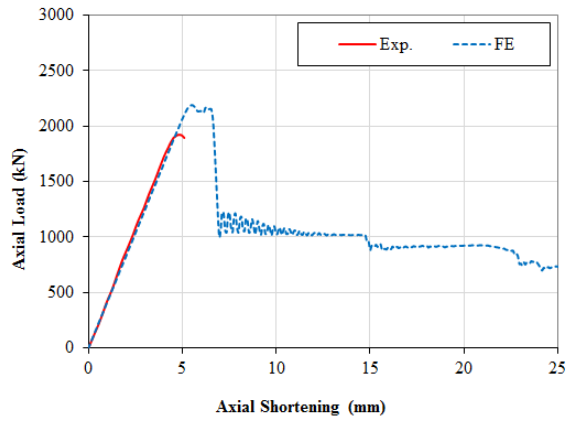




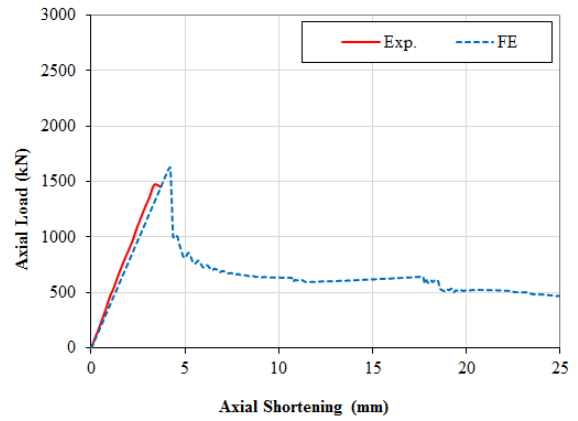
(a)



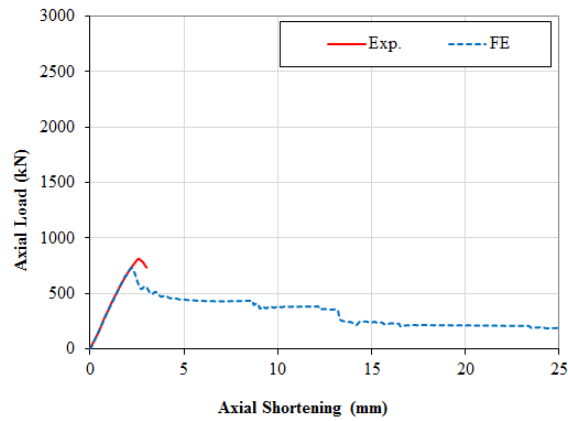
(b)



(c)



(d)



(e)

**Figure 2.4** Experimental (Belarbi and Dawood 2015) versus FEMs for specimens: (a) 0/0, ( b) 0/20, (c) 20/40, (d) 40/60, and (e) 80/60.

**Table 2.2** Summary of Validated FE Results against the Experimental Results

Pile	Axial Capacity		Error (%)	Mode of failure	
	Experimental kN	FE kN		Experimental	FE
0/0	2771	2707	2	GB	GB
0/20	2688	2678	0.4	GB	GB
20/40	1936	2188	13	FLB	FLB
40/60	1481	1630	10	FLB,WLB	FLB,WLB
80/60	810	728	10	FLB,WLB	FLB,WLB

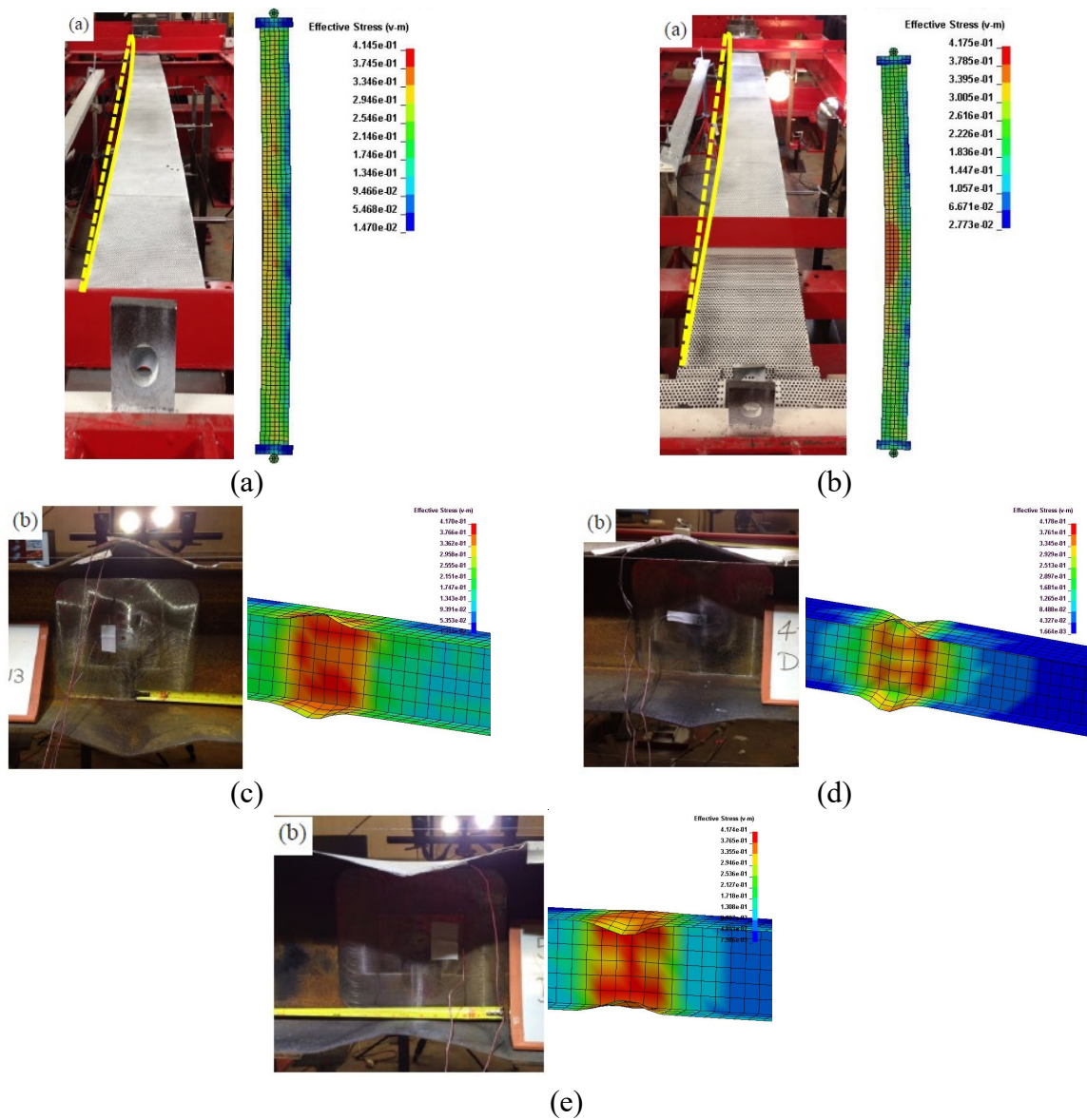


**Figure 2.5** Comparison between the modes of failure of the experimental and finite element models: (a) 0/0, (b) 0/20, (c) 20/40, (d) 40/60 and (e) 80/60.

## 2.4 Effects of Eccentricity on the Corroded Piles

The FEMs developed in this work were used to examine the effects of the eccentricity on the response of the corroded piles. Eccentricity values of 50 mm (2 in.), 100 mm (4 in.), and 150 mm (6 in.), corresponding to  $e/t$  values of 17%, 33%, and 50% where  $t$  is the width of the pile, being 306 mm (12.03 in.), were tested (fig. 2.6). This resulted in analysis of 15 piles.

The eccentricity of the applied load decreased the axial capacity of the investigated piles (figs. 2.7 and 2.8 as well as table 2.3). All specimens displayed significant reduction at  $e/t$  of 17% ranging from 25% to 47% of the peak axial load. Beyond that, the strength reduction was linear and approximately the same rate in the cases of no or minor corrosion or corrosion up to approximately 48% at  $e/t$  of 50%. Increasing the corrosion severity, however, increased the effect of the eccentricity on the peak axial loads. For pile 20/40, the strength reduction was nonlinear, as the mode of failure changed with increased load eccentricity. For lower eccentricity, the mode of failure was global buckling with a reduction of the peak load of 45% at  $e/t$  of 17%. However, for a high eccentricity of 100 mm (4 in.) or higher, the mode of failure changed to FLB/WLB with a reduction in the peak load up to 62% at  $e/t$  of 50%. For severe corrosion in the cases of piles 40/60 and 80/60, the reduction in strength was linear reaching approximately 79% at  $e/t$  of 50%.

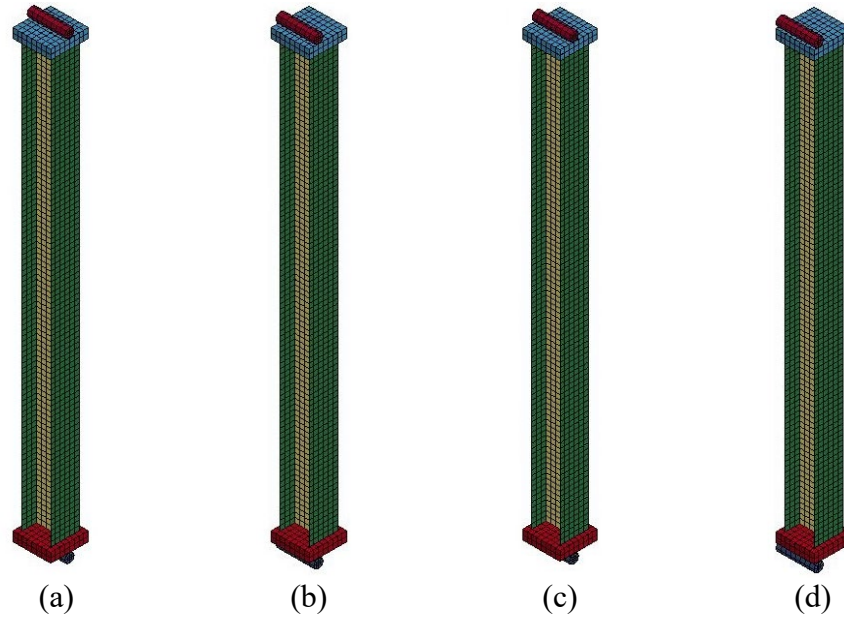
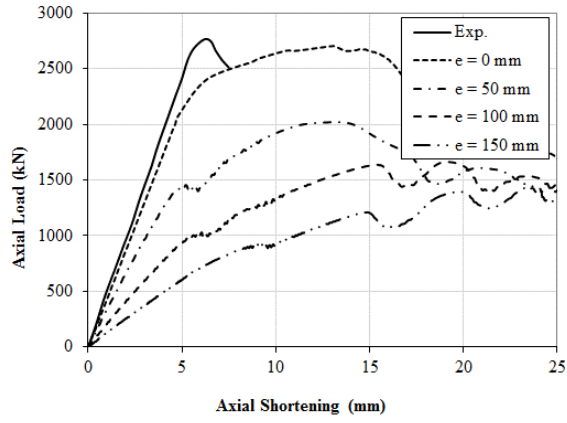


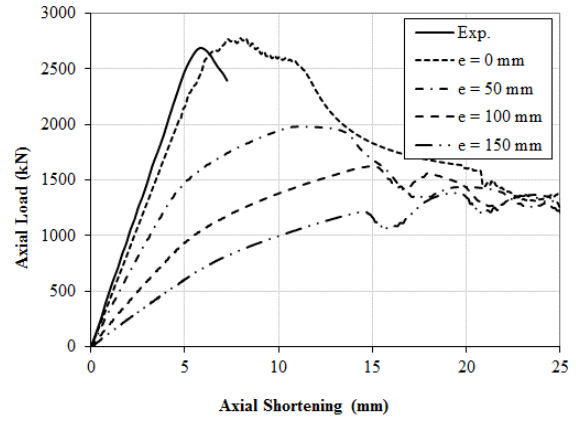
**Figure 2.6** Three-dimensional (3D) view of simulated H-piles with different eccentricity: (a)  $e=0$  mm; (b)  $e=50$  mm; (c)  $e=100$  mm; (d)  $e=150$  mm.

**Table 2.3** Failure Loads with Different Load Eccentricities

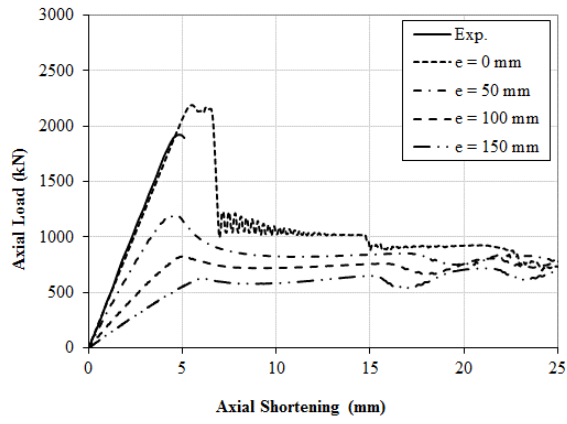
Group	Model name	Description (e)	m	Dimensions				FE Results	
				Flange	Web	Red. Flange	Red. web	Failure load	Failure Mode
			m	mm	mm	mm	mm	KN	
A	0-0	Eccentricity in the weak axis	50	11.63	11.0	---	---	2024	GB
			100					1670	
			150					1443	
B	0-20	Eccentricity in the weak axis	50	11.68	11.23	---	9.52	1977	GB
			100					1625	
			150					1383	
C	40-20	Eccentricity in the weak axis	50	11.18	11.10	7.34	7.82	1194	FLB
			100					848	
			150					822	
D	40-60	Eccentricity in the weak axis	50	11.02	10.82	6.15	4.09	835	FLB/WLB
			100					615	
			150					449	
E	80-60	Eccentricity in the weak axis	50	10.97	10.92	2.56	4.56	374	FLB/WLB
			100					229	
			150					154	



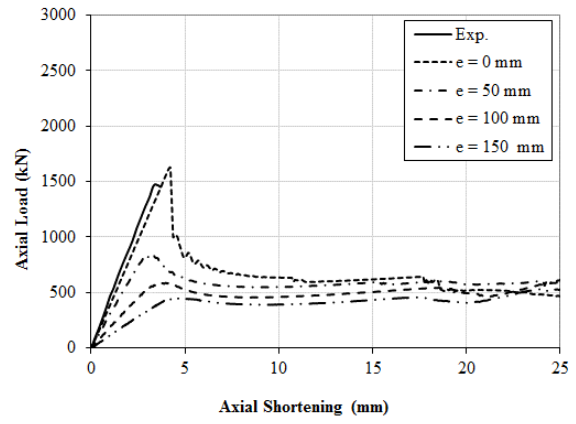
(a)



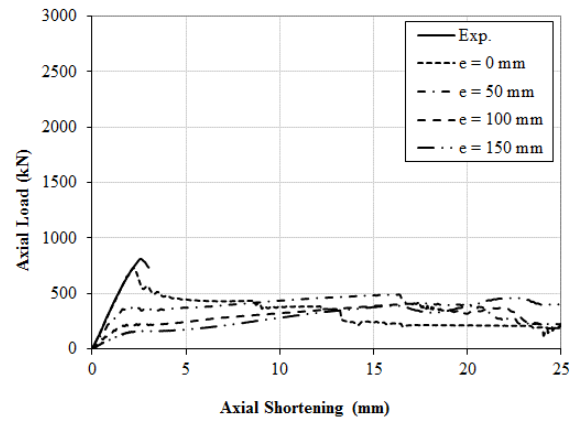
(b)



(c)



(d)



(e)

**Figure 2.7** Effect of eccentricity of load about minor axis on capacity of: (a) Pile (0-0); (b) Pile (0-20); (c) Pile (40-20); (d) Pile (40-60); (e) Pile (80-60).

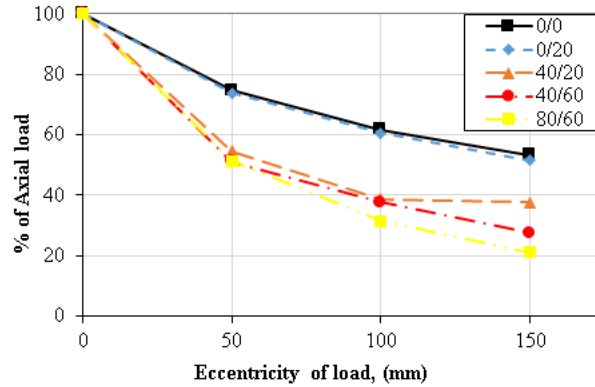


**Figure 2.8** Residual axial capacity with eccentric loads.

## 2.5 Model Validation

The boundary conditions in the FEMs were changed from using cylinders, which were preventing the rotation around the strong axis of the pile to using a solid sphere that allowed the H-pile to move freely in all directions (fig. 2.9). The calibrated FEMs developed in the previous sections were used to determine the response of ten columns HP 250 x 85 (10 x 42) H-piles (fig. 2.10) that were tested during the course of this research and reported in chapter three of this report.

The FEMs were also used to conduct parametric studies to investigate the effects of changing the corrosion percentage, extension, and location on the capacity of the steel H-piles. Also, different sizes of cuts in the flanges or voids in the webs of the H-piles were investigated to simulate the effect of having complete loss of a portion of a section in a corroded H-pile.

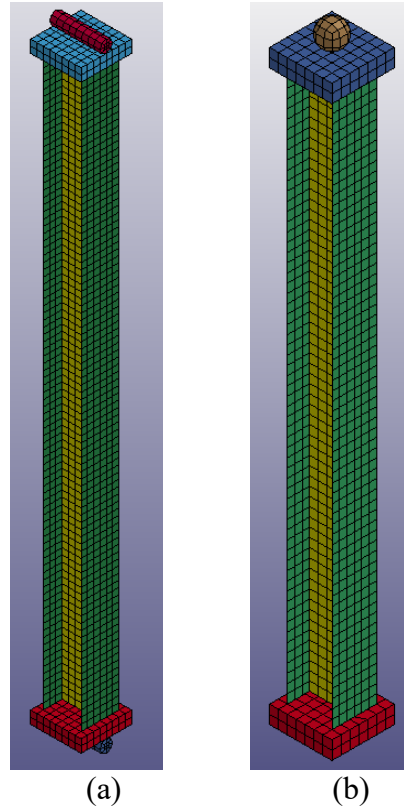


**Figure 2.9** Boundary conditions for the H-piles.

### *2.5.1 Effect of Corrosion Percentage*

In order to investigate the effect of changing the corrosion percentage on the capacity of the H-pile, groups A and B of FEMs were developed (Table 2.4). Group A consisted of four models with different corrosion percentages in the form of web thickness reductions of 25%, 50%, 70%, and 90% while having the same corrosion in the flange that was represented by a 50% reduction in the flange thickness. Group B consisted of four models with flange thickness reductions of 25%, 50%, 70%, and 90% while having a 50% reduction in the web thickness. Therefore, there is a common model between the two groups, which is 50% reduction in the web and 50% reduction in the flanges. The corrosion percentages were chosen to represent low corrosion with a 25% reduction in the web/flanges up to severe corrosion with a 90% reduction

in the thickness of web/flanges. Corrosion that exceeds 90% will be presented later as a void in a web or cut in flanges to simulate complete loss of part of a corroded section.

**Table 2.4** Summary of the Investigated Parameters for the FEMs

Group	Pile designation	Web Corrosion (%)	Flange Corrosion (%)	Axial Capacity (kN)	Loss of axial capacity (%)
A	CP 25/50	25	50	1718	20
	CP 50/50	50	50	1502	30
	CP 70/50	70	50	1115	48
	CP 90/50	90	50	986	54
B	CP 50/25	50	25	1990	7.5
	CP 50/70	50	70	859	60
	CP 50/90	50	90	629	70

The reference model failed due to yielding at the end of the pile (Fig. 2.10 (a)), while all the models in groups A and B failed at the corroded region due to local buckling (Fig. 2.10). The results of the FEMs of groups A and B were examined to determine the loss in the axial capacity compared to that of the reference specimen (Ref 0/0) (Fig. 2.11). Increasing the corrosion depth decreased the axial load carrying capacity due to the change in the failure mode from yielding to local buckling. The response of the pile is very sensitive to the corrosion in the flanges. Reductions by 90% and 50% in the thicknesses of the flanges and web, respectively, resulted in 70% loss in the axial load capacity of the pile, while only a 54% loss in the axial capacity occurred when reductions by 50% and 90% occurred in the thicknesses of the flanges and web, respectively, (table 2.4 and fig. 2.12).



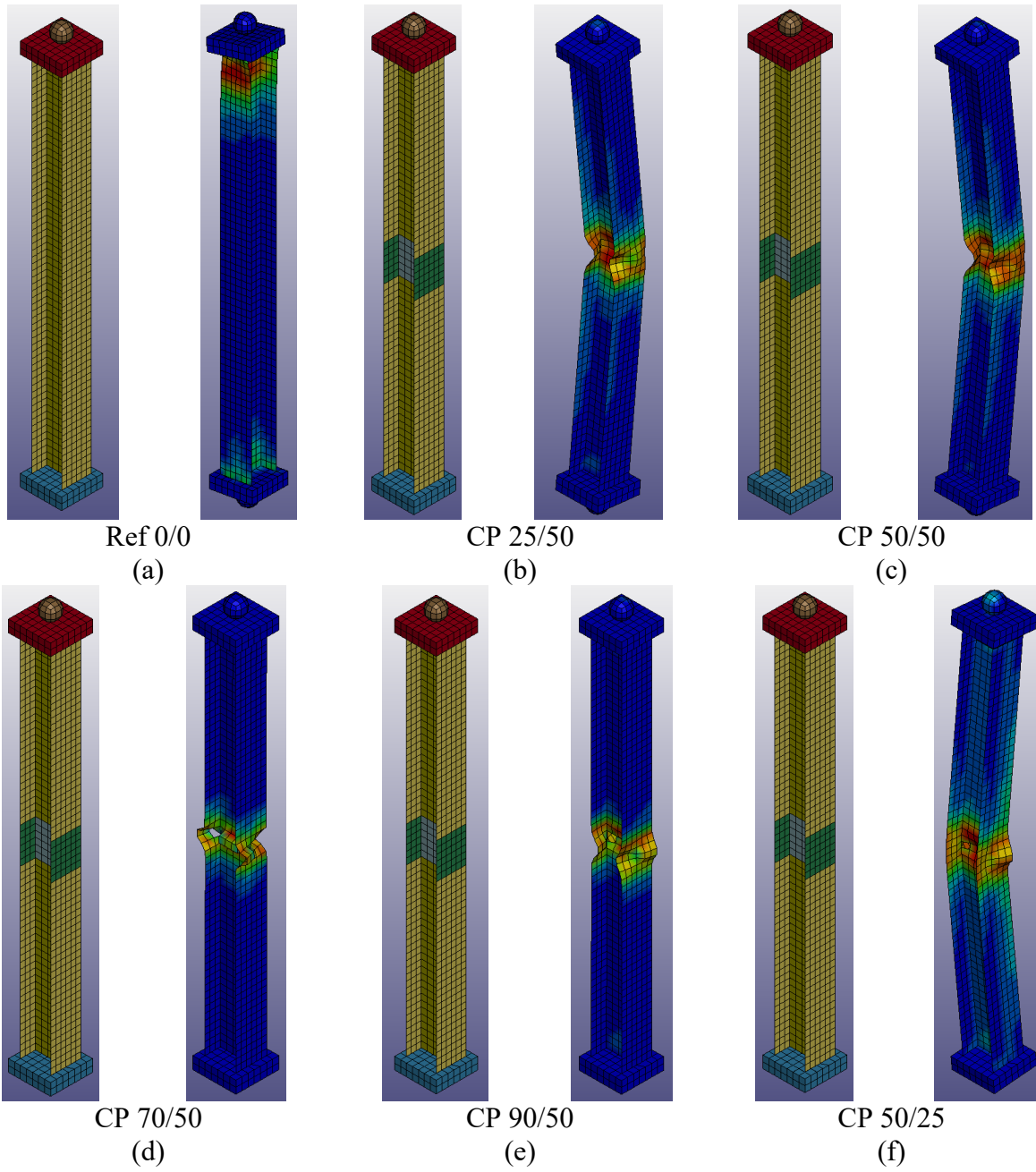
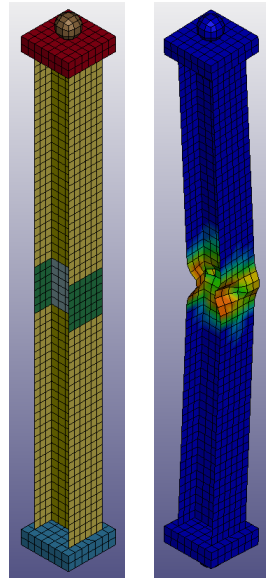
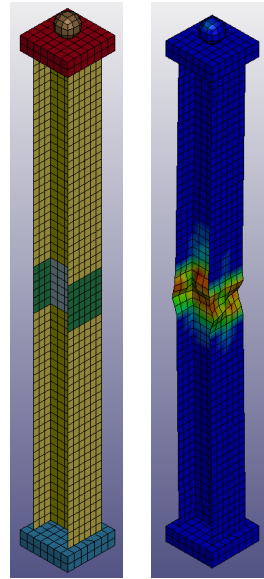


**Figure 2.10** Deformed shape of corroded piles (a)-(f)

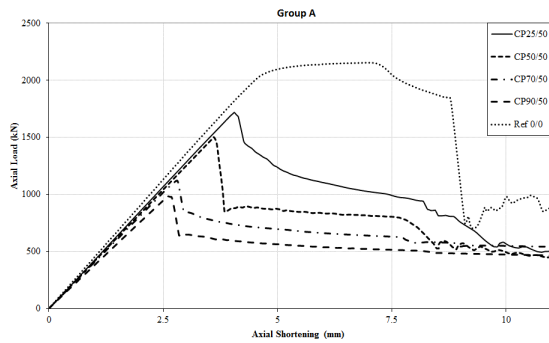


CP 50/70  
(g)

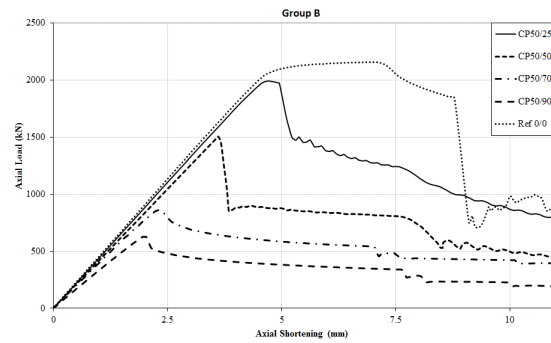


CP 50/90  
(h)

**Figure 2.10 cont.** Deformed shape of corroded piles (g)-(h)

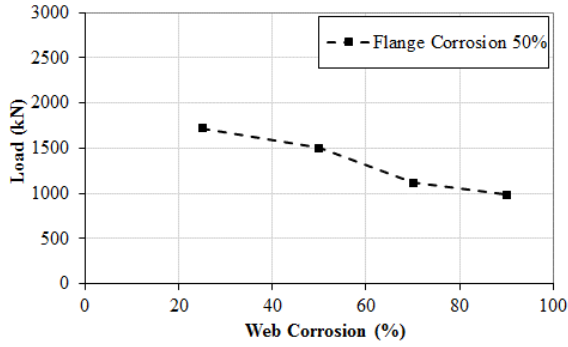


(a)

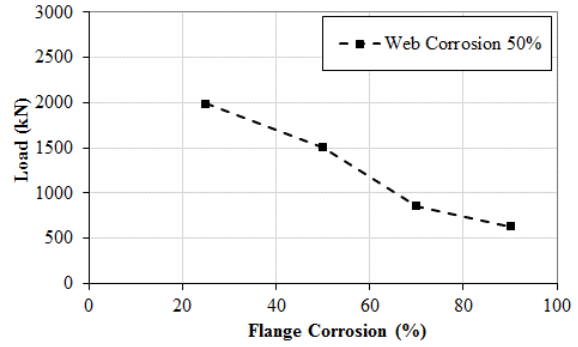


(b)

**Figure 2.11** Axial load vs axial shortening of corroded piles having 50% reduction in the thickness of: (a) flanges with different reductions in the thickness of web (b) web with different reductions in the thickness of flange.



(a)



(b)

**Figure 2.12** Reductions in the axial load capacity due to different reductions in the web and flanges.

### 2.5.2 Effect of Corrosion Extension

Two groups of FEMs, C and D, were developed to investigate the effects of corroded length on the axial capacity of the piles. Each group consisted of five models with different corrosion lengths of 100, 200, 300, 500, and 700 mm (4, 8, 12, 20, and 28 in.). Two different corrosion percentages were considered in this study, Group C had 70% corrosion in the web and 50% corrosion in the flange. Group D had 0% corrosion in the web and 50% corrosion in the flange. Table 2.5 presents the axial capacity of each pile and the loss in its axial capacity compared to the uncorroded reference model.

**Table 2.5** Summary of the Investigated FEMs for Corrosion Extension

Group	Pile designation	Web Corrosion (%)	Flange Corrosion (%)	Corrosion Length (mm)	Axial Capacity (kN)	Loss of axial capacity (%)
C	CE 70/50-4	70	50	100	1420	34
	CE 70/50-8			200	1219	43
	CE 70/50-12			300	1115	48
	CE 70/50-20			500	951	56
	CE 70/50-28			700	908	58
D	CE 0/50-4	0	50	100	2142	0
	CE 0/50-8			200	2006	7
	CE 0/50-12			300	1937	10
	CE 0/50-20			500	1956	9
	CE 0/50-28			700	1953	9

The corroded length of an H-pile affects the axial capacity of the pile and can change the failure mode from local to global buckling failure. Fig 2.13 shows both the undeformed and deformed shapes of group C models. Increasing the corroded length while having a high corrosion percentage in the web and flanges resulted in increased loss in the axial load capacity of the pile (Fig. 2.14). However, for group D, increasing the corroded section length while having minor corrosion did not reduce the axial capacity of the piles (Fig. 2.15). Furthermore, the losses in the axial capacities of the piles remained constant for piles having corroded lengths exceeding 500 mm and 300 mm (20 in. and 12 in.) for groups C and D, respectively (Fig 2.15).

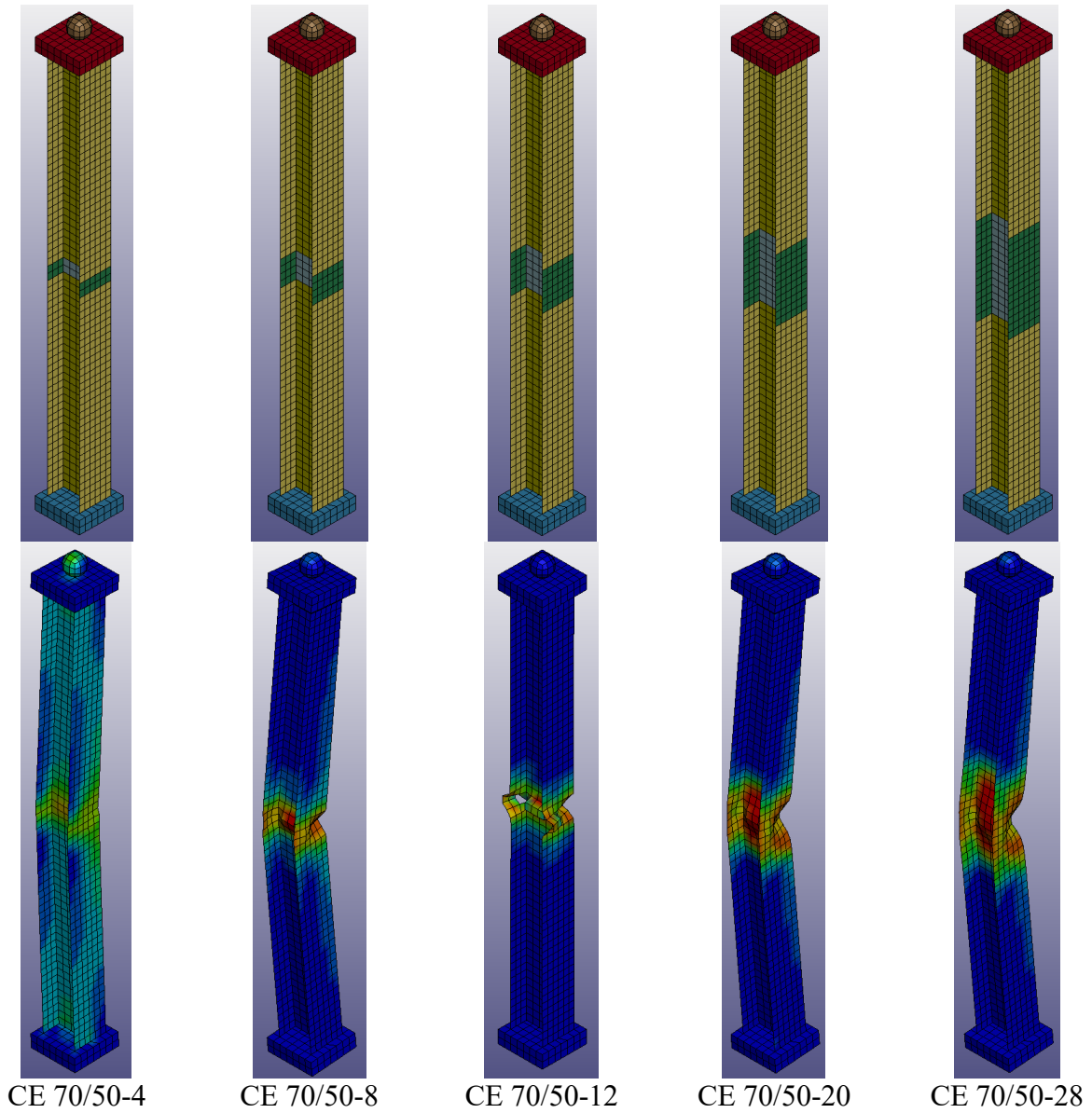


**Figure 2.13** Undeformed and deformed shapes of the corroded piles in groups C and D.

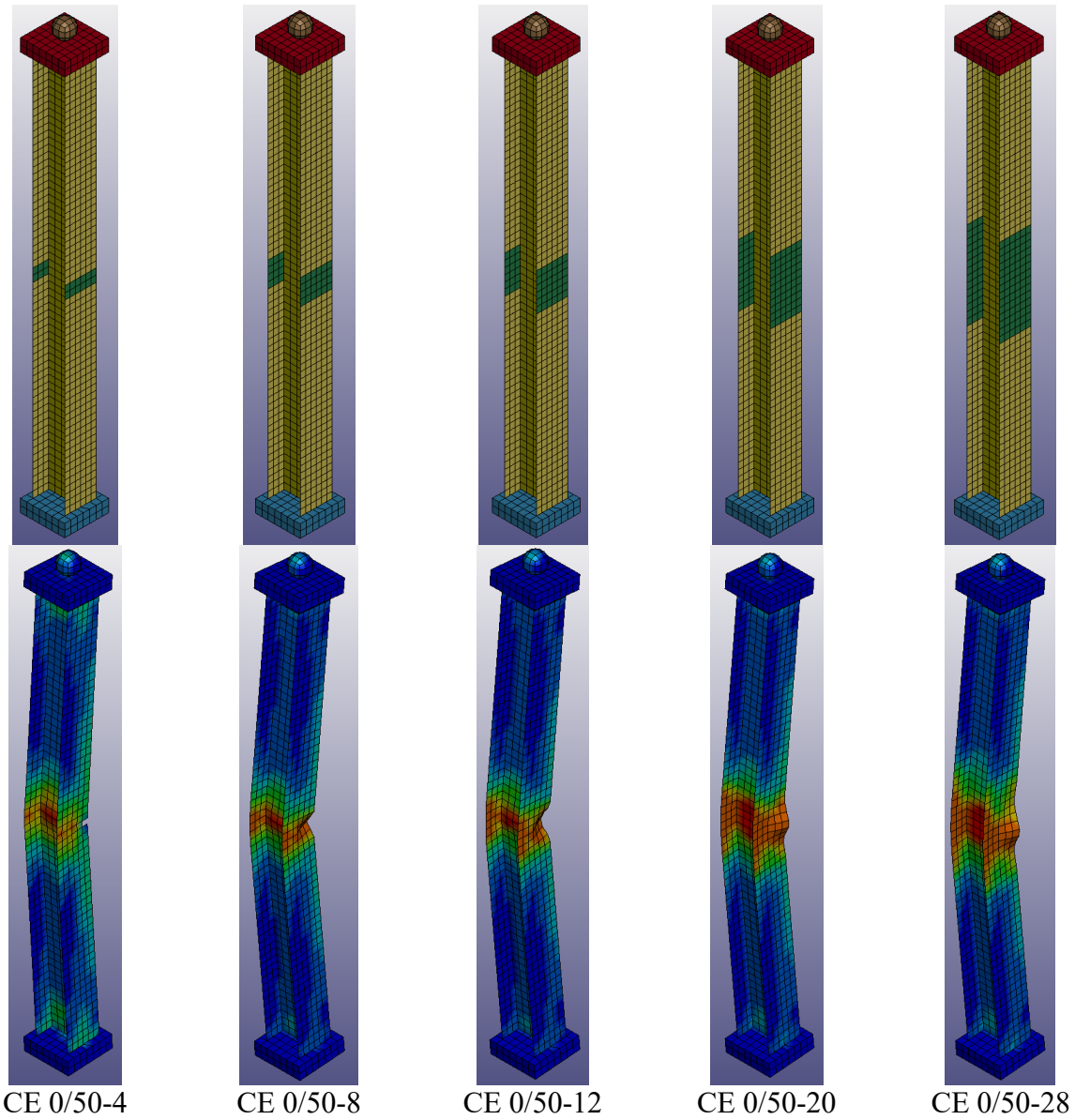


**Figure 2.13 cont.** Undeformed and deformed shapes of the corroded piles in groups C and D.

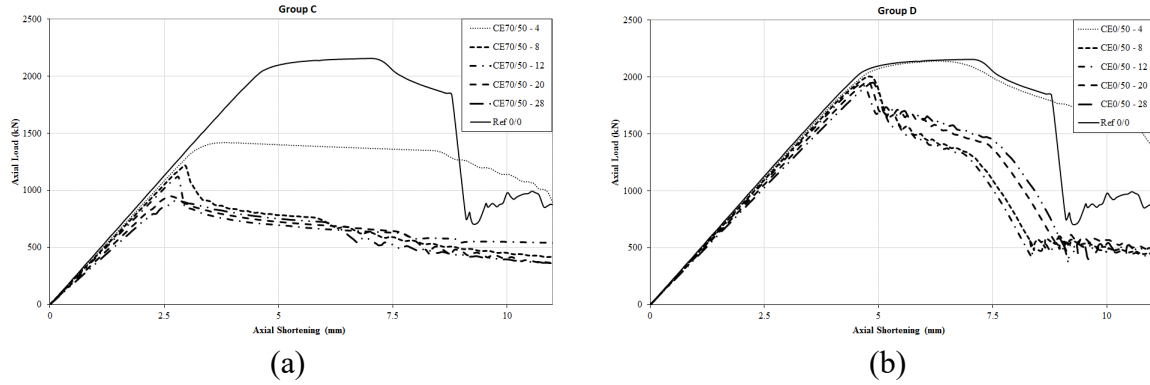


**Figure 2.14** Axial load vs axial shortening of corroded piles having different corroded lengths: (a) piles with reduction of 70% in the thickness of web and 50% in the thickness of flanges, and (b) piles with reduction of 0% in the thickness of web and 50% in the thickness of flanges.

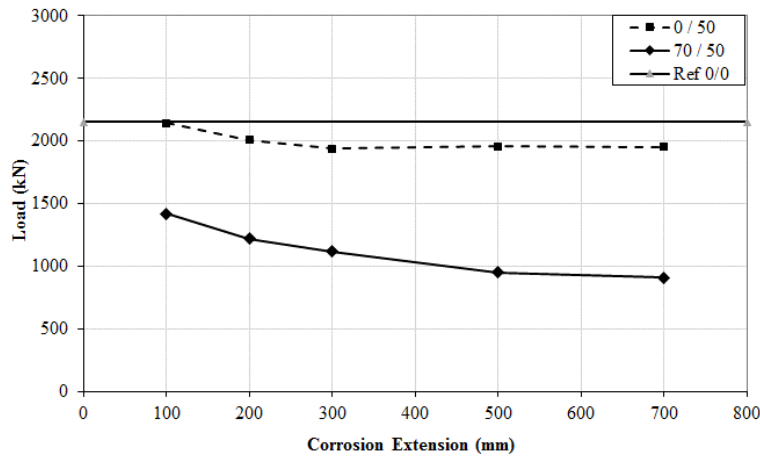


**Figure 2.15** Reductions in the axial load capacity due to different reductions in the corroded section lengths.

### 2.5.3 Effect of Corrosion Location

Three different locations along the steel H-pile were investigated to study the effect of the location of the corroded section on the axial capacities of the piles and their failure modes. Three groups of FEMs, E, F, and G were developed, where each group consisted of three models with a corrosion zone at 0.25, 0.35 and 0.50 L, where L is the total length of the pile. The main

difference between the three groups is the corrosion percentage in both the web and the flanges.

Table 2.6 represents a summary of the three groups with the maximum axial capacity for each pile and the percentage loss in the axial capacity compared to the reference model.

Changing the corrosion location along the length of the pile did not affect the failure mode (Fig 2.16) since failures were triggered by local buckling, which resulted in approximately the same axial capacity for all piles that have same severity of corrosion but with different corroded section locations (Fig 2.17).

**Table 2.6** Summary of the Investigated FEMs for Corrosion Location

Group	Pile designation	Web Corrosion (%)	Flange Corrosion (%)	Corrosion Location	Axial Capacity (kN)	Loss of axial capacity (%)
E	CL 50/70-0.25	50	70	0.25L	865	6
	CL 50/70-0.35			0.35L	862	6
	CL 50/70-0.50			0.50L	859	6
F	CL 70/50-0.25	70	50	0.25L	1124	48
	CL 70/50-0.35			0.35L	1118	48
	CL 70/50-0.50			0.50L	1115	48
G	CL 0/50-0.25	0	50	0.25L	1959	9
	CL 0/50-0.35			0.35L	1943	10
	CL 0/50-0.50			0.50L	1937	10



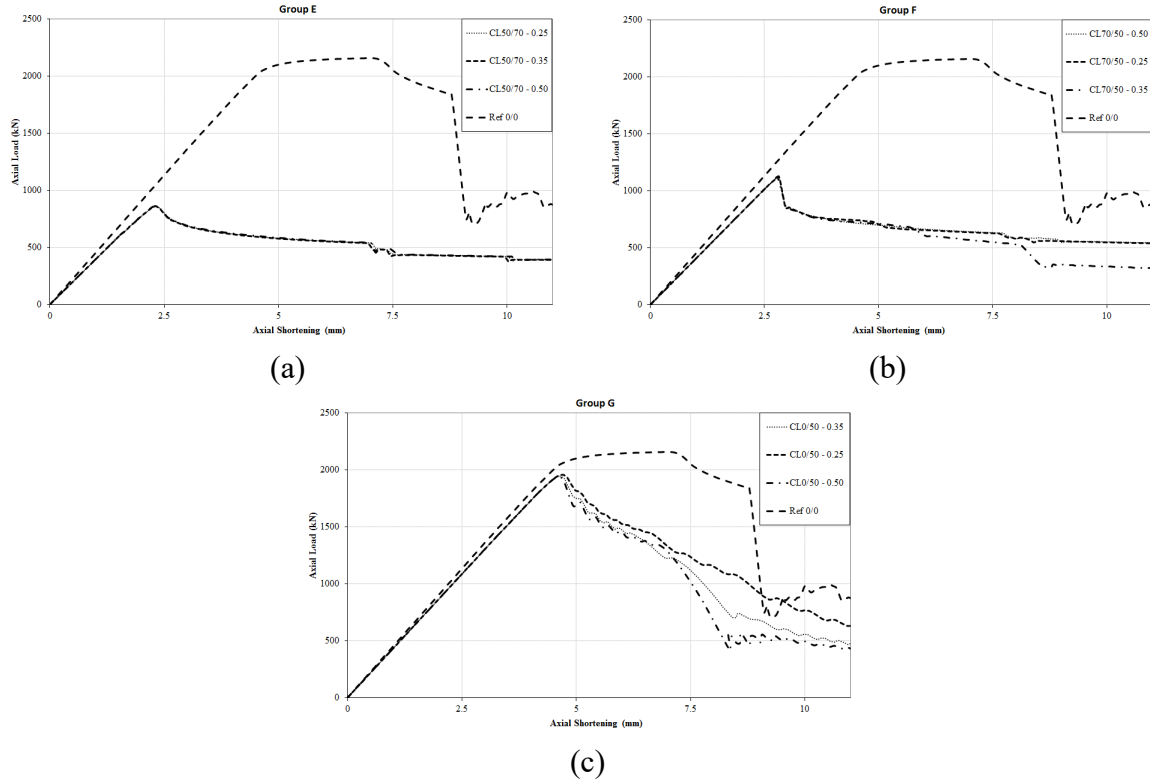


**Figure 2.16** Axial load vs axial shortening of corroded piles having different corroded section locations and a reduction of: (a) 50% in the thickness of web and 70% in the flanges, (b) 70% in the thickness of web and 50% in the flanges, and (c) 0% in the thickness of web and 50% in the flanges.

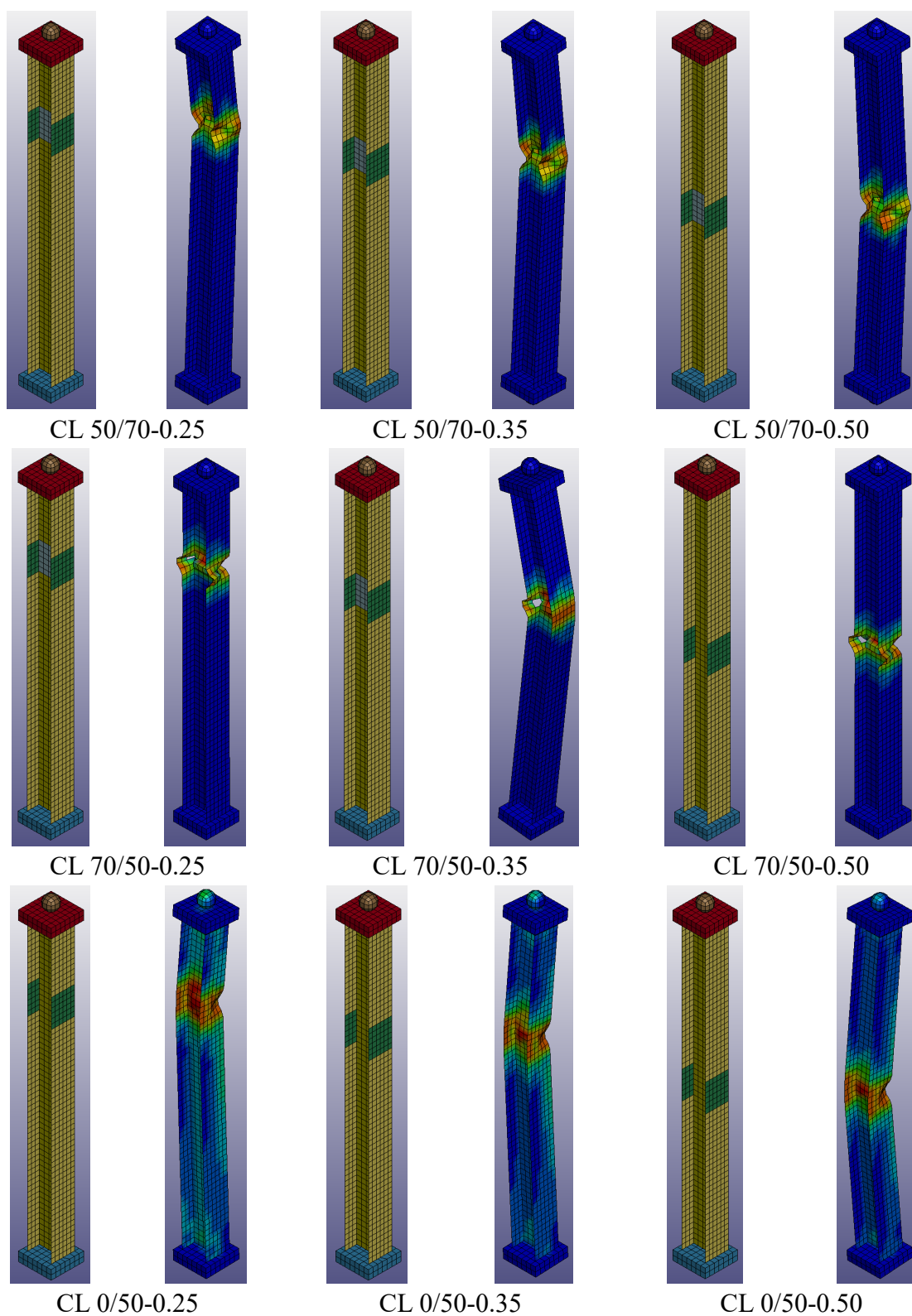


**Figure 2.17** Undeformed and deformed shapes of the corroded piles in groups E, F, and G.

#### 2.5.4 Effects of Web Voids and Flange Cuts

Severe corrosion in the web or the flanges of an H-pile may result in a void in the corroded zone, significantly affecting the axial capacity of the pile due to discontinuity along the length of the pile, which leads to huge stress concentrations at certain zones. To study the effect of such discontinuity in the pile, two groups of FEMs were developed. Group H consisted of four models with different rectangular voids having different sizes in the web and an identical cut in each flange (Table 2.7 and Fig 2.18). All piles had a corrosion percentage of 70% in the web and 50% in the flange.

**Table 2.7** Summary of the Investigated FEMs for Web Voids

Group	Pile designation	Web Void Dimensions (mm)	Flange Cut Radius (mm)	Axial Capacity (kN)	Loss of axial capacity (%)
H	WV 4x4	100 x 100	75	639	70
	WV 6x4	150 x 100		631	70
	WV 8x6	200 x 150		575	73
	WV 12x8	300 x 200		506	76

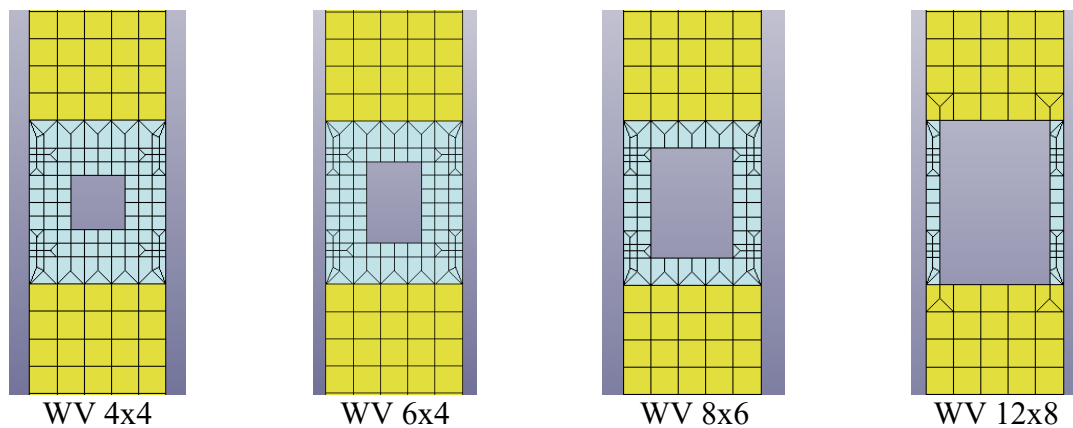


**Figure 2.18** Mesh generation and sizes of the voids in the webs.

Another group, I, having four models with different cut sizes in the flanges and a constant void size in the web, was investigated. The cuts were presented as half circles in each flange. Different radii were chosen to present different cut sizes in each pile (Fig 2.19 and Table 2.8). The void in the web of each pile remained 150 x 100 mm (6 x 4 in.). The cut was made in the corroded area of the pile in addition to the reductions of 70% in the thickness of the web and 50% in the thickness of the flanges.

**Table 2.8** Summary of the Investigated FEMs for Flange Cuts

Group	Pile designation	Web Void Dimensions (mm)	Flange Cut Radius (mm)	Axial Capacity (kN)	Loss of axial capacity (%)
I	FC R1.5	150 x 100	37.5	886	59
	FC R2		50	818	62
	FC R3		75	631	71
	FC R4		100	418	80

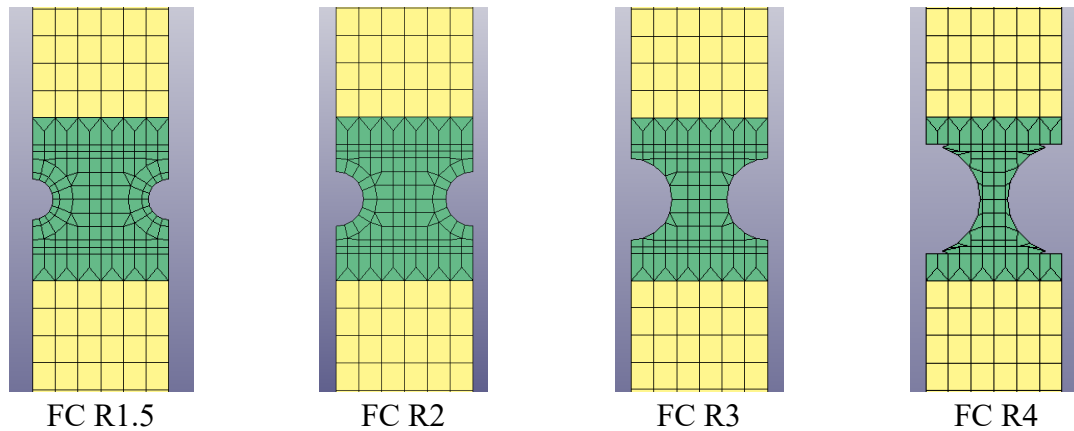


**Figure 2.19** Mesh generation and sizes of the cuts in the flanges.

The results for groups H and I are presented in Fig 2.20. Fig. 2.21 shows the reduction in the strength due to adding the voids or cuts compared to the reference pile as well as piles having 70% reduction in the web and 50% reduction in the flanges. Adding void to the web decreased

the axial load capacity by 42% to 54% compared to the corroded piles without voids. The size of the voids in the web had a relatively small effect on reducing the axial capacity as all four models lost approximately 70% in their axial load capacity compared to the reference model. Furthermore, increasing the cut size in the flanges significantly reduced the maximum axial capacity of the pile (Fig 2.22 and Table 2.8). Increasing the radius of the cut from 37.5 mm to 100 mm (1.5 in. to 4 in.) increased the loss in axial load capacity from 59% to 80% with respect to the reference pile.

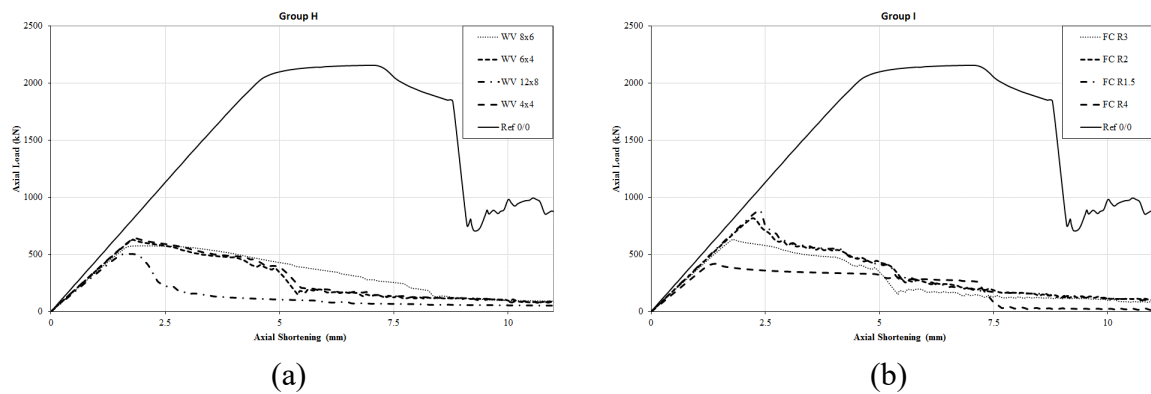


**Figure 2.20** Axial load vs axial shortening of corroded piles having different sizes for the cut in the: (a) Web with fixed cut size in the flanges, and (b) Flanges with fixed void size in the web.

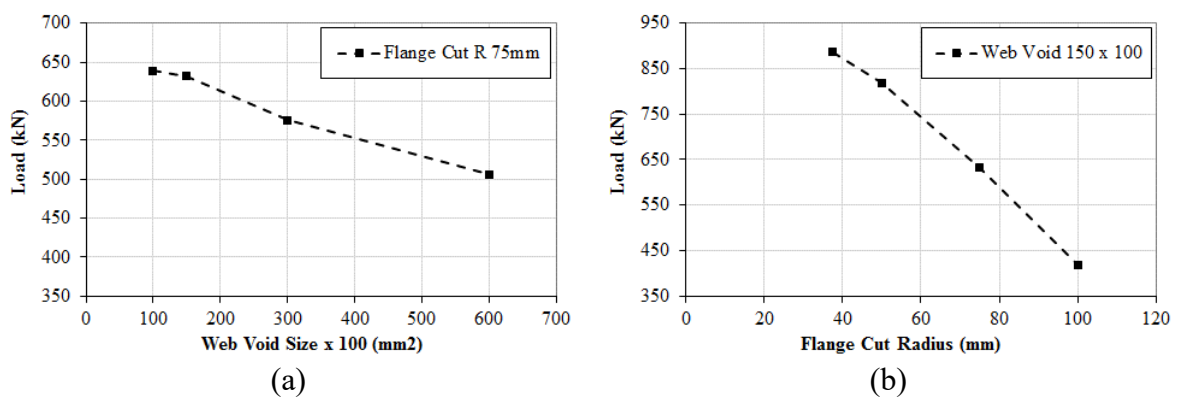


**Figure 2.21** Reductions in the axial load capacity due to different void and cut sizes in the pile.

## Chapter 3 Experimental Testing of Corroded Piles Under Concentric and Eccentric Loads

### 3.1 Introduction

This chapter presents the experimental results for ten H-pile HP 250 x 85 (10 x 42) under concentric loading and three HP 250 x 85 (10 x 42) under eccentric loading and comparing all the results with two existing specifications along with the FEMs that were described in Chapter 2 of this report.

### 3.2 Existing Design Specifications

#### *3.2.1 AISC and AASHTO*

AISC (2017) and AASHTO (2014) adopted eq. 3.1 to calculate the nominal axial strength of steel piles as a function of the effective cross-sectional area,  $A_e$ , and critical buckling stress,  $F_{cr}$ .

$$P_n = F_{cr}A_e \quad (\text{Eq. 3.1})$$

The design approach considers elastic buckling and inelastic buckling for hot-rolled steel members with or without slightly slender elements. The elastic flexural buckling capacity is based on a modified Euler buckling equation which considers the effect of initial out-of-straightness. The  $A_e$  can be calculated using eqs. 3.2 through 3.5 using the effective width method.

$$b_e = b \text{ for } \lambda \leq \lambda_r \sqrt{\frac{F_y}{F_{cr}}} \quad (\text{Eq. 3.2})$$

$$b_e = b \left( 1 - c_1 \sqrt{\frac{F_{el}}{F_{cr}}} \right) \sqrt{\frac{F_{el}}{F_{cr}}} \text{ for } \lambda > \lambda_r \sqrt{\frac{F_y}{F_{cr}}} \quad (\text{Eq. 3.3})$$

$$\lambda = b/2t, \lambda_r = 0.56 \sqrt{\frac{E}{F_y}} \text{ for flange} \quad (\text{Eq.3.4})$$

$$\lambda = h/t_w, \lambda_r = 1.49 \sqrt{\frac{E}{F_y}} \text{ for web} \quad (\text{Eq. 3.5})$$

where b is the width of the flange element, t is the thickness of the flange element, h is the height of the web, t<sub>w</sub> is the thickness of the web, and C<sub>1</sub> imperfection adjustment factor equaling 0.18 for the flange and 0.22 for the web (AISC 2017). The elastic local buckling stress (F<sub>el</sub>) is determined based on the yield stress as follows:

$$F_{el} = \left(c_2 \frac{\lambda_r}{\lambda}\right)^2 F_y \quad (\text{Eq. 3.6})$$

$$c_2 = \frac{1 - \sqrt{1 - 4c_1}}{2c_1} \quad (\text{Eq. 3.7})$$

While the critical stress is determined as follows:

$$F_{cr} = (0.658)^{\frac{F_y}{F_e}} F_y \text{ for } \frac{KL}{r} \leq 4.71 \sqrt{\frac{E}{F_y}} \quad (\text{Eq. 3.8})$$

$$F_{cr} = 0.877 F_e \text{ for } \frac{KL}{r} > 4.71 \sqrt{\frac{E}{F_y}} \quad (\text{Eq. 3.9})$$

$$F_e = \frac{\pi^2 E}{\left(\frac{KL}{r}\right)^2} \quad (\text{Eq. 3.10})$$

where the effective length factor, length of the member, and radius of gyration of the cross section are shown by  $K$ ,  $L$ , and  $r$ , respectively.

### 3.2.2 AISI Effective Width Method (AISI-EWM)

The AISI-EWM calculates the axial capacity by multiplying the  $A_e$  by the nominal global buckling stress,  $F_n$  per eq. 3.11.

$$P_n = F_n A_e \quad (\text{Eq. 3.11})$$

The AISI considers the effect of local buckling, and the width of a buckled section of a slender plate is deducted from the width of the element while the remaining part is assumed to have uniformly distributed stress (fig. 3.1).

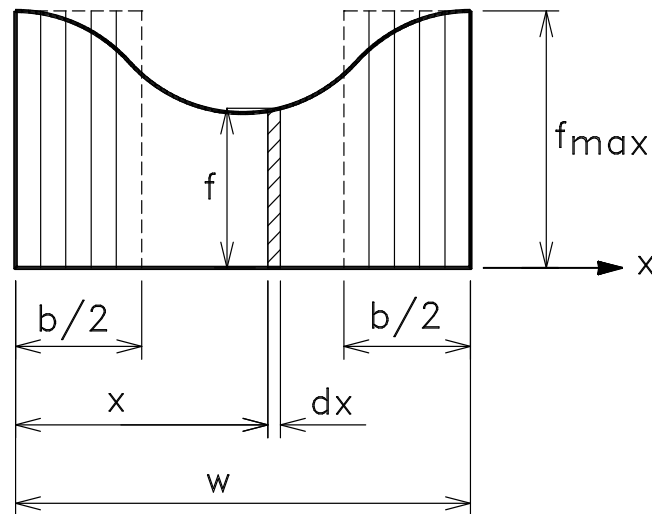


**Figure 3.1** Effective width method (AISI, 2012).



This method determines the local buckling strength of a cross section by examining each plate in the cross section. Therefore, the compatibility and equilibrium between cross-sectional elements are not considered (Schafer, 2008). The effective cross-sectional area  $A_e$  is determined as

$$A_e = \sum b_e t \quad (\text{Eq. 3-12})$$

where  $t$  is the thickness of the element, and  $b_e$  is the effective width of the element defined as

$$b_e = b \quad \text{for } \lambda \leq 0.673 \quad (\text{Eq. 3-13})$$

$$b_e = \rho b \quad \text{for } \lambda > 0.673 \quad (\text{Eq. 3-14})$$

where  $b$  is the original width of the element, and  $\rho$  is reduction factor which is calculated as

$$\rho = \left(1 - \frac{0.22}{\lambda}\right) / \lambda \quad (\text{Eq. 3-15})$$

$$\lambda = \sqrt{\frac{F_n}{F_{cr}}} \quad (\text{Eq. 3-16})$$

$$F_n = (0.658)^{\lambda_c^2} F_y \quad \text{for } \lambda_c \leq 1.5 \quad (\text{Eq. 3-17})$$

$$F_n = \frac{0.877}{\lambda_c^2} F_y \quad \text{for } \lambda_c > 1.5 \quad (\text{Eq. 3-18})$$

$$\lambda_c = \sqrt{\frac{F_y}{F_e}} \quad (\text{Eq. 3-19})$$

where  $F_e$  is the elastic buckling stress, and  $F_{cr}$  is the elastic local buckling capacity of a plate and is calculated as follows:

$$F_{cr} = k \frac{\pi^2 E}{12(1 - \mu^2)(b/t)^2} \quad (\text{Eq. 3-20})$$

where  $\mu$  is the Poisson's ratio of steel, and  $k$  is the plate buckling coefficient (Timoshenko, 1961).

The width and thickness of the plate are shown by  $b$  and  $t$  respectively, and  $E$  is the modulus of elasticity of steel.

### 3.3 Test Specimens

Thirteen 120 in. long 250 x 85 (10 x 42) H-piles were tested under axial compression load (table 3.1, fig. 3.2). This included a reference uncorroded pile and twelve corroded piles. Corrosion in a section was simulated through reduction in the thickness of and/or cuts in the webs and/or flanges at the corroded section. The reductions in a flange or a web thicknesses were 70% and 50% of their original thickness, respectively (table 3.2). Geometric properties of the cross sections of the tested piles, based on the measured dimensions of the smallest section, are illustrated in (table 3.3). The reductions were carried out, using a Bridgeport milling machine, from both sides of the targeted web and/or flange to maintain a symmetric section. The cut was done by reducing the section until the entire thickness was removed. The cuts to a web were 152.4 x 95.25 mm (6 x 3.75 in.), while those in a flange were two 152.4 mm (6 in.) diameter half-circles.

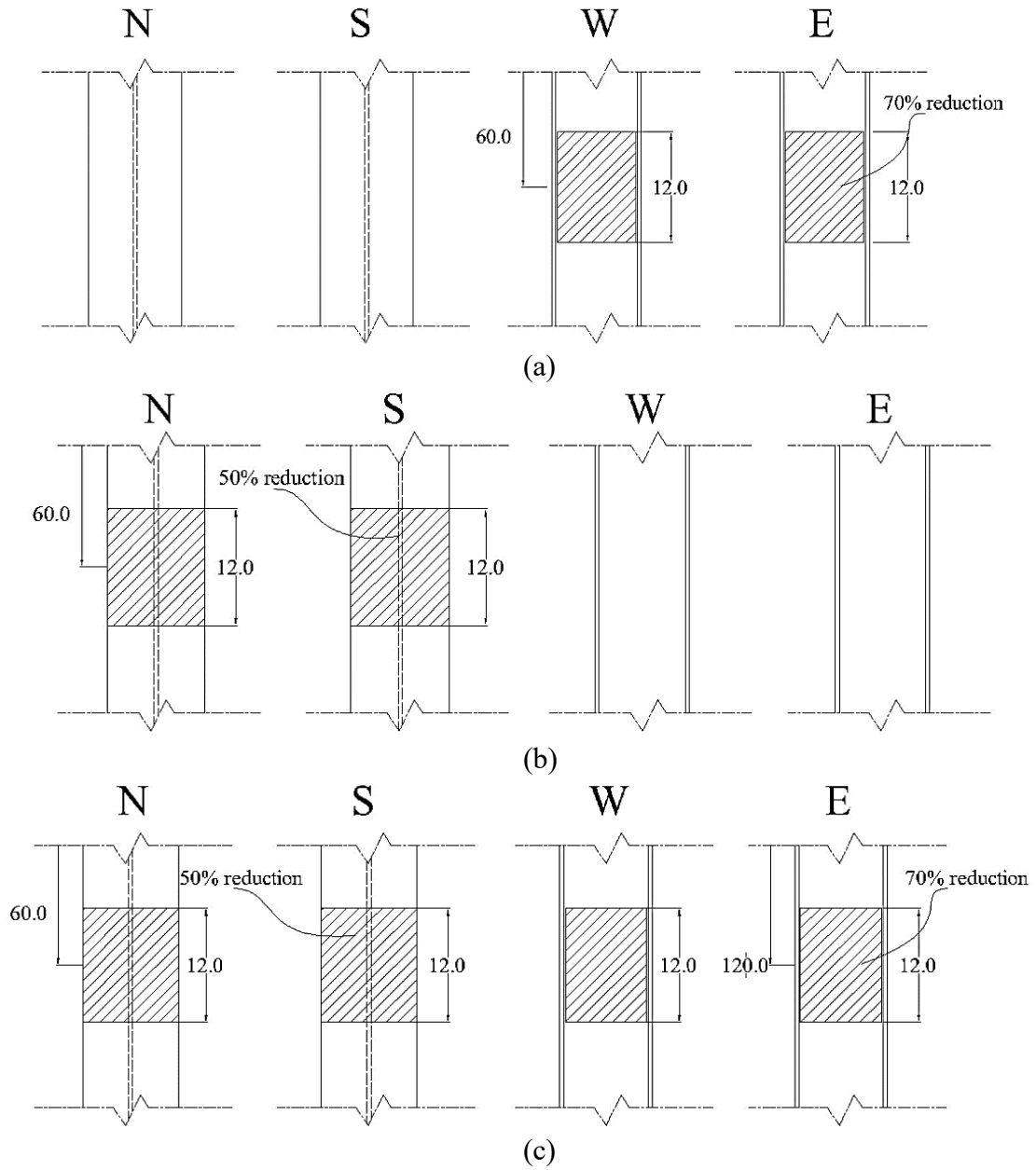


**Figure 3.2** Reduction details of the investigated piles: (a) W70-F00, (b) W00-F50, (c) W70-F50, (d) W70-F50/0, (e) W70V-F50, (f) W70-F50C, (g) W70V-F50C, (h) W70-F50-6.

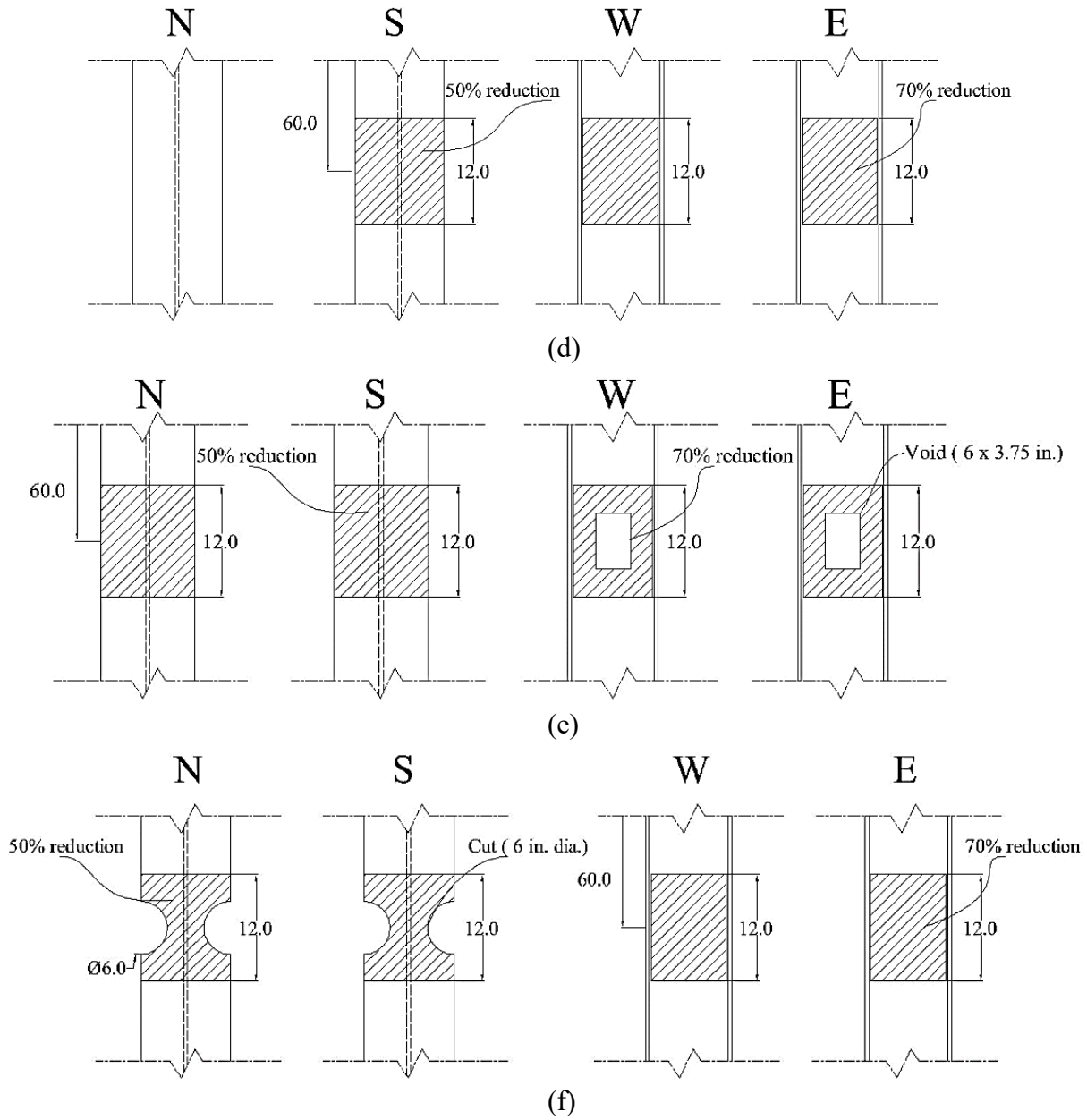


**Figure 3.2 cont.** Reduction details of the investigated piles: (a) W70-F00, (b) W00-F50, (c) W70-F50, (d) W70-F50/0, (e) W70V-F50, (f) W70-F50C, (g) W70V-F50C, (h) W70-F50-6.

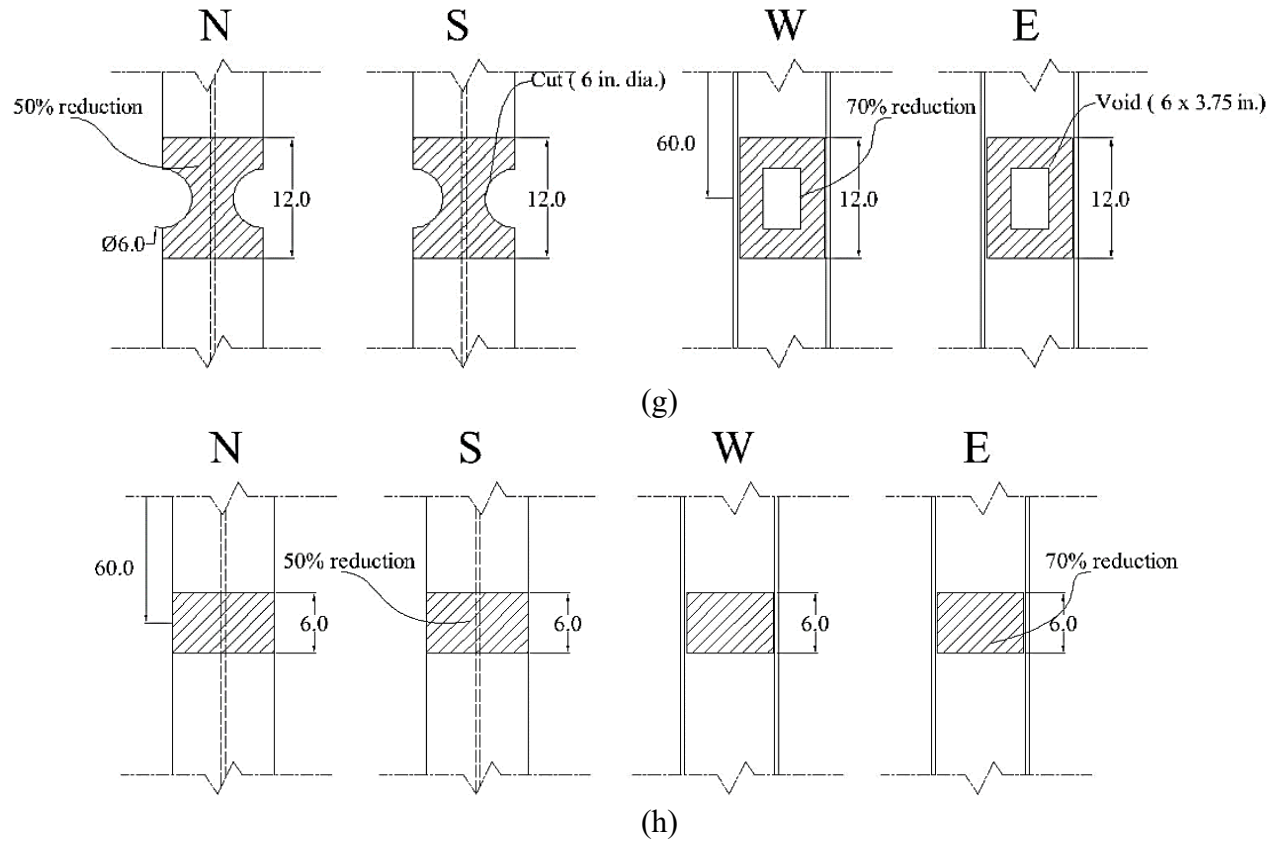


**Table 3.1** Summary of the Test Specimens

Group	H-Pile #	Web		Flange		Corrosion Extension	Longitudinal symmetry
		Reduction %	Void	Reduction %	Cut		
Corroded piles	W00-F00	--	--	--	--	--	--
	W70-F00	70	--	--	--	12 in.	Y
	W00-F50	--	--	50	--	12 in.	Y
	W70-F50	70	--	50	--	12 in.	Y
	W70-F50/0	70	--	0/50*	--	12 in.	Y
	W70V-F50	70	V	50	--	12 in.	Y
	W70-F50C	70	--	50	C	12 in.	Y
	W70V-F50C	70	V	50	C	12 in.	Y
	W70-F50-6	70	--	50	--	6 in.	Y
Eccentricity	W70-F50-10%	70	V	50	C	12 in.	Y
	W70-F50-30%	70	V	50	C	12 in.	Y
	W70-F50-30%	70	--	50	C	12 in.	Y
Repaired	R-W70V-F50C	70	V	50	C	12 in.	Y
	R-W70V-F50C	70	V	50	C	12 in.	Y
	R-W70V-F50C	70	V	50	C	12 in.	Y

\* One flange was corroded while the other was not

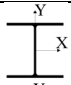
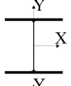
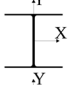
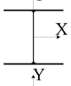
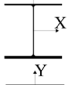
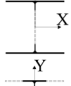
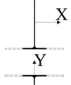
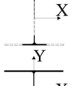
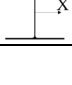
Three piles displayed minor to moderate corrosion where the corroded section was simulated by reducing the thicknesses of the flanges and/or webs. A fourth specimen, W70-F50/0, had a reduction in the web and a reduction in one flange, while the other flange had no reduction in the thickness, to simulate asymmetric corrosion. Three specimens displayed more severe corrosion that was simulated using reductions in the thicknesses as well as cuts in the webs and/or flanges (fig. 3.2).

**Table 3.2** Actual Dimensions of the Tested Piles

H-Pile #	Flange		Web (in.)	Reduced Flange				Reduced Web		Void (in.)
	North (in.)	South (in.)		North		South		East	West	
				Red. (in.)	Cut (in.)	Red. (in)	Cut (in.)	Red. (in.)	Red. (in)	
W00-F00	0.425	0.426	0.374	--	--	--	--	--	--	--
W70-F00	0.415	0.428	0.385	--	--	--	--	0.135	0.134	--
W00-F50	0.421	0.426	0.373	0.21	--	0.213	--	--	--	--
W70-F50	0.423	0.425	0.377	0.212	--	0.213	--	0.132	0.13	--
W70-F50/0	0.424	0.428	0.383	0.2	--	--	--	0.134	0.132	--
W70V-F50	0.425	0.424	0.411	0.212	--	0.212	--	0.144	0.142	6x3.75
W70-F50C	0.418	0.411	0.379	0.209	3	0.213	3	0.133	0.131	--
W70V-F50C	0.419	0.426	0.368	0.209	3	0.213	3	0.12	0.128	6x3.75
W70-F50-6	0.426	0.423	0.373	0.21	--	0.212	--	0.13	0.131	--
W70V-F50C-10%	0.416	0.424	0.375	0.208	3	0.212	3	0.131	0.131	6x3.75
W70V-F50C-30%	0.4005	0.408	0.409	0.20	3	0.204	3	0.143	0.143	6x3.75
W70-F50-10%	0.408	0.4005	0.409	0.204	--	0.2	--	0.143	0.141	--

The piles' label used in the current experimental work consisted of two segments. The first segment is the letter W, referring to the web, followed by the percentage of the reduction in the web thickness and presence of rectangular void in web using the letter V; the second segment is the letter F, referring to the flange, followed by the percentage of the reduction in flange and presence of a cut in the flange using the letter C. For example, specimen W00-F00 was a reference pile without any reduction in the cross section.

**Table 3.3** Sectional Properties at Minimum Cross Section based on the Measured Dimensions for Centrally loaded Specimens

Designation	Shape	$A_{min}$ (in. <sup>2</sup> )	$A_f$ (in. <sup>2</sup> )	$A_w$ (in. <sup>2</sup> )	$A_w/A_f$	$r_{min}$ (in.)	$L$ (in.)	$KL/r_{min}$	$b_f/2t_f$	$h/t_w$
W00-F00		12.04	8.57	3.46	0.40	2.46	120	48.87	12.14	21.46
W70-F00		9.67	8.49	1.18	0.14	2.73	120	44.03	12.14	69.18
W00-F50		7.68	4.22	3.45	0.82	2.16	120	55.60	24.22	21.51
W70-F50		5.43	4.26	1.17	0.27	2.58	120	46.57	23.87	69.78
W70-F50/0		7.76	6.57	1.19	0.18	2.68	120	44.83	22.49	68.59
W70V-F50		4.79	4.39	0.40	0.09	2.75	120	43.63	23.76	8.10
W70-F50C		2.83	1.61	1.21	0.75	0.90	120	133.03	10.29	69.78
W70V-F50C		2.22	1.73	0.49	0.28	1.04	120	115.09	9.74	8.44
W70-F50-6		5.44	4.30	1.14	0.27	2.59	120	46.41	23.87	71.65

All specimens had the corroded section located in the mid-span of the pile except specimen W70V-F50C-N, where the letter N stands for nonsymmetrical corrosion in the longitudinal direction of the pile where the corrosion section was located at the quarter span of the pile. The corrosion consisted of reductions in the web and flanges combined with cuts in the web and flange.

Each of the corroded sections extended over a length of 304.8 mm (12.in.) except specimen W70-F50-6 where the corroded section was extended over 152.4 mm (6 in.).

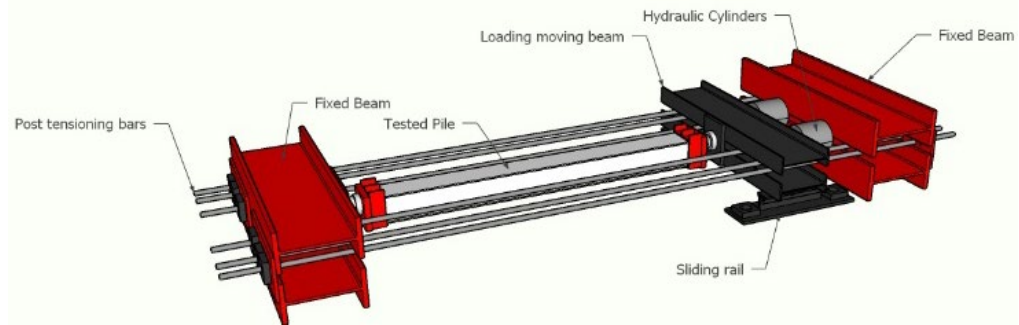


### 3.4 Test Setup and Loading Protocol

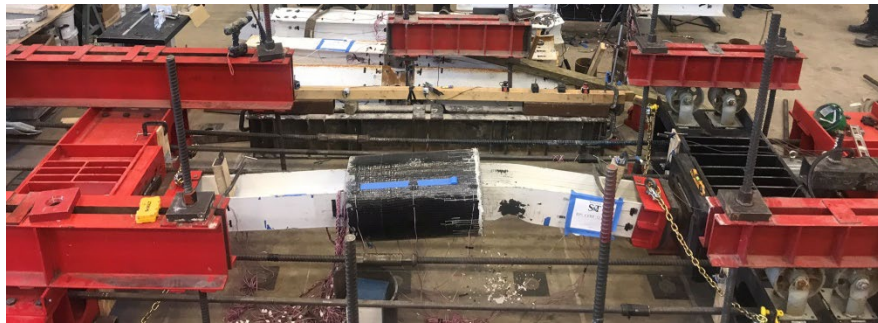
Figure 3.3 shows the 4450kN (1000 kips) self-sustained test frame that was used for testing the piles. The frame consists of two exterior rigid beams that were connected using six 35 mm (1.375 in.) diameter Grade150 Dywidag bars. A movable rigid beam sandwiched between four bottom and four top rollers and guided using a rail track to ensure unidirectional movement was also used to apply the axial load to the test specimens (fig. 3.3). Two 2225kN (500 kips) hydraulic jacks (fig. 3.4) applied the load against one of the exterior beams at one end and the movable beam at the other end. The movable beam then applied the load to the test specimen.

A test specimen had pin-pin boundary conditions. Each end of the pile was placed inside a steel shoe, which in turn was connected to a half-sphere that was rotating on a swivel plate that was connected to the exterior beam at one end of the pile or the movable beam at the other end of the pile (fig 3.5).

The load was applied monotonically, at a rate of 155 kN/min (35 kip/min) using an oil pump and two 2225 kN (500 kips) hydraulic jacks, until rupture occurred and the test specimen became unstable. Ten piles were loaded concentrically, and three piles were loaded eccentrically using eccentricity values of 10% and 30% of the width of the pile. The required eccentricity was applied by shifting the swivel plate (fig. 3.6).

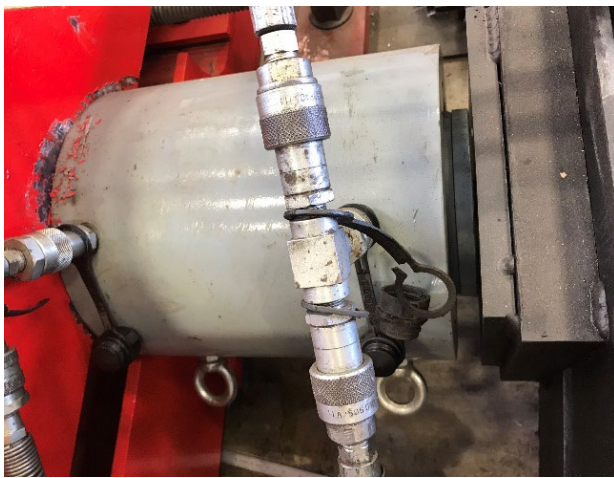


(a)



(b)

**Figure 3.3** Test setup: (a) drawing, and (b) picture.



(a)



(b)

**Figure 3.4** Loading instruments: (a) hydraulic jack, and (b) rail track with rolling cylinders.

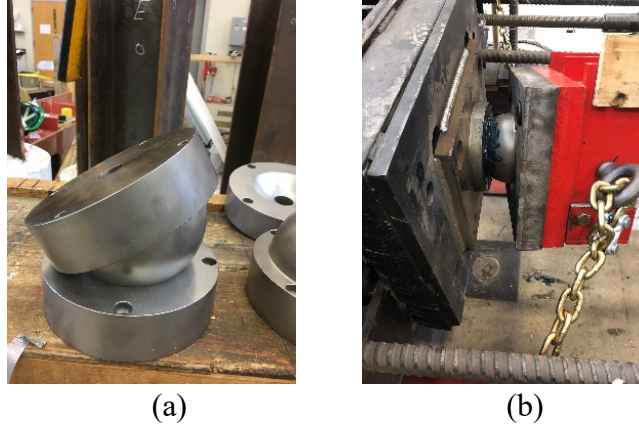


**Figure 3.5** Swivel plates (a) maximum rotation, and (b) installed in the setup.

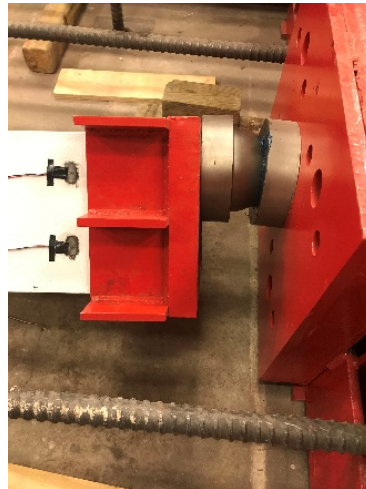


**Figure 3.6** Eccentricity of the swivel with the pile.

### 3.5 Instrumentation

The displacements in the strong and weak axis directions of the pile were measured using nine string potentiometers (SPs) (fig. 3.7). Two more SPs were attached between the moving beam and the end beam next to the specimen for measuring the differential displacements in the loading plates and connections.

The load was monitored using six 890kN (200 kips) load cells placed on each of the Dywidag bars. Forty-nine strain gauges were installed on each steel pile at seven sections on the span of the pile following either Type 1 or Type 2, according to the profile of the piles (fig. 3.8). Two sections were spaced 152.4 mm (6 in.) from each end of the pile, and the remaining five sections were positioned at the middle of the pile at the reduced section; each section had 7 strain gauges placed on each face of the pile (fig. 3.8). Six strain gauges were installed (fig. 3.9) to monitor the force in each post-tension bar. Two webcams were used to monitor the rotation of the two swivel plates. One webcam and one high-definition camera were also installed on both sides of the corroded segment of the pile to monitor the initiation of buckling of each pile.

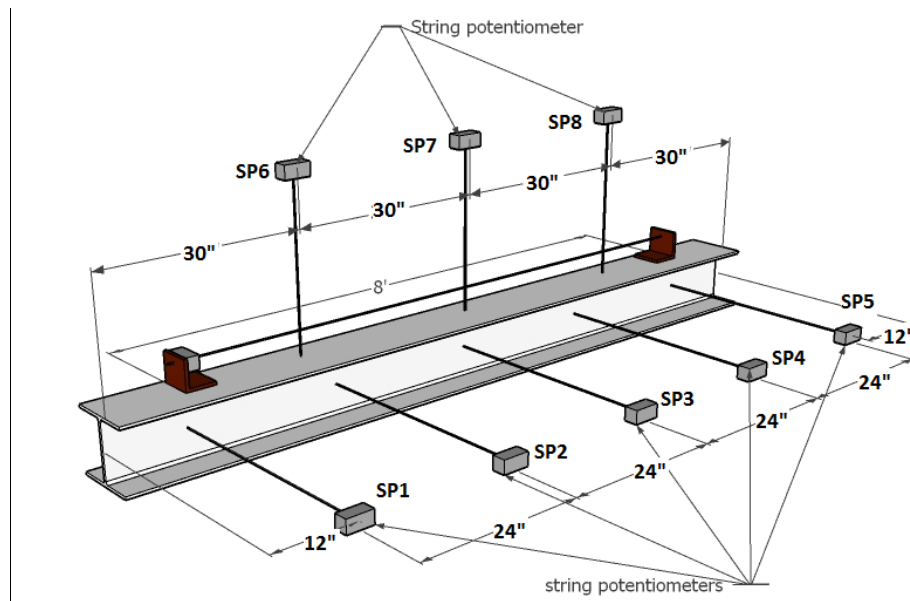


**Figure 3.7** Layout of the SPs.

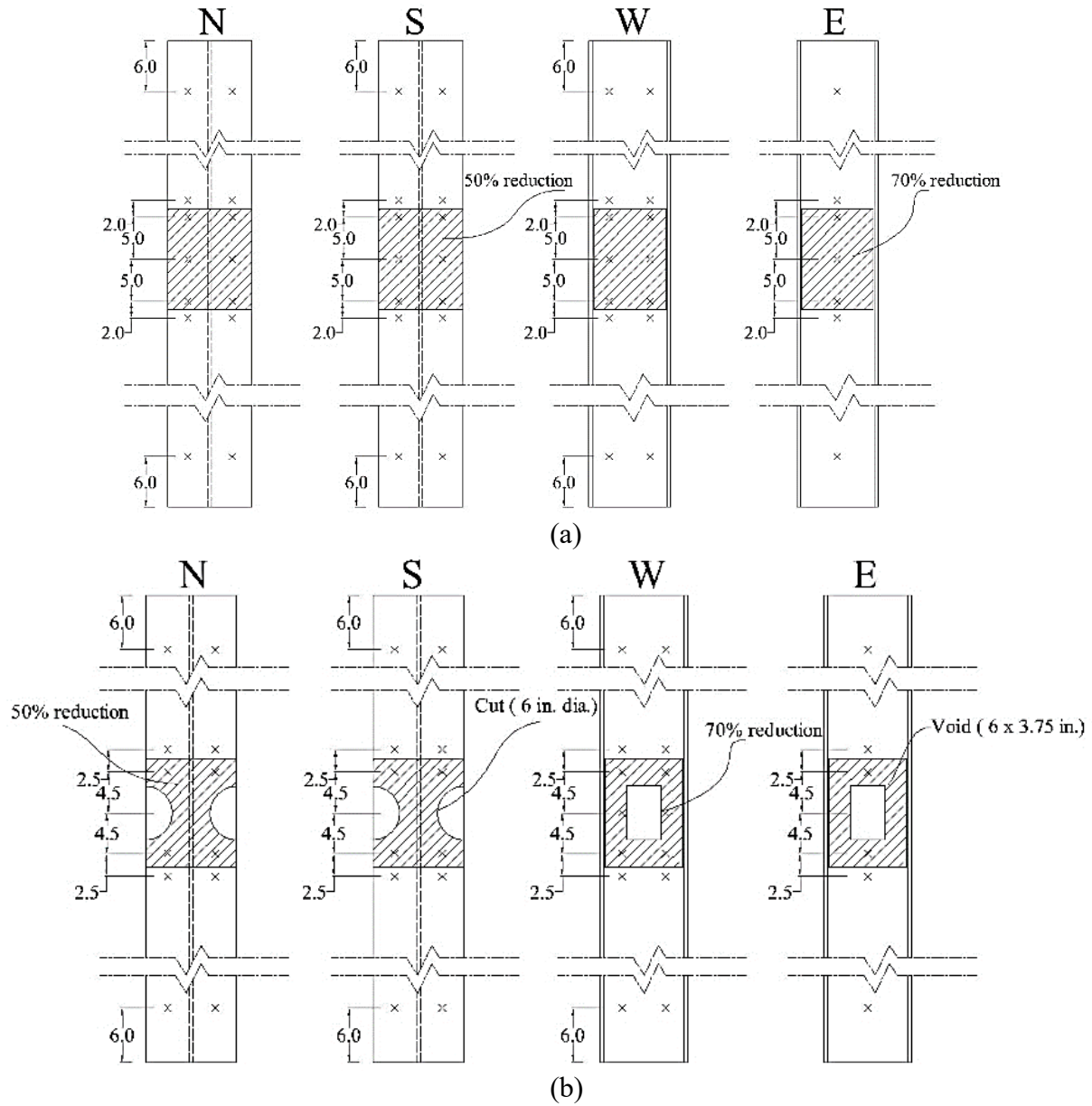


**Figure 3.8** Installation of strain gauges on H-pile: (a) Type 1, and (b) Type 2.



**Figure 3.9** Installation of strain gauges on post-tensioned bar.

### 3.6 Results and Discussion

Table 3.4 shows summaries of the peak loads, axial shortenings at peak loads, and failure modes. Figure 3.10 illustrates the axial force versus axial shortening for all the piles. Also shown in figure 3.10 are the strengths calculated using the FEMs presented in Chapter Two and the analytical models presented earlier in this chapter. Appendix A presents the axial strain gauges on each pile. The axial force was obtained as the sum of the values of the load cells installed on the post-tensioned bars. The axial shortening was obtained from two SPs placed between the moveable beam at one end of the pile and the fixed beam at the other end of the pile.

As shown in figure 3.10 (a), the peak load of the reference pile HP-W00-F00 was 2970kN (668.5 kips.) This was accompanied with yielding and local buckling in the flange (fig. 3.11 (a)).

For the HP-W70-F00, the peak load was 2535kN (570 kips) with failure due to local buckling in the flange, but the failure was at 482 kips where the web started to fail locally (fig. 3.11 (b)); after this the pile started to harden until a complete collapse occurred at the peak load due to

local buckling of the flange. The load then dropped abruptly (fig 3.10 (b)), and the pile maintained a residual capacity of 247kN (55.7 kips).

Figure 3.10 (c) illustrates that the peak load for HP-W00-F50 was 1605 kN (360.8 kips) accompanied with local failure in the flange (figs. 3.11 (c)), which triggered global buckling of the pile.

For the HP-W70-F50, the pile failed due to combined local buckling in both the web and flange at a peak load of 1245 kN (280 kips) (figs. 3.11 (d)). While loading continued, the pile maintained a residual capacity of 333 kN (75 kips) which represented 27% of the peak load (fig. 3.10 (d)).

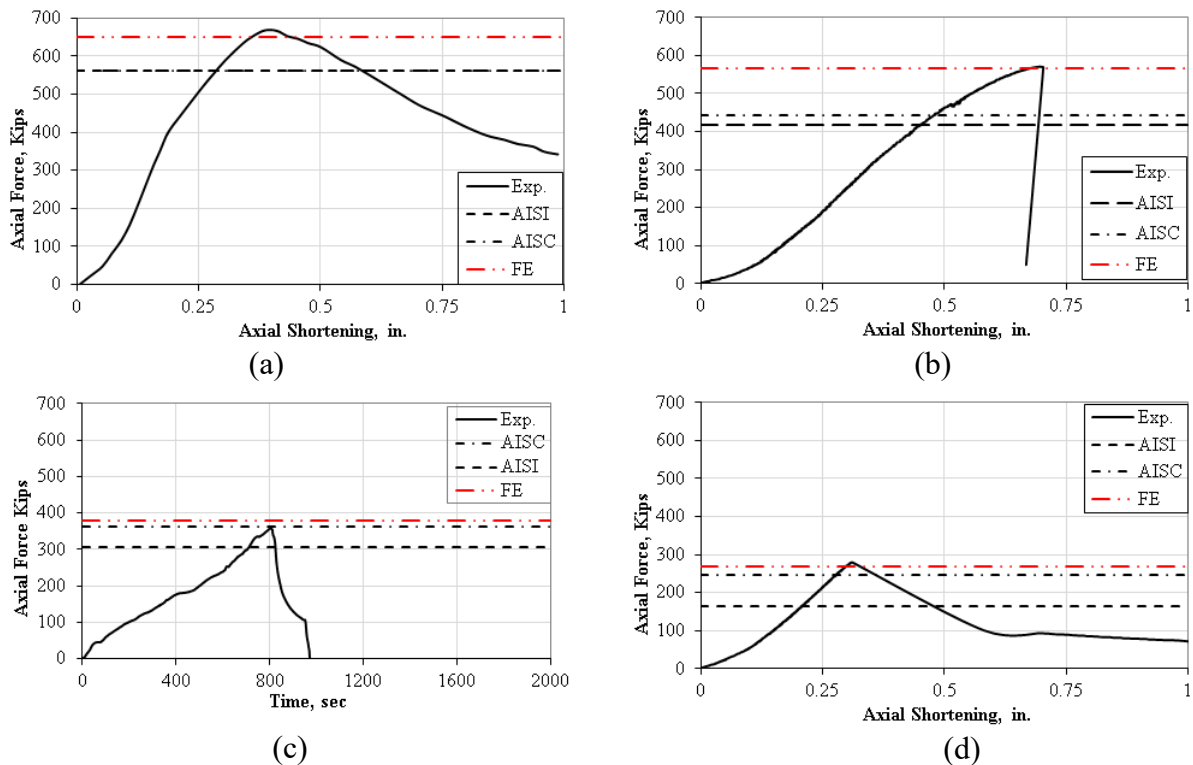
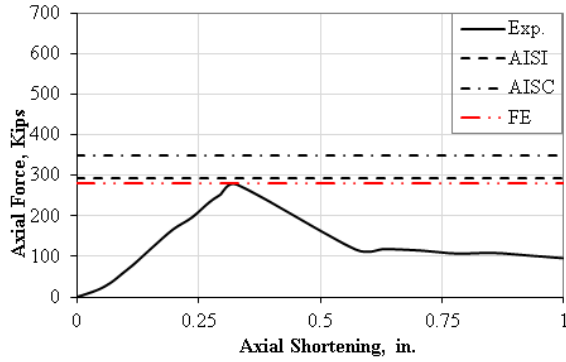
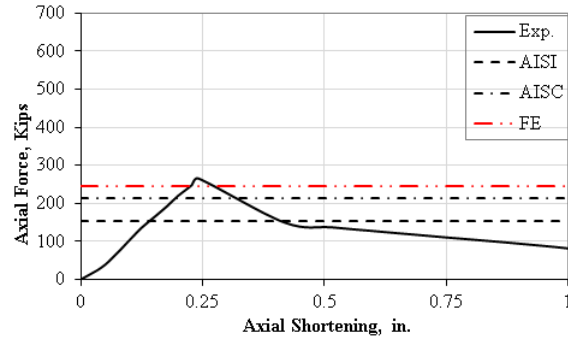


**Figure 3.10** Axial force-Axial shortening relation: (a) W00-F00, (b) W70-F00, (c) W00-F50, (d) W70-F50, (e) W70-F50/0, (f) W70V-F50, (g) W70-F50C, (h) W70V-F50C, (i) W70-F50-6, (j) W70V-F50C-10%, (k) W70V-F50C-30%, (l) W70-F50-10%.

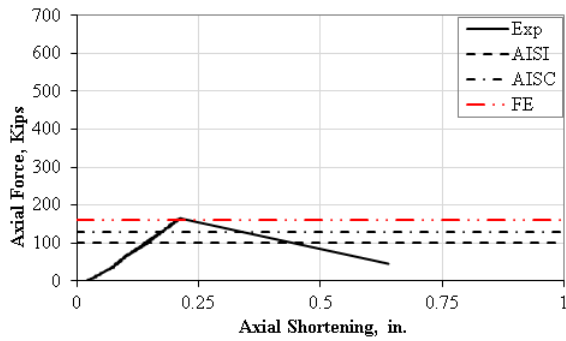




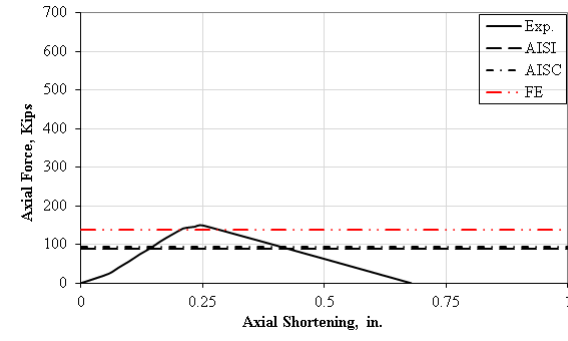
(e)



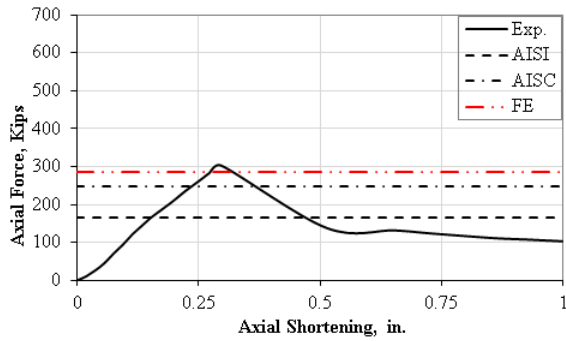
(f)



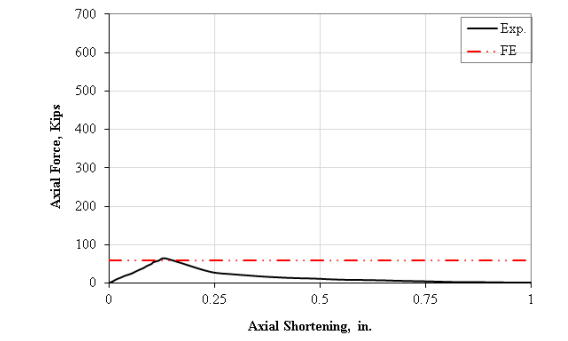
(g)



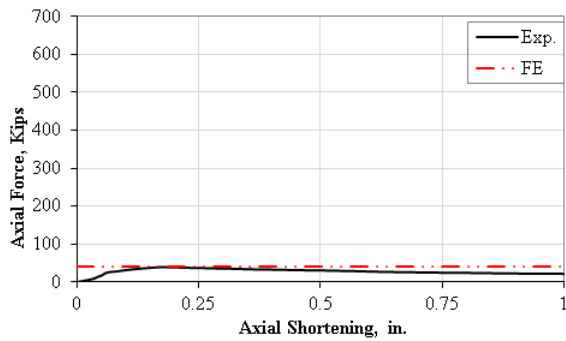
(h)



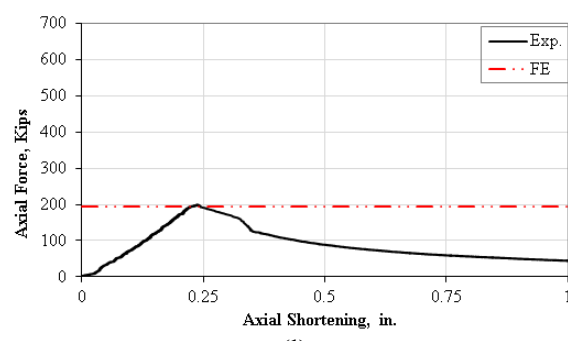
(i)



(j)



(k)



(l)

**Figure 3.10 cont.** Axial force-Axial shortening relation: (a) W00-F00, (b) W70-F00, (c) W00-F50, (d) W70-F50, (e) W70-F50/0, (f) W70V-F50, (g) W70-F50C, (h) W70V-F50C, (i) W70-F50-6, (j) W70V-F50C-10%, (k) W70V-F50C-30%, (l) W70-F50-10%.



**Table 3.4** Summary of the Results for the Tested Piles

Pile	Axial Capacity	Axial Shortening	Mode of failure
	Kips	In.	
W00-F00	668.5	0.403	FLB,GB
W70-F00	570.6	0.693	WLB,GB
W00-F50	360.81	--	FLB
W70-F50	279.67	0.309	FLB,WLB
W70-F50/0	277.7	0.33	FLB,WLB
W70V-F50	265.3	0.242	FLB,WLB
W70-F50C	166.037	0.214	FLB,WLB
W70V-F50C	149.63	0.25	FLB,WLB
W70-F50-6	302.86	0.296	FLB,WLB
W70V-F50C-10%	65.31	0.133	FLB,WLB
W70V-F50C-30%	39.27	0.17	FLB,WLB
W70-F50-30%	199.2	0.24	FLB,WLB

HP-W70-F50/0 had a peak load of 1236 kN (278 kips) (fig. 3.10 (e)) with local buckling failure in the flange and web (figs. 3.11 (e)), which triggered global buckling failure. The severely corroded HP-W70V-F50 failed at a peak load of 178 kN (265 kips) (fig. 3.10 (f)), due to local buckling in the flange (figs. 3.12 (a)) due the position of the opening in the web. Beyond failure, the pile maintained a capacity of 244 kN (55 kips) which is 20.74% of the peak load.

The peak load of the HP-W70-F50C was 738 kN (166 kips) (fig. 3.10 (g)) due to local buckling in the flange and web (fig. 3.12 (b)), which triggered global buckling. For pile W70V-F50C, the added void significantly decreased the peak load to 667 kN (150 kips) due to local buckling in the web followed with local buckling in the flanges (fig. 3.10 (h)). In the case of reducing the extension of corrosion to 152.4 mm (6 in.) in pile W70-F50-6, the peak load was

higher than that of the corresponding pile with a 12 in. long corroded section. Pile W70-F50-6 reached a peak load of 1347.8kN (303 kips) due to local buckling in the flange (fig. 3.10 (i)).

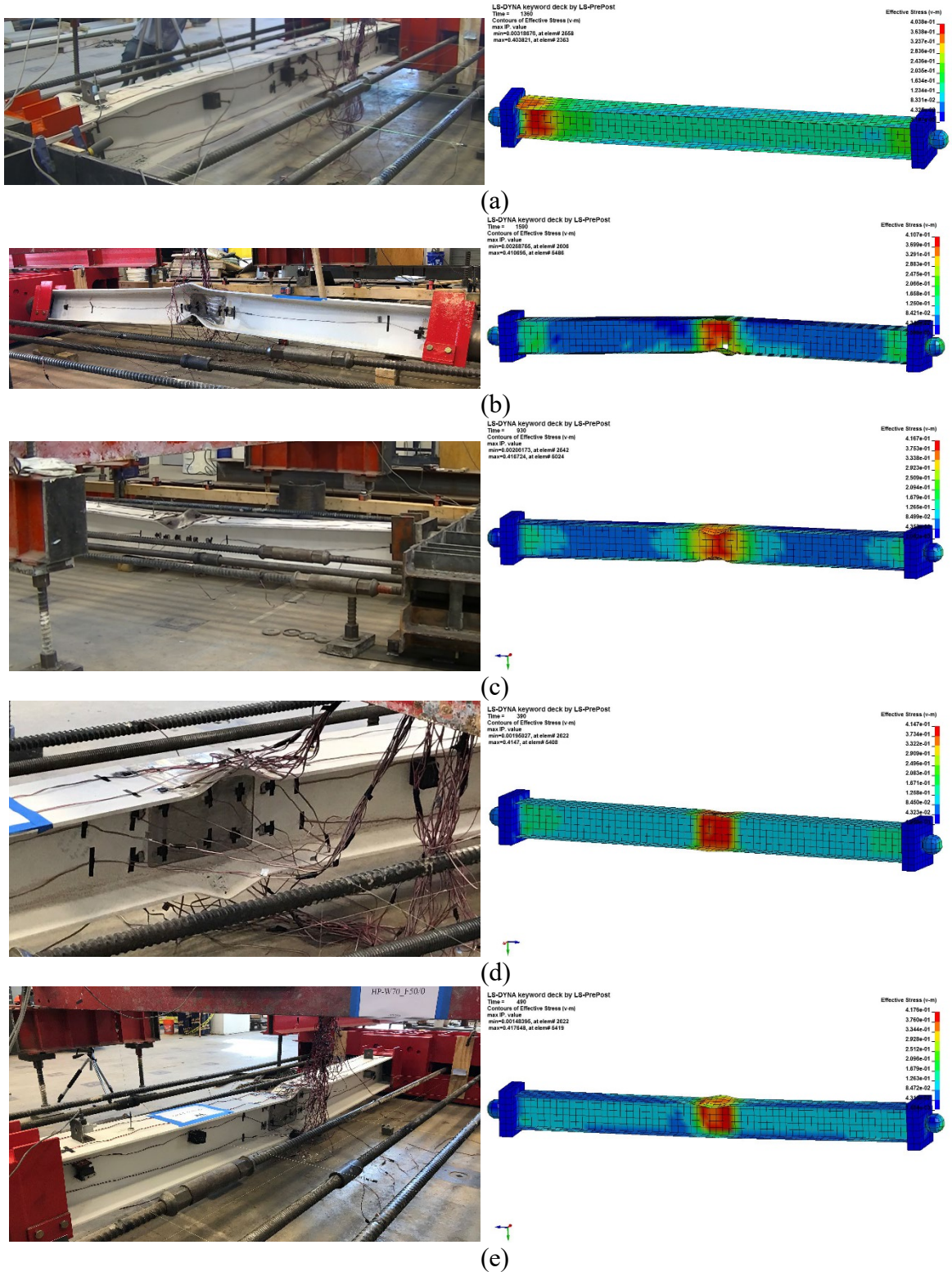


**Figure 3.11** Failure during the experimental vs. FEMs (a) W00-F00 , (b) W70-F00, (c) W00-F50, (d) W70-F50, and (e) W70-F50/0.

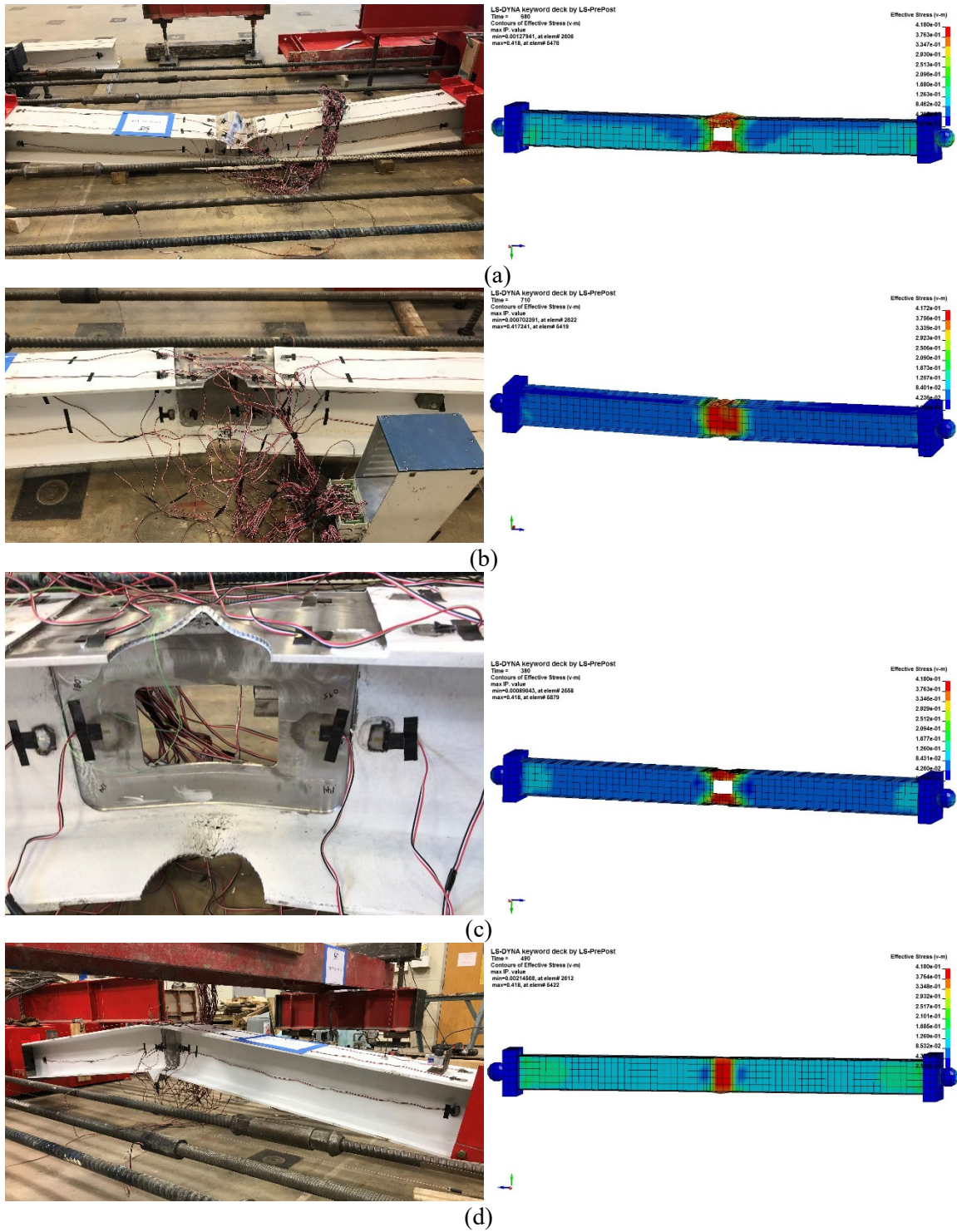


**Figure 3.12** Failure during the experimental vs FEMs (a) W70V-F50 , (b) W70-F50C, (c) W70V-F50C, (d) W70-F50-6in.

As for the eccentric loading, the percentage of eccentricity had a significant effect on the capacity of the pile. W70V-F50C-10 % failed at a peak load of 289 kN (65 kips) (fig. 3.10 (j)). This represented 43.6% of the corresponding pile with no eccentricity. Pile W70V-F50-30 %, having 30% eccentricity, failed at a peak load of 174 kN (39.3 kips) (fig. 3.10 (k)). This represented 26.2% of the corresponding pile with no eccentricity. Pile W70-F50-10 %, having 10% eccentricity, failed at a peak load of 886 kN (199.2 kips) (fig. 3.10 (l)). This represented 71.2% of the corresponding pile with no eccentricity.

The FEMs developed in Chapter two of this report were able to correctly predict the strength and modes of failure of the investigated piles. The FEMs predicted axial capacities ranging from 0.7% to 11% of those measured during the experimental work with an average measured-to-predicted strength of 4.4%.

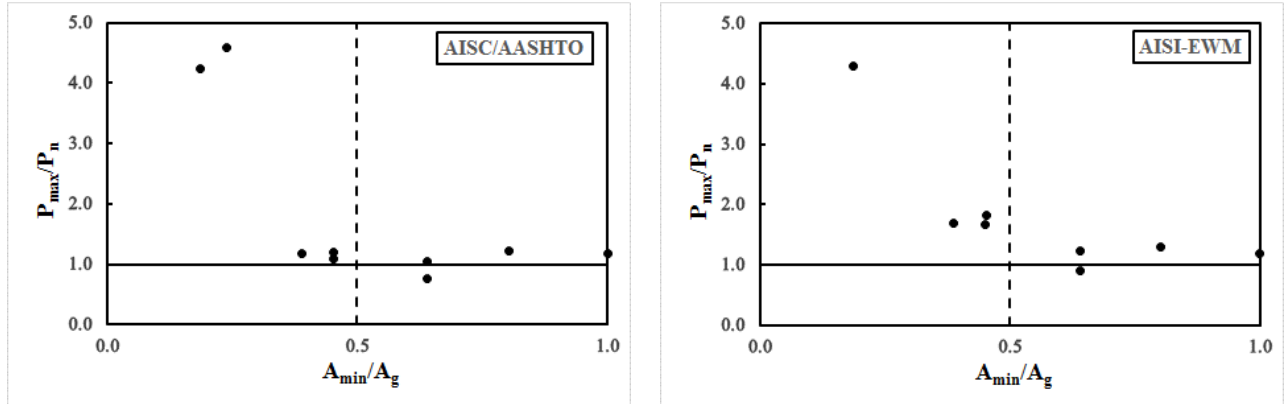
### *3.6.1 Comparisons of the Experimental Results and Existing Analytical Models*

Table 3.5 presents the calculated axial capacities of the tested columns using the two design methods presented in section 3.2 of this report. The effective length factor,  $K$ , for global buckling about the weak and strong axes was considered one. Table 3.5 also presents the ratio of the maximum load  $P_{max}$  - to - the predicted capacity  $P_n$ . Figure 3.13 shows  $P_{max}/P_n$  as a function of the  $A_{min}/A_g$  for both design models. Both analytical methods were conservative in predicting the strengths of the investigated piles. The peak strengths measured during the experimental work ranging from 0.76 to 4.59 and 0.91 to 5.04 of those predicted using AISC/AASHTO and AISI, with an average measured-to-predicted strength of 1.83 and 2.12, respectively.



**Table 3.5** Evaluating the axial capacity of the tested specimens using existing design specifications

Designation	Experimental		AISC & AASHTO		AISI-EWM	
	$A_{min}/A_g$	$P_{max}$ (Kips)	$P_n$ (Kips)	$P_{max}/P_n$	$P_n$ (Kips)	$P_{max}/P_n$
W00-F00	1	668.50	567.00	1.18	567.45	1.18
W70-F00	0.802273	570.60	466.05	1.22	437.14	1.31
W00-F50	0.640296	360.81	343.41	1.05	293.18	1.23
W70-F50	0.451269	279.67	254.62	1.10	167.00	1.67
W70-F50/0	0.639496	277.70	363.18	0.76	304.04	0.91
W70V-F50	0.387937	265.30	225.70	1.18	157.62	1.68
W70-F50C	0.238379	166.04	36.19	4.59	32.97	5.04
W70V-F50C	0.18643	149.63	35.32	4.24	34.86	4.29
W70-F50-6	0.453361	302.86	254.83	1.19	166.98	1.81



**Figure 3.13** Correlation between experimental to analytical axial capacity and remaining cross-sectional area

## Chapter 4 Bond Behavior of Steel Bridge H-Pile Columns Encased In Concrete Jacket

### 4.1 Introduction

This chapter investigates experimentally the bond behavior of 14 full-scale composite columns consisting of steel H-piles encased in concrete jackets. The composite columns were tested using the push-out test. The concrete encasement technique is proposed to detect the corrosion deficiencies in the steel columns of the existing bridges. Different concrete types (mainly conventional and geopolymer mixes) and embedded lengths were used for the concrete encasements and considered as the main parameters investigated in this study. Moreover, the effect of using different, unconfined concrete strengths were examined. The bond performance of the tested composite columns was evaluated and assessed. From the experimental results, it was observed that bond strength increased with an increase in the embedded length. Furthermore, compared to cement concrete mixes, the use of geopolymer concrete had a greater effect on load carrying capacity that related to the generated interface bond strength.

#### *4.1.1 Objectives*

This study presents the experimental results of push-out tests on 14 full-scale steel H-piles encased in concrete jackets. Different concrete types and embedded lengths were used for the concrete encasements. The load-slip curves at the loading and free ends were obtained; in addition, the distribution of steel H-Pile/concrete interface strains and the bond stress along the embedded length were analyzed.

The main objectives of this test series study are 1) to evaluate the bond performance of different concrete encased steel H-piles in terms of the effects on load carrying capacity for corroded steel H-pile bridge columns and to assess its ability under cast in-situ conditions, and 2)

to propose a local bond stress-slip model for use as a constitutive material model for this particular test assembly.

## 4.2 Experimental Program

### 4.2.1 Test Program

Fourteen specimens, having four types of concrete jackets with diameters of 508 mm (20 in.) and three different embedment lengths,  $L_{CE}$ , of 254, 508, 762 mm (10, 20, and 30 in.) (fig. 4.1), were examined using push-out testing in this chapter (table 4.1). The designation of each specimen includes three parts: 1) the concrete mix type (CC for conventional concrete, HES for high early strength, GA for ambient cured geopolymer concrete, or GT for thermally cured geopolymer concrete), 2) the targeted concrete strength in ksi, and 3) the  $L_{CE}$  value in inches.

**Table 4.1** Parametric Study

Group	Specimen	Concrete type	$f'_c$ MPa (ksi)	$L_{CE}$ mm (in.)
A	CC-5-10	CC2	34.5 (5)	254 (10)
	CC-5-20			508 (20)
	CC-5-30			762 (30)
B	HES-5-10	HES	39 (5.5)	254 (10)
	HES-5-20			508 (20)
	HES-5-30			762 (30)
C	GA-5-10	GA	39 (5.5)	254 (10)
	GA-5-20			508 (20)
	GA-5-30			762 (30)
D	GT-5-10	GT	39 (5.5)	254 (10)
	GT-5-20			508 (20)
	GT-5-30			762 (30)
E	CC-3-10	CC1	20.7 (3)	254 (10)
	CC-10-10	CC3	65.5 (9.5)	254 (10)



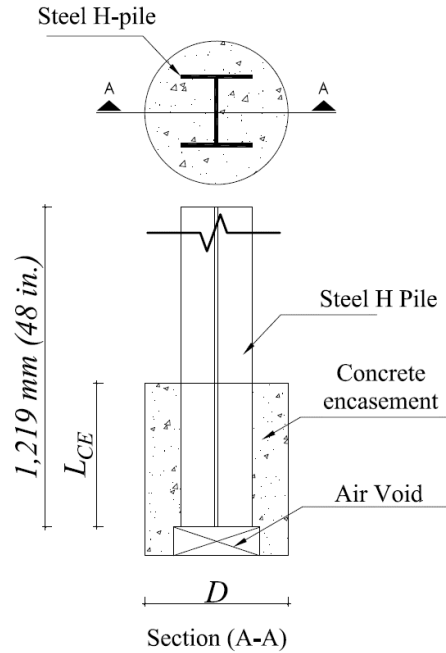


**Figure 4.1** Test specimen layout.

## 4.2.2 Material Properties

### 4.2.2.1 Steel H-pile

Three steel coupons were cut from a flange and another three from a web of a steel H-pile, and tested per ASTM E8/E8M – 16a (2016) to determine their tensile strengths (table 4.2). The axial strains at the middle region were determined using a 25.4 mm (1 inch) clip gauge (fig. 4.2). The steel coupons exhibited necking and elongation before rupture.

**Table 4.2** Mechanical Properties of Steel H-Pile Flange and Web

	Yield stress MPa (ksi)	Ultimate stress MPa (ksi)	Elastic modulus GPa ( $10^3$ ksi)	Rupture strain ( $\epsilon_u$ , in/in)
Flange	324 (47)	517 (75)	181 (26.25)	0.100
Web	407 (59)	503 (73)	182 (26.40)	0.125

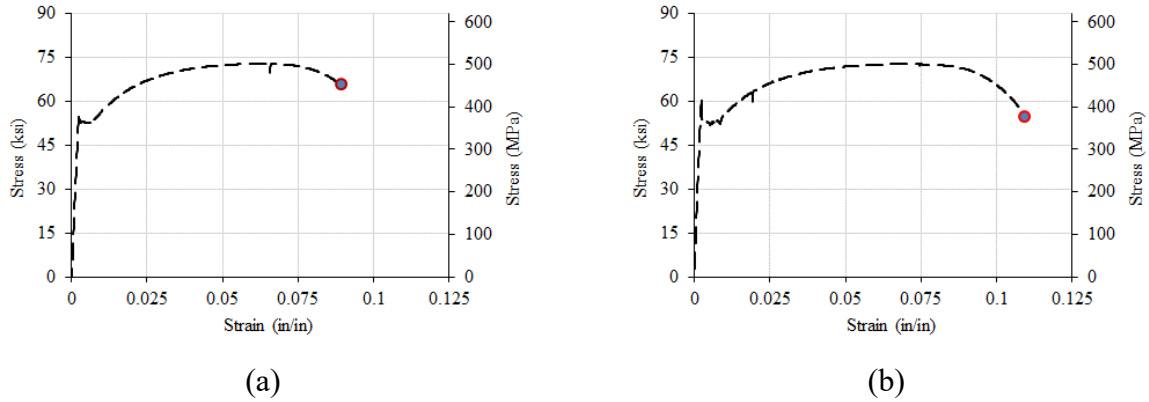


**Figure 4.2** Steel tubes average stress-strain curve (a) flange, and (b) web.

#### 4.2.2.2 Concrete

Three concrete types were used in this study: conventional concrete (CC), high early strength concrete (HES), and geopolymer concrete (GC). The first and second concrete types were synthesized using ordinary Portland cement (OPC) type I and III, respectively. The first type of CC had three different  $f'_c$  of 20.6, 34.5, and 65.5 MPa (3, 5, and 9.5 ksi) on the day of testing. The third concrete type was synthesized using fly ash class C (FA) activated using alkali activators. The concrete mixtures were prepared using dolomite having a specific gravity of 2.76 per ASTM C127-15 (Zmetra 2015) and Missouri river sand having a specific gravity of 2.60 per ASTM C128-15 (Yu et al. 2009). Aggregates were prepared to have saturated surface dry condition prior to mixing. The particles size distribution of aggregates were within the acceptable limits of the ASTM C33-16 (2016) (fig. 4.3). Two class C FAs sourced from two different power plants located in Missouri, USA were used in this study. The chemical composition of the FAs were determined following ASTM D4326-13(2013) (table 4.3).

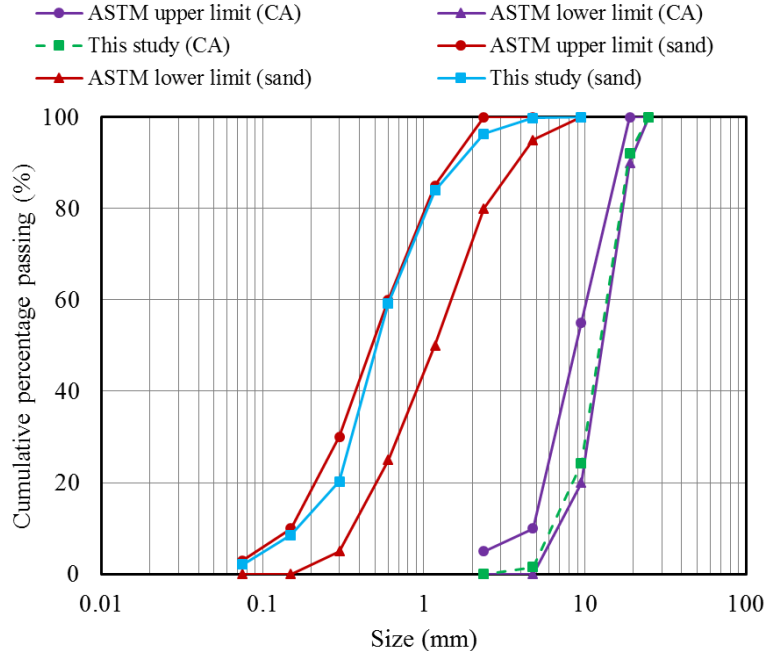


**Figure 4.3** Particle size distribution of the coarse and fine aggregates. (Note: CA: coarse aggregate)

**Table 4.3** Chemical Composition of FAs by XRF

Fly ash	Oxides										LOI <sup>a</sup>
	SiO <sub>2</sub>	Al <sub>2</sub> O <sub>3</sub>	Fe <sub>2</sub> O <sub>3</sub>	CaO	MgO	Na <sub>2</sub> O	K <sub>2</sub> O	TiO <sub>2</sub>	P <sub>2</sub> O <sub>3</sub>	MnO	
FA1	36.89	13.99	3.52	36.96	4.80	1.62	0.62	0.87	0.70	0.03	0.50
FA2	43.91	20.12	4.96	21.24	4.29	2.87	0.70	1.36	0.51	0.05	0.40

<sup>a</sup>LOI: Loss on ignition

Alkali activator solutions, including sodium silicate (SS) and sodium hydroxide (SH) with molarity of 10 M, were used in this study. The SS had 14.7% of Na<sub>2</sub>O, 29.4% of SiO<sub>2</sub>, and 55.9% of H<sub>2</sub>O. According to a previous study (Gomaa et al. 2017), the sum of the alkali activators (Alk)-to-FA and SS/SH ratios were 0.30 and 1.0, respectively (Gomaa et al. 2017).

#### 4.2.2.3 Concrete Jacket Mix Design

Table 4.4 illustrates the different mix designs that were used for the concrete jackets during this study. The mixing procedure of the three conventional concrete mixtures (CC1, CC2, and CC3) as well as one high early strength (HES) mixture were following ASTM C192-16 (2016). The mixing procedure of the two geopolymer concrete mixtures GA and GT were following Gomaa et al. (2017).

**Table 4.4** Mix Design of CC, HES, and Geopolymer Concrete Mixtures

Mix	CC1 kg/m <sup>3</sup> (lb/yd <sup>3</sup> )	CC2 kg/m <sup>3</sup> (lb/yd <sup>3</sup> )	CC3 kg/m <sup>3</sup> (lb/yd <sup>3</sup> )	HES kg/m <sup>3</sup> (lb/yd <sup>3</sup> )	G1 kg/m <sup>3</sup> (lb/yd <sup>3</sup> )	G2 kg/m <sup>3</sup> (lb/yd <sup>3</sup> )
CA <sup>a</sup>	1033 (1742)	1033 (1742)	837 (1411)	848 (1430)	959 (1616)	959 (1616)
sand	1597 (1597)	701 (1182)	837 (1411)	848 (1430)	799 (1347)	799 (1347)
W <sup>b</sup>	162.0 (273)	195.8 (330)	213 (359)	192.8 (325)	82.8 (140)	87.3 (147)
C <sup>c</sup>	249 (420)	356 (600)	386 (650)	451 (760)	-	-
HRWR <sup>d</sup>	-	-	2.1 (3.6)	1.2 (2)	-	-
FA	-	-	175 (295)	-	450 (758)	450 (758)
W/B	0.65	0.55	0.38	0.43	0.35	0.36
SS	-	-	-	-	67.5 (114)	67.5 (114)
SH	-	-	-	-	67.5 (114)	67.5 (114)

<sup>a</sup>CA: coarse aggregate

<sup>b</sup>W: water

<sup>c</sup>C: cement

<sup>d</sup>HRWR: high range water reducer

<sup>e</sup>B: the total binder

#### 4.2.3 Test Specimen Preparation

Table 4.5 and figure 4.4 illustrate the repair process of the repaired piles. A steel H-pile was placed inside a Sonotube and placed atop of an H-shaped 101.6 mm (4 in.) high wooden template (fig. 4.4 (b)), which was used to form a void inside the concrete jacket underneath the steel H-pile specimen (fig. 4.4 (c)). This allowed the steel H-pile to slip downward freely inside the concrete jacket to the steel pile without any restraints when the applied axial load exceeded the bond capacity of the concrete jacket (fig. 4.4 (d and e)).

#### 4.2.4 Test Set-up and Instrumentation

Electrical strain gauges were mounted on the web faces and outer surfaces of the flanges of each H-pile specimen, before casting the concrete, to measure the strain distributions (fig. 4.5 (a)). Twenty-eight, thirty-five, and forty-nine strain gauges were mounted on the 254, 508, and 762 mm (10, 20, and 30 in.) long jackets, respectively, in seven longitudinal lines and at different horizontal levels (fig. 4.5 (c through e)). Two linear variable displacement transducers (LVDTs) were placed vertically on each flange side to measure the slip between the concrete and steel (fig. 4.5 (b)).

**Table 4.5** Specimen Geometrical Properties

Steel H-pile		Concrete Encasement	
Section	Length, $H$ mm (in.)	Diameter, $D_{CE}$ mm (in.)	length, $L_{CE}$ mm (in.)
$250 \times 62$ (10 $\times$ 42)	1219.2 (48)	508 (20)	254 (10) to 762 (30)

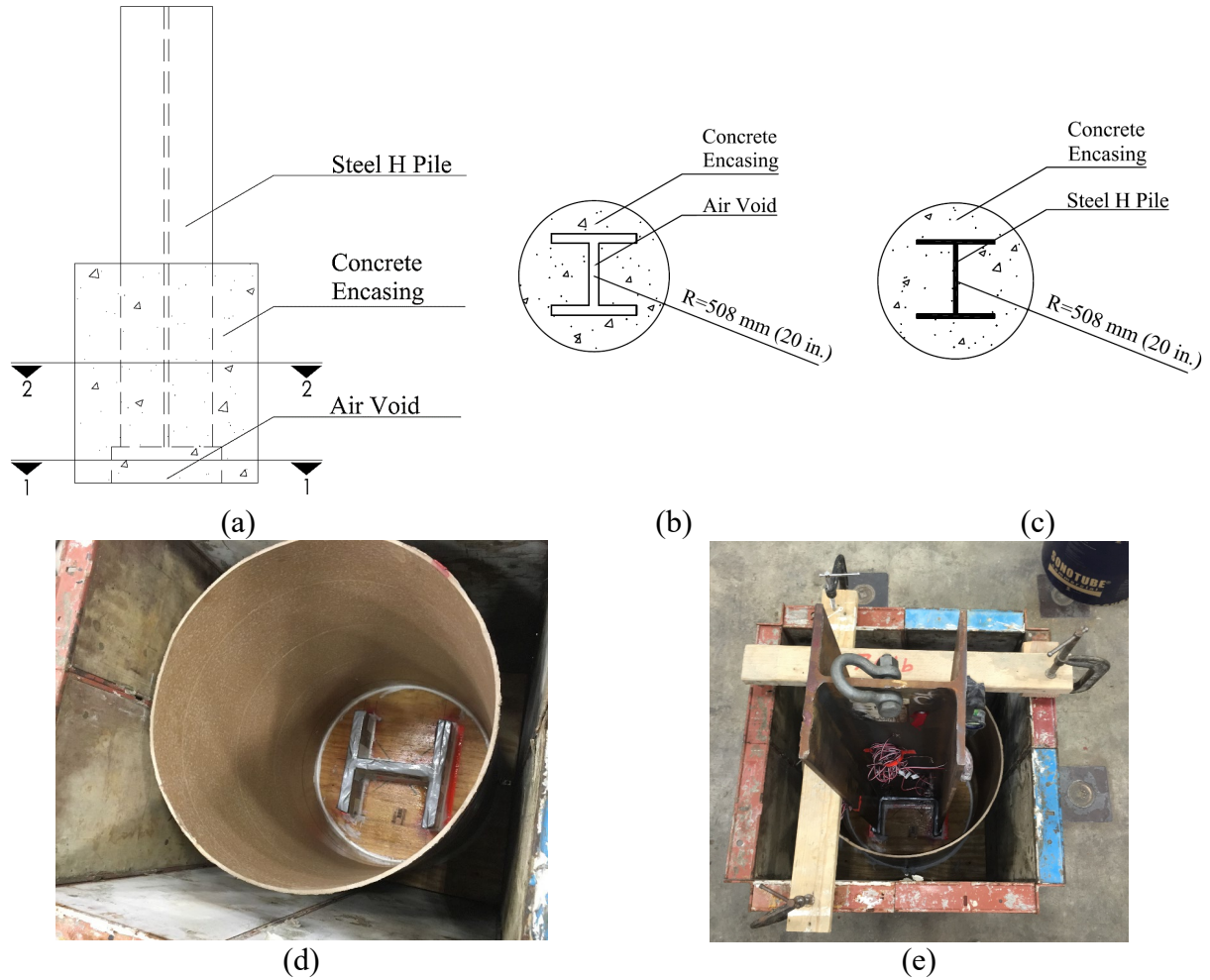


**Figure 4.4** H-pile repair (a) assembly, (b) section 1-1, (c) section 2-2, (d) Sonotube installation, and (e) the assembly ready for concrete placement.

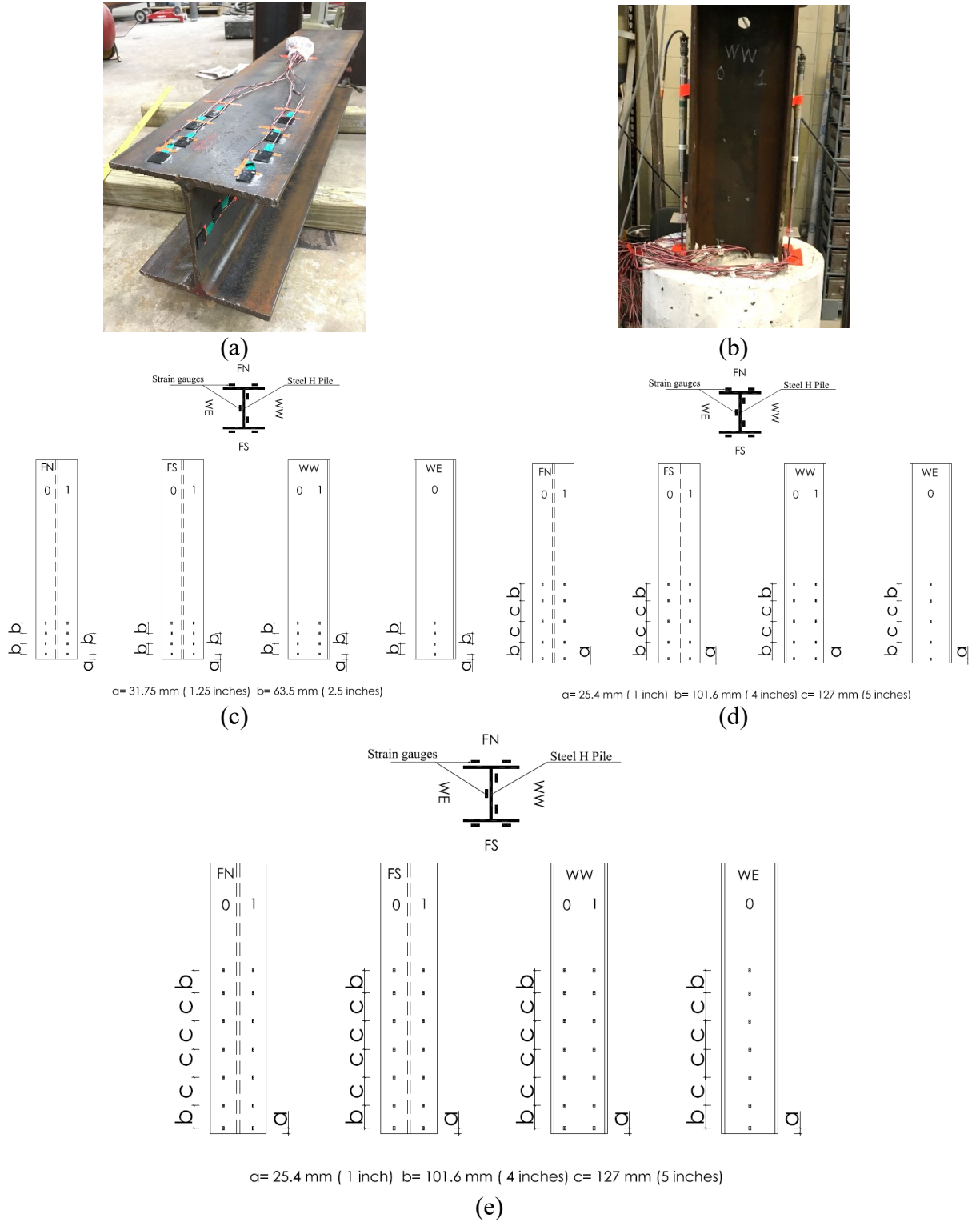


**Figure 4.5 Instrumentation:** (a) strain gauges mounted on the steel H-pile, (b) two LVDTs on each pile, (c, d, and e) strain gauges layout for  $L_{CE}=254, 508, 762$  mm (10, 20, and 30 in.).

#### *4.2.5 Concrete Jacket Casting and Curing*

The concrete jackets using the different concrete mixes (table 4.4, fig. 4.6) were placed and numerous 101.6 x 203.2 mm (4 x 8 in.) concrete cylinders were placed using the same concrete mixtures used for the column jackets. All specimens, i.e., the cylinders and the steel piles encased in the concrete jackets, were then cured using one of the following two curing regimes.

##### *4.2.5.1 Ambient curing regime*

An ambient curing regime was used for mixtures CC, HES, and GA. The ambient curing regime was applied to the GA mixture since the FA used to synthesize this mixture had a high calcium content (table 4.5). Gomaa et al. (2017) recommended ambient curing for geopolymer concrete synthesized using high-calcium content FA.

The Sonotube was demolded two days after placing the encasement concrete. Then, the concrete was covered with wet burlap sheets and cured at an ambient temperature of  $23 \pm 2^\circ \text{C}$  ( $73 \pm 3^\circ \text{F}$ ) until the testing day (fig. 4.7 (a)). The concrete cylinders were also exposed to the same ambient curing regime and were tested periodically during the curing period. Once the target compressive strength was achieved, the curing was stopped and the pile was tested.

##### *4.2.5.2 Elevated heat temperature curing regime*

An elevated heat curing regime was used for the GT mixture that was synthesized using FA2 since it had a relatively low calcium content (table 4.5).

A thin steel sheet was rolled around the concrete jacket diameter. Three thermal wires were spirally mounted on the steel sheet to supply the required heat curing (fig. 4.7 (b)). The concrete had a resting time of 12 hours before the start of the elevated heat-curing regime. The temperature of the thermal wires was set at  $60^\circ \text{C}$ . Eight thermocouples were inserted at different



locations inside the geopolymer concrete to monitor and ensure that the heat was distributed equally during the curing period. During the curing period, the specimen including the heat system was wrapped and sealed using insulation sheets to sustain a constant temperature (fig. 4.7 (b and c)). The GT mix cylinders were also wrapped inside the insulation sheets to be subjected to the same temperature as the concrete casing. The temperature of the geopolymer concrete gradually increased with time, reaching 60° C after approximately two days of curing. The maximum difference in the internal temperature of the geopolymer concrete measured using the thermocouples was 4° C. Concrete cylinders were tested periodically during the curing period. Once the target compressive strength was achieved, the curing was stopped, and the column was left one day to cool down followed by demolding the Sonotube.

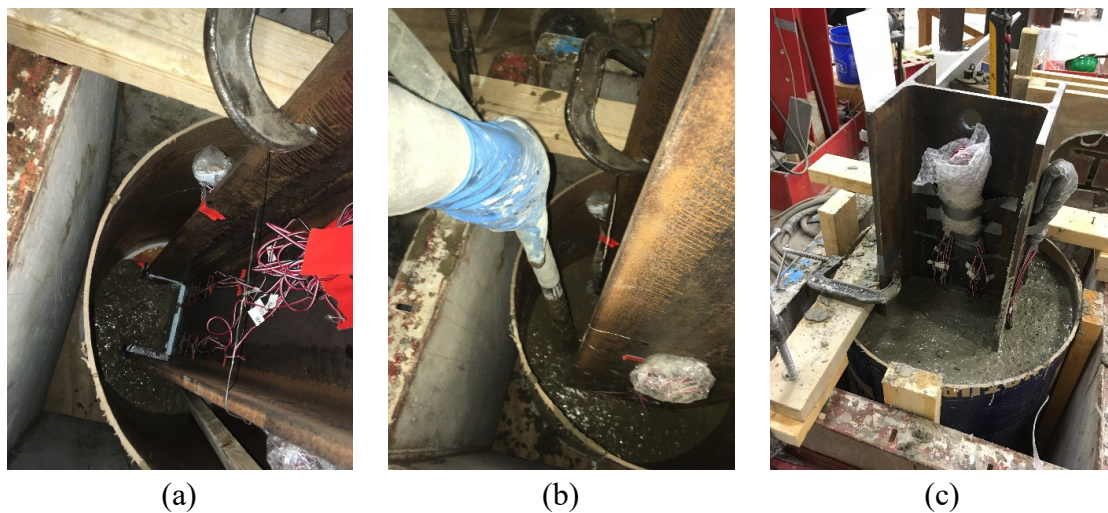


**Figure 4.6** Concrete encasement procedure (a) placing, (b) vibrating, and (c) finalizing.

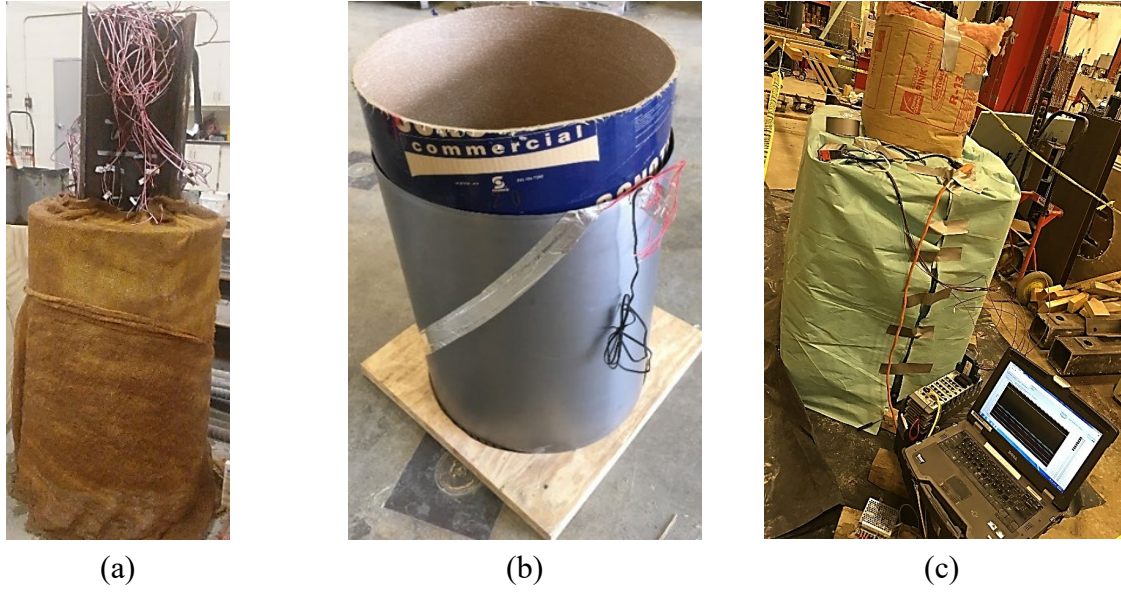


**Figure 4.7** Geopolymer concrete curing process (a) GA, and (b and c) GT.

#### *4.2.6 Push-out Test*

The fifteen specimens were tested with an MTS universal testing machine with a capacity of 2,250 kN (560 kips) (fig. 4.8). The specimens were monotonically axially loaded in a displacement control with a rate of 1.27 mm/min (0.05 in./min). The compressive force was applied vertically on the top of the steel pile using the MTS swivel plate, while the bottoms of the concrete encasement were supported on a rigid steel base.

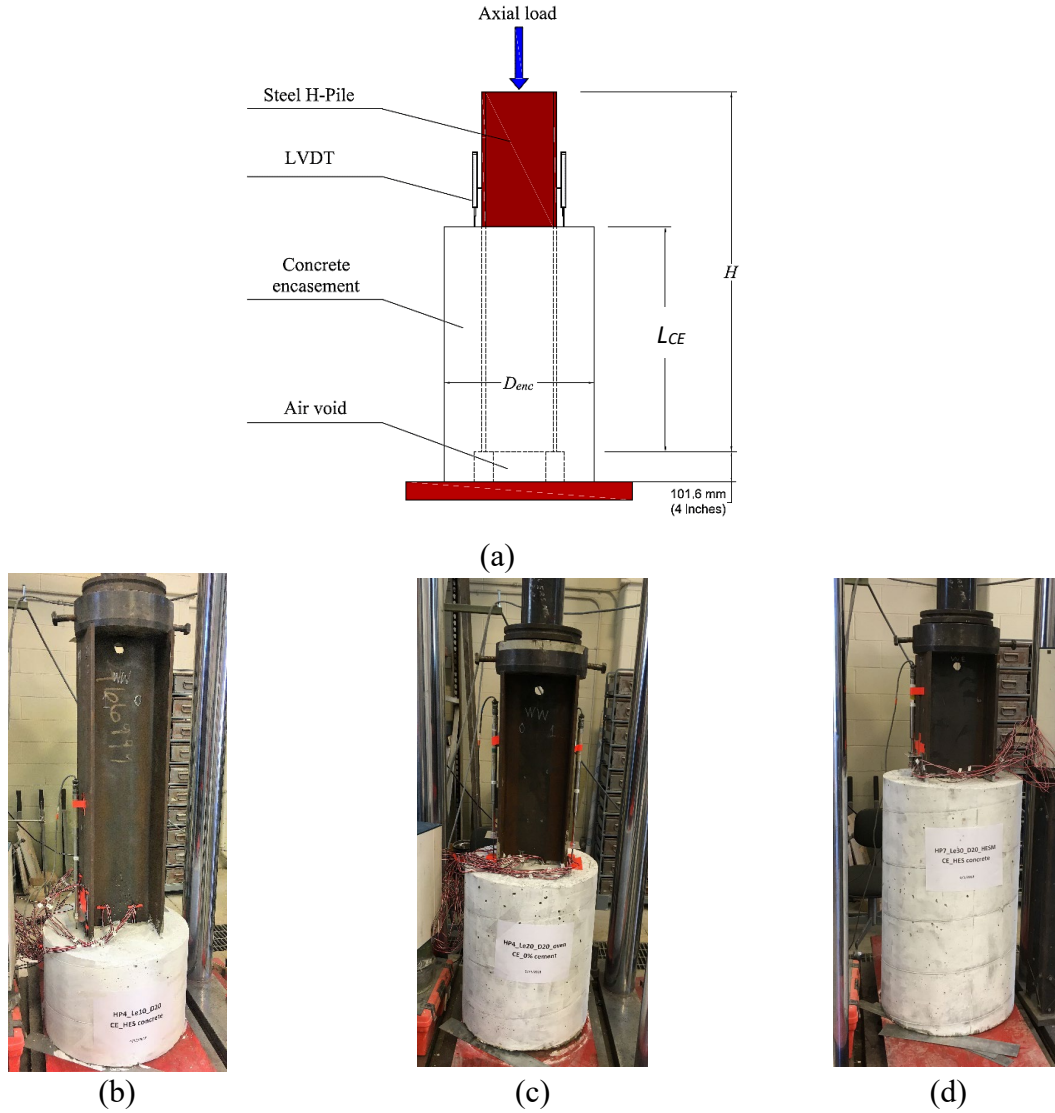


**Figure 4.8** Concrete encased steel H-pile columns under push-out test (a) test layout, (b)  $L_{CE}$  = 254 mm (10 in.), (c)  $L_{CE}$  = 508 mm (20 in.), and (d)  $L_{CE}$  = 762 mm (30 in.).

### 4.3 Results and Discussion

The push-out test results are summarized in table 4.6. The bond stress ( $\tau$ ) is defined, using equation 4.1, as the axial load normalized by the contact area between the jacket and steel pile. Equation 4.1 assumes uniform bond stress distribution along the embedment length of the steel pile.

$$\tau = \frac{F}{p L_{CE}} \quad (4.1)$$

where  $F$  is the applied axial load at the free loaded end in kips,  $p$  is the perimeter of the H-pile section = 1,473 mm (58 in.), and  $L_{CE}$  is the embedded bond length in inches. The relative slip between the steel H-pile and the concrete jacket at the loaded end was obtained from the LVDT readings.

**Table 4.6** Test Results of the Push-Out Tests of Concrete Encased H-Pile Columns

Concrete type	Specimen name	$L_{CE}$ , mm (in.)	$P$ , kN (kips)	$\tau$ , MPa (psi)	$\delta_{max}^*$ , mm (in.)	$(f'_c)^{**}$ MPa (psi)
CC	CC-3-10	254 (10)	200.6 (45.1)	0.54 (78)	2.35 (0.09)	20.6 (2,985)
	CC-10-10	254 (10)	315.4 (70.9)	0.84 (122)	2.93 (0.12)	65.5 (9,492)
	CC-5-10	254 (10)	211.3 (47.5)	0.56 (81)	1.75 (0.07)	34.5 (4,999)
	CC-5-10	508 (20)	607.2 (136.5)	0.81 (117)	2.93 (0.12)	37.8 (5,477)
	CC-5-10	762 (30)	688.6 (154.8)	0.61 (88)	3.1 (0.12)	35.8 (5,195)
HES	HES-5-10	254 (10)	272 (61.15)	0.72 (104)	2.18 (0.086)	37.8 (5,480)
	HES-5-20	508 (20)	590 (132.6)	0.78 (113)	3.5 (0.14)	42.8 (6,208)
	HES-5-30	762 (30)	721 (162)	0.64 (92.4)	3.72 (0.15)	40.9 (5,928)
GA	GA-5-10	254 (10)	187.7 (42.2)	0.5 (72.2)	2.4 (0.095)	32.8 (4,759)
	GA-5-20	508 (20)	271.3 (61)	0.36 (52.1)	2.91 (0.11)	39.8 (5,769)
	GA-5-30	762 (30)	436 (98)	0.39 (56.5)	3.2 (0.13)	36.2 (5,249)
GT	GT-5-10	254 (10)	181.5 (40.8)	0.48 (69.7)	1.8 (0.07)	37.1 (5,377)
	GT-5-20	508 (20)	422.6 (95)	0.55 (80.7)	2.95 (0.11)	41.9 (6,070)
	GT-5-30	762 (30)	480.9 (108.1)	0.43 (61.8)	5.26 (0.21)	32.9 (4,770)

\* At the peak load

\*\* Average of three cylinders results at the day of test



### 4.3.1 Failure Modes

Figure 4.9 shows the failure modes of the 14 tested specimens in this study. Generally after performing the push-out loads, the surface of the steel H-pile was intact (fig. 4.10), which indicated a shear failure occurred on the interface between the concrete jacket and the steel section.

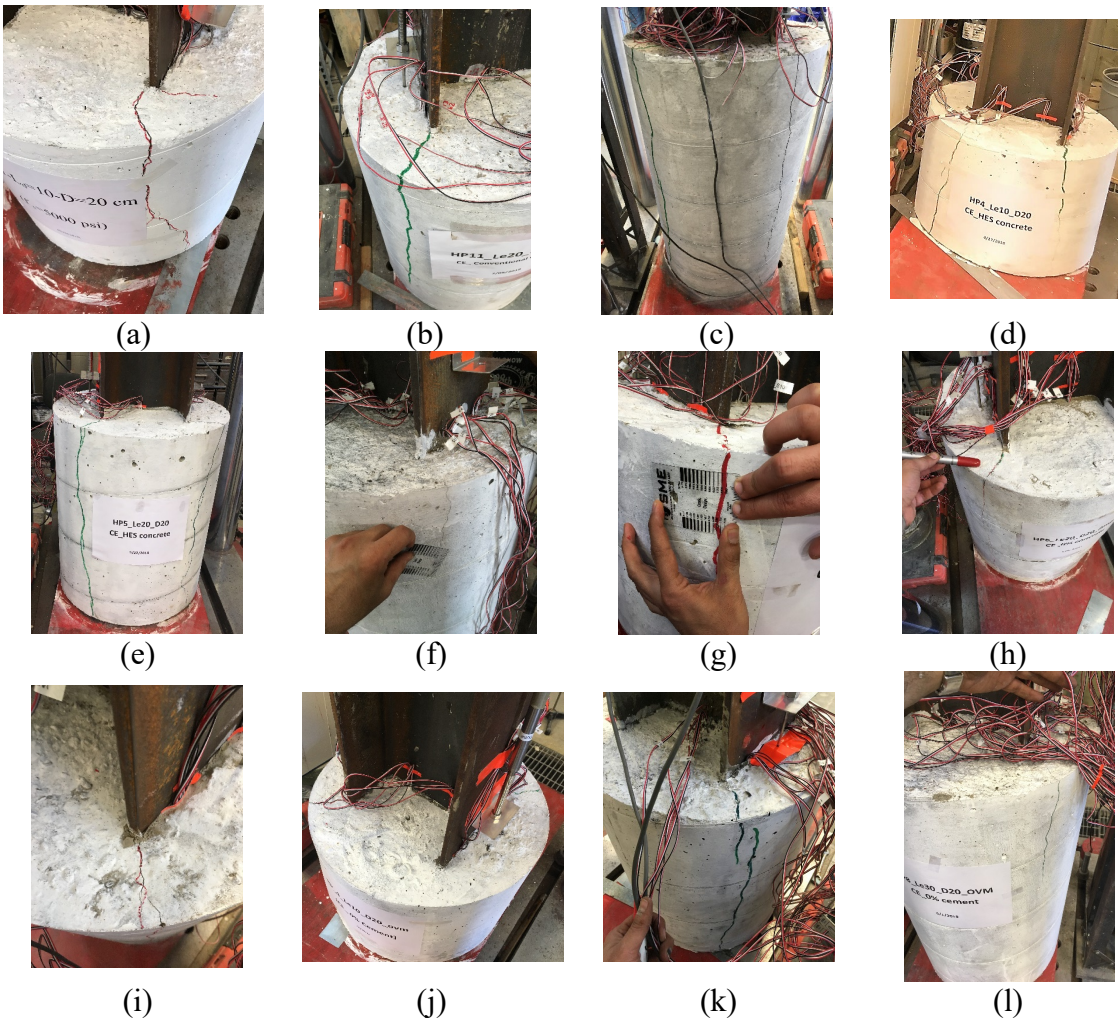


**Figure 4.9** Concrete encasement crack patterns with different embedment length ( $L_{CE}$ ) of 254, 508, 762 mm (10, 20, and 30 in.) (a-c) CC, (d-f) HES, (g-i) GA, and (j-l) GT.

The characteristic feature of this failure mechanism is the downward slip of the steel H-pile followed by a sudden failure at the ultimate load without any concrete crushing. This sudden failure was accompanied by splitting the concrete followed by decreasing in the axial load. Stress concentration occurred at the tips of the steel flanges combined with high hoop strains, which led to vertical cracking. Most of the specimens experienced the same crack pattern (fig. 4.9).



**Figure 4.10** Concrete encasement – steel H-pile contact area condition (a)  $L_{CE} = 254$  mm (10 in.), (b)  $L_{CE} = 508$  mm (20 in.).

#### 4.3.2 Bond Stress-Slip Curves

The general mechanics of stress transfer by bond between a steel rebar and concrete are mainly controlled by three factors: 1) chemical adhesion provided by the concrete, 2) friction, and 3) mechanical interlocking offered by the deformation of the reinforcement's surface (du Béton 2000; Hadi 2008; Harajli 2009; Raynor et al. 2002). The three mechanisms are not independent, and isolating one component during the slip process is not possible. For the experimental work considered in the current study, the surface of the steel H-pile is smooth,

therefore, mechanical interlocking does not exist, and only chemical adhesion and friction are considered.

Figure 4.11 shows a schematic of a typical bond stress-slip model curve for the tested piles in this study. In the initial loading stage, the response consists of a stiff linearly ascending part A-B in which the bond resistance is composed mainly of chemical adhesion and/or static friction, with practically very little increase in the slip. After that, as the slip increases, micro cracks appear at the smallest concrete encasement thickness near the flanges' edges; then, the cracks propagate gradually toward the concrete jacket surface. Finally, the radial component of the bond force increases and the widths of the cracks increase significantly, leading to splitting failure at point B. The presented model is similar to bond-slip models between an internal reinforcing bar and concrete where a residual constant friction force (residual bond stress at region C-D) remains at large slip (Cao et al. 2007).

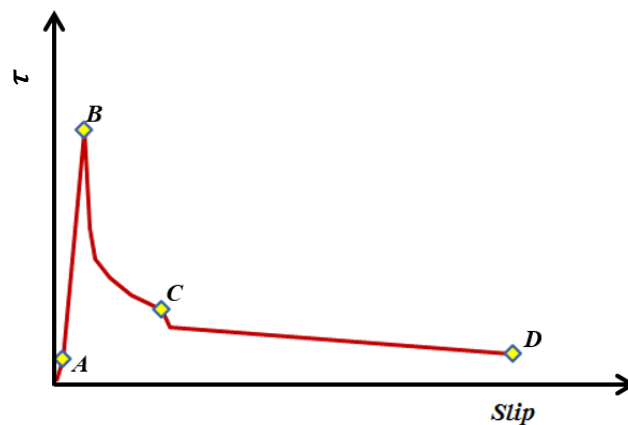


**Figure 4.11** Typical bond stress ( $\tau$ ) versus slip curve

#### 4.3.3 Bond Stress Distribution

The obtained bond stress of the 14 tested piles are depicted in figure 4.12. Steel H-piles that were encased in CC and HES concrete showed approximately 45% higher bond strength than those encased in GA and GT concretes. This may be attributed to the chemical adhesion interaction between the concrete paste with and without a cement component. The residual bond stress was approximately less than one-third the ultimate values in the range of 0.067-0.200 MPa (10-25 ksi) for all the tested piles.

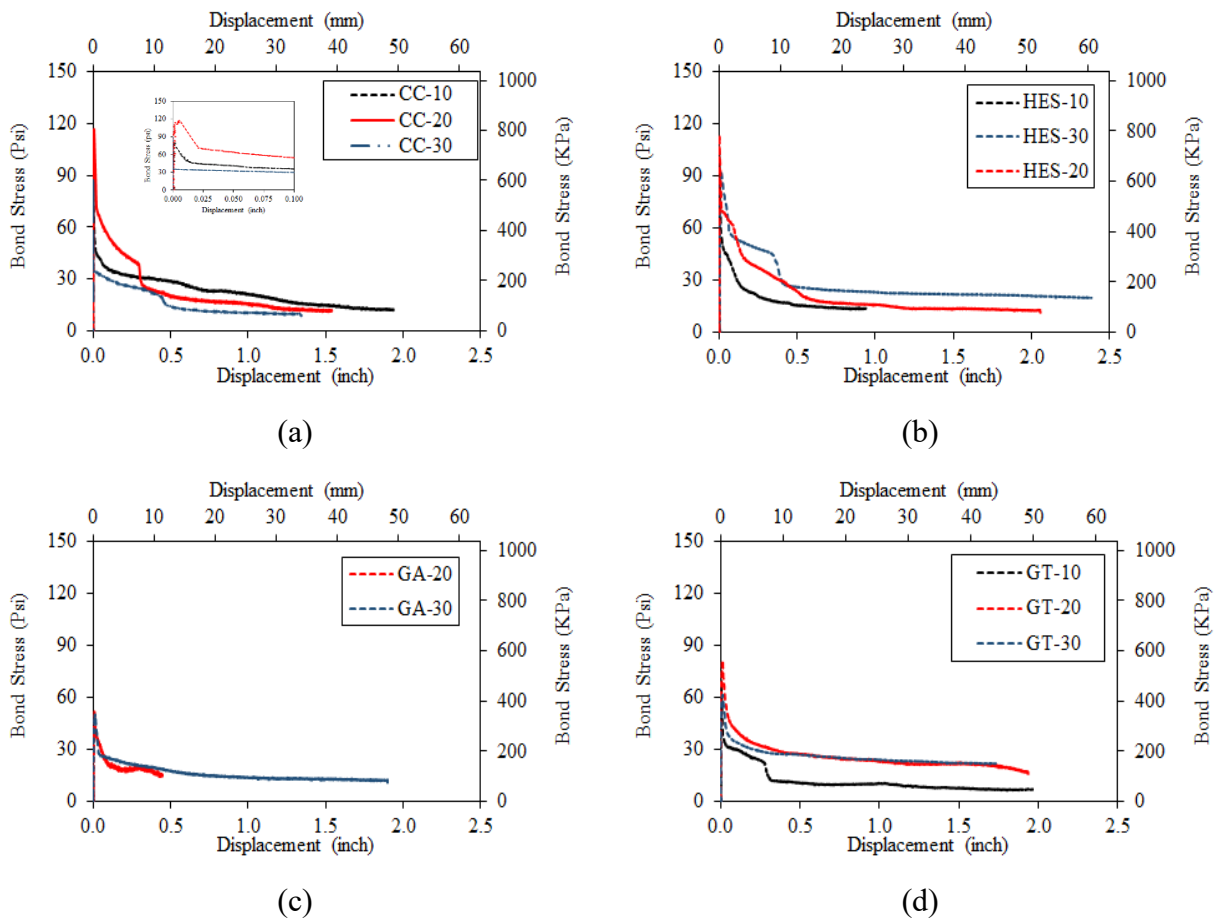


**Figure 4.12** Bond stress versus slip of the tested H-pile columns encased with concrete (a) CC, (b) HES, (c) GA, and (d) GT.



Figure 4.13 illustrates the bond strength ratio of the tested in this study. Concrete strength is generally considered one of the most important factors that determine bond strength. The local bond strength  $\tau_{max}$  is related to  $\sqrt{f_c}$ . Thus, researchers have studied the local bond strength in terms of the normalized bond strength ( $\tau_{max}/\sqrt{f_c}$ ) (ACI 1999; Esfahani and Kianoush 2005; Harajli et al. 1995; Ichinose et al. 2004; Orangun et al. 1977). Given this common consensus, the local bond strength is also studied in this paper with respect to the bond strength ratio.

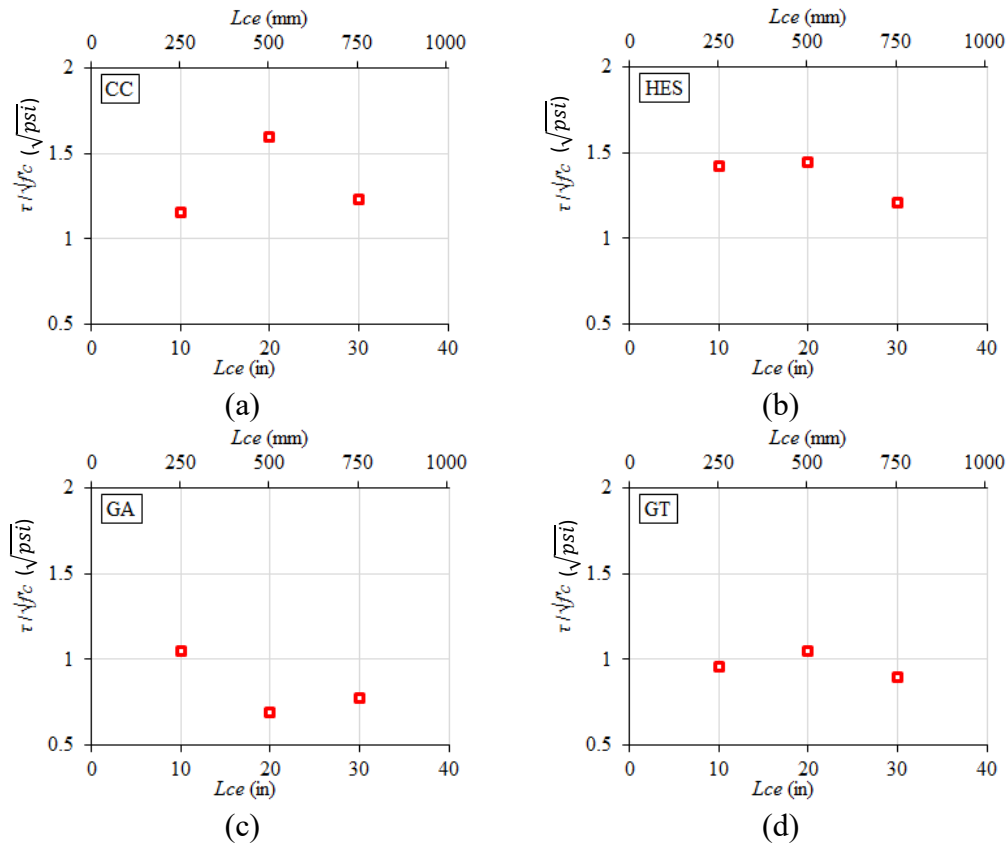


**Figure 4.13** Bond strength ratio of the tested composite columns.

As shown in figure 4.12, the CC and HES concrete encasement achieved a bond strength ratio ranging from 1.25 to 1.65. GA jackets displayed the lowest bond strength ratio (fig. 4.12

(c)). The reason may be attributed to the formation of a passive film (protective iron oxide film) on the steel surface due to the alkaline solution's presence in the GA mix (fig. 4.14), which is more damaged and degraded when subjected to loads (Angst et al. 2017).

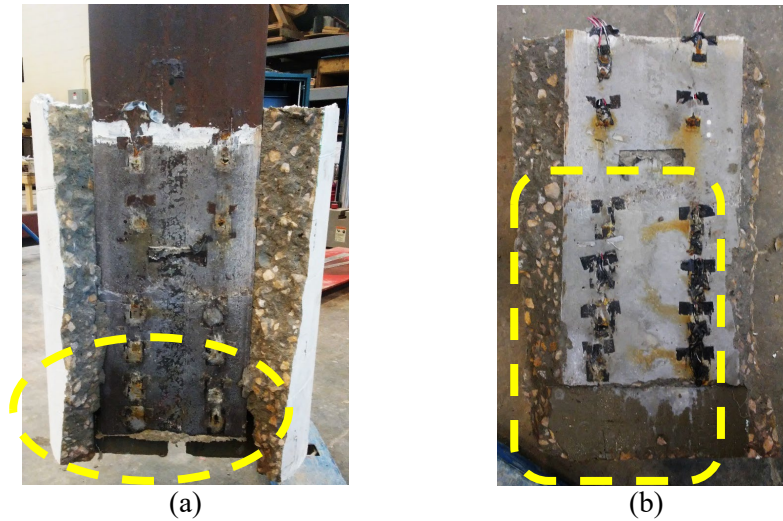


**Figure 4.14** Passive film formation (a) GA specimen ( $L_{CE}=508$  mm (20 in.)), (b) closer view.

#### 4.3.4 Effect of Concrete Encasement (CE) Strength

Three different unconfined concrete strengths of 20.6, 34.5, and 65.5 MPa (3, 5, and 9.5 ksi) for concrete encasement type CC were investigated in this study. All the concrete encasement specimens have the same  $L_{CE}$  of 254 mm (10 in.). As the concrete strength increased, the load carrying capacity of the specimens increased. As shown in figure 4.14 (a), the ultimate bond strength increased by 55% from 0.537 MPa (78 psi) to 0.834 MPa (121 psi) when the  $f'_c$  increased by 216% from 20.6 MPa (3 ksi) to 65.5 MPa (9.5 ksi), respectively. Moreover, as explained in the next section, all the tested specimens exhibited similar patterns of failure, governed by concrete encasement splitting.

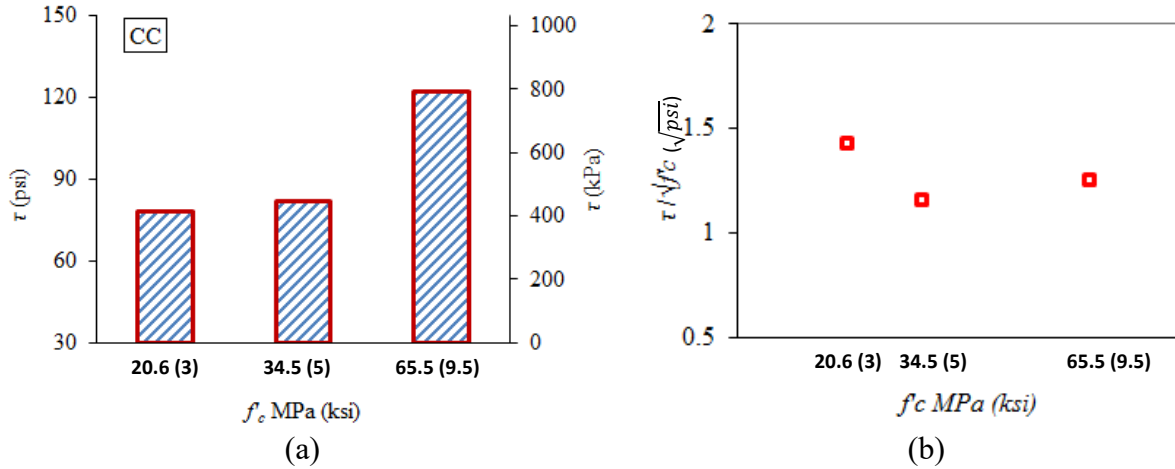


**Figure 4.15** Bond strength versus  $f'_c$ : (a) absolute, and (b) normalized values.

#### 4.3.5 Bond Strain Distribution

Figures 4.15 through 4.17 show the strain distribution for different types of concrete with variable  $L_{CE}$  under different loading levels. The strain distribution was taken from the strain gauges at the interface between the flange and web of the steel H-piles and the concrete encasement surface. The obtained strain distribution was classified and arranged according to the three concrete encasement embedded lengths ( $L_{CE}$ ) 254, 508, 762 mm (10, 20, and 30 in.). The strain distribution of the concrete encasement specimens type GA with 508 mm (20 in.) and GT with 762 mm (30 in.) was not discussed in this study due to a malfunction of the data acquisition system while performing the test.

In general, the obtained strain values increased as the  $L_{CE}$  increased, by almost 100% and 200% for 508 mm (20 in.) and 762 mm (30 in.)  $L_{CE}$  specimens, respectively, compared to 254 mm (10 in.) concrete encasement. The strains at the top of the concrete encasement close to the loaded end showed a significant increase over the strain near the free unloaded end. The main reason is that the applied load near the loaded end had been counteracted by the bond stress

generated between the steel H-pile and concrete. Therefore, the load had little effect on the unloaded end, thus causing lower strain readings.

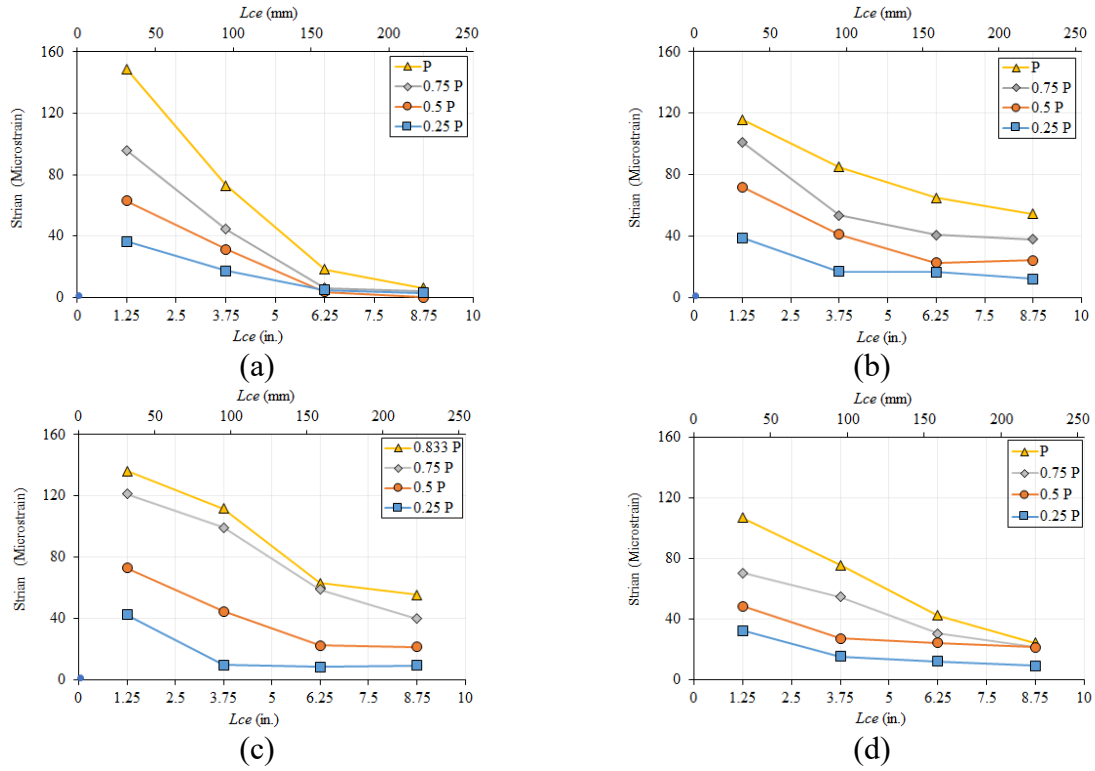


**Figure 4.16** Strain distribution along 254 mm (10 in.) embedded length ( $L_{CE}$ ) of different concrete encasement (a) CC, (b) HES, (c) GA, and (d) GT.

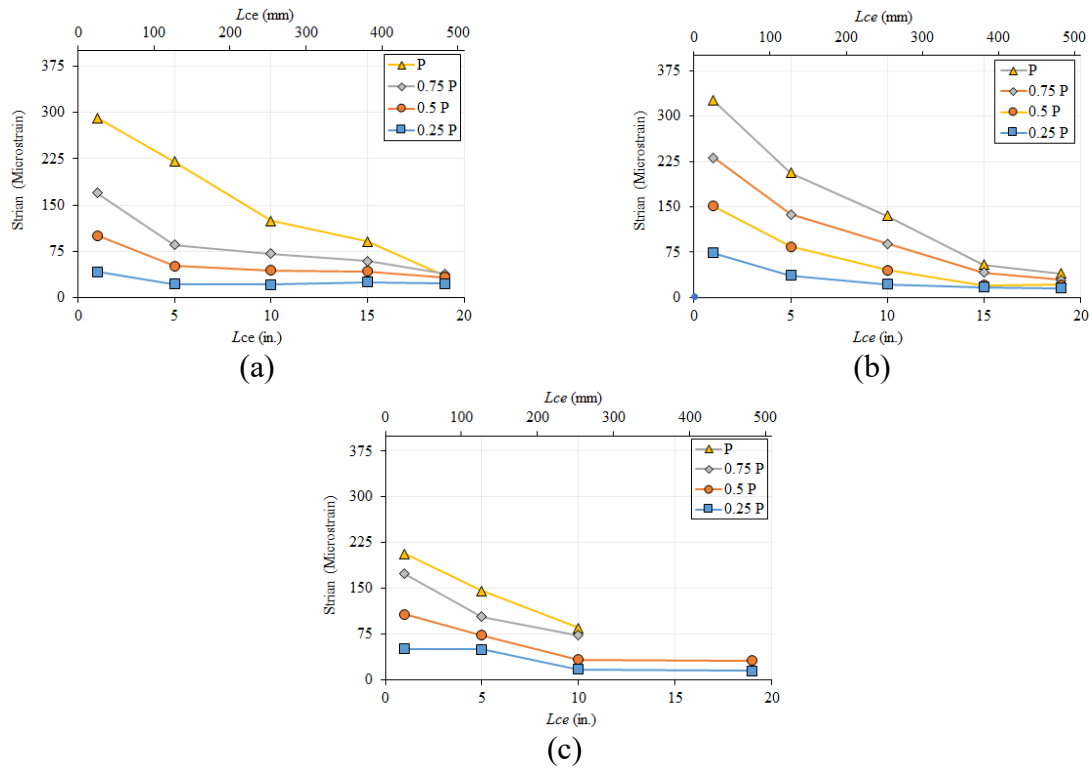


**Figure 4.17** Strain distribution along 508 mm (20 in.) embedded length ( $L_{CE}$ ) of different concrete encasement (a) CC, (b) HES, and (c) GT.

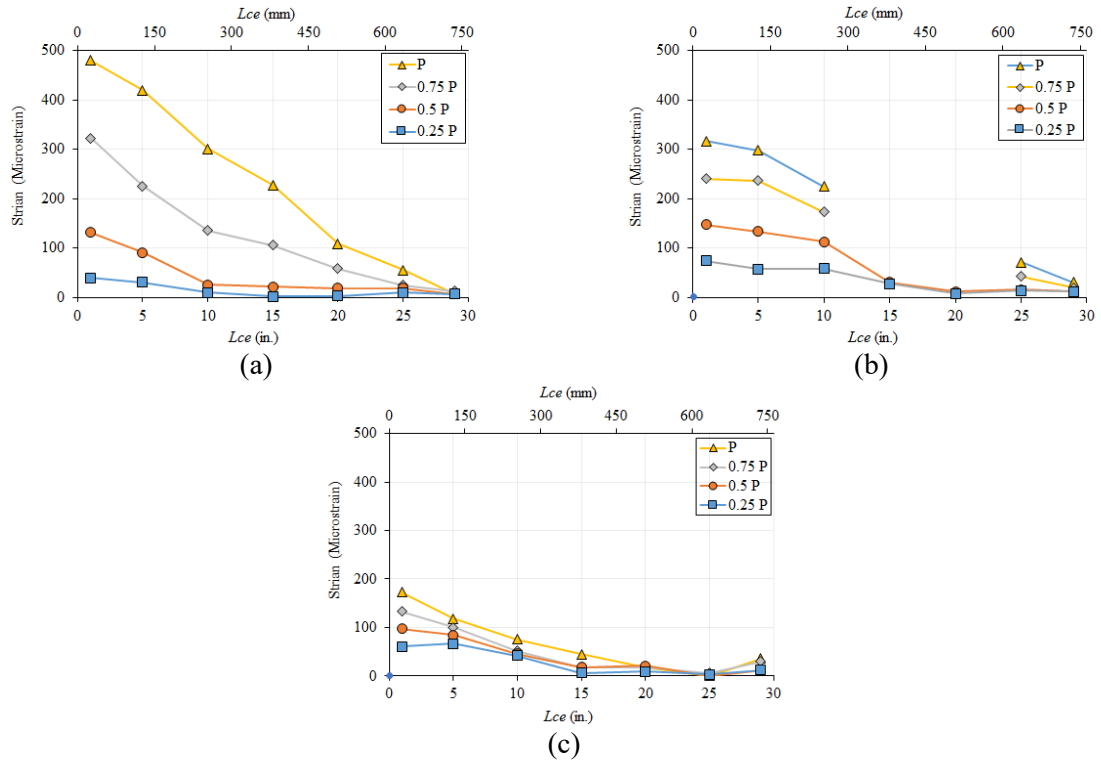


**Figure 4.18** Strain distribution along 762 mm (30 in.) embedded length ( $L_{CE}$ ) of different concrete encasement (a) CC, (b) HES, and (c) GA.

## Chapter 5 Interfacial Shear Strength of Steel H-Piles Encased in Concrete Filled Cfrp Jackets

### 5.1 Introduction

This chapter presents the experimental results of push-out tests on eighteen full-scale steel H-piles containing headed (shear) studs encased in concrete confined by carbon fiber reinforced polymer (CFRP) jackets. Two types of high-strength, high modulus unidirectional carbon fiber laminates and fabrics with two-component high-strength QuakeBond™ J300SR epoxy for the laminates and Tyfo S epoxy for the fabrics were used during this study. The distribution of steel pile/concrete and concrete interface/CFRP jacket strains, as well as the bond stress along the embedded length were analyzed and compared with the available design codes. The main objectives of this chapter test series are:

- 1) to propose a repair method for corroded steel H-pile bridge columns to improve their axial loading capacity, and
- 2) to evaluate the bond strength of steel piles with and without headed studs attached to it embedded into concrete encasement confined with and without CFRP in term of the effects on load carrying capacity for corroded steel pile bridge columns.

### 5.2 Experimental Program

Eighteen 250 x 62 mm (10 x 42) steel H-piles specimens were subjected to push-out testing during this study (table 5.1 and fig. 5.1). The nominal thicknesses of the web and flange are 10.76 mm (0.42 in.) and 9.4 mm (0.37 in.), respectively. However, the actual thicknesses for each pile are shown in table 5.1. The specimens are divided into the following four groups: 1) concrete jackets, 2) concrete jackets with headed studs (HSs), 3) concrete encased in CFRP jackets, and 4) concrete having HSs that were encased in CFRP jackets. A specimen designation begins with the number of CFRP piles, followed by the letter P, the number of HSs, followed by

the letters HS, and the diameter of the HSs in inches followed by a letter, either F or W, for studs located at the flanges or webs.

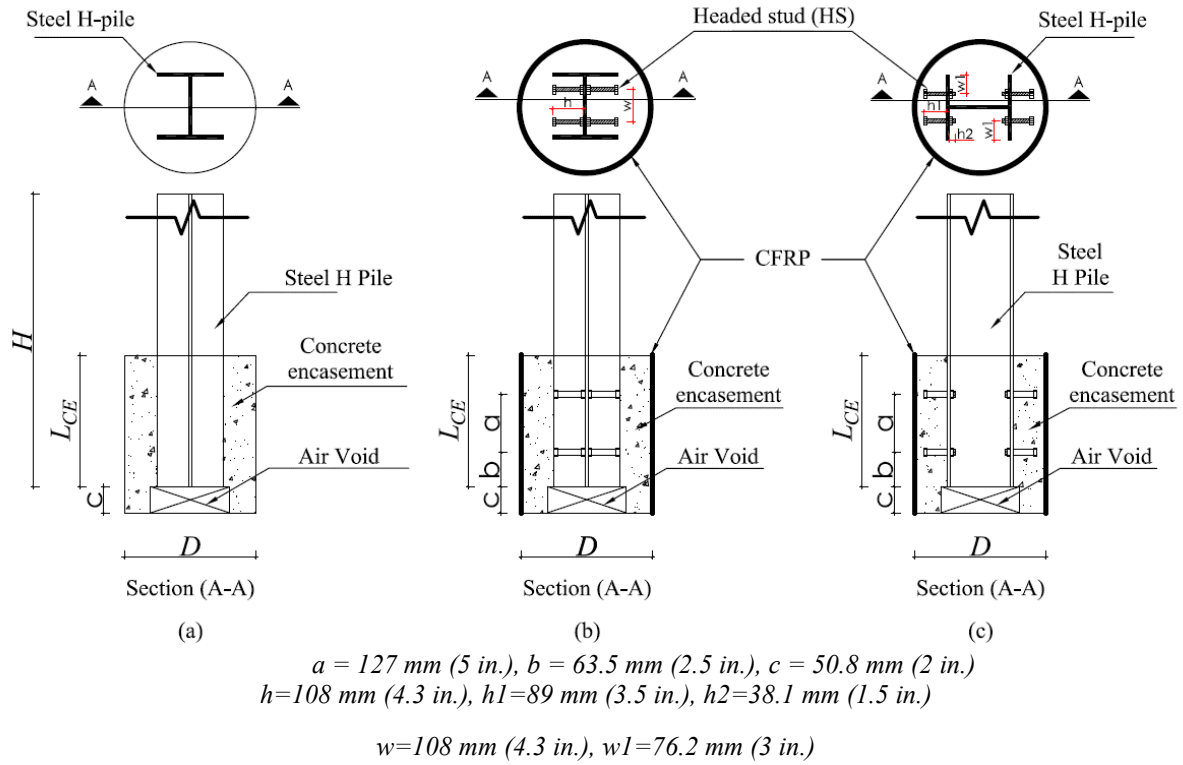
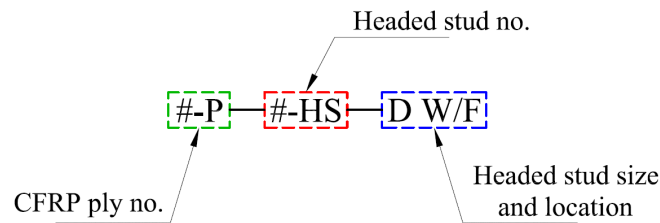


**Figure 5.1** Test specimens (a) RS, (b) repaired with studs on the web and CFRP, (c) repaired with studs on the flanges and CFRP.



**Table 5.1** Parametric Study of the Tested Specimens

	Specimen name	Designation (code)	CR*	$A_{hs}$ mm <sup>2</sup> (in. <sup>2</sup> ) (Eq. 2)	$t_w$ , mm (in.)	$t_f$ , mm (in.)	$P_y$ (kips)
A	RS	0P-0HS	-	-	9.95 (0.392)	10.6 (0.417)	726.23
B	C1	0P-4HS-1W	-	1755 (2.72)	9.81 (0.386)	11.78 (0.464)	777.90
	C2	0P-8HS-1W	-	3503 (5.44)	10.8 (0.425)	11.7 (0.461)	795.43
C	C3	1P-0HS**	0.105	-	9.825 (0.387)	10.9 (0.429)	737.43
	C4	2P-0HS**	0.21	-	10.4 (0.409)	11.1 (0.437)	759.10
	C5	2P-0HS***	0.18	-	9.94 (0.391)	11.58 (0.456)	771.42
	C6	4P-0HS**	0.42	-	9.8 (0.386)	10.9 (0.429)	736.89
	C7	4P-0HS***	0.36	-	10.1 (0.398)	11.18 (0.44)	756.33
D	C8	1P-8HS-1W**	0.105	3503 (5.44)	9.5 (0.374)	11.4 (0.449)	753.62
	C9	2P-4HS-1W**	0.21	1755 (2.72)	9.8 (0.386)	12.56 (0.494)	813.86
	C10	2P-8HS-1W**	0.21	3503 (5.44)	9.7 (0.382)	11.77 (0.463)	775.08
	C11	2P-8HS-3/4W**	0.21	1877 (2.91)	9.76 (0.384)	11.32 (0.446)	755.50
	C12	2P-8HS-1/2W**	0.21	748.4 (1.16)	10.48 (0.413)	10.74 (0.423)	744.17
	C13	3P-8HS-1W**	0.31	3503 (5.44)	9.6 (0.378)	11.18 (0.44)	745.56
	C14	3P-8HS-1F**	0.31	3503 (5.44)	9.8 (0.386)	10.94 (0.431)	738.74
	C15	4P-4HS-1W**	0.42	1755 (2.72)	10.8 (0.425)	12.56 (0.494)	835.14
	C16	6P-8HS-1W**	0.63	3503 (5.44)	10.4 (0.409)	11.1 (0.437)	759.10
	C17	8P-8HS-1W**	0.84	3503 (5.44)	9.75 (0.384)	11.14 (0.439)	746.94



\* CR values were calculated using the average  $f'_c$  (=5.41 ksi) at the day of test.

\*\* Laminate

\*\*\* Fabric

\*\*\*\* For the steel H-pile,  $F_y = 414$  Mpa (60 ksi)

### 5.2.1 Material Properties

#### 5.2.1.1 Steel H-Pile

The tensile stress-strain of the steel pile materials were determined, per ASTM E8/E8M – 16a (2016), by testing coupons cut from a flange and a web of a pile. Three replicate coupons were tested, and the average results are reported (Table 5.2). The strains at the middle 25.4 mm (one-in.) of each coupon were also measured using clip gauge (Fig. 5.2).

**Table 5.2** Mechanical Properties of Steel H-pile Flange and Web

Section	Yield stress *, MPa (ksi)	Ultimate stress *, MPa (ksi)	Elastic modulus *, GPa (ksi)	Rupture strain *, mm/mm (in/in)
Flange	324 (47)	517 (75)	181 (26,250)	0.087
Web	407 (59)	503 (73)	182 (26,400)	0.098

\* Average of three specimens

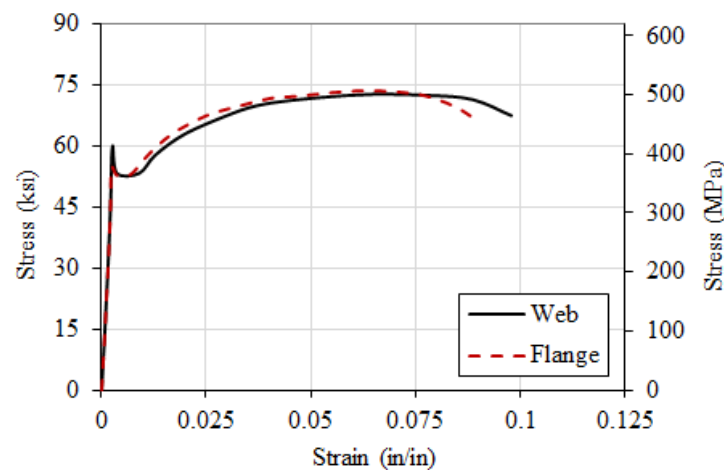


**Figure 5.2** Average steel pile stress-strain curves.

#### 5.2.1.2 Concrete

Conventional concrete (CC) was prepared and mixed per ASTM C192-16 (2016) using ordinary Portland cement (OPC) type I, dolomite aggregate having maximum aggregate size of

19 mm (0.75 in.) and Missouri river sand (Table 5.3). The particle size distribution of the aggregates were within the acceptable limits of ASTM C33-16 (2016). Numerous 101.6 x 203.4 mm (4 in. x 8 in.) standard concrete cylinders were cast using the same concrete mixtures used for the concrete encasing. The average compressive strength of three replicate specimens at the day of testing of each specimen ranged from 34.5 MPa (5.00 ksi) to 41.20 MPa (6.00 ksi) (Table 5.1).

**Table 5.3** Mix Design of the Conventional Concrete (CC) Mixture

w/c	CA, kg/m <sup>3</sup> (lb/yd <sup>3</sup> )	Sand, kg/m <sup>3</sup> (lb/yd <sup>3</sup> )	Water, kg/m <sup>3</sup> (lb/yd <sup>3</sup> )	Cement, kg/m <sup>3</sup> (lb/yd <sup>3</sup> )
0.55	1033 (1742)	701 (1182)	195.8 (330)	356 (600)

#### 5.2.1.3 CFRP

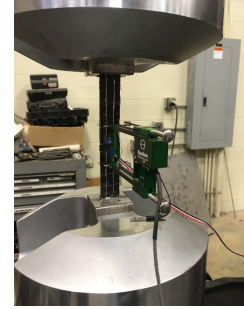
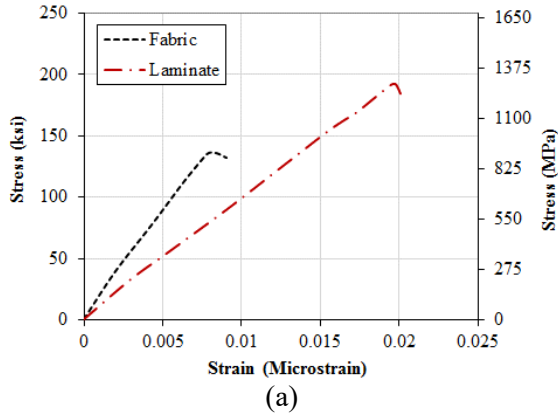
Unidirectional CFRP in the form of laminates and fabrics were used during this study. Three replicate CFRP coupons from each type were tested under uniaxial tension, per ASTM D3039 (Standard 2008), to determine their material properties (Fig. 5.3 and Table 5.4). Aluminum tabs were bonded at the ends of the CFRP coupons to ensure uniform gripping pressure distribution during testing (Fig. 5.3). The QuakeBond™ 220UR epoxy, an underwater resin, were used for the laminate while the epoxy Tyfo®S was used for the fabric (Table 5.5).

**Table 5.4** Measured Mechanical Properties of CFRP

CFRP type	Thickness per ply, mm (in.)	Tensile modulus, GPa (ksi)	Tensile strength, MPa (ksi)	Design rupture strain, mm/mm (in/in)
Laminate (QuakeWrap)	0.635 (0.025)	79.43 (11,520)	1,434 (208)	0.0197
Fabric (Tyfo)	0.762 (0.034)	111.5 (16,179)	950 (137)	0.0085

**Table 5.5** Mechanical Properties of the Epoxy Resins per Manufacturers' Data

Type	Curing time (hour)	Compressive strength, MPa (ksi)	Tensile strength, MPa (ksi)
QuakeBond UR220	12	80.7 (11.7)	38.6 (4.4)
Tyfo <sup>®</sup> S	10	86.2 (12.5)	72.4 (10.5)

**Figure 5.3** Tested CFRP coupon results.

#### 5.2.1.4 Headed studs (HS) properties

All threaded Grade B7 rods, having diameters ranging from 12.5 mm (0.5 in.) to 25.4 mm (1.0 in.), with a minimum tensile strength of 720 MPa (105 ksi) were used during this experimental work as shear studs. The area of a stud,  $A_{hs}$ , was calculated using Eq. 5.1 (ACI318 2014).

$$A_{hs} = \frac{\pi}{4} \left( d_a - \frac{0.9743}{n_t} \right)^2 = \frac{\pi}{4} (d_a - 0.0696)^2 \quad (5.1)$$

where  $n_t$  = number of threads per inch length of the threaded rod being 14 for the used studs, and  $d_a$  = diameter of the threaded rod in inches.

### 5.2.2 Test Specimens Preparation

A total of eighteen specimens, each having a height of 1,219 mm (48 in.) were prepared (table 5.6). This includes the reference specimen divided into group A where a concrete jacket encased a steel pile, and group B where concrete jackets incorporated HS-encased steel piles. Another fifteen specimens where the steel piles were encased in concrete filled CFRP jackets were prepared and divided into group C where no HSs were used, and group D where HSs were used.

For each pile, the required number of HS was passed through holes drilled in the web/flanges. Heavy-duty nuts were installed at the beginning and end of each HS to form a headed stud (fig. 5.4).

**Table 5.6** Specimen Geometrical Properties

Steel H-pile		CE and CFRP jacket	
Section	Length, $H$	Diameter, $D$	length, $L_{CE}$
mm (in.)	mm (in.)	mm (in.)	mm (in.)
$250 \times 62$ (10 $\times$ 42)	1219.2 (48)	508 (20)	254 (10)



**Figure 5.4** HS attached to web and flanges of the steel pile.

Different numbers of CFRP piles, ranging from one to eight piles, with confinement ratios ( $CR$ ) calculated per equation 5.2 (ACI-440 2008) were used.

$$CR = \frac{f_l}{f'_c} = \frac{2t_f E_f \varepsilon_f}{f'_c D_f} \quad (5.2)$$

where  $f_l$  is the confining pressure,  $f'_c$  is the average unconfined concrete compressive strength,  $E_f$  is the CFRP axial modulus of elasticity,  $t_f$  is the total thickness of the CFRP jacket,  $\varepsilon_f$  is the axial ultimate tensile strain of the CFRP, and  $D_f$  is the internal diameter of the CFRP jacket.

The laminates were hand sanded to roughen their surfaces and wiped clean with acetone. Then, a 2 mm (0.08 in.) thick epoxy layer, per the manufacturer's requirements, was applied to the cut CFRP of each jacket. Then, the CFRP was wrapped around a 508 mm (20 in.) diameter Sonotube with an overlap length in the circumferential direction of 203.4 mm (8 in.) (fig. 5.5). The tube diameter was selected to ensure a minimum concrete thickness of 508 mm (2 in.) between the CFRP jacket and the edges of the flanges of the repaired steel pile. After one day, the Sonotube was removed from the CFRP jacket. A constant height of 254 mm (10 in.) was used for all jackets. Each CFRP jacket was placed firmly atop of a 38.1 mm (1.5 in.) thick plywood end cap, which was fixed to the laboratory floor. A 50.8 mm (2 in.) high H-shaped foam template was concentrically placed inside each CFRP jacket. Then, the prepared test H-piles were concentrically inserted and placed atop the foam templates. In the case of the reference specimens, Sonotubes were used instead of the CFRP jacket. Then, concrete was placed to fill the CFRP (or Sonotubes). Prior to testing, the foam templates were removed from



underneath the test specimen and the created gap was thoroughly cleaned of any concrete so that the pile could slip freely during testing. Concrete was placed (fig. 5.6) and left to cure at an ambient temperature of  $23 \pm 2^{\circ}\text{C}$  ( $73 \pm 3^{\circ}\text{F}$ ) inside the laboratory.

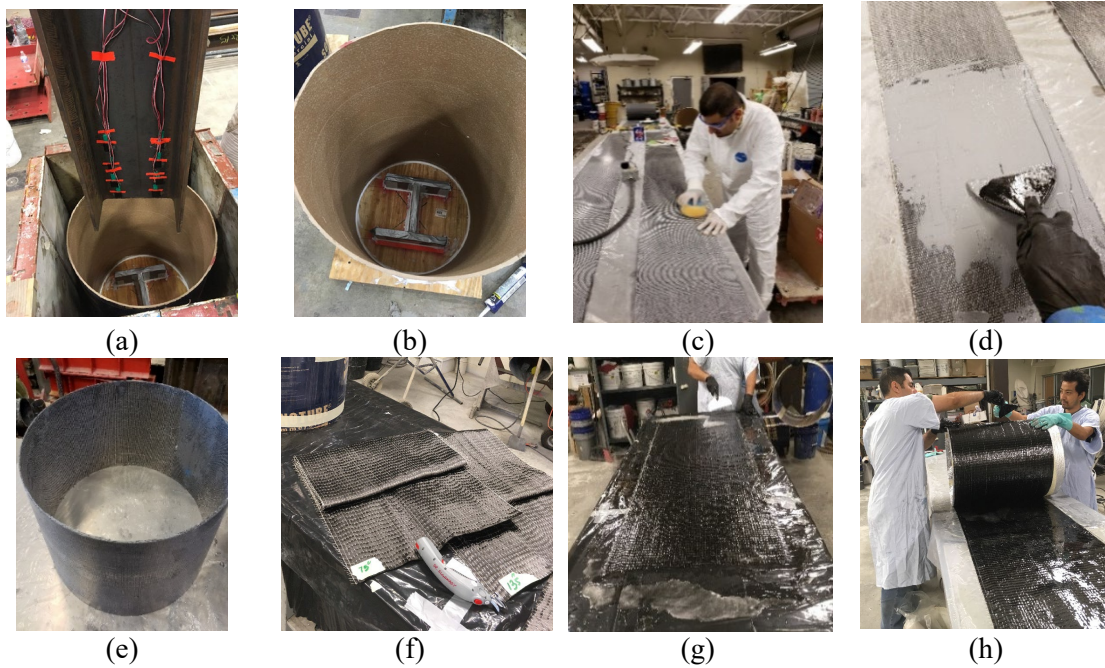


**Figure 5.5** CFRP wrapping process.

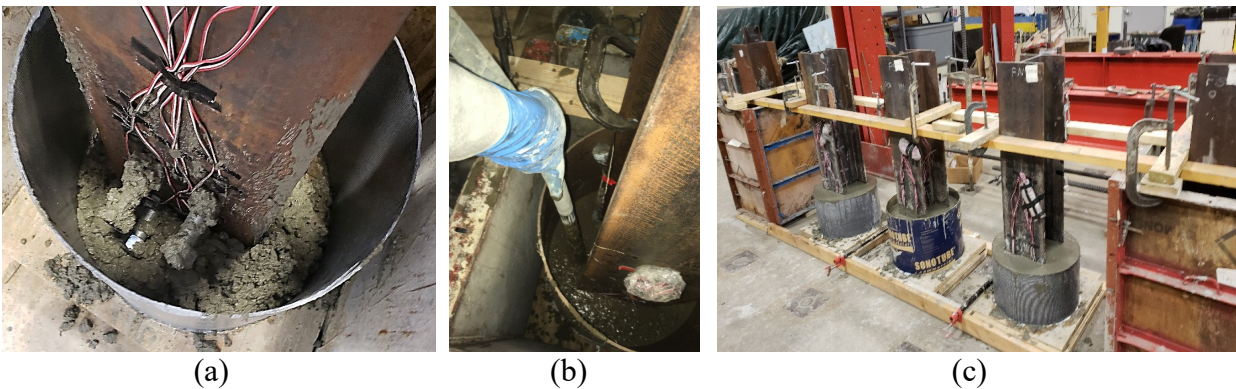


**Figure 5.6** Concrete encasement: (a) placement, (b) vibrating, and (c) finalizing.

### *5.2.3 Test Instrumentation*

Thirty-three strain gauges were attached to the web and flanges of each pile specimen (fig. 5.7), before casting the concrete, in order to measure the axial strains. An additional sixteen strain gauges were mounted on each CFRP jacket to measure the hoop strains during testing. Two linear variable displacement transducers (LVDTs) were placed vertically on each flange side to measure the slip between the concrete and steel (fig. 5.7).



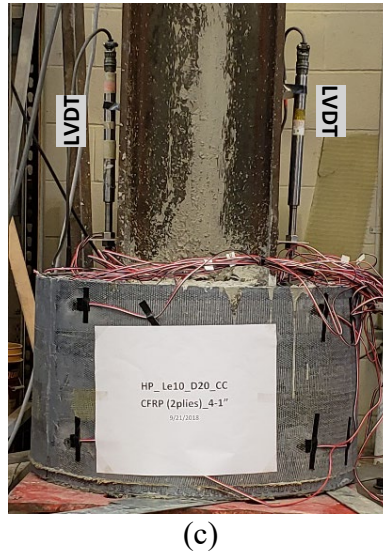
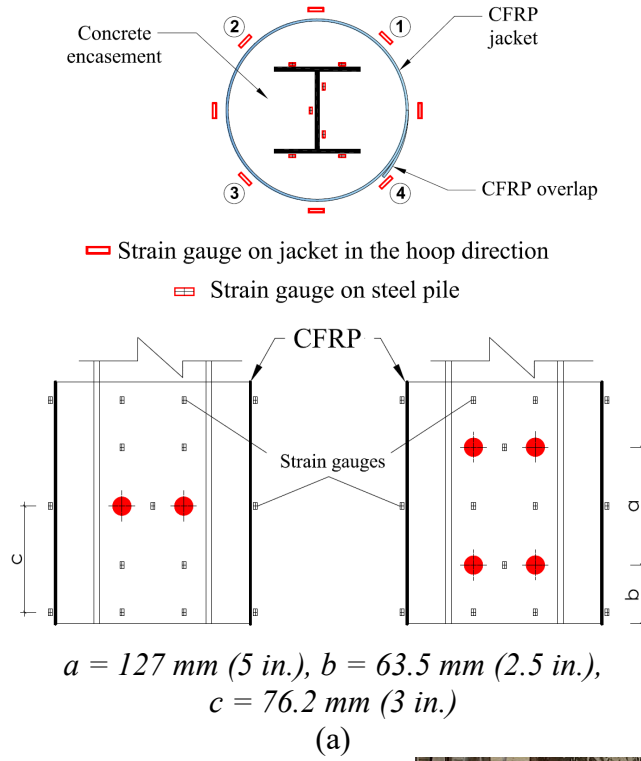


**Figure 5.7** Test instrumentation (a) strain gauges layout, mounted on the steel H-piles and the CFRP jacket, (b) strain gauges covered with mastic rubber protection, (c) two LVDTs set up on each steel H-pile flanges sides.

#### 5.2.4 Push-out Test

The push-out tests were performed using an MTS universal testing machine with a capacity of 2,404 kN (545 kips) (fig. 5.8). The specimens were monotonically axially loaded in a

displacement control with a rate of 1.27 mm/minute (0.05 in./minute). The compressive force was applied on the top of each pile using the MTS swivel plate while the bottoms of the concrete encasement were supported on a rigid steel base (fig. 5.8).

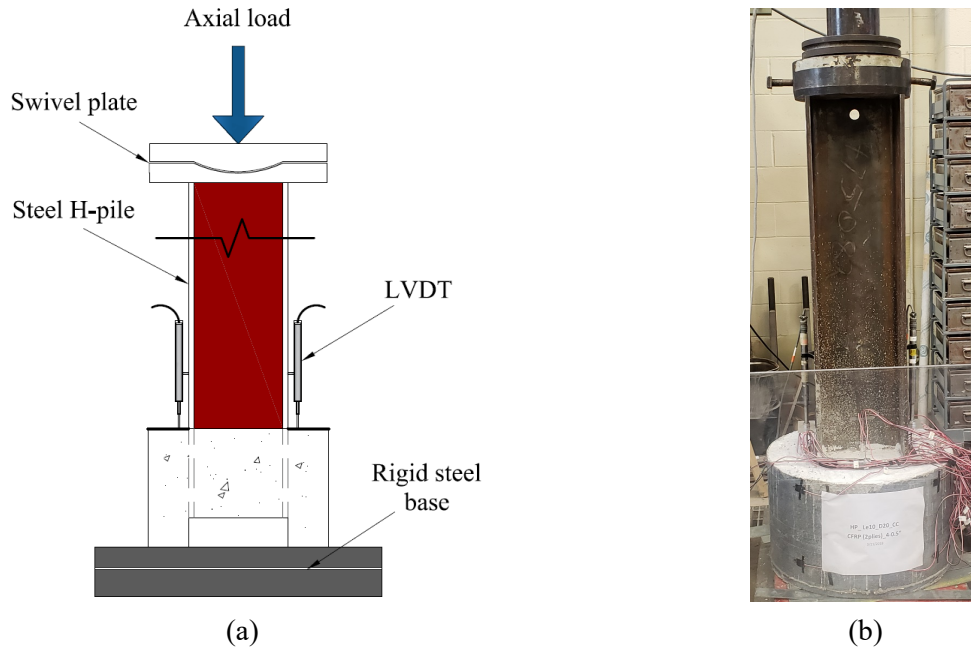


**Figure 5.8** Push-out test setup: (a) layout, and (b) specimen during the test.

## 5.3 Results and Discussion

### 5.3.1 General Description

The push-out test results are summarized in table 5.7 where the bond stress ( $\tau$ ) is defined using equation 5.3.

$$\tau = \frac{F}{p L_{CE}} \quad (5.3)$$

where  $F$  is the peak axial load on the pile,  $p$  is the perimeter of the pile section, being approximately 1,473 mm (58 in.), and  $L_{CE}$  is the bond length, being 254 mm (10 in.).

**Table 5.7** Test Results of the Investigated Specimens

	Specimen	$F$ kN (kips)	$\tau_{max}$ , MPa (psi)	$\delta_{max}$ mm (in.)	$f'_c$ * MPa (ksi)	$f'_t$ ** MPa (psi)
RS	0P-0HS	211 (48)	0.56 (81.0)	0.05 (0.002)	34.5 (5.0)	3.6 (520.5)
C1	0P-4HS-1W	731 (164)	1.94 (281.2)	8.40 (0.33)	36.1 (5.2)	3.1 (439.8)
C2	0P-8HS-1W	1,437 (323)	3.81 (553.1)	11.18 (0.44)	37.1 (5.4)	2.6 (381.3)
C3	1P-0HS	313 (70)	0.83 (120.5)	0.05 (0.002)	37.1 (5.4)	2.6 (381.3)
C4	2P-0HS	283 (64)	0.75 (109.1)	0.05 (0.002)	37.4 (5.4)	3.4 (493.8)
C5***	2P-0HS	272 (61)	0.72 (104)	0.08 (0.003)	37.4 (5.4)	3.41 (494.0)
C6	4P-0HS	257 (58)	0.68 (99.0)	0.091 (0.004)	37.4 (5.4)	3.4 (493.8)
C7***	4P-0HS	329 (74)	0.87 (127)	0.154 (0.006)	35.6 (5.2)	3.5 (513.7)
C8	1P-8HS-1W	1,615 (363)	4.29 (621.7)	11.43 (0.45)	37.1 (5.4)	2.6 (381.3)
C9	2P-4HS-1W	1,225 (275)	3.25 (471.5)	13.00 (0.51)	41.2 (6.0)	3.6 (526.5)
C10	2P-8HS-1W	2,038 (458)	5.41 (784.5)	20.32 (0.80)	39.4 (5.7)	3.2 (460.6)
C11	2P-8HS-3/4W	1,200 (270)	3.18 (462.1)	8.90 (0.35)	39.4 (5.7)	3.2 (460.6)
C12	2P-8HS-1/2W	668 (150)	1.77 (257.2)	29.12 (1.15)	39.4 (5.7)	3.2 (460.6)
C13	3P-8HS-1W	2,025 (455)	5.37 (779.4)	24.13 (0.95)	37.9 (5.5)	3.7 (541.3)
C14	3P-8HS-1F	2,404 (540)*	6.32 (917.8)	6.35 (0.25)	34.7 (5.1)	3.2 (469.3)
C15	4P-4HS-1W	1,347 (303)	3.57 (518.4)	12.12 (0.48)	37.9 (5.5)	3.7 (541.3)
C16	6P-8HS-1W	2,223 (499)	5.90 (854.6)	25.50 (1.01)	34.7 (5.1)	3.2 (469.3)
C17	8P-8HS-1W	2,404 (540)*	6.32 (917.8)	12.30 (0.49)	34.7 (5.1)	3.2 (469.3)

\* The maximum capacity of the machine has been reached

\*\* At the day of test

\*\*\* Specimens with Tyfo CFRP jackets

### 5.3.2 Failure Mode

Figure 5.9 shows the failure modes of the eighteen specimens. Concrete splitting cracks initiated in all specimens at displacement of approximately 0.051 mm (0.002 in.). This was followed by different failure modes depending on the provided number of CFRP piles and HSs.

#### 5.3.2.1 Group A specimen (RS)

Specimen RS failed at a load of 211 kN (48 kips) due to concrete longitudinal splitting cracks and bond failure (figs. 5.9 and 5.11), followed by a sudden reduction in the axial load carrying capacity.

#### 5.3.2.2 Group B specimens (HS)

Depending on the number of HSs (Table 5.7), specimens in Group B displayed stresses 246% to 583% higher than those of the reference specimens, where specimen C1, with 4 HSs failed at 731 kN (164 kips), and C2, with 8 HSs failed at 1437 kN (323 kips). For both specimens, at an average load of 365 kN (82 kips), longitudinal splitting cracks occurred at the tips of the flanges. However, due to the existence of the HSs, the specimens were able to carry more load while the applied displacement was increased. A major diagonal crack developed along the circumference of the concrete jacket starting at the level of the HS (fig. 5.9 (C1)) at an axial load of approximately 721 kN (162 kips) and 8.9 mm (0.35 in). At an applied displacement of 9.1 mm (0.36 in.), specimen C1 reached its peak load followed by loss of strength and significant opening of the splitting cracks, and the specimen became unstable. The loss of strength was gradual compared to that which occurred in the reference specimen. Forensic investigation of the studs after testing showed that there was a bending of the HS against the concrete but no shear off took place. Specimen C2 reached its peak strength at an axial displacement of 12.2 mm (0.48 in.) followed by a gradual softening due to bending of the upper studs and hardening. This gradual softening was followed by hardening, and the specimen reached its peak strength at an axial load of 1570 kN (353 kips) and displacement of 43.8 mm (1.7 in.). After that, a complete collapse occurred due to shear-off of one HS that was observed after testing.





**Figure 5.9** Failure modes of the test specimens.



**Figure 5.9 cont.** Failure modes of the test specimens.

#### 5.3.2.3 Group C specimens (CFRP)

Having CFRP wrapping without HSs increased the strength by 21% to 54% compared to the RS with peak loads ranging from 258 kN (58 kips) to 329 (74 kips). Hence, the CFRP wrapping alone did not significantly increase the strength. All specimens failed in a mode similar to that of the reference specimen with splitting cracks initiated at the tips of the flanges and slowly extended up to the CFRP jackets at the peak loads. This was followed by a gradual degradation in the stress.

#### 5.3.2.4 Group D specimens (HS+CFRP)

This group included ten specimens. With exception of specimen C14, all of the rest of the specimens developed bond breaking at an axial load of approximately 365 kN (82 kips). This was followed by splitting cracks that started from the tips of the flanges and extended toward the

CFRP jacket at approximately 890-1,160 kN (200-261 kips). This was followed by different failure modes depending on the confinement ratio and the studs' stiffness.

For specimens having 8 HSs, corresponding to  $A_{hs}$  of at least 3503 mm<sup>2</sup> (5.44 in<sup>2</sup>), i.e., C8, C13, and C16, a horizontal crack extending between the tips of the two flanges appeared at an approximate load of 1,548 kN (348 kips). At failure, a prism of concrete was formed that was bounded by the web, two flanges, and the horizontal crack. This concrete prism moved upward. Specimens having at least two layers of CFRP, corresponding to CR of at least 0.21 and a minimum of four 25.4 mm (1 inch) diameter HSs, corresponding to  $A_{hs}$  of at least 1755 mm<sup>2</sup> (2.72 in.<sup>2</sup>), i.e., C9 and C15, reached axial capacities ranging from 1,225 kN (275 kips) to 1,347 kN (303 kips), representing improvements of 380% to 530%, compared to the reference specimen. In addition to the splitting and horizontal cracks, delamination in the CFRP occurred for specimen C9. Specimens having smaller sizes of HSs, no CFRP delamination, and more concrete damage in the form of radial cracking were observed.

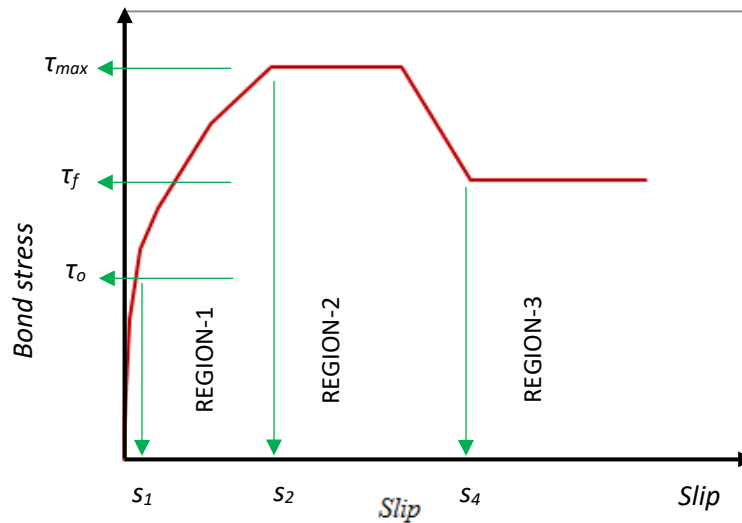
For the specimens having at least three layers of CFRP, corresponding to CR of at least 0.31 and at least four studs corresponding to  $A_{hs}$  of at least 3503 mm<sup>2</sup> (5.44 in.<sup>2</sup>), i.e., C15, C16, and C17, there was no FRP rupture or delamination. This group was able to reach axial capacities ranging from 1,347 kN (303 kips) to 2,404 kN (540 kips) representing improvements of 530% to 1,039%, compared to the reference specimen. These loads also represent 44% to 74% of the yielding squash load of the pile. It is worth noting that specimens C14 and C17 reached the capacity of the testing machine without CFRP jacket rupture. Due to the high loads within this group, the widths of the splitting cracks and horizontal cracks were relatively large.



### 5.3.3 Bond Stress vs Axial Displacement

Bond stress transfers between steel and concrete through the following three mechanisms: (a) chemical adhesion, (b) friction, and (c) mechanical interlocking offered by the HSs, if they exist (du Béton 2000; Hadi 2008; Harajli 2009; Raynor et al. 2002). The three mechanisms are not independent, and isolating one of these components during the slip process is not possible.

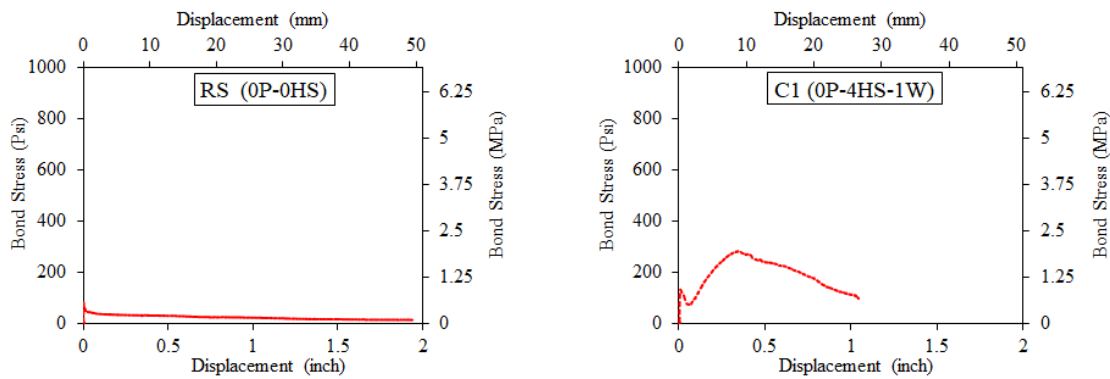
The model in figure 5.10 includes three regions, according to the failure mechanism: 1) CE with splitting failure (groups A and B) up to  $s_1$  equal to 0.051 mm (0.002 in.), corresponding to  $\tau_o$ , 2) CE splitting and crushing followed by HS shear failure (group C) up to  $s_2$  equal to 19 mm (0.75 in.), corresponding to  $\tau_{max}$ , 3) failure of CFRP-confined concrete including HSs where splitting failure, CFRP rupture/delamination, and HSs rupture occurred at a displacement ( $s_3$ ) of approximately 38.1 mm (1.5 in.), corresponding to  $\tau_f$  (fig. 11).



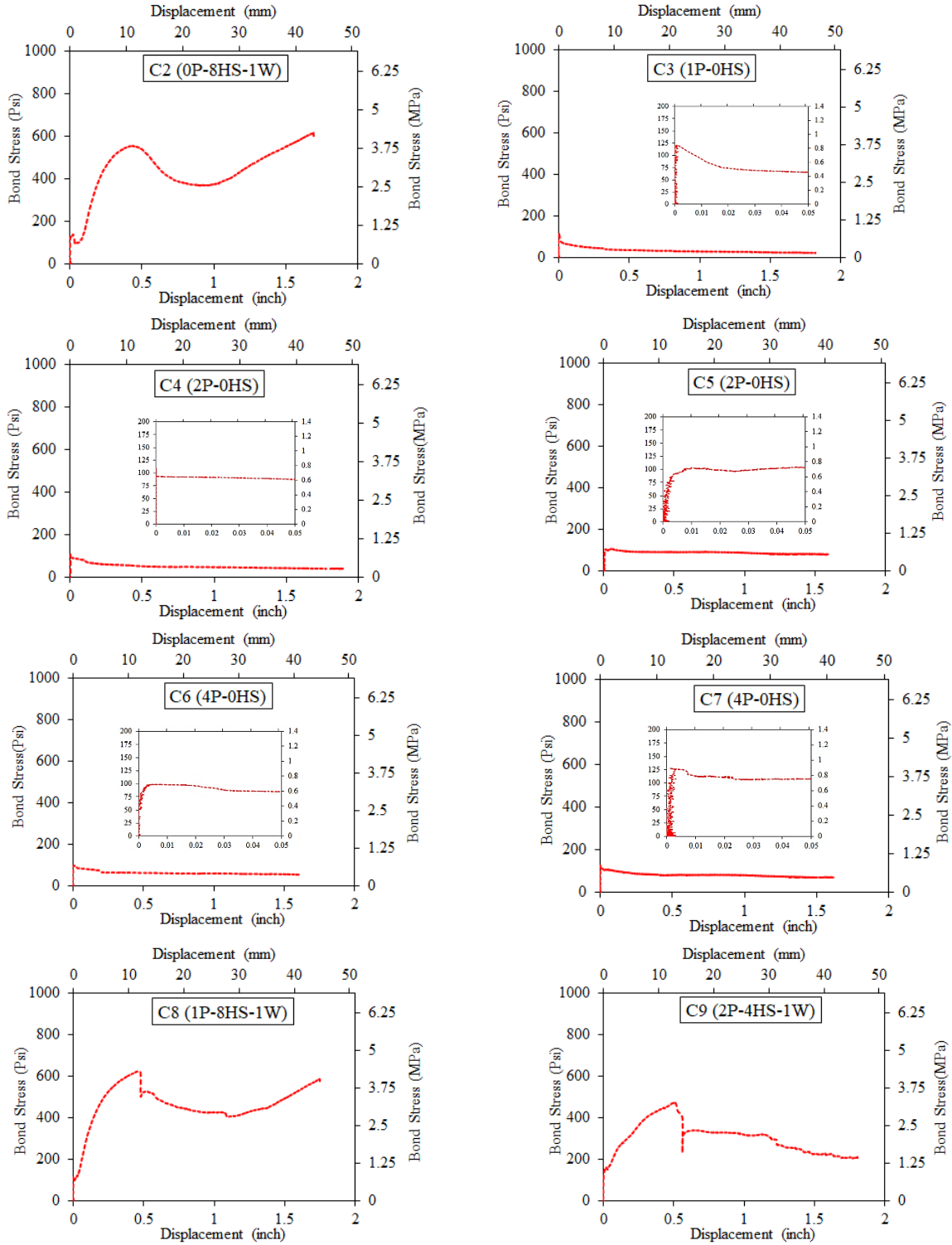
**Figure 5.10** Bond stress-slip model.



Figure 5.11 shows the bond stress ( $\tau$ ) vs. displacement relationships for the 18 specimens tested in this study. The results show that, regardless of whether the specimen has HSs or CFRP, most bond stress-slip curves consisted of three parts: ascending, descending, and stable residual. Generally, the bond stress increased remarkably, when the specimen incorporating HS attached to the steel pile. However, it is worth mentioning that the bond stress for group C with only CFRP jackets was lower than the value of the maximum average bond stress of 3.6 MPa (0.52 ksi) that was obtained by Liu et al. (2005). The bond stress ( $\tau$ ) increased by 580% for C2 in group B and by 1,130% for C14 and C17 in group D, compared to the RS. Implementing a high  $A_{hs}$  accompanied with a high CR value of 0.824 keeps the maximum bond stress at high values, as observed in specimen C17 where the MTS machine reached the maximum load capacity of 2,403 kN (540.3 kips) without failure occurring (fig. 5.11). The same results were recorded for specimen C14 with a smaller CR of 0.31 (64% less than C17) which is attributed to positioning the HS on the flanges.



**Figure 5.11** Bond stress ( $\tau$ ) vs. axial displacement.



**Figure 5.11** Bond stress ( $\square$ ) vs. axial displacement.

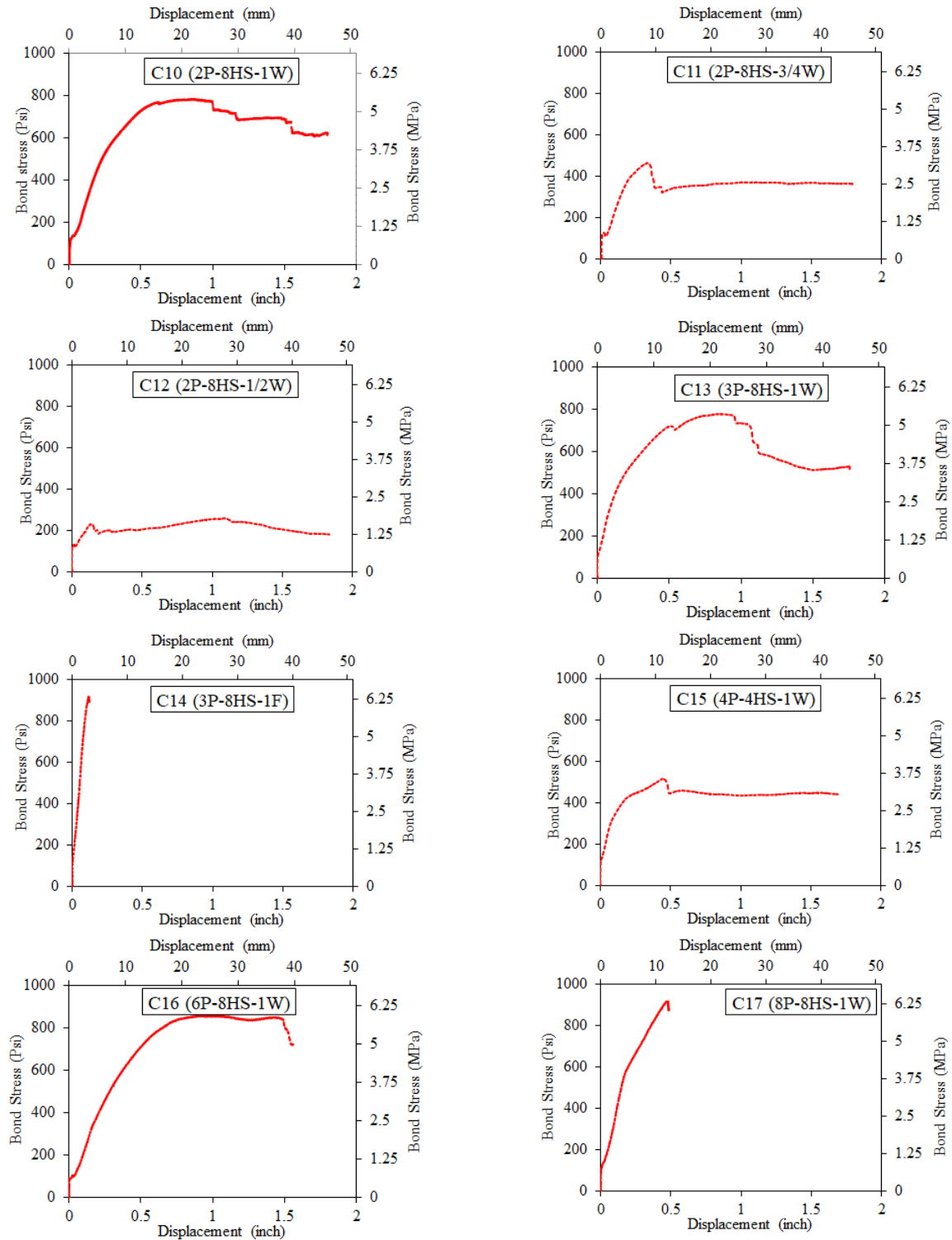


**Figure 5.11 cont.** Bond stress ( $\tau$ ) vs. axial displacement.

The existence and type of repair controls the post-peak performance of the test specimens. Specimen RS displayed very small residual bond stress ( $\tau_f$ ) (fig. 5.12). The specimens in group C displayed a 39% higher residual bond stress. After the concrete splitting cracks began to form, a retrofit jacket controls the splitting propagation, thus increasing the value of  $\tau_f$ . The residual stresses for specimens having CFRP jackets and HSs were higher than the obtained bond stress of the RS and CE+CFRP jacket specimen together. This was attributed to the higher residual stress of the specimens with large headed stud's cross-sectional area  $A_{hs}$  as well as the confinement ratio CR (C2, C3, and C7-C16). The highest residual stress was observed for the specimens C13 (3P-8H-1F) and C16 (8P-8H-1W) with a 500% increase compared to groups A and C (fig. 5.12). It is interesting to note that, independently of the concrete encasement crack propagation, the development of a residual stress – associated to friction mechanism – was observed for a slip of approximately 19 mm (0.75 in.) for all the specimens with HS in groups B and D (fig. 5.11).

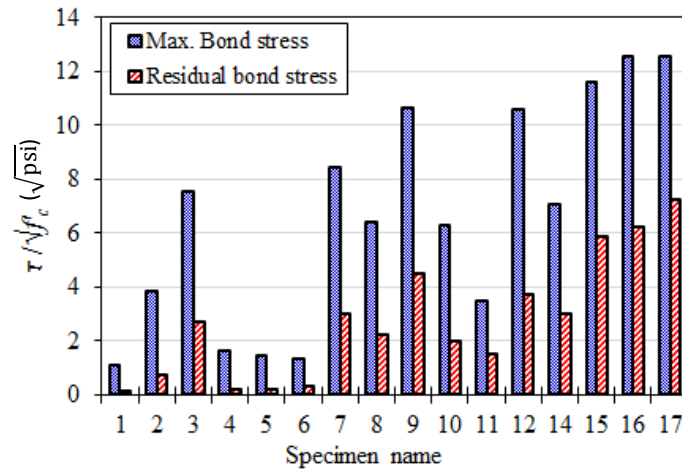


**Figure 5.12** Residual strength of the tested specimens.

#### 5.3.4 Headed Studs (HS)

Most of the specimens investigated during this study displayed shear off failure (fig. 5.13), and the tests were ended with the shear off of the HSs. When an axial load applied to a pile encased in a concrete jacket, the headed studs were subjected to combined shear and bending stresses leading to deflections and rotations of the HS bearing against the surrounding concrete, thereby triggering concrete splitting cracking when the concrete tensile strength was exceeded (Ollgaard 1971). These cracks triggered more stud deflection and hence increased the stresses at the HS-to-web connection leading to the stud rupture. In some cases, the tensile crack circumvented the HS, producing a typical shear embedment failure cone (fig. 5.13 (a)).

The CFRP jackets in group D increased concrete compressive strength due to confinement and also increased the resistance to splitting and cracking, and therefore led to a higher capacity for specimens having adequate confinement and head studs. The bond stress increased linearly as the  $A_{hs}$  increased (fig. 5.14). Increasing the  $A_{hs}$  by 370% from 748 mm<sup>2</sup> (1.16 in<sup>2</sup>) to 3503 mm<sup>2</sup> (5.44 in<sup>2</sup>) increased the normalized bond stress by 1200%.



(a)



(b)



(c)

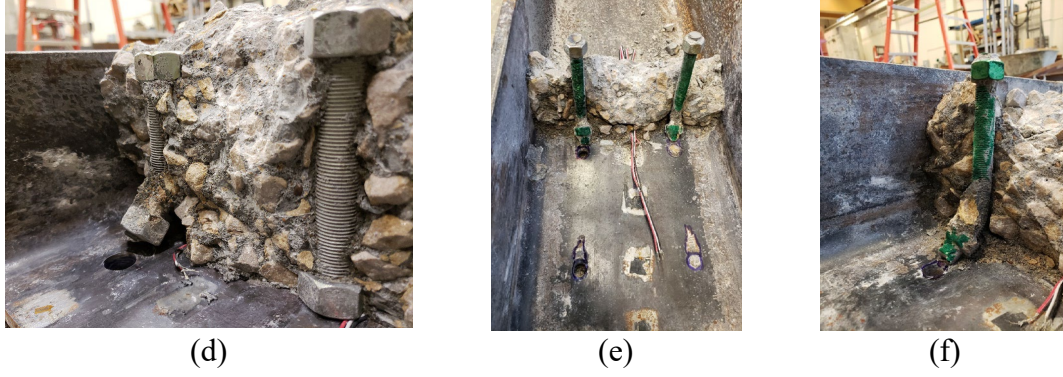


**Figure 5.13** Headed stud conditions (a and b)  $d_a=25.4$  mm (1 in.), (c and d)  $d_a=19$  mm (0.75 in.), (e and f)  $d_a=12.5$  mm (0.5 in.).

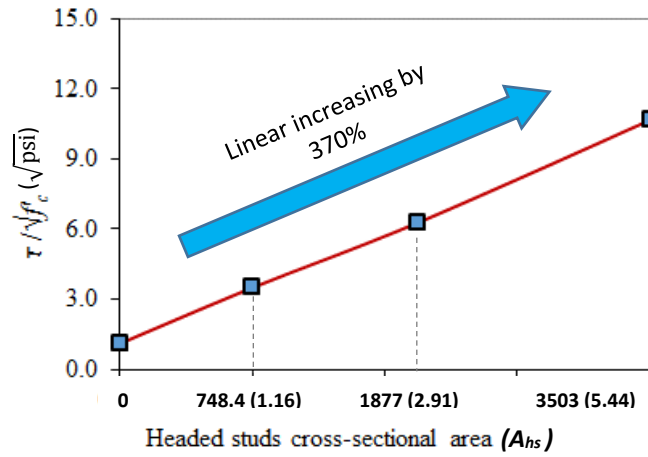


**Figure 5.14** Bond strength ratio vs.  $A_{hs}$ .

The shear resistance ( $P_{u(hs)}$ ) of the HS were calculated according to provisions for steel headed-stud anchors in composite columns in AASHTO\_LRFD (AASHTO 2012) (eq. 5.4) and Eurocode-4 (Standardization 2004) (eq. 5.5) to transfer the load,  $F$ , from the steel pile to the repair system. The calculated  $P_{u(hs)}$  values of the HS are illustrated in table 5.8 and fig. 5.15.

$$P_{u(hs)} = 0.5A_{hs}\sqrt{E_c\hat{f}_c} \quad (5.4)$$

$$P_{u(hs)} = 0.29\alpha d^2 \sqrt{E_c \dot{f}_c / \gamma_v} \quad (5.5)$$

where  $E_c$  = modulus of elasticity of concrete;  $f_c'$  = compressive stress of concrete cylinder;  $f_u$  = tensile stress of the studs;  $d$  = diameter of the studs;  $\gamma_v$  = material partial factor (=1.25);  $\alpha = 0.2(H/d+1) \leq 1$ ; and  $H$  = height of the studs. Here, the value of  $\alpha$  was 1.

**Table 5.8** Shear Resistance ( $P_{u(hs)}$ ) Results of the Investigated Specimens

Specimen name	Designation (code)	<i>AASHTO-LRFD</i>	<i>Eurocode-4</i>
		$P_{u(hs)}, kN (kips)$	$P_{u(hs)}, kN (kips)$
C1	0P-4HS-1W	884.3 (198.8)	603.5 (135.7)
C2	0P-8HS-1W	1,819.3 (409.0)	1,241.6 (279.1)
C8	1P-8HS-1W	1,819.3 (409.0)	1,241.6 (279.1)
C9	2P-4HS-1W	984.5 (221.3)	671.9 (151.0)
C10	2P-8HS-1W	1,894.6 (425.9)	1,293.0 (290.7)
C11	2P-8HS-3/4W	1,013.2 (227.8)	727.3 (163.5)
C12	2P-8HS-1/2W	405.4 (91.1)	323.3 (72.7)
C13	3P-8HS-1W	1,844.5 (414.7)	1,258.8 (283.0)
C14	3P-8HS-1F	1,743.0 (391.8)	1,189.5 (267.4)
C15	4P-4HS-1W	922.3 (207.3)	629.4 (141.5)
C16	6P-8HS-1W	1,743.0 (391.8)	1,189.5 (267.4)
C17	8P-8HS-1W	1,743.0 (391.8)	1,189.5 (267.4)

As shown in the table and figure, the obtained axial capacity in the case of unconfined CE specimens were between the predicted strength in equations 5.4 and 5.5. Equation 5.4 resulted in a 26% higher strength of 1,819.3 kN (409.0 kips), compared to the test result of 1,445 kN (325 kips) in case of C2 with 8 HS. However, the predictions of the strength of specimens having CFRP jackets were significantly underestimated with the error increasing along with an increase in the number of CFRP layers to reach 21.5% decreasing percentage for specimen C16 with  $P_{u(hs)}$  of 1,743.0 kN (391.8 kips), compared to the obtained test result of 2,223 kN (499 kips).



### 5.3.5 CFRP Jacketing

Specimens having two or fewer piles of laminates and HSs displayed delamination that started at the location of the concrete splitting cracks due to a high stress concentration (fig. 5.16). The bond stress, normalized by  $\sqrt{f'_c}$  increased linearly as the CR increased for a given number of HSs (fig. 5.17). This was not the case for specimens in group C where no HSs were used (fig. 5.17 (a)). For specimens with 8 HSs (fig. 5.17 (a)), increasing the CR from 0 to 0.824 increased the  $\tau_{max}/\sqrt{f'_c}$  by 75%. Using regression analysis, the rate of increase of the  $\tau_{max}/\sqrt{f'_c}$  was  $6.2 \sqrt{MPa}$ . Similar behavior was observed for specimens with 4 HSs but with a rate of increase of  $7.5 \sqrt{MPa}$  (fig. 5.17 (a)).

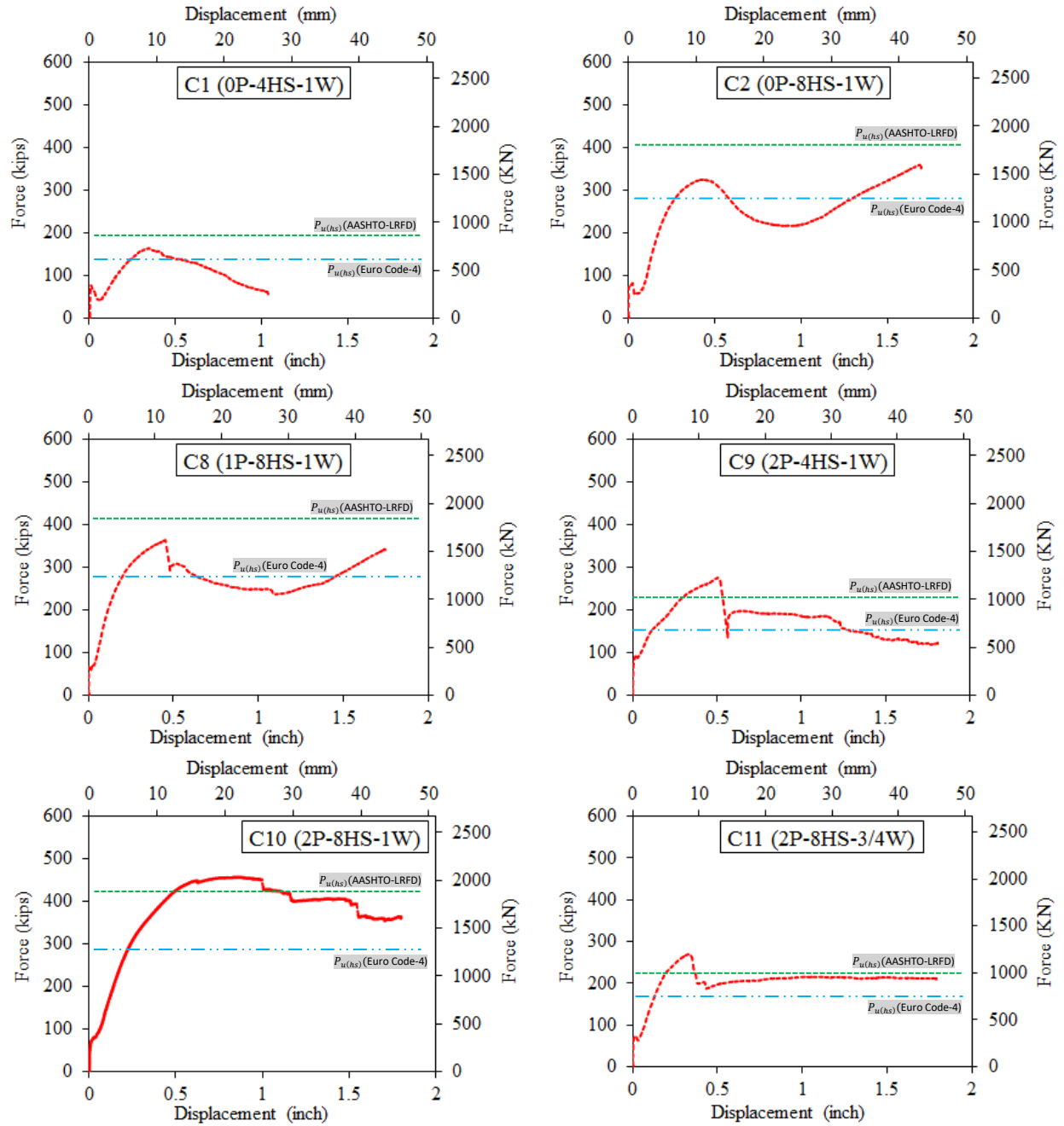


**Figure 5.15** Axial force vs. displacement with shear resistance ( $P_{u(hs)}$ ) of the HS.

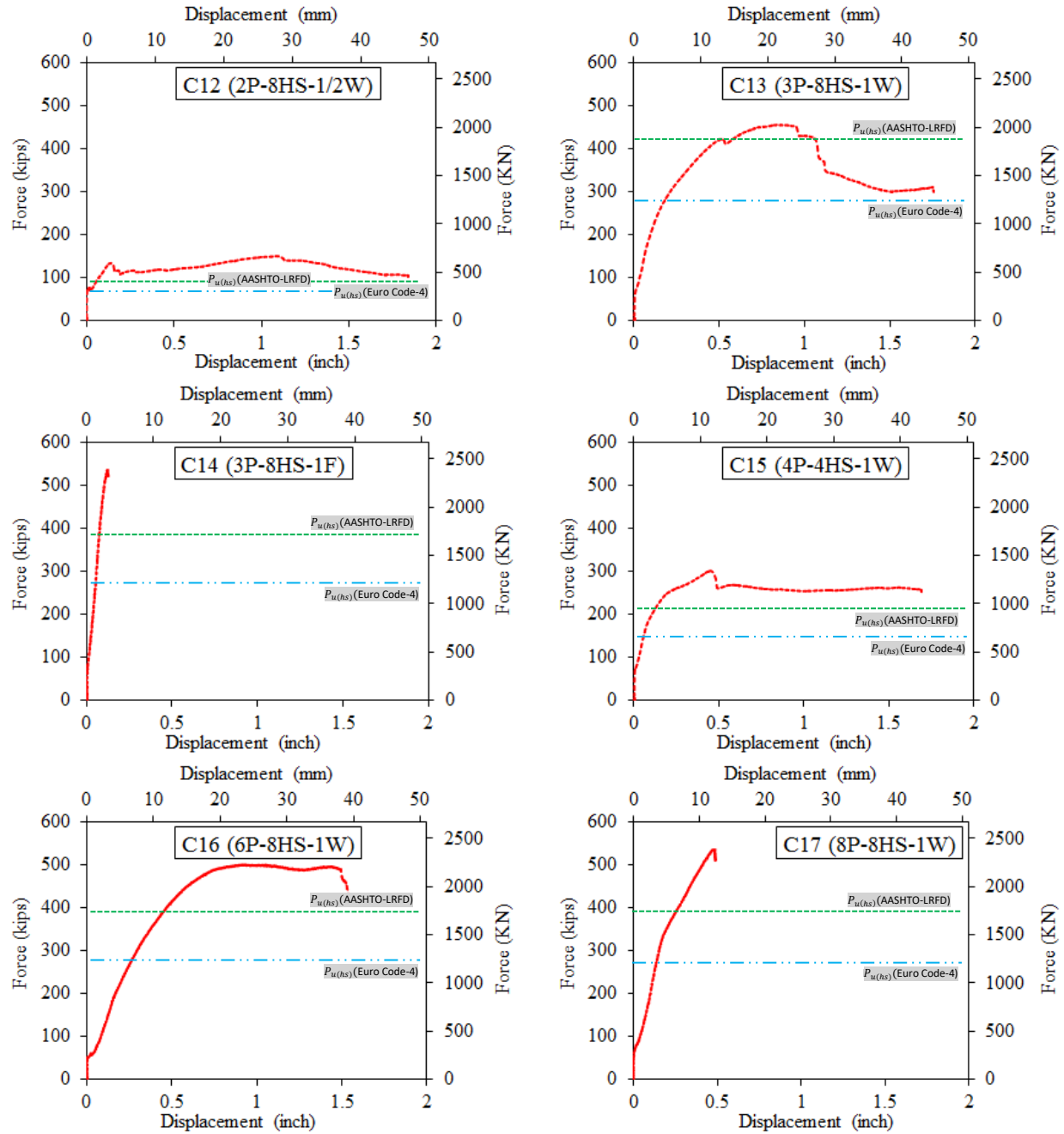


**Figure 5.15 cont.** Axial force vs. displacement with shear resistance ( $P_{u(hs)}$ ) of the HS.

The experimental axial load ( $P_{exp}$ ) for each specimen having eight HSs – to – its yield load ( $P_y$ ) versus the CR for that pile is presented in figure (5.18 (b)). Based on assumed linear relationship, the retrofit system needs a CR of 1.03 combined with 8 HSs to reach  $P_y$  of the

investigated piles. It is worth mentioning that the hoop strain in the CFRP jackets remained approximately zero until an axial displacement demand on the piles of approximately 2.5 - 3.81 mm (0.1-0.15 in.) indicating engaging the CFRP jacket to control and mitigate the concrete splitting cracks; thus, increasing the axial load capacity of the repaired system (fig. 5.17 (b)).

The hoop strain values ranged from 2,653  $\mu$  to 10,382  $\mu$  at the peak strength of the piles for specimens with a CFRP jacket and HS. Furthermore, the hoop strains were found to be higher at the bottom level due to the maximum concrete expansion.



(a)



(b)



(c)

**Figure 5.16** CFRP failure mode (a) C6 (1P-8HS-1W), (b) C7 (2P-4HS-1W), (c) C8 (2P-8HS-1W).

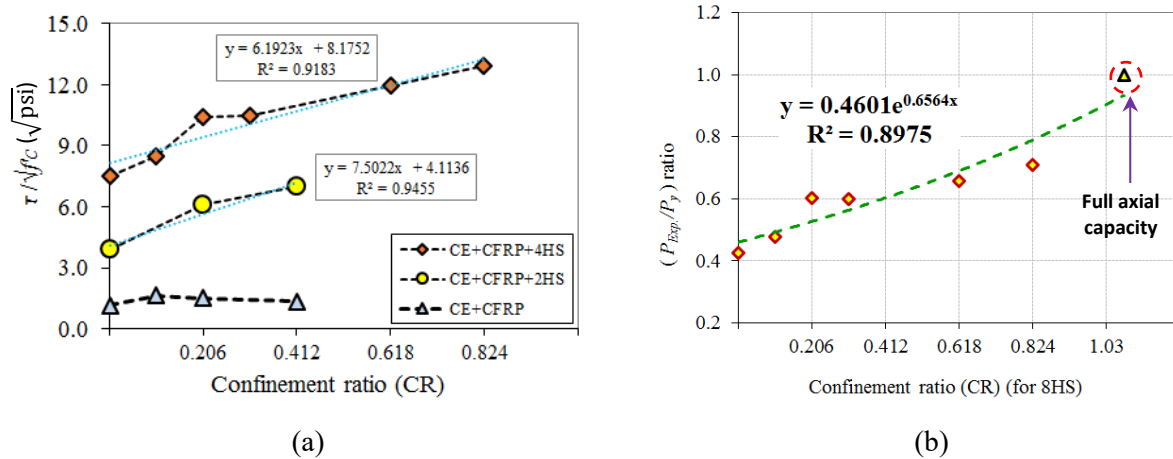


**Figure 5.17** CR versus (a) bond stress ratio, and (b) 8HS specimen experimental axial load ( $P_{exp}$ )— to —yield load ( $P_y$ )

**Table 5.9** CFRP Jacket Hoop Strain Gauges Readings at Peak Strength

Group	Specimen name	Designation (code)	CFRP type	Hoop strain (Microstrain)	
				Top level	Bottom level
C	C3	1P-0HS	Laminate	1,039	1,249
	C4	2P-0HS	Laminate	-	-
	C5	2P-0HS	Fabric	899.5	1,275
	C6	4P-0HS	Laminate	-	-
	C7	4P-0HS	Fabric	170.5	388
D	C8	1P-8HS-1W	Laminate	6,665	9,379
	C9	2P-4HS-1W	Laminate	2,555	8,826
	C10	2P-8HS-1W	Laminate	3,284	10,382
	C11	2P-8HS-3/4W	Laminate	3,031	8,590
	C12	2P-8HS-1/2W	Laminate	2,427	5,325
	C13	3P-8HS-1W	Laminate	3,540	9,037
	C14	3P-8HS-1F	Laminate	436.8	4,415
	C15	4P-4HS-1W	Laminate	1,600	6,636
	C16	6P-8HS-1W	Laminate	2,432	5,577
	C17	8P-8HS-1W	Laminate	1,741	2,653

### 5.3.6 Bond Strain Distribution

Figure 5.18 shows the axial strain distribution along the embedded depth of each steel pile for  $0.25P_{exp}$ ,  $0.50P_{exp}$ ,  $0.75P_{exp}$ , and  $P_{exp}$ . In addition, solid lines representing the axial strains

at the onset of bond breaking are shown in the figure. The strains were measured using the strain gauges attached to the piles. As shown in the figure, once the bond breaking occurred, no strains were recorded for specimens in groups A and C where no HSs were used. Concrete jackets in group C with specimens having no HSs displayed significant displacement at the bond breaking, which led to rupture of the strain gauges wires, and there were no further readings.

The strains increased as the applied axial loads increased. The strains were also higher at the loaded end and decreased along the embedded length. Specimen *RS* showed that the shear stresses were transferred along 165 mm (6.5 in.) before the occurrence of splitting failure. However, specimens having HSs and/or CFRP jackets showed more shear stress distribution along the embedded length with non-uniform stress distribution.

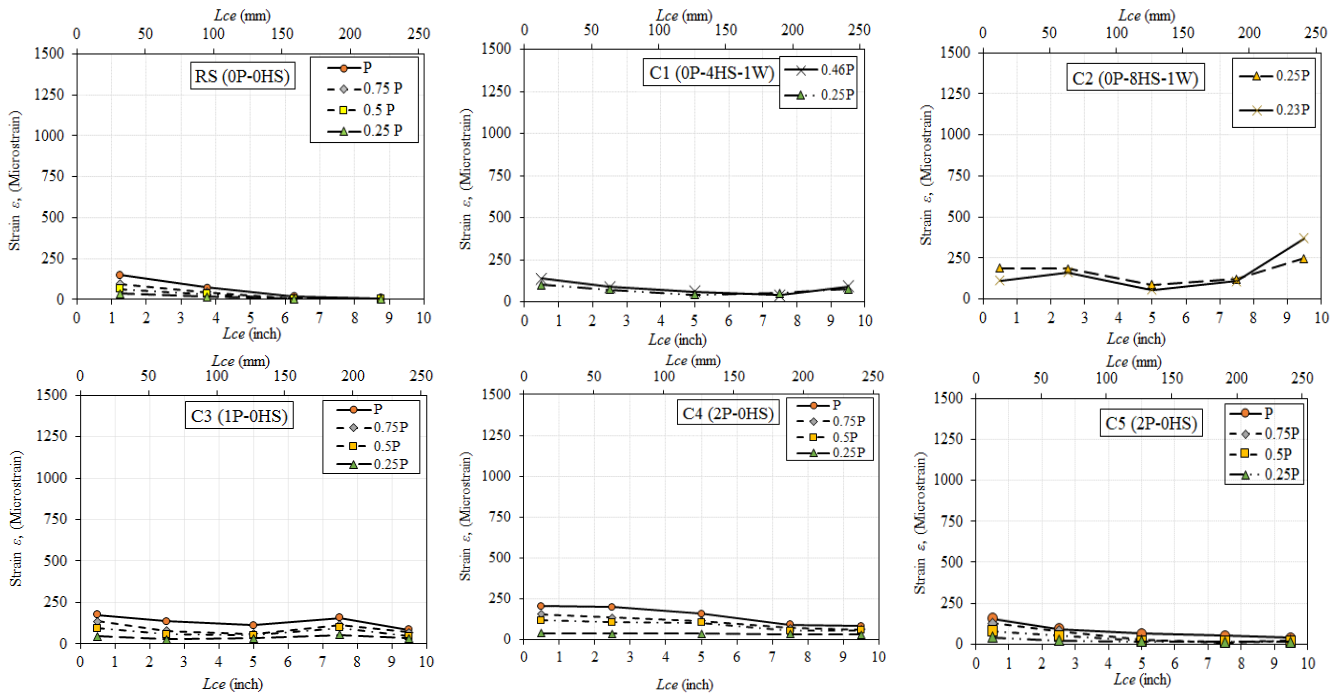
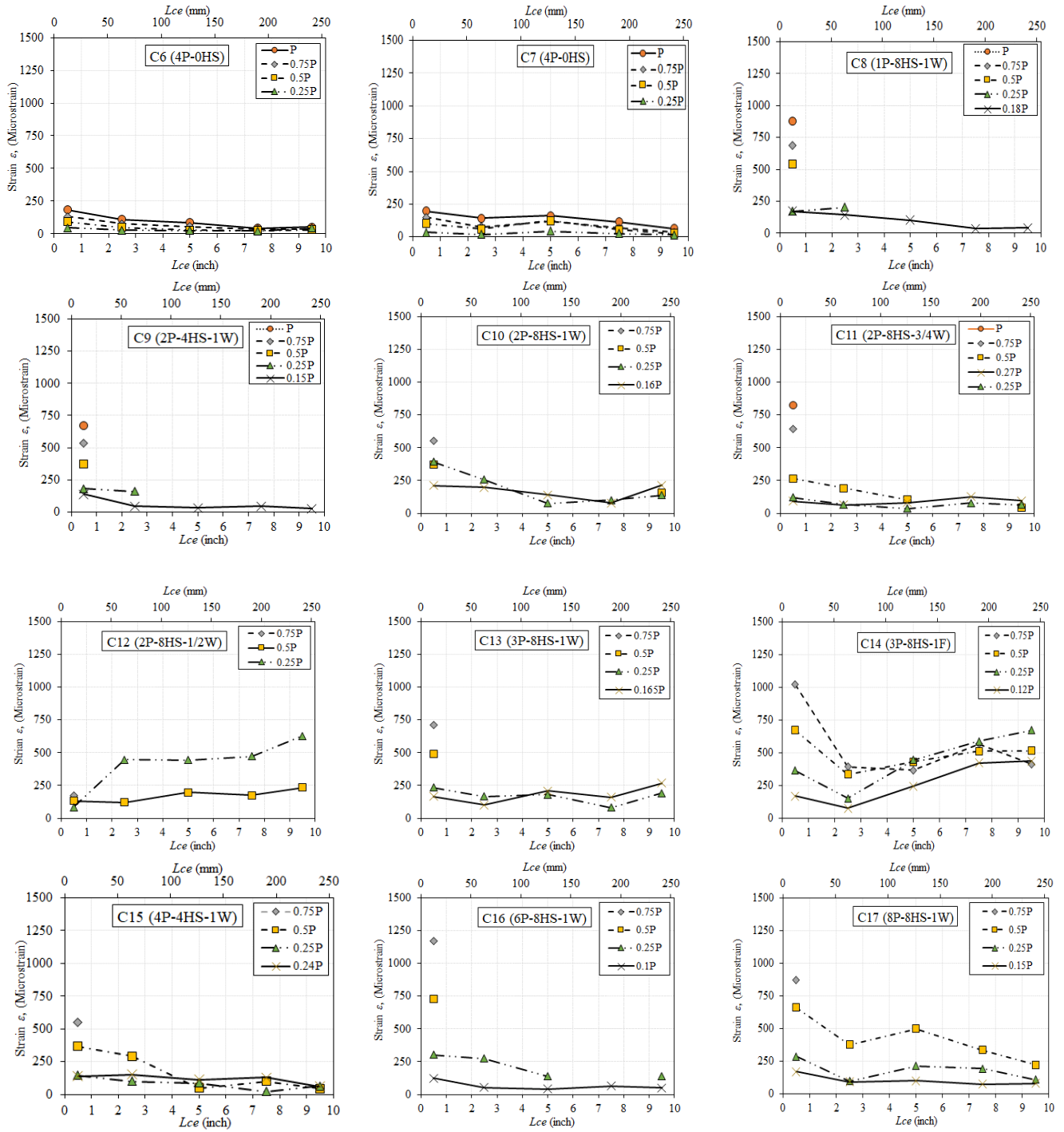


**Figure 5.18** Strain vs. CE length ( $L_{CE}$ ) for the tested specimens.



*Solid lines represent the axial strains at the onset bond breaking*

**Figure 5.18 cont.** Strain vs. CE length ( $L_{CE}$ ) for the tested specimens.



## Chapter 6 Experimental Testing and Finite Element Analyses of Retrofitted Full-Scale Steel H-Piles

### 6.1 Experimental Work

This section presents the details of the experimental and numerical modeling program conducted to evaluate the behavior of corroded steel piles repaired with CFRP jackets. The materials used, fabrication, installation, and experimental and numerical results of the repaired piles were presented in this chapter.

### 6.2 Materials

#### *6.2.1 Steel H-piles*

Piles W70V-F50C, W70V-F50C-10%, and W70V-F50C-30% that were tested during the assessment task in Chapter 3 of this report were used to represent severely corroded piles since the corroded regions in these piles reached their yield strains and displayed significant buckling. The piles were straightened to restore as much as possible their as-built alignments. Then, CFRP jackets repair were installed, and then the specimens were tested under concentric axial load.

#### *6.2.2 CFRP Jacket*

The properties of the CFRP fabrics and Tyfo S epoxy used for applying the CFRP repair jacket were presented in Chapter 5 of this report.

#### *6.2.3 Headed Studs*

One-inch diameter all threaded rods having an ultimate strength of 60 ksi were cut to the required lengths and used as headed studs (HSs) (fig. 6.1). Heavy-duty nuts were added to the ends of each stud to act as stud heads (fig. 6.2).



**Figure 6.1** All threaded bars and heavy-duty nuts used as HSs.

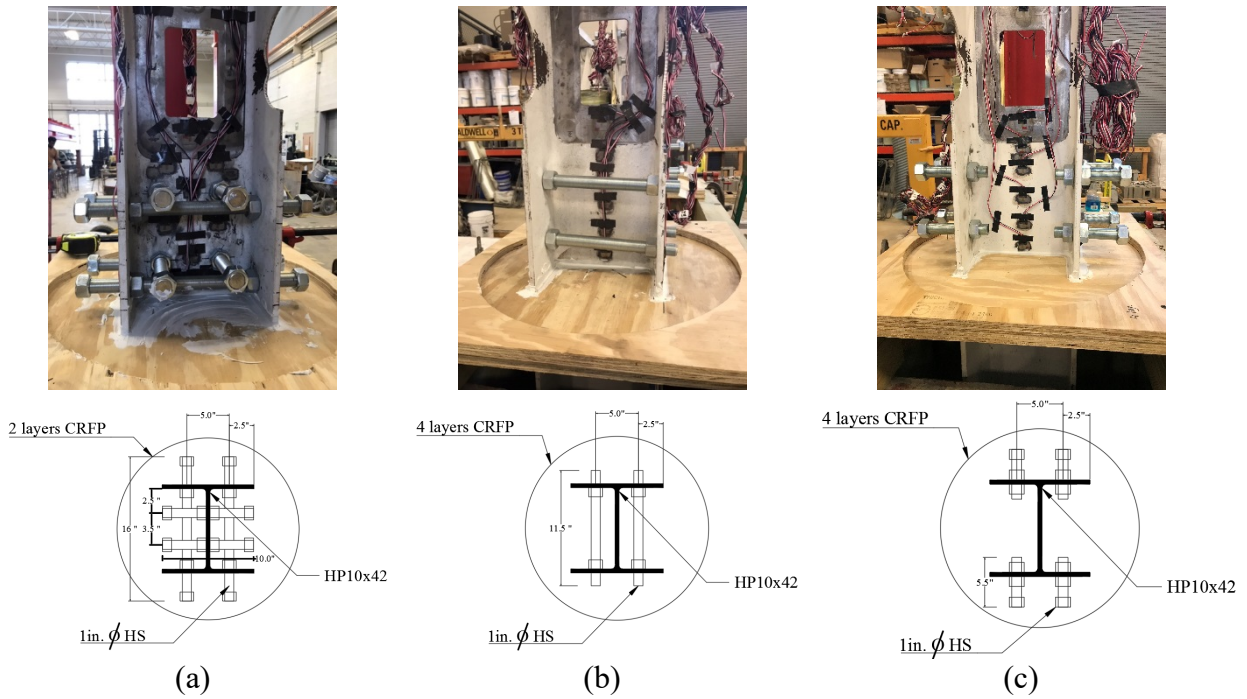


**Figure 6.2** Distributions of the HSs in the three H-piles: (a) R-1, (b) R-2, and (3) R-3.

#### 6.2.4 Longitudinal Reinforcing Bars

The reinforcing bars have been designed to withstand a bending moment corresponding to  $e/t$  of 5% at the yield strength of the uncorroded H-pile. However, due to availability and even distributions of the rebar, the bending moment capacity of rebar was corresponding to  $e/t$  of

6.22% at yield strength of the uncorroded pile. Eight #4 two-leg closed bars having 180 hooks were used (fig. 6.3). The shape of the bars was selected to ensure there is an adequate development length for #4 bars per ACI 318 (ACI318 2014).

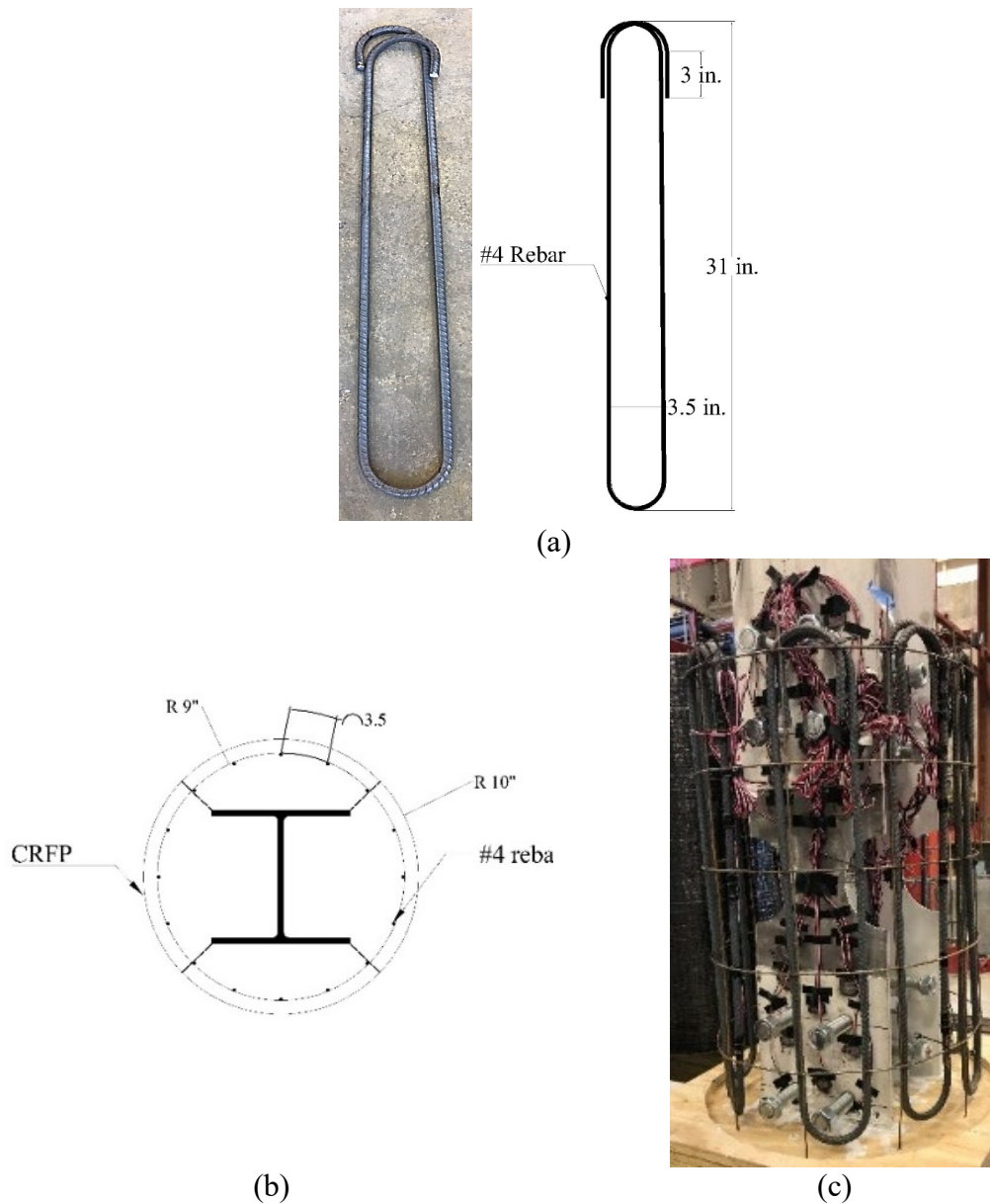


**Figure 6.3** Longitudinal reinforcement in the repair region: (a) closed bar profile, (b) distributions of rebars, and (c) reinforcement cage.

### 6.2.5 Concrete

SCC concrete mix (table 6.1) was used, to ensure concrete flowability, while filling the CFRP jackets. Three replicate concrete cylinders were tested in compression per ASTM C39 (Standard 2008) and the average concrete compressive at the day of testing of the piles was 7.49 ksi with a standard deviation of 200 psi.

The SCC had a slump flow of 546 mm (21.5 inch) diameter. Passingability using J-Ring were also conducted to determine the flowability of the concrete with 533 mm (20 inch) diameter (fig. 6.4). Blocking assessment per ASTM C1611 found that the difference between the slump flow and J-ring flow was 12.6 mm (0.5 inch); therefore, there was no visible blocking. L-box test was also carried out per ASTM C1621.

**Table 6.1** Mixture Used for the Concrete

w/c	Cement (lb/yd <sup>3</sup> )	Fly Ash (lb/yd <sup>3</sup> )	Water (lb/yd <sup>3</sup> )	Fine aggregate (lb/yd <sup>3</sup> )	Coarse aggregate (lb/yd <sup>3</sup> )	HRWR (lb/yd <sup>3</sup> )
0.5	350	101	225	848	848	1.9

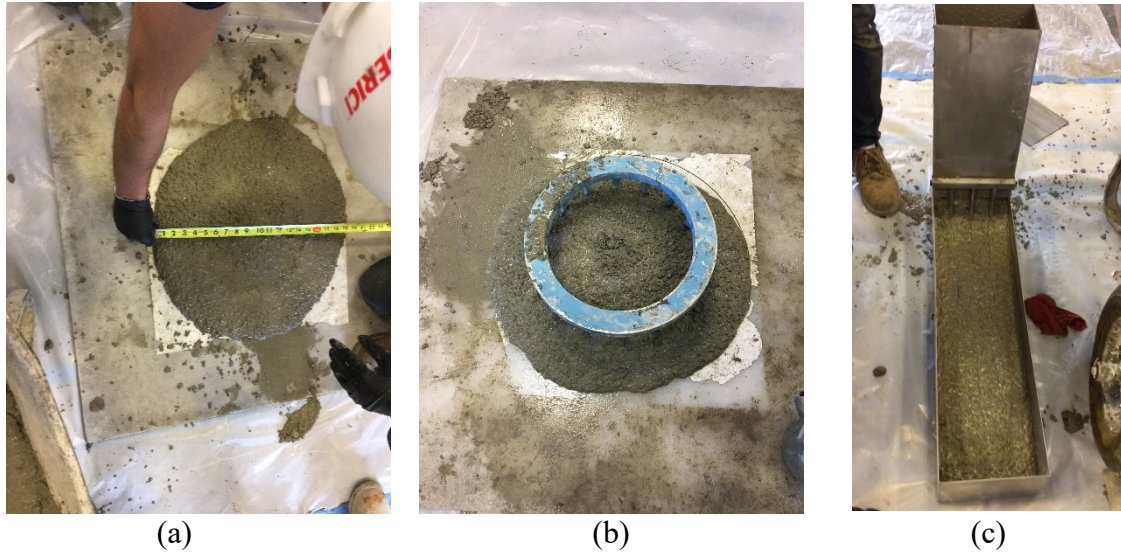


**Figure 6.4** ASTM tests: (a) Slump flow, (b) Passing ability using J-ring, and (c) L-box.

### 6.3 Fabrication and Installation of the Repair System

The repair was conducted as follows: (i) preparation of the steel pile, (ii) preparation of the CFRP jackets, (iii) preparation of the steel cage, and (iv) inserting the CFRP repair jacket and fill with SCC.

#### *6.3.1 Preparation of the Steel Pile*

After straightening the tested piles to restore their original alignments, the required number of holes for the HSs were drilled, using a magnetic driller, in the webs and/or flanges (fig. 6.5 and table 6.2).

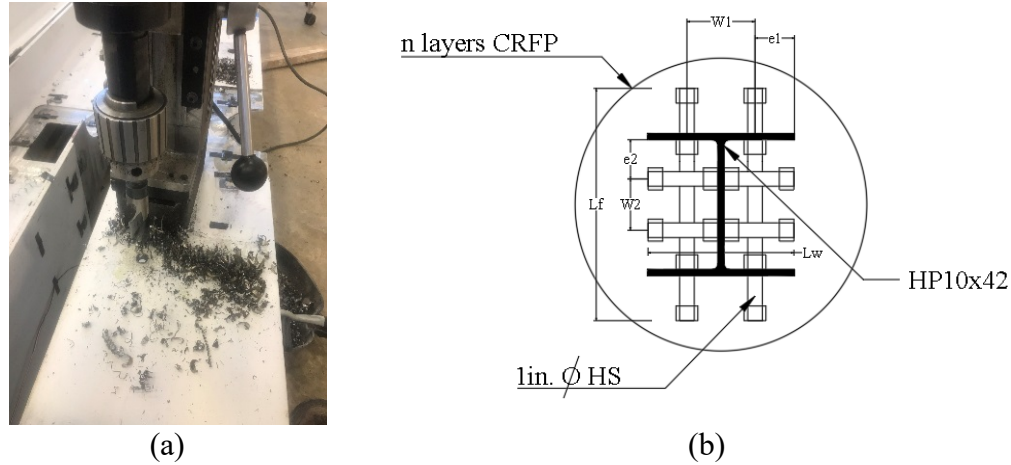


**Figure 6.5** (a) Magnetic drill used to drill holes for the HSs, and (b) general distribution for studs.

**Table 6.2** Arrangement of HSs in Different Test Specimens

Specimen designation	HSs								CFRP Layers no.
	Flange				Web				
	No.	L <sub>f</sub> (in.)	W1 (in.)	e <sub>1</sub> (in.)	No.	L <sub>w</sub> (in.)	W2 (in.)	e <sub>2</sub> (in.)	
R1	2	16			2	10	3.5	2.5	2
R2	2	11	5.0	2.5	N/A	--	--	--	4
R3	4	5.5			N/A	--	--	--	4

### 6.3.2 Preparation of the CFRP Jackets

The CFRP was cut to the desired length and then a 2 mm (0.08 inches) thick epoxy layer, per the manufacturer's requirements, was applied to each CFRP jacket. Then, the CFRP jacket was wrapped around a 508 mm (20 inches) diameter Sonotube with an overlap length in the circumferential direction of 203.4 mm (8 inches). The tube diameter was selected to ensure a minimum concrete thickness of 508 mm (2 inches) between the CFRP jacket and the edges of the

flanges of the repaired steel H-pile. After one day, the Sonotube was removed from the CFRP jacket.

### *6.3.3 Preparation of the Steel Cage*

Welded 9 gauge steel wire, 6 x 6 3.75mm (0.148 in.) mesh, was wrapped with a diameter of 19 in. The eight #4 closed reinforcement were uniformly distributed at 88.9 mm (3.5 in.) spacing (fig. 6.3) and secured in place by attaching them to the wire mesh using steel wires.

### *6.3.4 Installing the Repair Jacket and Filling with SCC*

A 610 x 610 mm (24 x 24 in.) plywood end cap was placed on top of a formwork. The end cap had an H-shaped cut at its center where the prepared steel pile was inserted and aligned in the center of the formwork. The steel and end cap were firmly fixed in their locations using C-clamps that attached the pile to the formwork.

The CFRP jacket was inserted from the top of the corresponding pile and placed atop of the end cap. The interface joint between the jacket and end cap was sealed with fast dry caulk. The steel cage was also inserted from the top of the pile and fixed in its place inside the CFRP jacket. SCC was placed to fill the CFRP jackets.



**Figure 6.6** Specimens after CFRP Installation.



#### 6.4 Instrumentation

Ninety-two strain gauges were attached to the web and flanges of each H-pile specimen (fig. 6.7), before casting the concrete, to measure the axial strains.

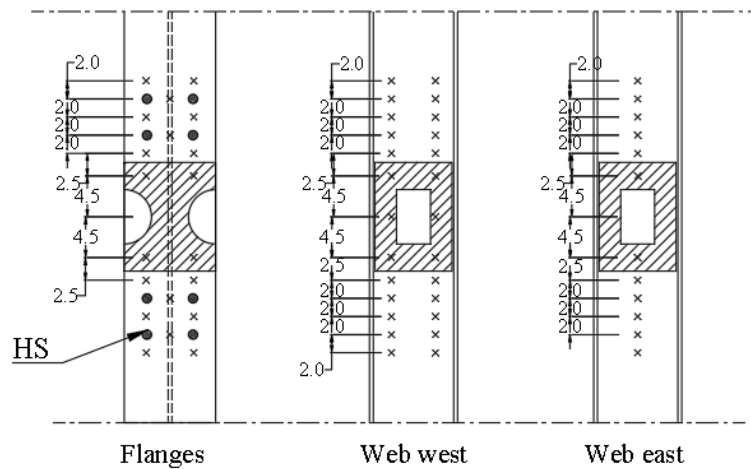


**Figure 6.7** Strain gauges distribution on the flanges and web of H-pile

Additional twelve strain gauges were mounted on each CFRP jacket to measure the hoop strains during testing (fig. 6.8). Twelve strain gauges attached to the longitudinal rebar's to monitor the axial strains. Eight string pots were installed to measure the displacements of each H-pile in both the horizontal and vertical directions (fig. 6.9).



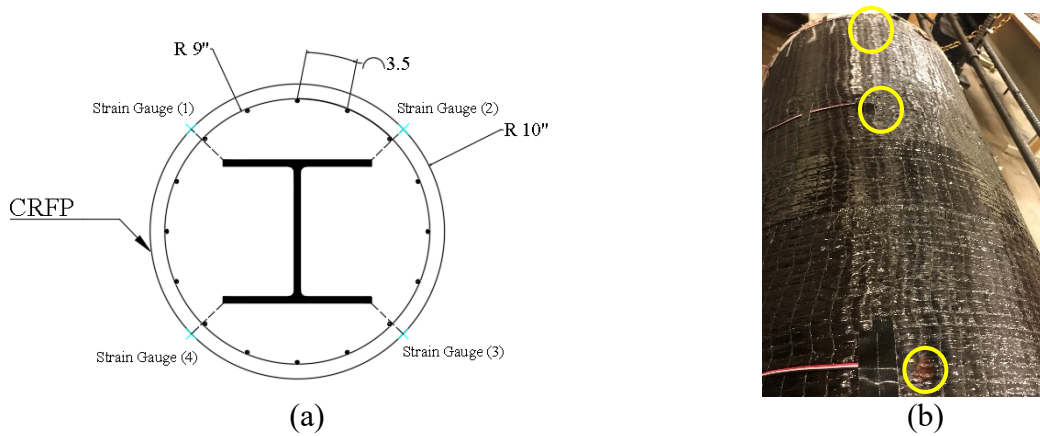


**Figure 6.8** Strain gauges distribution on the CFRP cross-section (a) Cross section (b) longitudinal direction.



**Figure 6.9** String potentiometer vertical and horizontal measurements.

### 6.5 Piles Testing

Once the CFRP jackets were filled with concrete, they were left to cure at an ambient temperature of  $23 \pm 2^{\circ}\text{C}$  ( $73 \pm 3^{\circ}\text{F}$ ) inside the laboratory (Fig 6.6). The formwork was removed after three days and the piles were installed in the test setup that was used for testing the bare piles described in Chapter 3 of this report. The specimens were axially loaded as discussed in Chapter 3 of this report.

## 6.6 Results and Discussion

Figure 6.10 illustrates the axial force versus axial shortening of the repaired piles. As shown in figure. 6.10 (a), the peak load of specimen R1 was 2228 kN (490.3 kips) with increase in the capacity of the original pile W70V-F50C by 272%. The peak load was accompanied by yielding stress at the section of the steel pile just outside the concrete jacket.

For the repair R2 the peak load was 2466 kN (542.5 kips) where the pile section locally failed then followed with global buckling afterwards. While for repair R3 the peak load was 2,318 kN (510 kips) and it failed due to local buckling accompanied by global buckling in the pile.

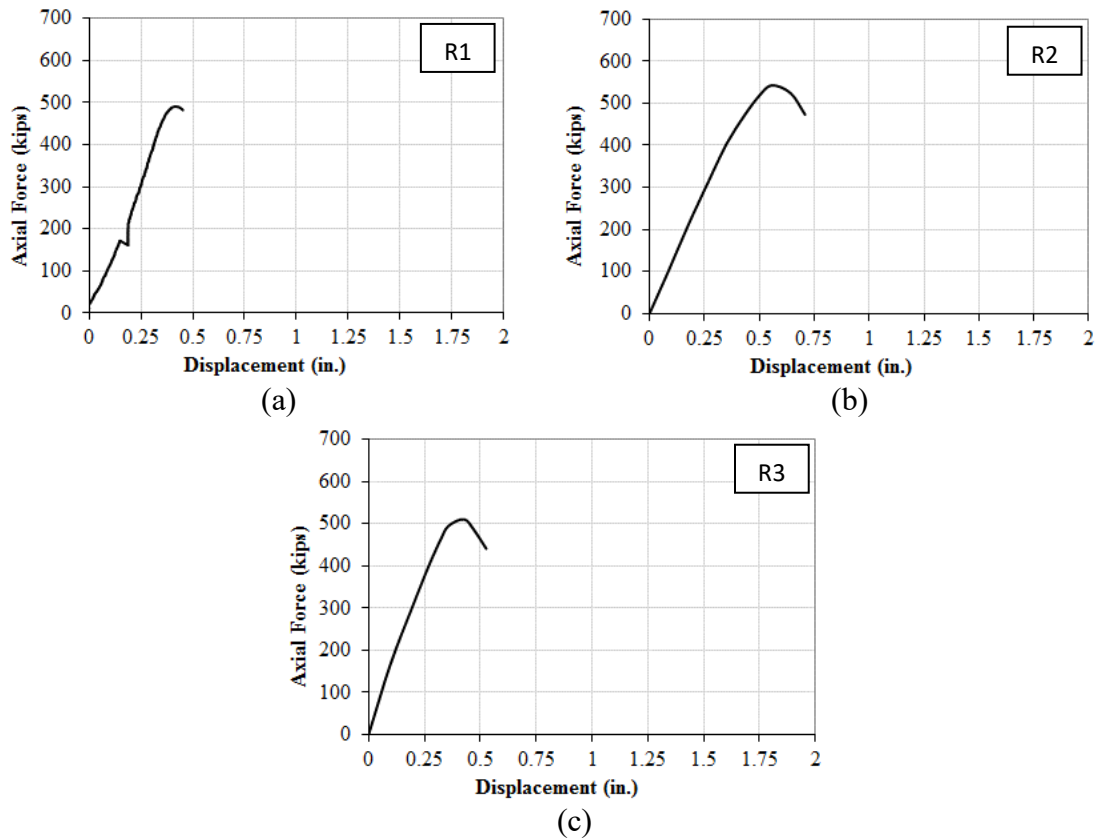


**Figure 6.10** Experimental axial load vs. displacement curves (a) R1, (b) R2, and (c) R3.

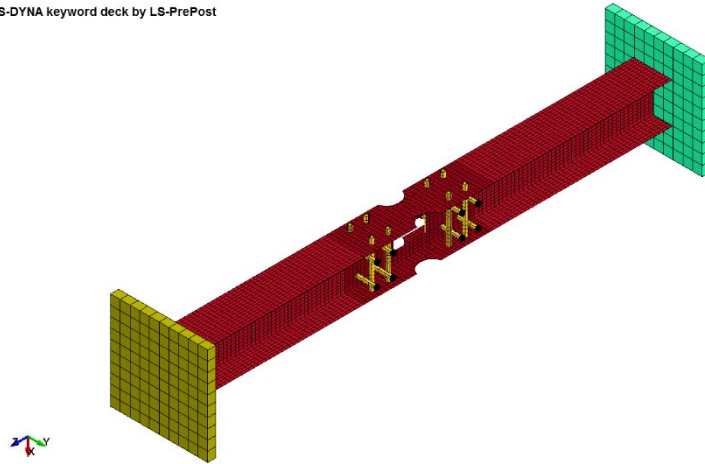
## 6.7 FE Modeling

The material properties were determined from tensile coupon tests, and the initial local and overall imperfections were measured from the test specimens before loading. The geometric imperfections were included by using a linear perturbation analysis to establish the probable buckling modes of the column for nonlinear analysis. Residual stresses were not considered since the measurements obtained from Young and Rasmussen (1995, 1998) indicated they were negligible.

### *6.7.1 Model Geometry*

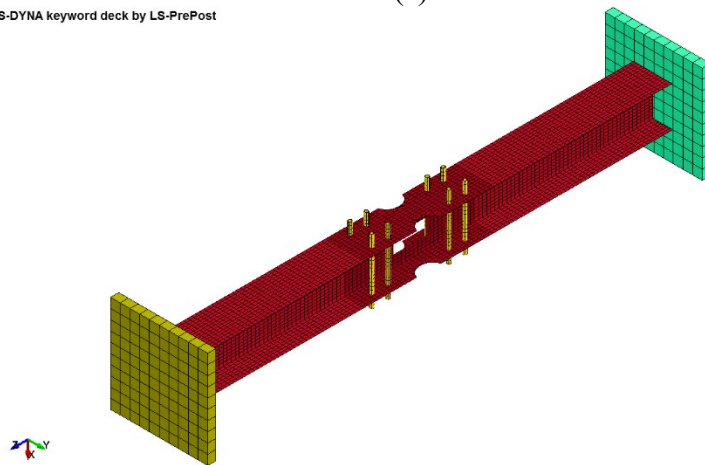
The geometric properties and material properties of the repaired steel pile is illustrated in section 6.1.1. Figure 6.11 shows the general 3D view of the FE model of the retrofitted piles. A sensitivity analysis was conducted to determine the different element sizes. The element type and size were determined according to a sensitivity study, which indicated that the chosen type and size provided best predictions for the strengths and deformations of the piles. Each FE model had approximately 41,862 elements and 35,857 nodes. Figure 6.12 shows the final finite element model of the different parts of the simulated retrofit steel h-pile.

LS-DYNA keyword deck by LS-PrePost



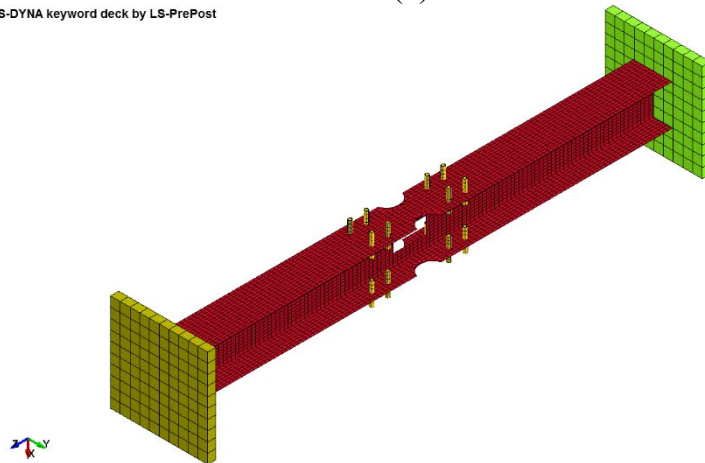
(a)

LS-DYNA keyword deck by LS-PrePost



(b)

LS-DYNA keyword deck by LS-PrePost



(c)

**Figure 6.11** FE of the repaired piles and HSs layout of (a) R-1, (b) R-2, and (c) R-3.

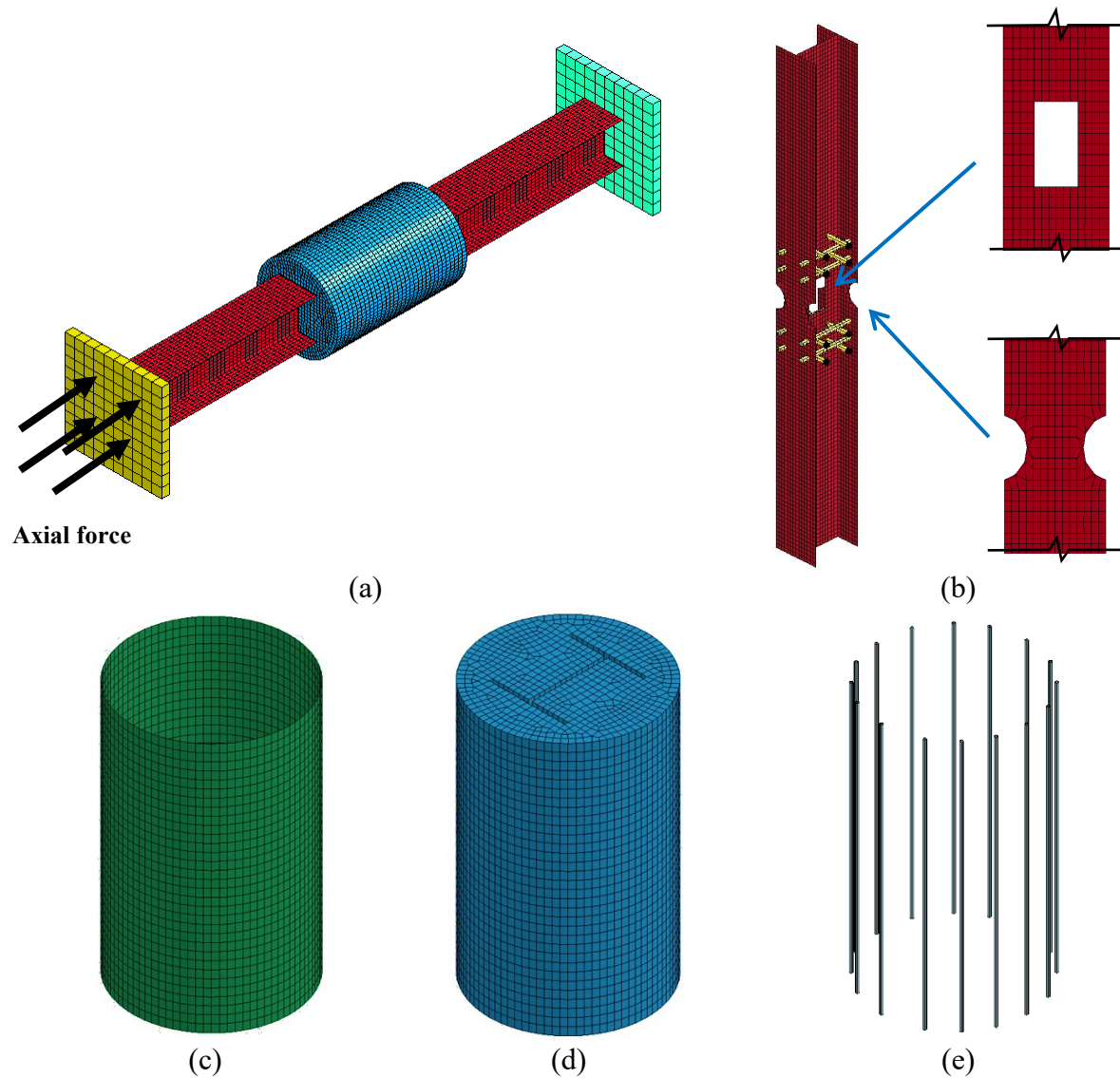


**Figure 6.12** FE modeling: (a) 3D view of the repaired steel pile, (b) steel H-pile, (c) CFRP tube, (d) concrete filling, and (e) steel rebar.

## 6.7.2 Material Models

### 6.7.2.1 Concrete

Release III of the Karagozian and Case (K&C) was used to model the concrete material. The model was developed based on the theory of plasticity and has three shear failure surfaces: (1) yield, (2) maximum, and (3) residual shear (Malvar et al. 1997). Several investigators used

this material model to predict the performance of concrete structures under lateral cyclic loads (Abdelkarim and ElGawady 2014; Ryu et al. 2013; Youssf et al. 2014). Automatic option was used during the course of this research to generate all the model parameters, i.e., given the uniaxial unconfined compressive strength  $f'_c$ ; the model is able to create all the constants required for the finite element analysis.

The concrete encasement was modeled using constant-stress solid elements, which uses single point integration and reduces the computational time over the full integration element with a good accuracy.

#### 6.7.2.2 CFRP tube

The outer CFRP jacket was simulated using Belytshko-Tsay four-node shell elements with six degrees of freedom per node. An orthotropic elastic material denoted as 002-orthotropic\_elastic was used to simulate the FRP tube. This material is defined by the elastic modulus, shear modulus, and Poisson's ratio in the three principal axes. A failure criterion for the GFRP elements was implemented in LS\_DYNA by defining the ultimate strain by using \*MAT\_ADD\_EROSION keyword. The elastic moduli of the CFRP tube was 16,200 ksi. The axial elastic moduli and axial ultimate stress of the CFRP jacket was 140 ksi and the rupture strain is 0.85%. The major Poisson's ratio was 0.4.

#### 6.7.2.3 Headed Stud Connectors

Material model 003-plastic\_kinematic was used to model the headed studs in LS-DYNA. This material model considers the steel as elasto-plastic material, which can be defined using: (1) the elastic modulus, E; (2) the yield stress; and (3) Poisson's ratio. It has the option of including strain-hardening effects using a linear relationship for plastic behavior. The effective diameter

was calculated by considering the effect of threads in reducing the cross-sectional area. Table 6.3 summarizes the properties of the simulated headed studs.

**Table 6.3** Mechanical Properties of the Headed Stud Elements

Effective Diameter (in)	Tensile modulus (ksi)	Yield strength (ksi)	Poisson's ratio
0.9	29,000	75	0.3

#### 6.7.2.4 Steel Rebars

The steel rebars modeled using truss-rebar elements. The steel rebars was included explicitly using the constrains method. The rebars embedded into the concrete encasement using constrains-lagrange-in-solids (CLIS) input. The required inputs are the part IDs of the rebars (as the slave) coupled to the concrete (as the master). Tables 6.4 summarize the properties of the simulated headed studs.

**Table 6.4** Mechanical Properties of the Steel Rebar Elements

Diameter (in)	Tensile modulus (ksi)	Yield strength (ksi)	Poisson's ratio
0.25	29,000	75	0.3

#### 6.7.3 Boundary Conditions and Loading

Boundary conditions were modeled to represent the test set-up at the supports. At the fixed end of the pile, translation was restrained in three perpendicular directions. At the jacking end, translation was restrained in the global X and Y directions but the pile was free to translate in the axial, global Z, direction. The piles were loaded by imposing an axial displacement at one end to simulate the action of the hydraulic jack in the experimental program.



Surface-to-surface contact elements were used to simulate the interface between the CFRP jacket and the concrete encasement. In this approach, the master and slave surfaces are generated internally within LS-DYNA from the parts ID's given for each surface. Contact elements surface-to-surface were also used to simulate the interface between the CFRP jacket and the concrete encasement and between the concrete encasement and the steel pile. Node-to-surface contact elements were used between the loading plates and the steel pile ends. The coefficient of friction for all of the contact elements was taken as 0.6. The hourglass stiffness based control type and coefficient used during this study were 5 and 0.03, respectively.

Initial perturbations were produced using the “perturbation” with “shell-thickness” keyword option in LS-DYNA software where the shell thickness was perturbed for the specific shell set on the simulated steel pile shell surface.

#### *6.7.4 Model Results*

##### *6.7.4.1 Axial Load-Displacement*

Figure 6.13 shows the axial load vs displacement curves of the the FE results compared to the obtained experimental results. In general, the FE model shows a good correlation with the test results for ultimate loads, stiffness and onset of non-linearity.

The repaired piles with 70% void in the web and 50% cut in the flange thickness as described previously, demonstrated a localized failure mode in the experimental test. The FE model was able to predict the axial-load displacement response and pre-peak behavior for the piles accurately. Comparison of the measured and predicted responses and peak loads for these piles suggests that failure was imminent. For the piles with 70% reduction in the thickness of the flanges, the onset of non-linearity of the repaired piles was predicted accurately. However, the initial stiffness were accurately predicted for the retrofitted steel pile R-1. While it was 10%

and 6% higher than the measured values for piles R-2 and R-3, respectively. This occurred as the steel piles underwent large plastic deformation during straightening the piles prior to the repair. Hence, large residual stresses were generated and it was difficult to simulate them accurately in the FE.

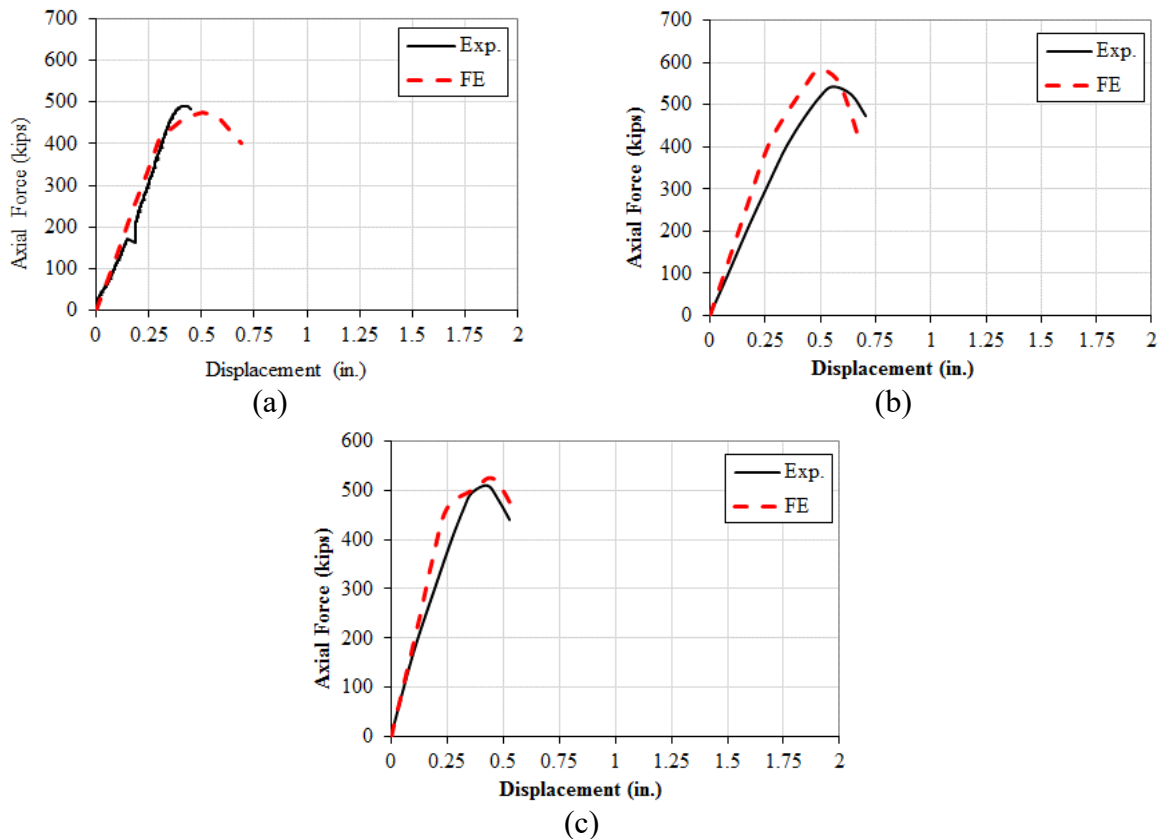
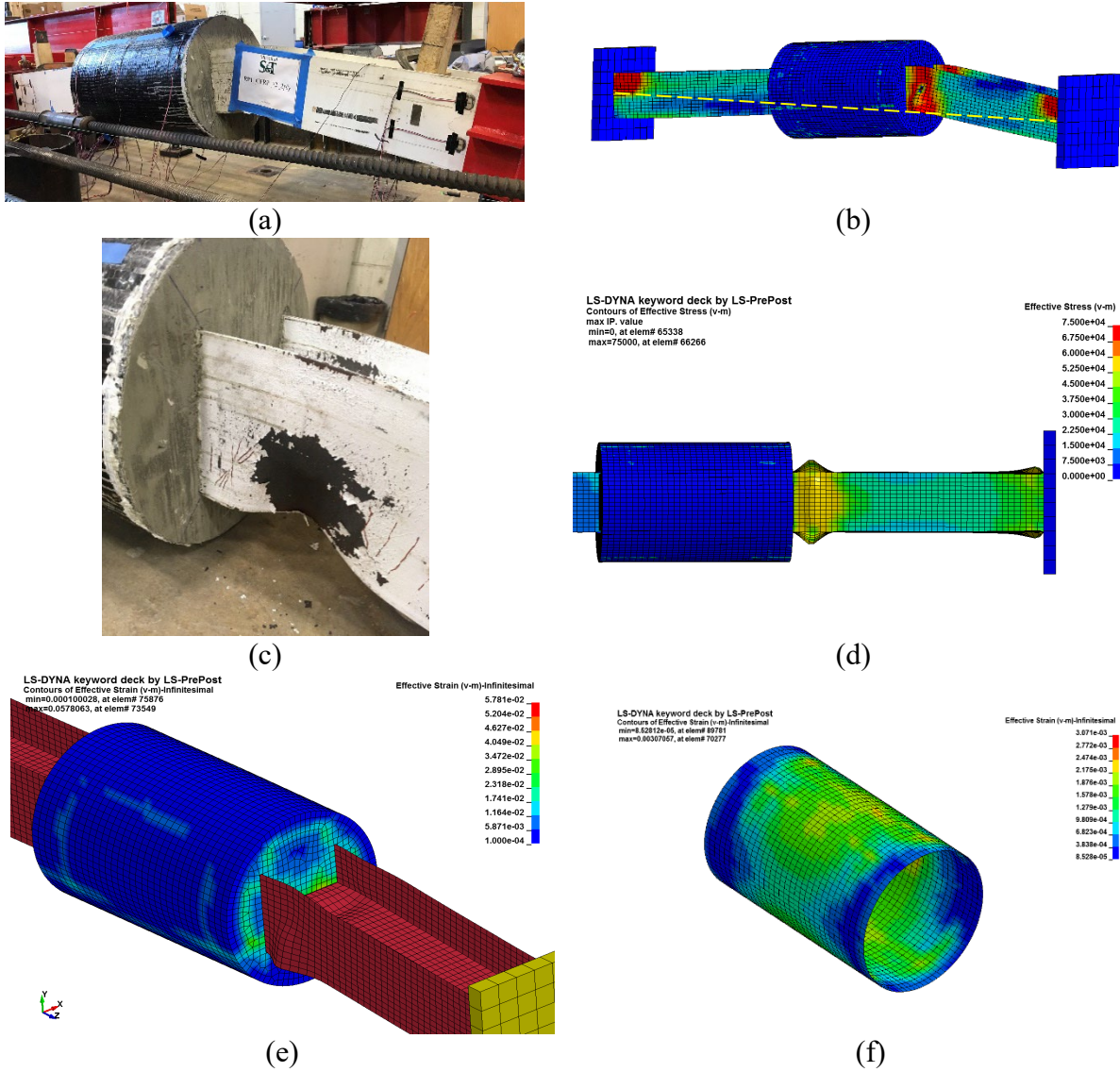


**Figure 6.13** Axial load vs. displacement curves (a) R1, (b) R2, and (c) R3.

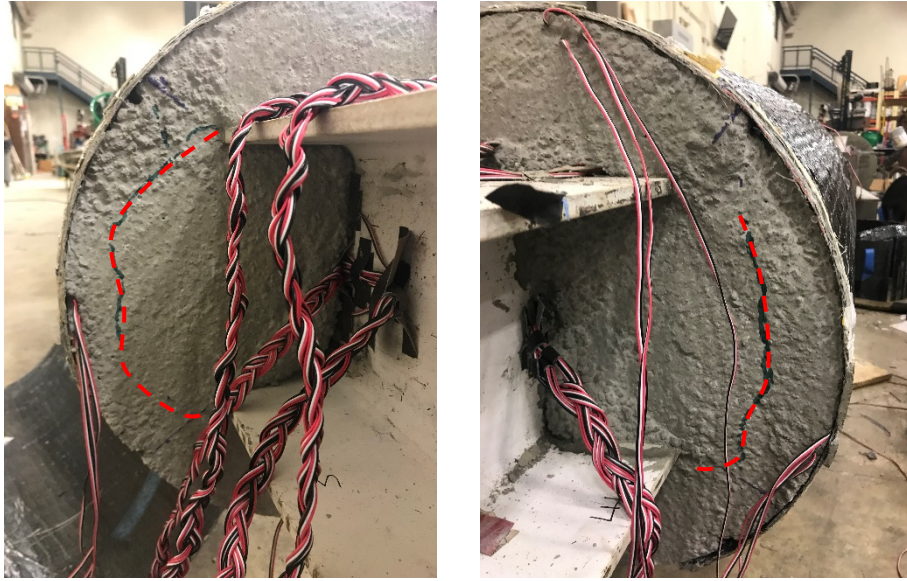
#### 6.7.4.2 Failure Modes

The predicted failure modes of the simulated piles R-1 and R-3 were flange local buckling outside of the repaired region followed by global lateral deformation (figs. 6.14 and 6.16). As shown in figure 6.14, by comparing deformed shape of the tested piles and the corresponding deformed shape obtained from the FE models, the model accurately predicted

the failure mode and deformation pattern of these two tested piles (fig. 6.14 and 6.16). Figure 6.14 (a and b) shows the global deformation of the repaired pile after 12.7 mm (0.5 in.) axial displacement. Figure 6.14 (c and d) shows a closer view on the steel pile damaged region, where the steel pile section yielded and then buckled at a distance of 940 mm (37 in.) from the loading plate. Figure 6.14 (e) revealed some stress concentration appeared in the simulated concrete encasement, observed as minor cracks in the experimental test (fig. 6.15). Figure. 6.14 (f) indicates stress concentrations in the middle of the CFRP jacket at the ultimate loading stage. This is due to the thinnest CFRP jacket that used in R-1 (2-ply) method compared to the other methods (with 4-ply) was less stiff in the hoop direction. Moreover, the large concrete encasement expansion occurred at that region. No rupture was found in simulated CFRP jacket, matching the experimental test observations.



**Figure 6.14** Failure modes of the simulated repaired pile R1 (a) exp., (b) FE whole system, (c) Exp. steel pile localized buckling, (d) FE steel pile localized buckling, and (e) concrete encasement stress concentration.



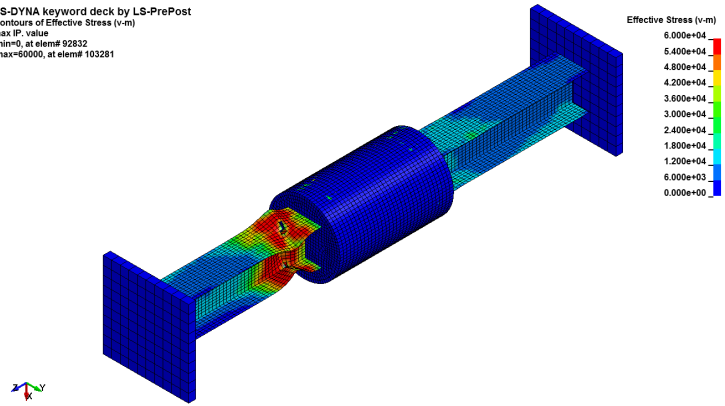
**Figure 6.15** Stress concentration at the tips of flanges on the concrete encasement.

Figure 6.17 indicates stress concentrations at the tips of the flanges in the CFRP jacket at the ultimate loading stage for the pile R-2. This pile demonstrated rupture of the CFRP jacket, which occurred along the tips of the bottom flange of the simulated pile. The FE model shows a large concrete encasement expansion at the flange sides towards the CFRP jackets leads to high hoop stress on the latter followed by rupture. However, this was not observed with the tested pile using R-2 where no CFRP rupture was noticed (fig. 6.17).

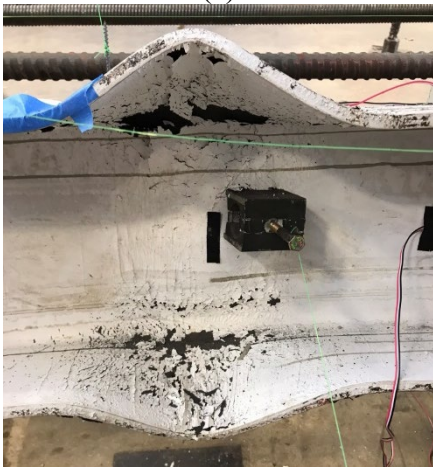


(a)

LS-DYNA keyword deck by LS-PrePost  
Contours of Effective Stress (v-m)  
max IP: value  
min=0, at elem# 92832  
max=60000, at elem# 103281

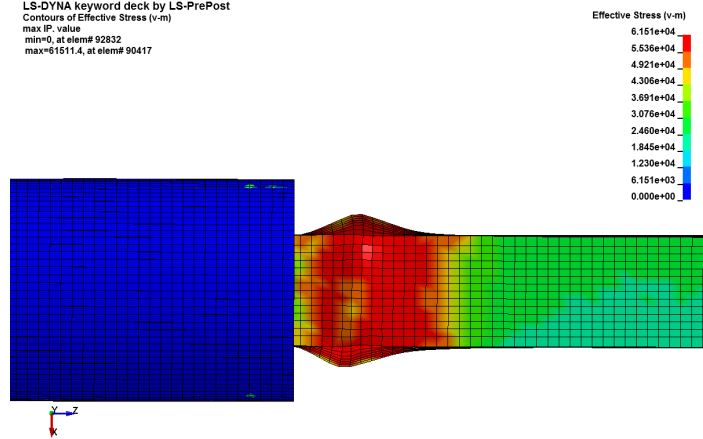


(b)



(c)

LS-DYNA keyword deck by LS-PrePost  
Contours of Effective Stress (v-m)  
max IP: value  
min=0, at elem# 92832  
max=61511.4, at elem# 90417

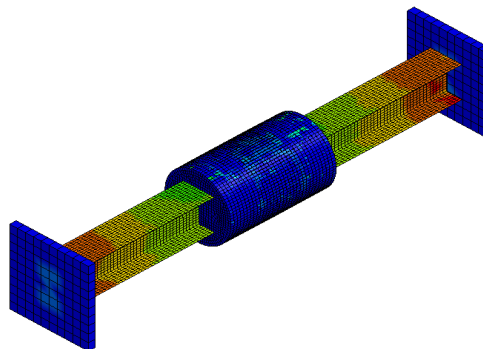


(d)

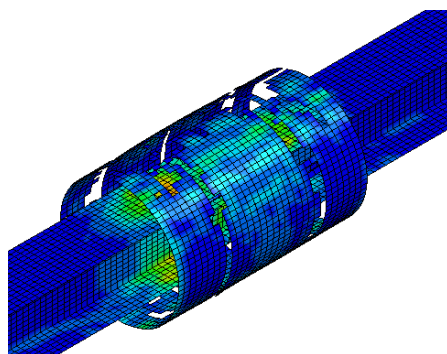
**Figure 6.16** Failure modes of the simulated repaired pile R3 (a and c) exp., (b and d) FE.



(a)



(b)



(c)

**Figure 6.17** Failure modes of the simulated repaired pile R2 (a) exp., (b and c) FE.



## Chapter 7 Conclusions

This report summarizes the details of an experimental work and finite element modeling that were conducted to evaluate: 1) the remaining axial capacity of steel H-piles having different corrosion severity and extension levels, and 2) the performance of repaired corroded steel H-piles. The research consisted of 32 steel H-piles ( $10 \times 42$ ) encased in different types of concrete including conventional concrete, high strength concrete, high-early strength concrete, and geopolymer concrete. Different embedment lengths and shear studs were used. In some specimens, the concrete jacket was confined using a carbon fiber-reinforced polymer (CFRP) jacket. Different confinement ratios were investigated as well. The specimens were subjected to push-out testing. The capacity of the shear studs was calculated using AASHTO\_LRFD (AASHTO 2012) and Eurocode-4 (Standardization 2004) codes.

Thirteen steel H-piles ( $10 \times 42$ ) were milled to represent the loss of cross-sectional area associated with corrosion and tested under concentric and eccentric axial loads. Different corrosion levels and patterns were considered. This included a reduction of 70% in the web, 50% in the flanges, a  $152 \times 95$  mm ( $6 \times 3.75$  in.) cut in the web, and/or a 152 mm (6 in.) diameter half-circle cut in the flanges. The capacities of the corroded piles were predicted analytically using three different existing design approaches: AASHTO (2014), AISC (2017), and AISI (2012) using the effective width method.

The experimental work was accompanied with finite element models (FEMs) that were developed and validated against experimental results from the literature. The validated FEMs were used to predict the performance of the investigated piles. Furthermore, the FEMs were used to conduct a parametric study to investigate the influence of various parameters on the remaining capacity of corroded steel H-piles.



Three steel H-piles were also repaired using concrete-filled carbon-fiber reinforced polymer jackets, shear studs, and longitudinal reinforcement. The specimens were tested under concentric axial loads.

The experimental and finite element study of the corroded steel H-piles revealed the following conclusions:

1. The axial capacity of the concentrically loaded corroded H-piles decreases as the corrosion severity increases. Both the FEMs and experimental work showed that the buckling load is more susceptible to corrosion in the flanges. For less than 25% reduction in the thickness of the flanges and 50% reduction in the thickness of the web, the axial capacity remained approximately constant, as the failure was due to global buckling. For less than 25% reduction in the thickness of the web and 50% reduction in the thickness of the flanges, the axial capacity decreased by up to 20% of the axial capacity of the uncorroded pile, as the failure was due to flange local buckling. Beyond that, local buckling of the flanges and webs controlled the behavior, and the strength of the corroded piles significantly decreased reaching up to 30% of the capacity of the uncorroded pile.
2. Introducing axial load eccentricity altered the modes of failure of all piles regardless of the severity of corrosion. All specimens displayed local buckling, and at eccentricity of 30%, the corroded pile lost 80% of its axial load capacity compared to the uncorroded pile.
3. Increasing the corroded region length up to 304 mm (12 in.) decreases the axial load capacity for different corrosion scenarios. Beyond 304 mm (12 in.), the length of the corroded region had no effect on the axial load capacity.

4. The mode of failure for all push-out test specimens started with bond breaking at small slip values followed by concrete jacket splitting. However, there was no damage or strain concentrations observed in the steel H-piles.
5. Increasing the concrete compressive strength increased the bond strength.  
  
Furthermore, the technique developed and used to apply heat curing to geopolymer concrete jackets was successful in producing compressive strengths similar to those of the conventional concrete. However, the bond strengths between the geopolymer concrete jackets that were either ambient or thermally cured and steel piles at embedment lengths greater than 254 mm (10 in.) were lower than those with conventional concrete and high early strength concrete jackets. More research is still required on optimizing the water content of the geopolymer concrete mixtures that formed a thin water film between the pile and concrete jacket. This film resulted in reduced bond strength.
6. Using headed studs considerably increased the bond strength between the concrete jackets and steel piles. Hence, a high axial capacity was achieved. AASHTO\_LRFD (AASHTO 2012) and Eurocode-4 (Standardization 2004) underestimated the shear capacity of the headed studs for concrete jackets with a CFRP confinement ratio higher than 0.21. AASHTO\_LRFD and Eurocode-4 predicted shear capacities ranging from 884.3 kN (198.8 kips) to 1,894.6 kN (425.9 kips) and 603.5 kN (135.7 kips) to 1,293.0 kN (290.7 kips) of the experimental strengths, respectively.
7. Using the CFRP jackets without headed studs slightly increased the bond stress between the concrete jackets and steel piles. Using headed studs and CFRP jackets

- increased the bond strength between the jackets and steel piles by a range of 580% to 1,130%, compared to the reference specimen.
8. The specimen having eight 25.4 mm (1 in.) diameter headed studs anchored to the web of the H-pile and eight plies of CFRP reached a maximum axial capacity of 2,403 kN (540.3 kips), representing 82% of the pile yielding load. Similar strength was achieved with three plies of CFRP and eight-headed studs anchored to the flanges of the H-pile.
  9. The FEMs for the retrofitted piles accurately predicted the axial load vs displacement curves. The difference between the ultimate capacity obtained using the FEMs and those obtained during the experimental work was less than 10%. Moreover, the FEMs generally predicted accurately the failure modes and deformation patterns of the experimentally tested piles R-1 and R-3, which failed due to localized buckling that occurred outside of the repair region with no CFRP rupture. For the retrofitted pile R-2, the FEM predicted CFRP rupture while the experimental work displayed concrete cracking inside the CFRP jacket. However, this crack did not trigger CFRP rupture, and the pile failed due to localized buckling that occurred outside of the repair region.

## References

- (2013). "Standard Test Method for Major and Minor Elements in Coal and Coke Ash By X-Ray Fluorescence." ASTM International.
- (2016). "Standard Practice for Making and Curing Concrete Test Specimens in the Laboratory." ASTM International.
- (2016). "Standard Specification for Concrete Aggregates." ASTM International.
- (2016). "Standard Test Methods for Tension Testing of Metallic Materials."
- AASHTO, L. (2012). "Bridge Design Specifications." *American Association of State Highway and Transportation Officials, Washington, DC*, 4.
- Abdelkarim, O. I., and ElGawady, M. A. (2014). "Analytical and Finite-Element Modeling of FRP-Concrete-Steel Double-Skin Tubular Columns." *Journal of Bridge Engineering*.
- ACI318 "Building code requirements for structural concrete (ACI 318-14) ", American Concrete Institute.
- ACI-440 "Guide for the Design and Construction of Externally Bonded FRP Systems for Strengthening Concrete Structures: ACI 440.2 R-08." American Concrete Institute.
- ACI "Building code requirements for structural concrete:(ACI 318-99); and commentary (ACI 318R-99)." American Concrete Institute.
- Alenezi, K., Tahir, M., Alhajri, T., Badr, M., and Mirza, J. (2015). "Behavior of shear connectors in composite column of cold-formed steel with lipped C-channel assembled with ferrocement jacket." *Construction and building materials*, 84, 39-45.
- Angst, U. M., Geiker, M. R., Michel, A., Gehlen, C., Wong, H., Isgor, O. B., Elsener, B., Hansson, C. M., François, R., and Hornbostel, K. (2017). "The steel–concrete interface." *Materials and Structures*, 50(2), 143.

- Army and Air Force (1994). "Bridge Inspection, Maintenance, and Repair."
- Beaulieu, L.-V., Legeron, F., and Langlois, S. (2010). "Compression strength of corroded steel angle members." *Journal of Constructional Steel Research*, 66(11), 1366-1373.
- Cao, S., Chen, J., Pan, J., and Sun, N. (2007). "ESPI measurement of bond-slip relationships of FRP-concrete interface." *Journal of composites for construction*, 11(2), 149-160.
- Dahou, Z., Castel, A., and Noushini, A. (2016). "Prediction of the steel-concrete bond strength from the compressive strength of Portland cement and geopolymer concretes." *Construction and Building Materials*, 119, 329-342.
- Dawood, M., Karagah, H., Shi, C., Belarbi, A., Vipulanandan, C., Bae, S.-W., and Lee, S. (2017). "Repair systems for deteriorated bridge piles." University of Houston.
- Department of the Army, D. o. t. A. (1991). "Pile construction." Department of the Army US, Washington, DC: Headquarters.
- Doguparti, R. S. (2015). "A study on bond strength of geopolymer concrete." *International Journal of Civil Environmental, Structural, Construction and Architectural Engineering*, 9(3), 355-358.
- du Béton, F. I. (2000). "Bond of reinforcement in concrete: state-of-art report." *Bulletin*, 10, 160-167.
- Esfahani, M. R., and Kianoush, M. R. (2005). "Development/splice length of reinforcing bars." *ACI structural journal*, 102(1), 22.
- FHWA (2015). "National Bridge Inventory." *U.S. Department of Transportation, Federal Highway Administration*.
- Florida Department of Transportation, O. o. M. (2011). "Bridge Maintenance and Repair Handbook."

- Georgia Department of Transportation (2012). "Bridge Structure Maintenance and Rehabilitation Repair Manual."
- Gomaa, E., Sargon, S., Kashosi, C., and ElGawady, M. (2017). "Fresh properties and compressive strength of high calcium alkali activated fly ash mortar." *Journal of King Saud University - Engineering Sciences*.
- Grzeszykowski, B., and Szmigiera, E. (2017). "Ductility assessment of two-chord composite steel-concrete battened columns." *Structure and Infrastructure Engineering*, 13(11), 1414-1424.
- Hadi, M. N. (2008). "Bond of high strength concrete with high strength reinforcing steel."
- Harajli, M. (2009). "Bond stress–slip model for steel bars in unconfined or steel, FRC, or FRP confined concrete under cyclic loading." *Journal of structural engineering*, 135(5), 509-518.
- Harajli, M., Hout, M., and Jalkh, W. (1995). "Local bond stress-slip behavior of reinforcing bars embedded in plain and fiber concrete." *Materials Journal*, 92(4), 343-353.
- Ichinose, T., Kanayama, Y., Inoue, Y., and Bolander Jr, J. (2004). "Size effect on bond strength of deformed bars." *Construction and building materials*, 18(7), 549-558.
- Jaffar, M. I., Badaruzzaman, W. H. W., and Baharom, S. (2016). "Experimental tests on bending behavior of profiled steel sheeting dry board composite floor with geopolymer concrete infill." *Latin American Journal of Solids and Structures*, 13(2), 272-295.
- Karagah, H., and Dawood, M. "Axial capacity of partially corroded steel bridge piles." *Proc., Proceeding of the annual stability conference. St. Louis, Missouri*, 411-425.
- Kayser, J. R., and Nowak, A. S. (1989). "Capacity loss due to corrosion in steel-girder bridges." *Journal of Structural Engineering*, 115(6), 1525-1537.

- Liu, X., Nanni, A., and Silva, P. F. (2005). "Rehabilitation of compression steel members using FRP pipes filled with non-expansive and expansive light-weight concrete." *Advances in Structural Engineering*, 8(2), 129-142.
- Malvar, L. J., Crawford, J. E., Wesevich, J. W., and Simons, D. (1997). "A plasticity concrete material model for DYNA3D." *International Journal of Impact Engineering*, 19(9), 847-873.
- Ok, D., Pu, Y., and Incecik, A. (2007). "Computation of ultimate strength of locally corroded unstiffened plates under uniaxial compression." *Marine Structures*, 20(1), 100-114.
- Ollgaard, J. (1971). "Shear strength of stud connectors in lightweight and normalweight concrete." *AISC Engineering journal*(5), 55-64.
- Orangun, C., Jirsa, J., and Breen, J. "A reevaluation of test data on development length and splices." *Proc., Journal Proceedings*, 114-122.
- Paik, J., Lee, J., and Ko, M. (2003). "Ultimate compressive strength of plate elements with pit corrosion wastage." *Proceedings of the Institution of Mechanical Engineers, Part M: Journal of Engineering for the Maritime Environment*, 217(4), 185-200.
- Pecce, M., and Ceroni, F. (2010). "Bond tests of partially encased composite columns." *Advanced Steel Construction*, 6(4), 1001-1018.
- Raynor, D. J., Lehman, D. E., and Stanton, J. F. (2002). "Bond-slip response of reinforcing bars grouted in ducts." *Structural Journal*, 99(5), 568-576.
- Ryu, D., Wijeyewickrema, A. C., ElGawady, M. A., and Madurapperuma, M. (2013). "Effects of tendon spacing on in-plane behavior of posttensioned masonry walls." *Journal of Structural Engineering*, 140(4), 04013096.

- Sarveswaran, V., Smith, J., and Blockley, D. (1998). "Reliability of corrosion-damaged steel structures using interval probability theory." *Structural Safety*, 20(3), 237-255.
- Shi, C., Karagah, H., Dawood, M., and Belarbi, A. (2014). "Numerical investigation of H-shaped short steel piles with localized severe corrosion." *Engineering structures*, 73, 114-124.
- Soliman, K., Arafa, A., and Elrakib, T. M. (2013). "Review of design codes of concrete encased steel short columns under axial compression." *HBRC journal*, 9(2), 134-143.
- Standard, A. (2008). "Standard test method for tensile properties of polymer matrix composite materials." *ASTM D3039/D M*, 3039, 2008.
- Standardization, E. C. f. (2004). "Eurocode 4: Design of composite steel and concrete structures—Part 1.1: General rules and rules for buildings."
- Stauffer, S. T. (2016). "Performance Assessment of Deteriorated and Retrofitted Steel HP Piles."
- Vijay, P., Soti, P. R., GangaRao, H. V., Lampo, R. G., and Clarkson, J. D. (2016). "Repair and Strengthening of Submerged Steel Piles Using GFRP Composites." *Journal of Bridge Engineering*, 21(7), 04016038.
- Wan, B., Foley, C. M., Ainge, S. W., and Nguyen, C. (2013). "Procedures, Cost and Effectiveness for Deteriorated Bridge Substructure Repair."
- Wipf, T. J., Fanous, F., Klaiber, F., and Eapen, A. (2003). "Evaluation of Appropriate Maintenance, Repair and Rehabilitation Methods for Iowa Bridges." *Final Report, Iowa DOT Project TR-429*.
- Youssf, O., ElGawady, M. A., Mills, J. E., and Ma, X. (2014). "Finite element modelling and dilation of FRP-confined concrete columns." *Engineering Structures*, 79, 70-85.



- Yu, T., Teng, J., and Wong, Y. (2009). "Stress-strain behavior of concrete in hybrid FRP-concrete-steel double-skin tubular columns." *Journal of structural engineering*, 136(4), 379-389.
- Zheng, H., Chen, Z., and Xu, J. (2016). "Bond behavior of H-shaped steel embedded in recycled aggregate concrete under push-out loads." *International Journal of Steel Structures*, 16(2), 347-360.
- Zmetra, K. M. (2015). "Repair of Corrosion Damaged Steel Bridge Girder Ends by Encasement in Ultra-High Strength Concrete."
- AASHTO(LRFD) (2014). "Bridge design specifications." *American Association of State Highway and Transportation Officials*.
- AISC (2017). "American Institute of Steel Construction." *Steel construction manual. 15th edition*.
- ANSI (2012). "North American specification for the design of cold-formed steel structures."
- ASTM (2005). "C1610 Test method for column segregation of self-consolidating concrete."
- ASTM (2005). "C1611 Test method for slump flow of self-consolidating concrete."
- ASTM (2005). "C1621 Test method for passing ability(j-ring) of self-consolidating concrete."
- Gere, J. M., and Timoshenko, S. P. (1961). *Theory of elastic stability*.
- Karagah, H., Shi, C., Dawood, M., and Belarbi, A. (2015). "Experimental investigation of short steel columns with localized corrosion." *Thin-Walled Structures*, 87, 191-199.
- LS-DYNA(Manual) (1998). "Theoretical Livermore software technology corporation."
- Sciences, N. A. o. (2017). "Repair Systems for Deteriorated Bridge Piles."  
<<https://trid.trb.org/view/1464404>>.

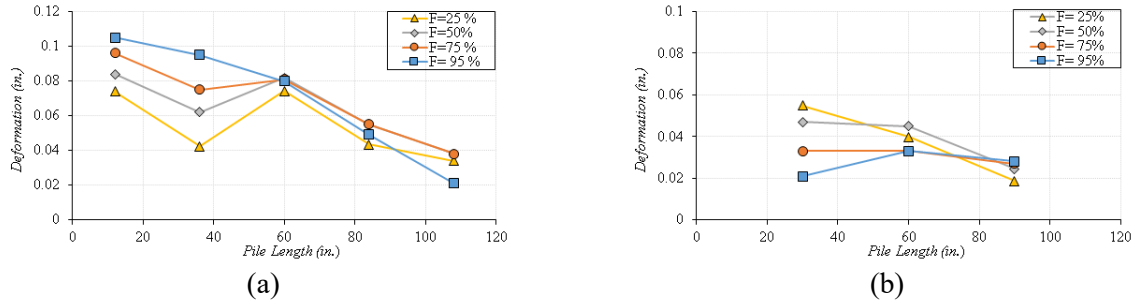
Shi, C., Karagah, H., Belarbi, A., and Dawood, M. (2016). "Inelastic buckling behavior of steel H-piles with localized severe corrosion." *Journal of Bridge Engineering*, 21(3), 04015069.

Shi, C., Karagah, H., Dawood, M., and Belarbi, A. (2014). "Numerical investigation of H-shaped short steel piles with localized severe corrosion." *Engineering structures*, 73, 114-124.

## Appendix A Summary of H-Piles Results

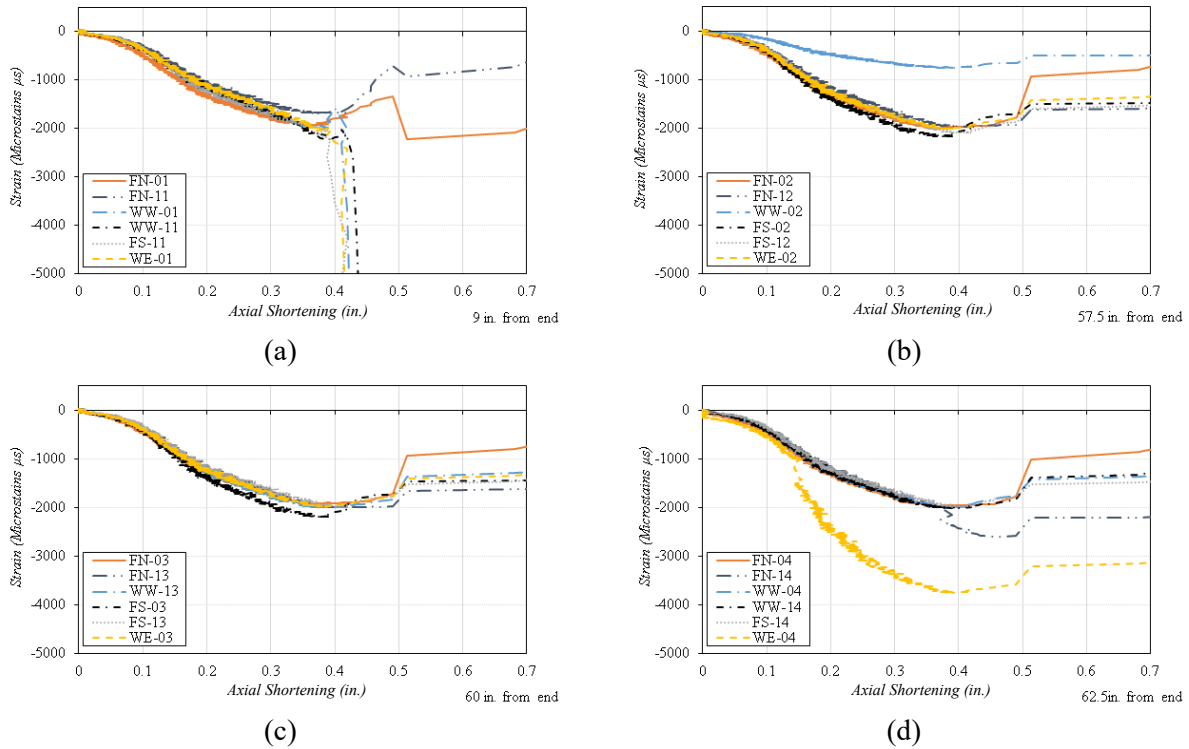
### A.1 W00-F00. Pile

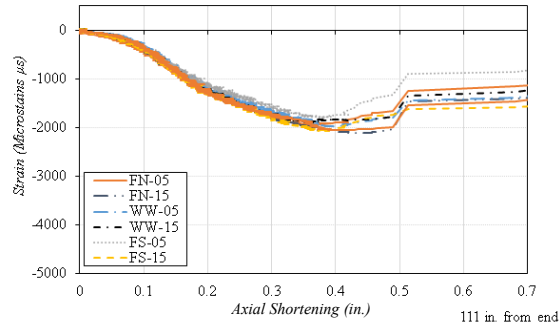
#### A.1.1 Profile of pile



**Figure A.1** Deformation profile with respect to the pile length: (a) Horizontal profile, (b) Vertical profile

#### A.1.2 Axial shortening-strain relation



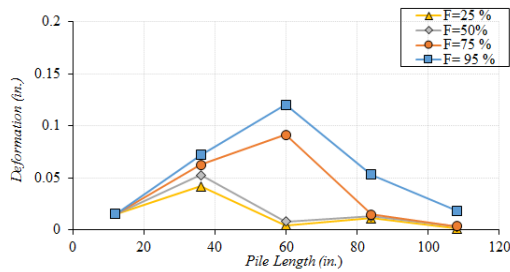


(e)

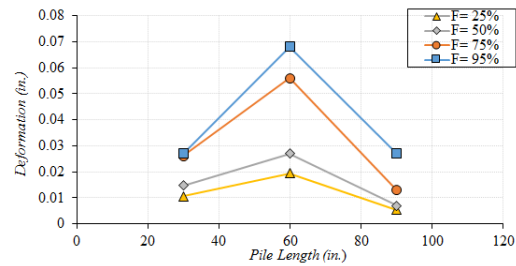
**Figure A.2** Axial shortening-steel strains in different position of pile: (a) 9in from edge,(b) 57.5in from edge, (c) 60in. from edge, (d) 62.5in. from edge, (e) 111in. from edge. FN: Flange north FS: Flange south WW: Web west WE: Web east

## A.2 W70-F00. Pile

### A.2.1 Profile of pile



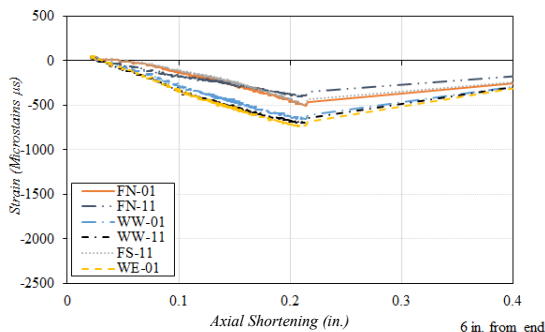
(a)



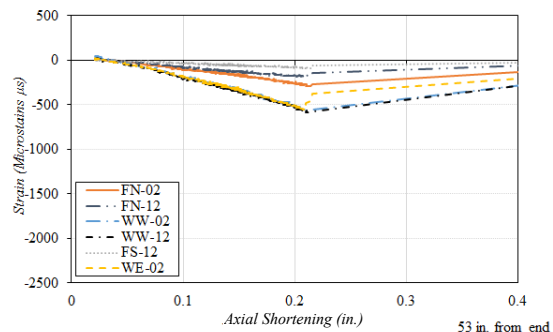
(b)

**Figure A.3** Deformation profile with respect to the pile length: (a) Horizontal profile, (b) Vertical profile

### A.2.2 Axial shortening-strain relation



(a)



(b)

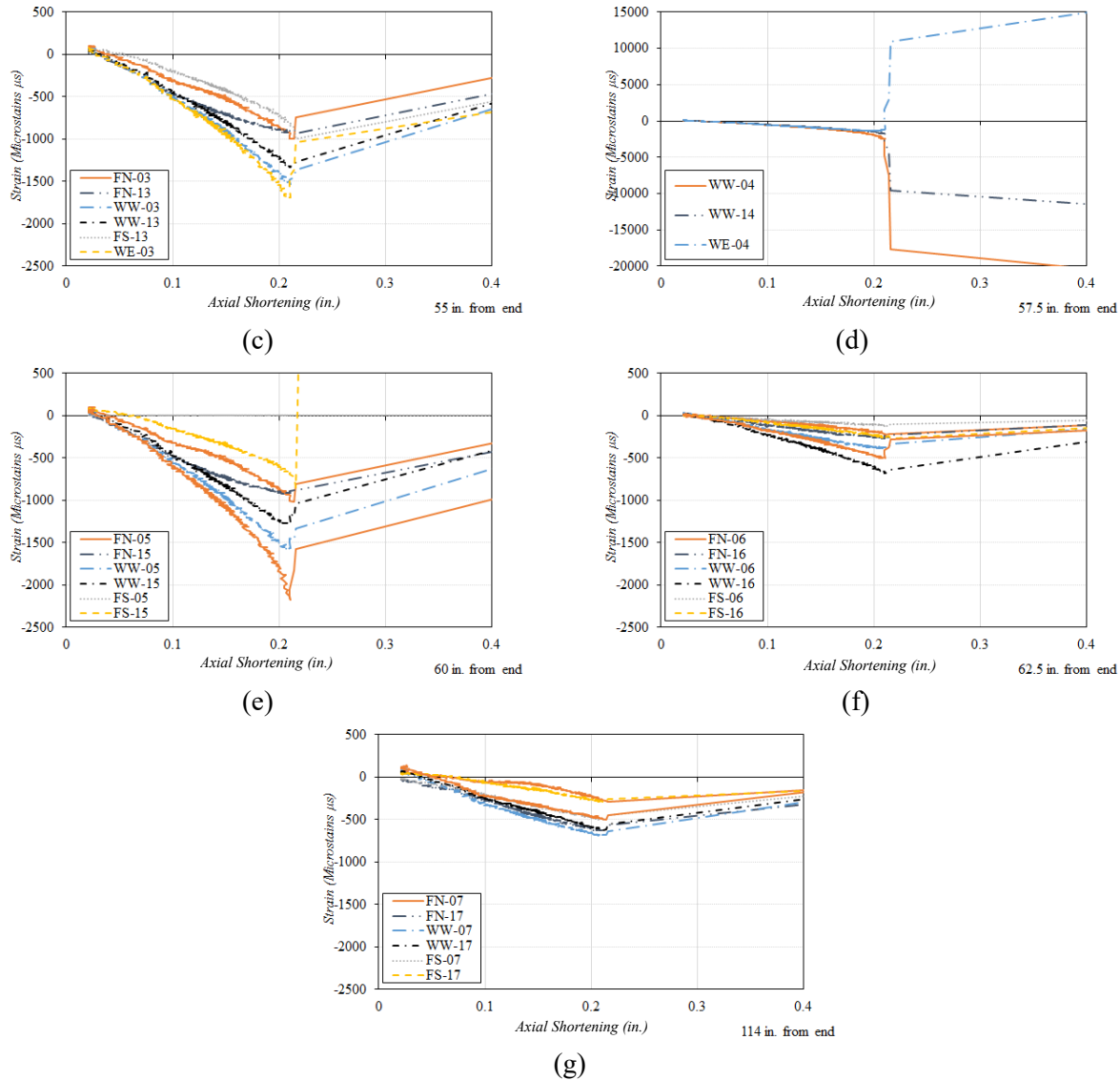


**Figure A.4** Axial shortening-steel strains in different position of pile: (a) 6in from edge, (b) 53in. from edge, (c) 55in. from edge, (d) 57.5in. from edge, (e) 60in. from edge, (f) 62.5 from edge, and (g) 114in. from edge

### A.3 W00-F50. Pile

#### A.3.1 Profile of pile

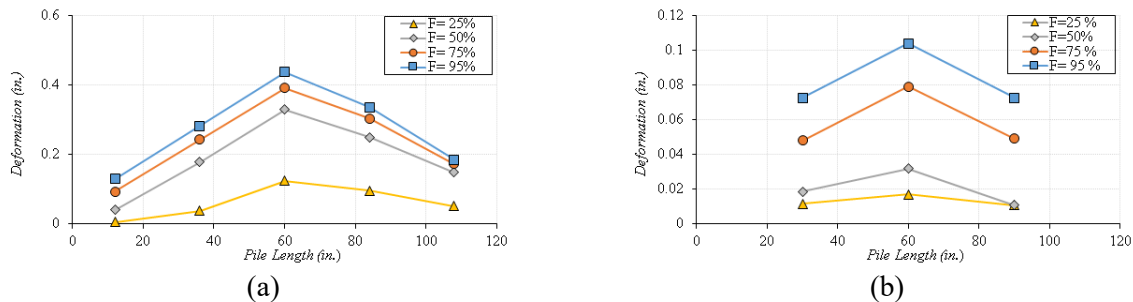


**Figure A.5** Deformation profile with respect to the pile length: (a) Horizontal profile, (b) Vertical profile

#### A.4 Axial Force-strain relation

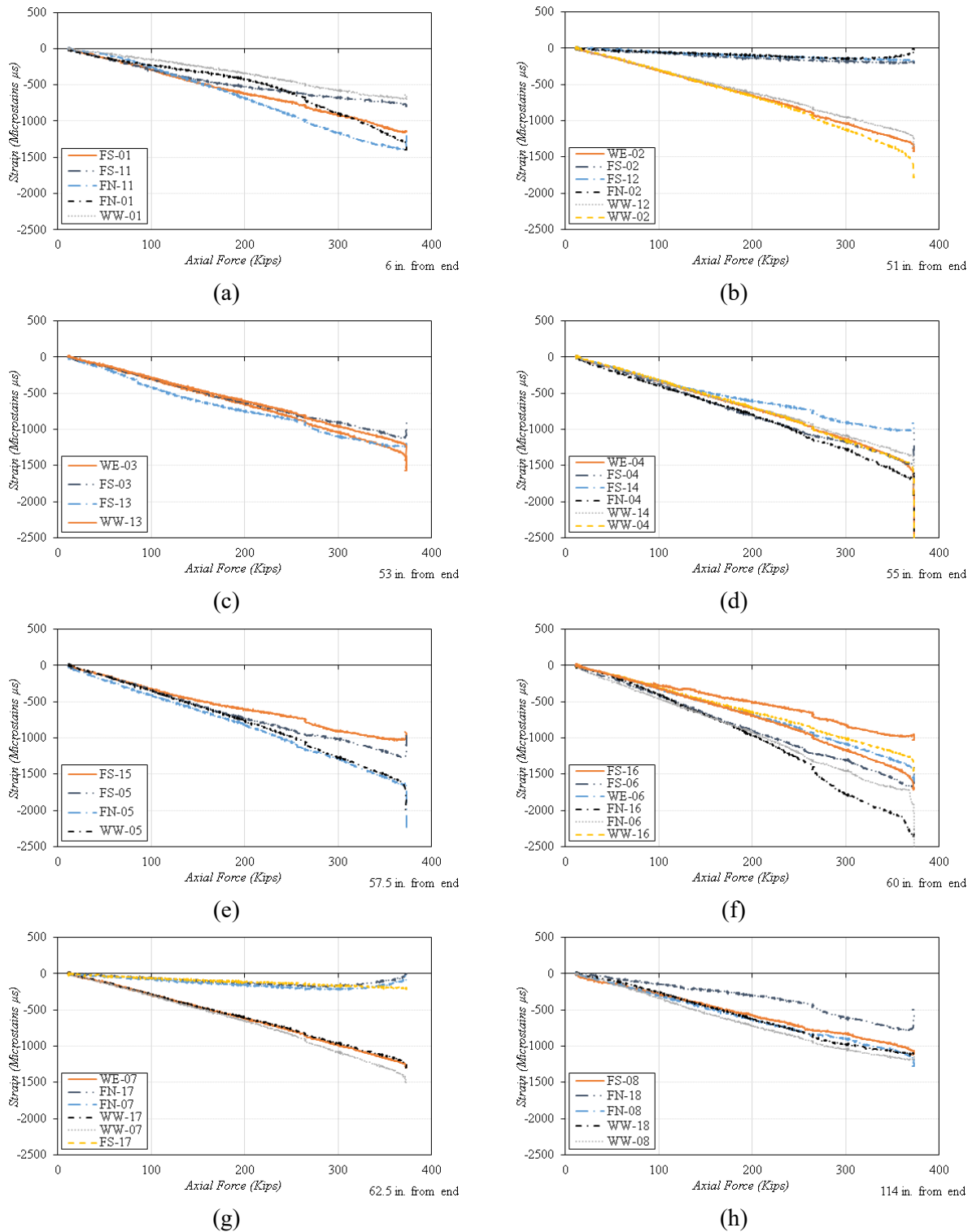
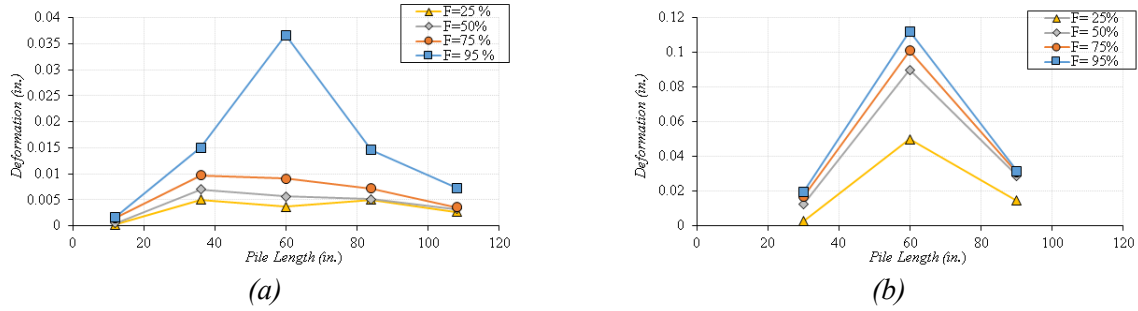


**Figure A.6** Axial shortening-steel strains in different position of pile: (a) 6in from edge,(b) 51in from edge, (c) 53in. from edge, (d) 55in. from edge, (e) 57.5in. from edge, (f) 60in. from edge, (g) 62.5 from edge, and (h) 114in. from edge

FN: Flange north FS: Flange south WW: Web west WE: Web east

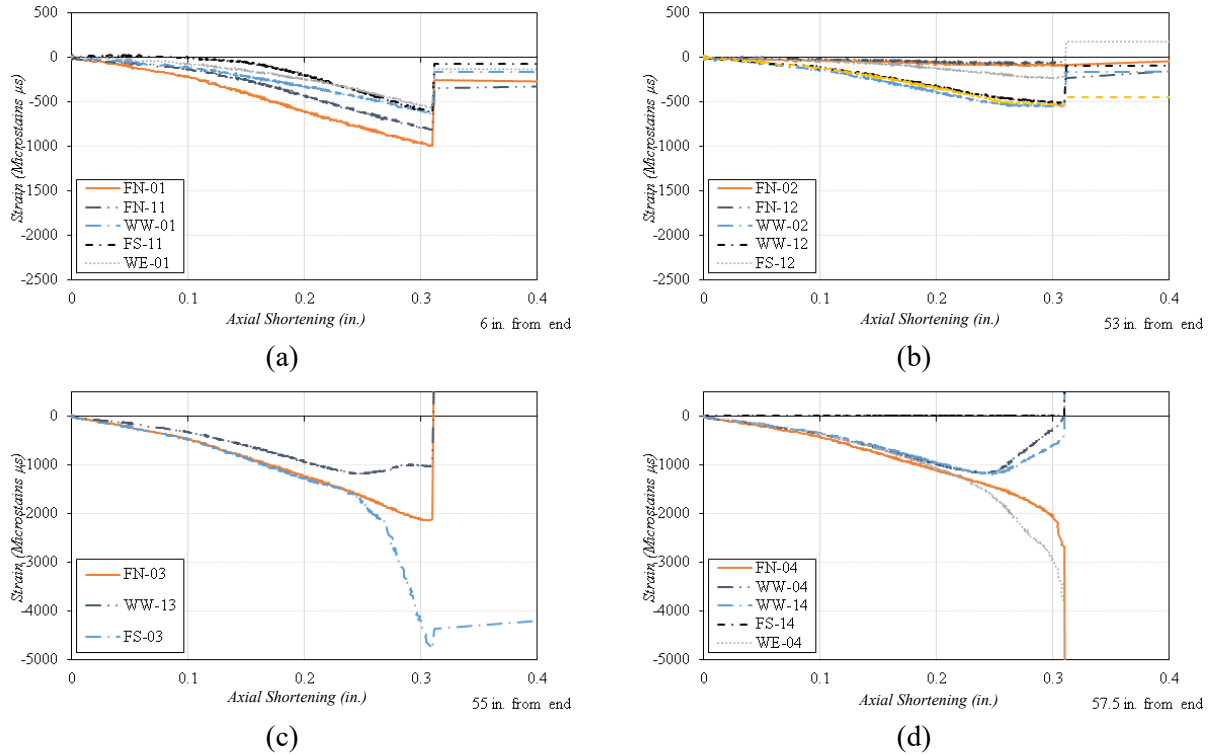
## A.5 W70-F50. Pile

### A.5.1 Profile of pile



**Figure A.7** Deformation profile with respect to the pile length: (a) Horizontal profile, (b) Vertical profile

### A.5.2 Axial shortening-strain relation



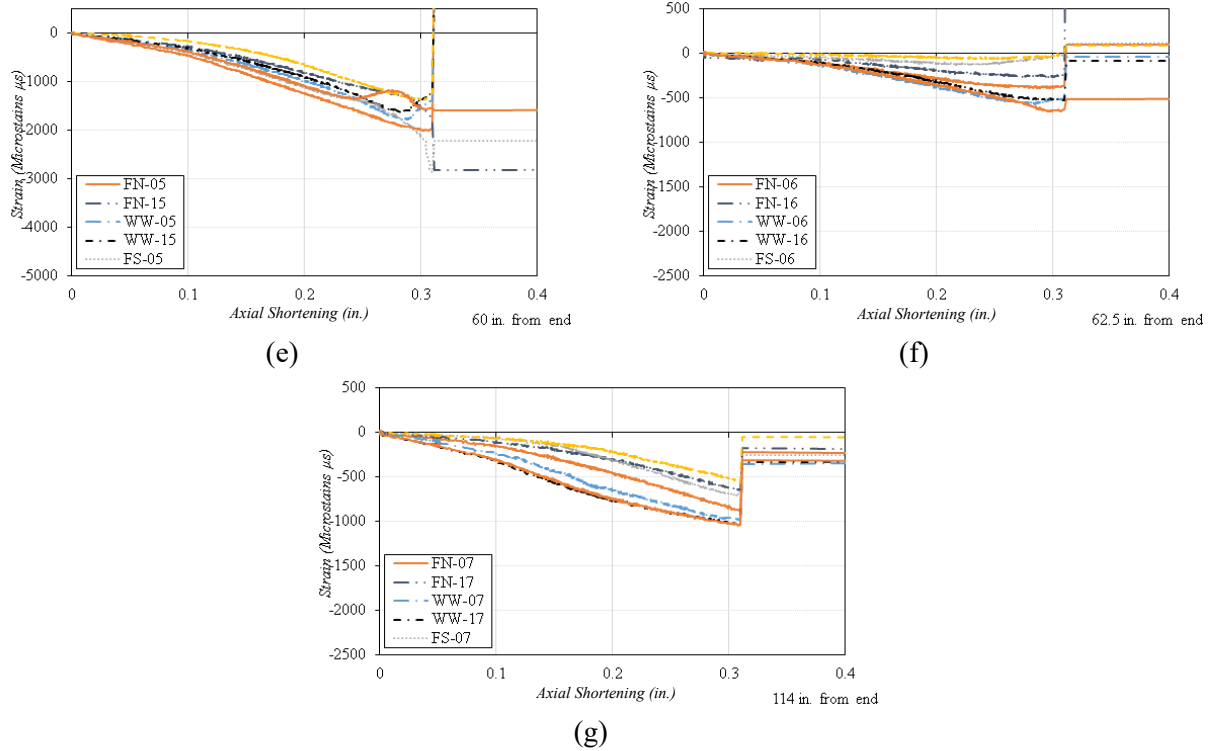


**Figure A.8** Axial shortening-steel strains in different position of pile: (a) 6in from edge, (b) 53in. from edge, (c) 55in. from edge, (d) 57.5in. from edge, (e) 60in. from edge, (f) 62.5 in. from edge, and (g) 114in. from edge

FN: Flange north FS: Flange south WW: Web west WE: Web east

## A.6 W70-F50/0. Pile

### A.6.1 Profile of pile

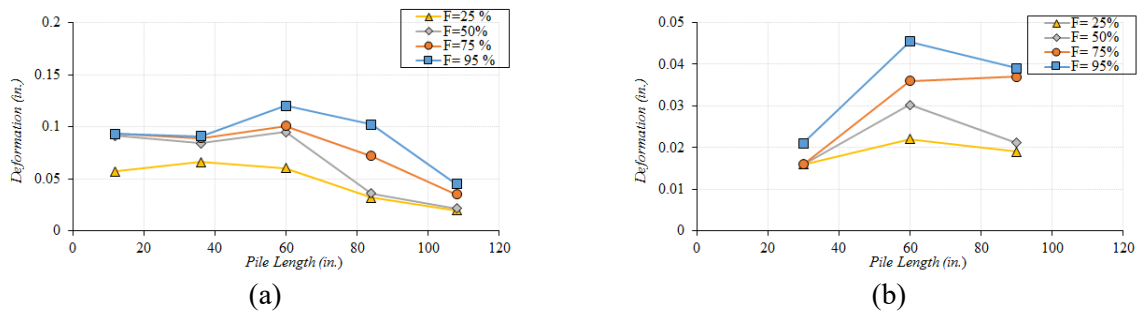


**Figure A.9** Deformation profile with respect to the pile length: (a) Horizontal profile, (b) Vertical profile



### A.6.2 Axial shortening-strain relation

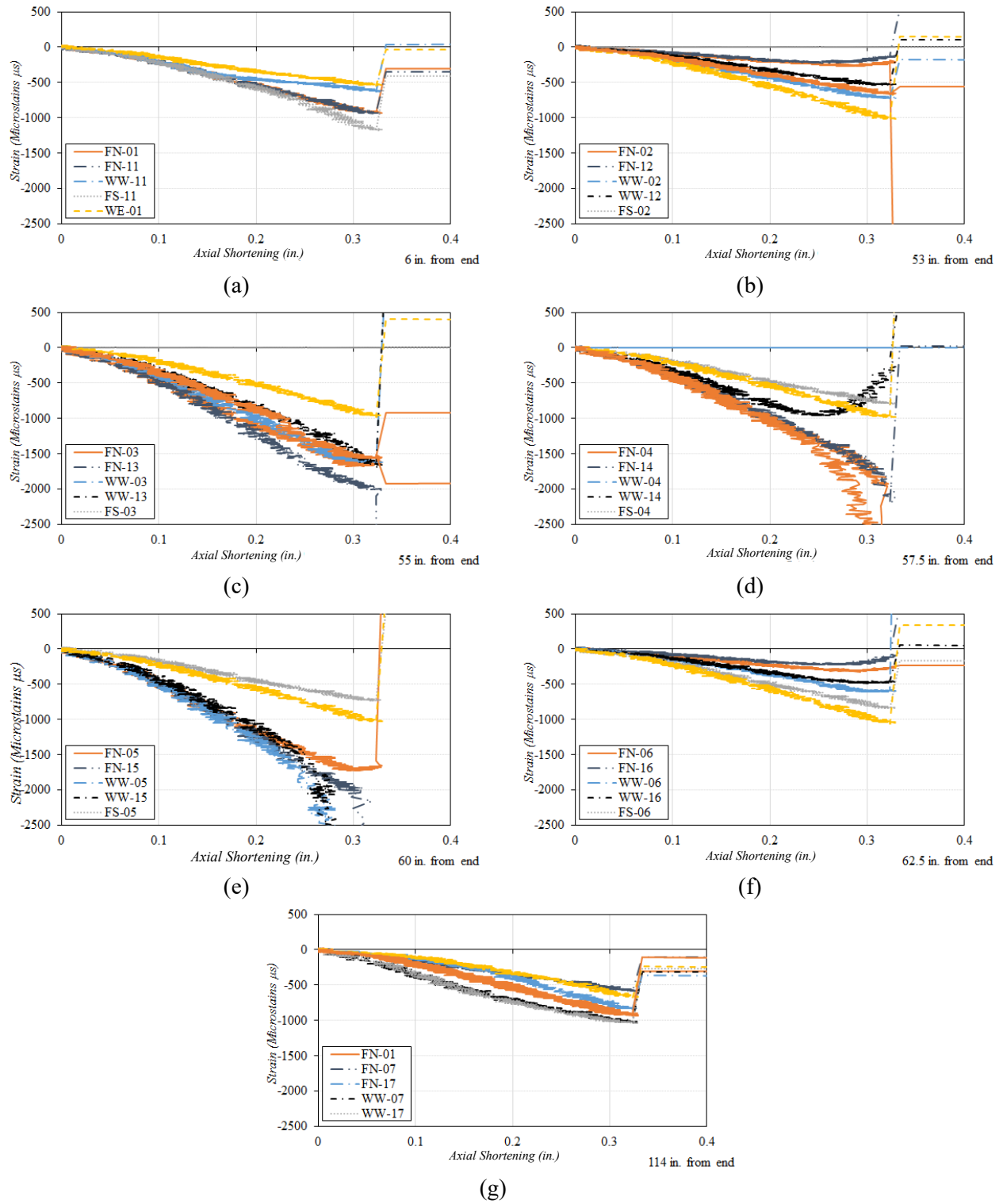
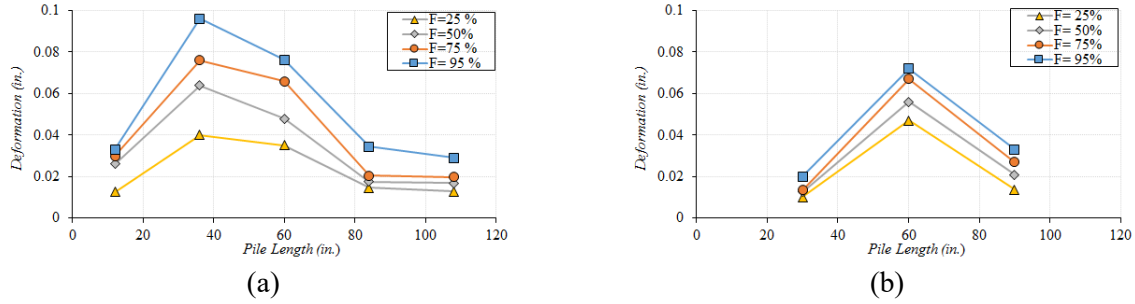


**Figure A.10** Axial shortening-steel strains in different position of pile: (a) 6in from edge, (b) 53in. from edge, (c) 55in. from edge, (d) 57.5in. from edge, (e) 60in. from edge, (f) 62.5 from edge, and (g) 114in. from edge

FN: Flange north FS: Flange south WW: Web west WE: Web east

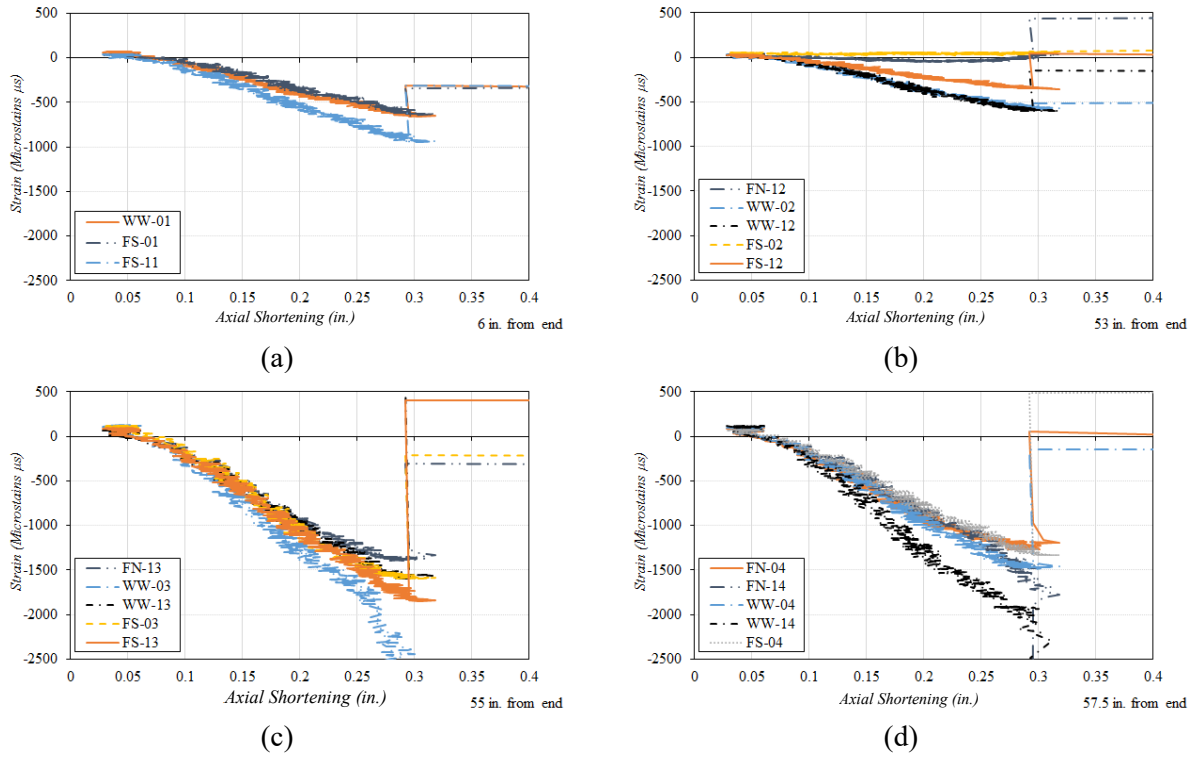
## A.7 W70V-F50. Pile

### A.7.1 Profile of pile



**Figure A.11** Deformation profile with respect to the pile length: (a) Horizontal profile, (b) Vertical profile

### A.7.2 Axial shortening-strain relation



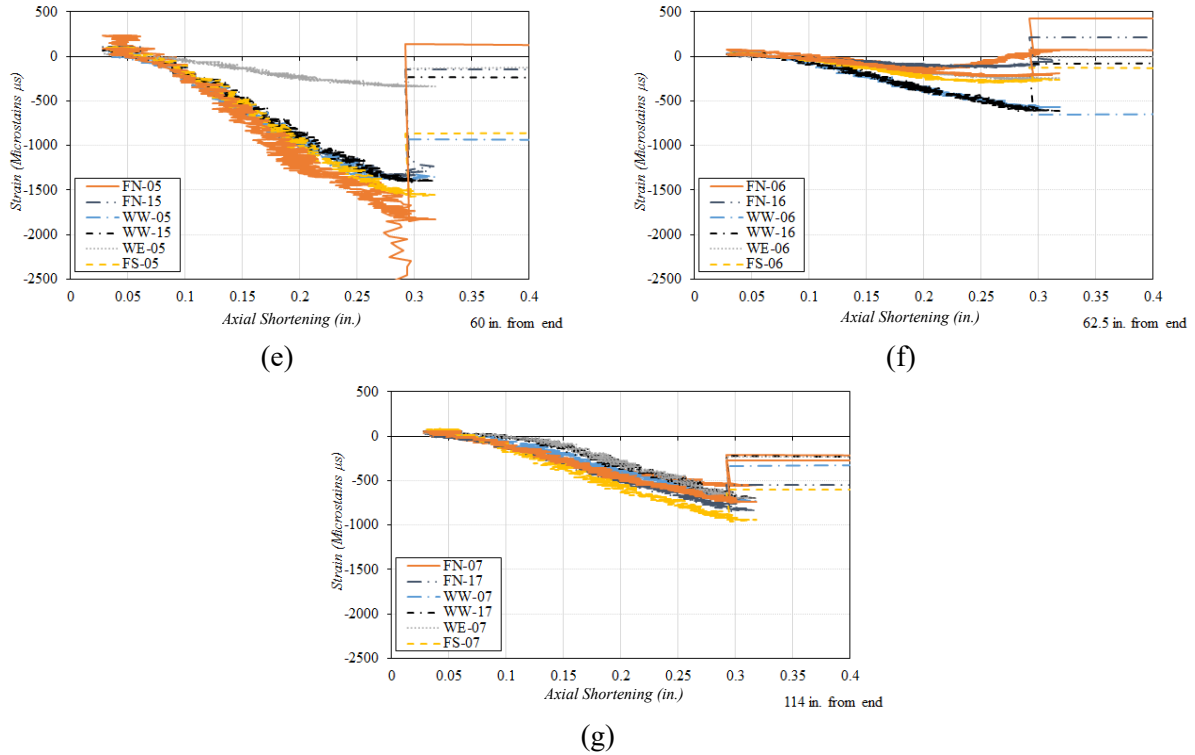


**Figure A.12** Axial shortening-steel strains in different position of pile: (a) 6in from edge, (b) 53in. from edge, (c) 55in. from edge, (d) 57.5in. from edge, (e) 60in. from edge, (f) 62.5 from edge, and (g) 114in. from edge

FN: Flange north FS: Flange south WW: Web west WE: Web east

## A.8 W70-F50C. Pile

### A.8.1 Profile of pile

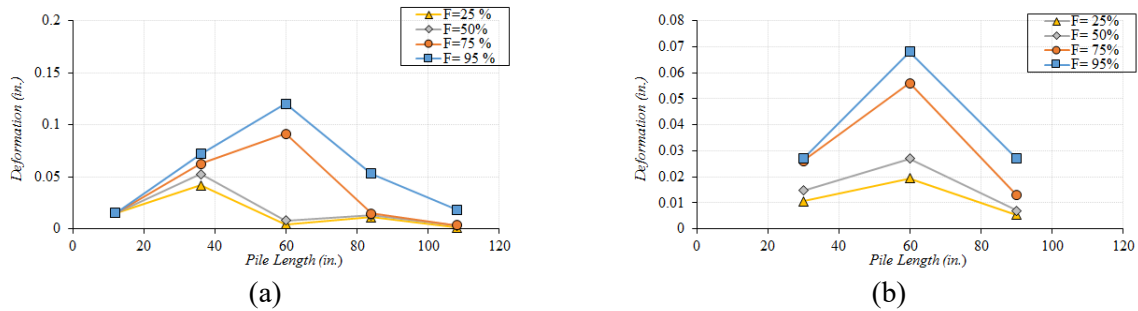


**Figure A.13** Deformation profile with respect to the pile length: (a) Horizontal profile, (b) Vertical profile

### A.8.2 Axial shortening-strain relation

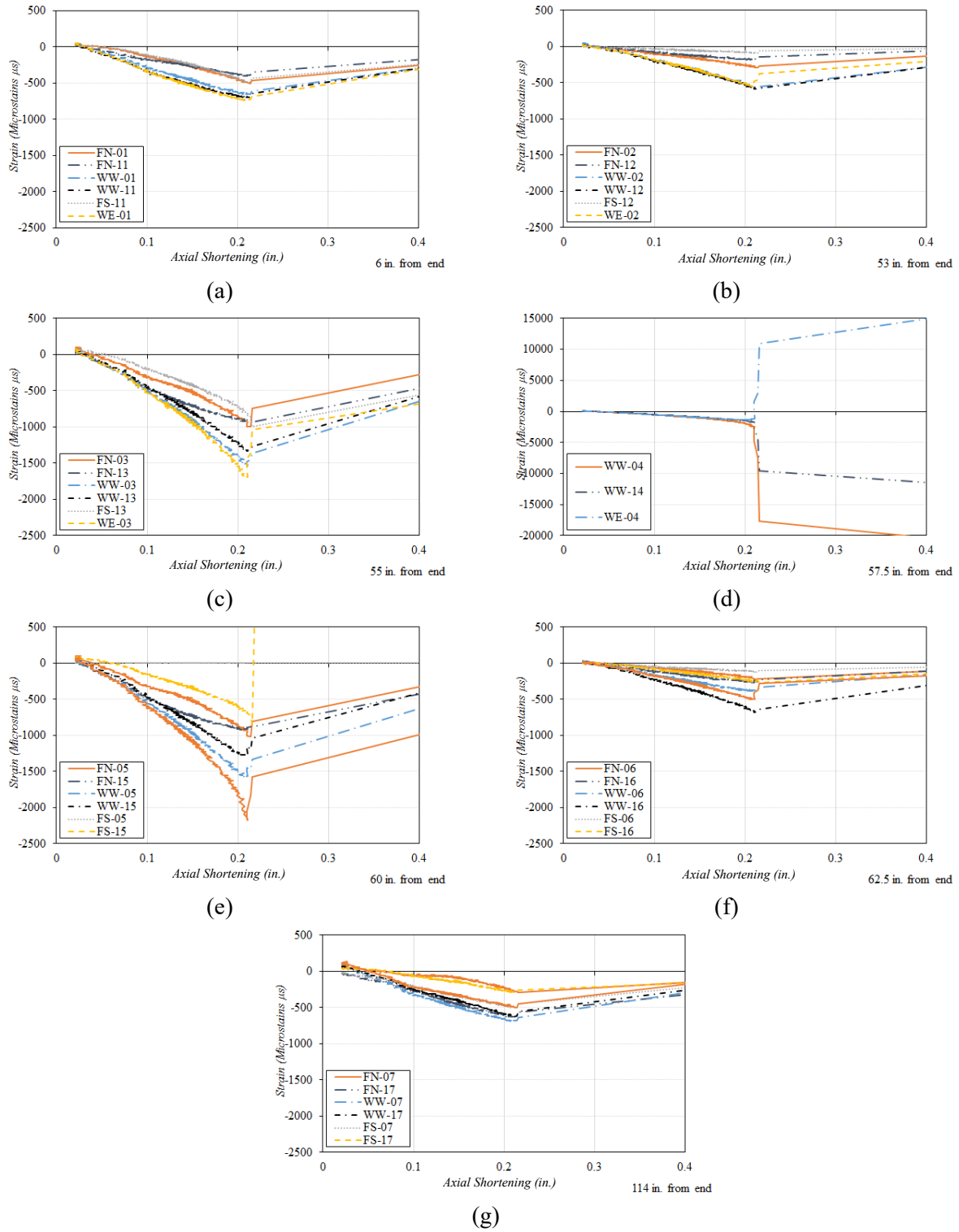
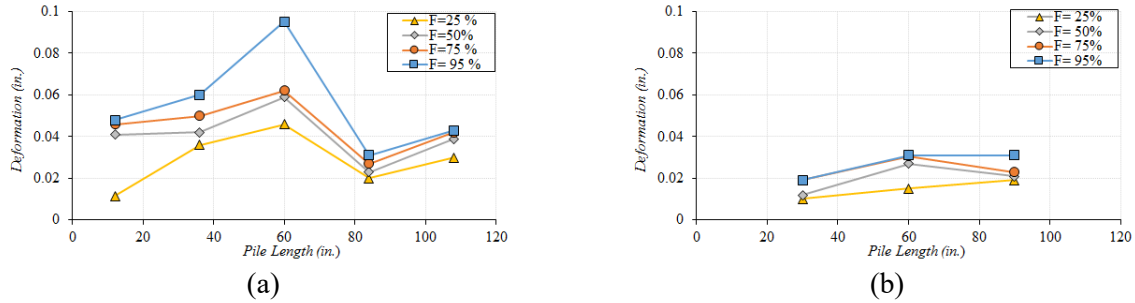


**Figure A.14** Axial shortening-steel strains in different position of pile: (a) 6in from edge, (b) 53in. from edge, (c) 55in. from edge, (d) 57.5in. from edge, (e) 60in. from edge, (f) 62.5 from edge, and (g) 114in. from edge

FN: Flange north FS: Flange south WW: Web west WE: Web east

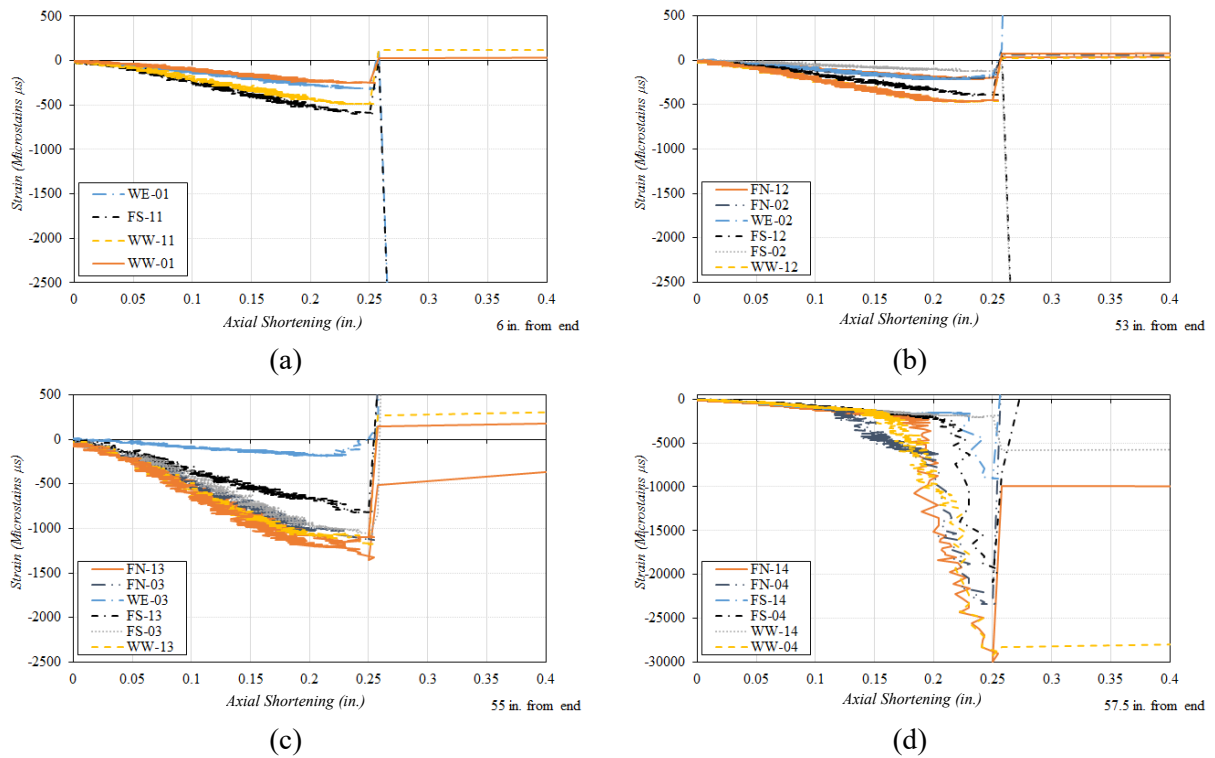
## A.9 W70V-F50C. Pile

### A.9.1 Profile of pile



**Figure A.15** Deformation profile with respect to the pile length: (a) Horizontal profile, (b) Vertical profile

### A.9.2 Axial shortening-strain relation



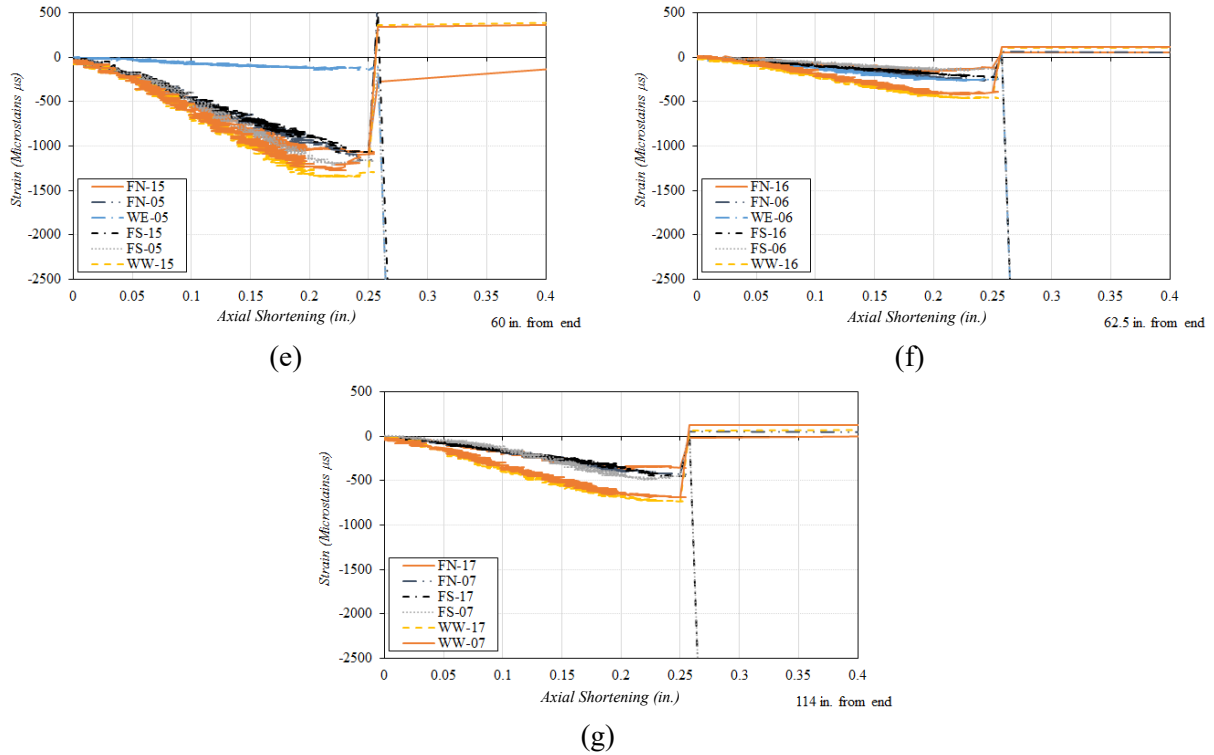


**Figure A.16** Axial shortening-steel strains in different position of pile: (a) 6in from edge, (b) 53in. from edge, (c) 55in. from edge, (d) 57.5in. from edge, (e) 60in. from edge, (f) 62.5 from edge, and (g) 114in. from edge

FN: Flange north FS: Flange south WW: Web west WE: Web east

#### A.10 W70-F50-6in. Pile

##### A.10.1 Profile of pile

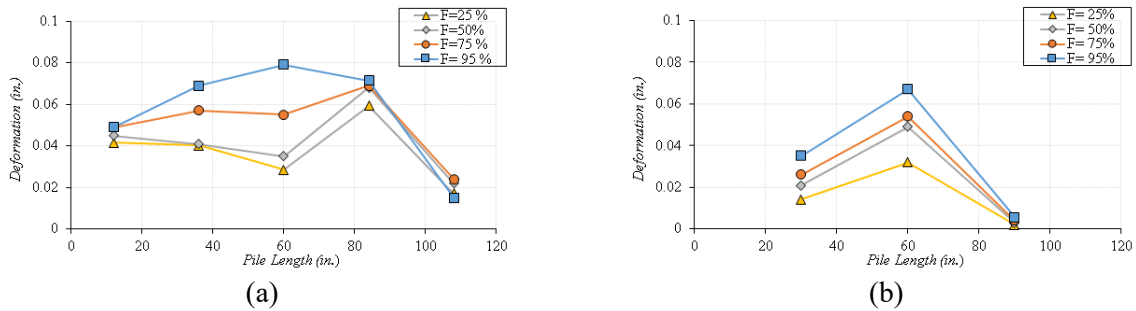


**Figure A.17** Deformation profile with respect to the pile length: (a) Horizontal profile, (b) Vertical profile

### A.10.2 Axial shortening-strain relation

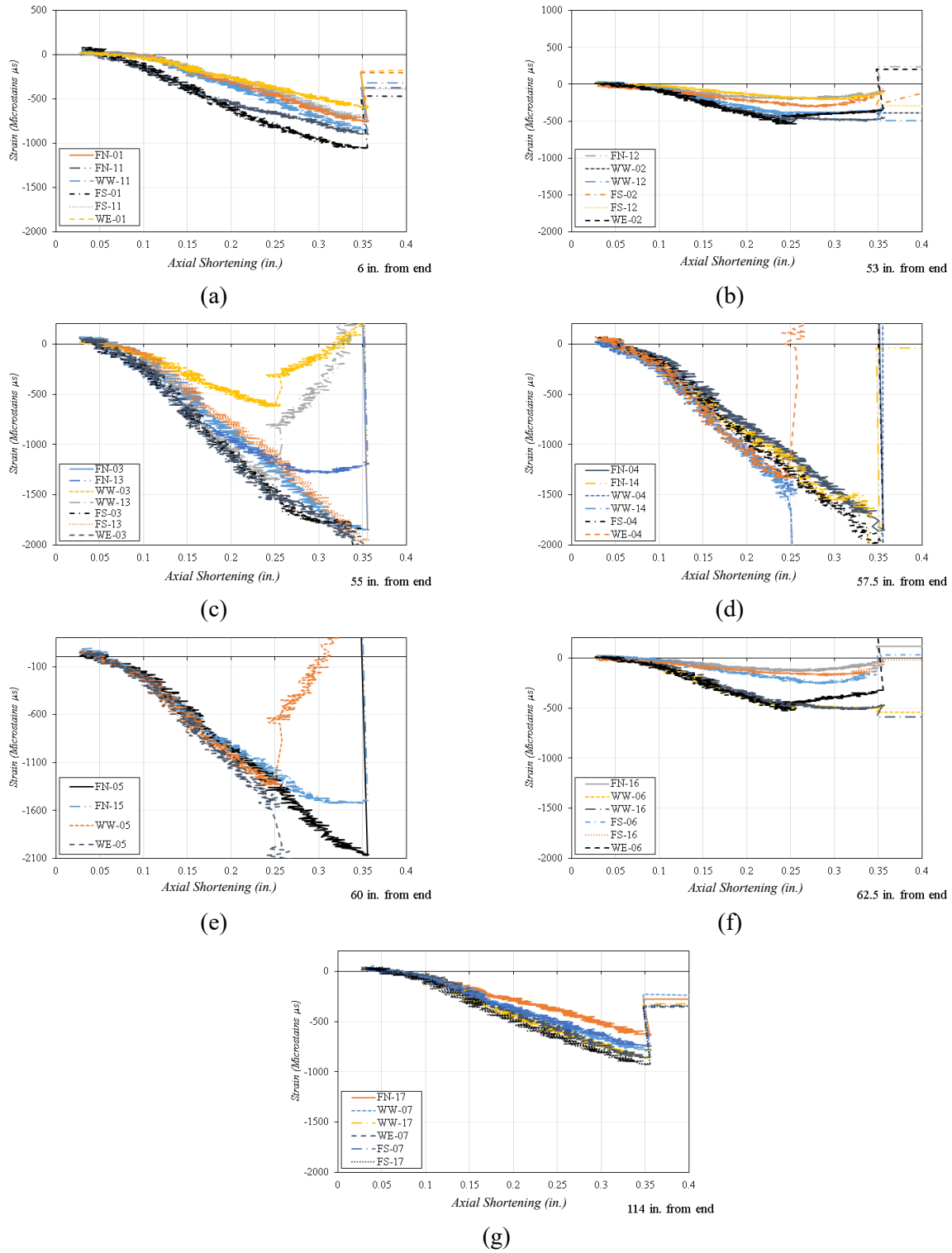
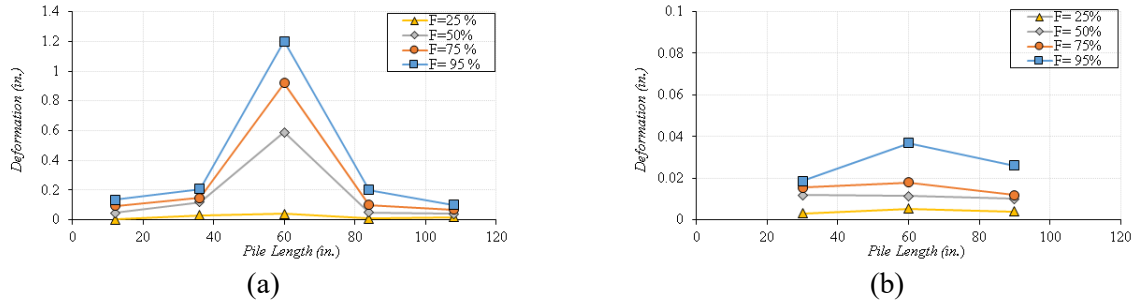


**Figure A.18** Axial shortening-steel strains in different position of pile: (a) 6in from edge, (b) 53in. from edge, (c) 55in. from edge, (d) 57.5in. from edge, (e) 60in. from edge, (f) 62.5 from edge, and (g) 114in. from edge

FN: Flange north FS: Flange south WW: Web west WE: Web east

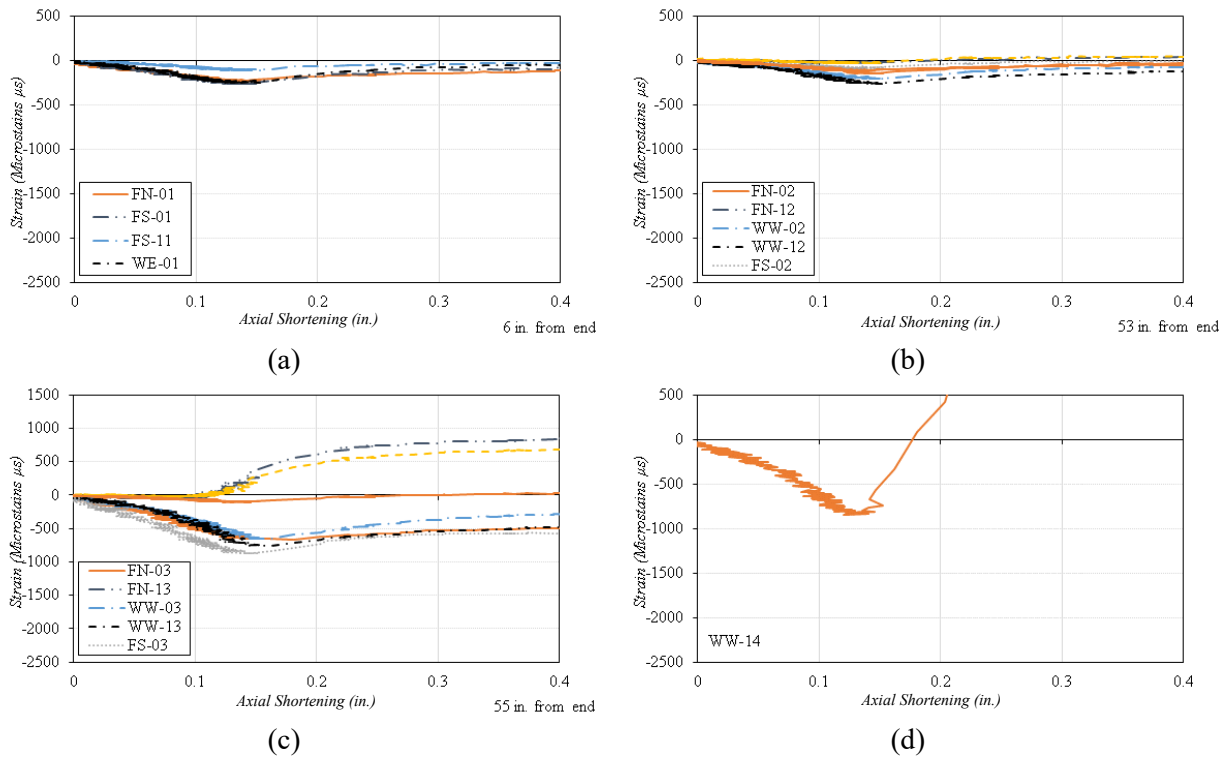
## A.11 W70V-F50C-10%. Pile

### A.11.1 Profile of pile



**Figure A.19** Deformation profile with respect to the pile length: (a) Horizontal profile, (b) Vertical profile

### A.11.2 Axial shortening-strain relation





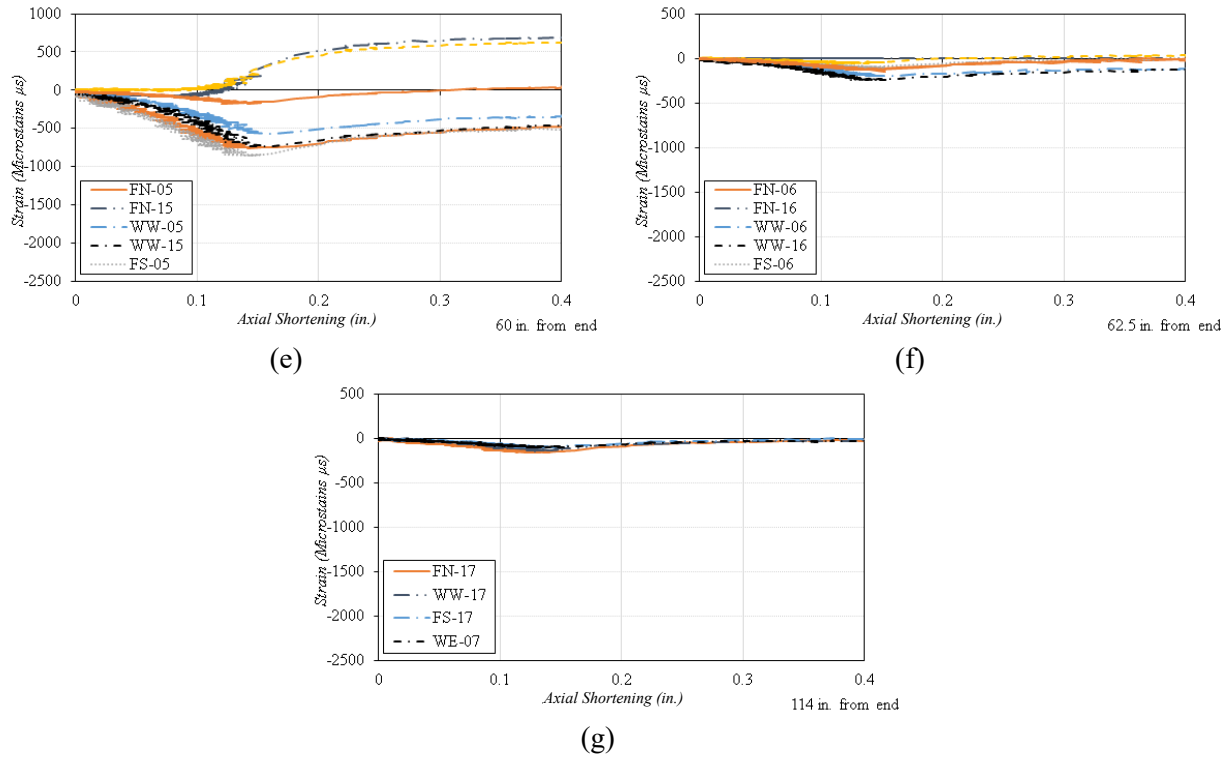


**Figure A.20** Axial shortening-steel strains in different position of pile: (a) 6in from edge, (b) 53in. from edge, (c) 55in. from edge, (d) 57.5in. from edge, (e) 60in. from edge, (f) 62.5 from edge, and (g) 114in. from edge

FN: Flange north FS: Flange south WW: Web west WE: Web east

#### A.12 W70V-F50C-30%. Pile

##### A.12.1 Profile of pile

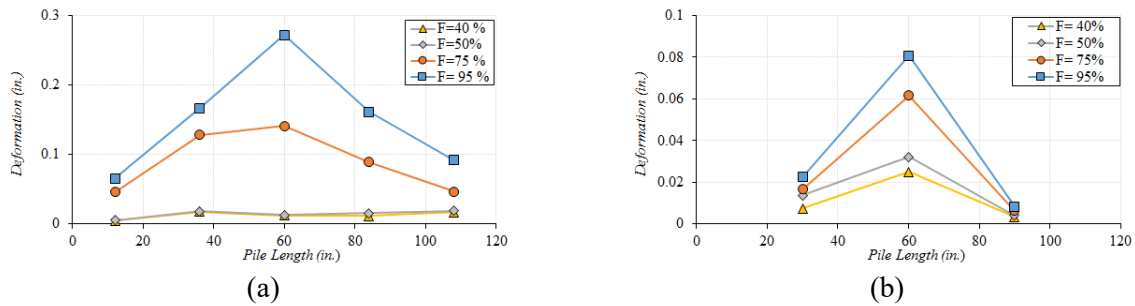
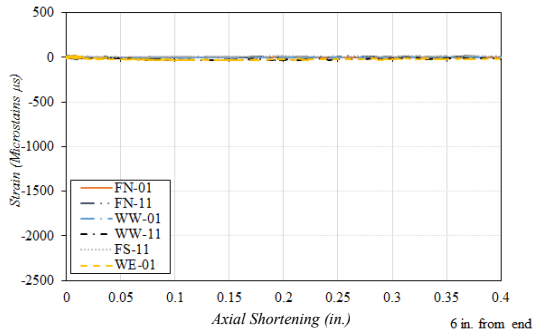
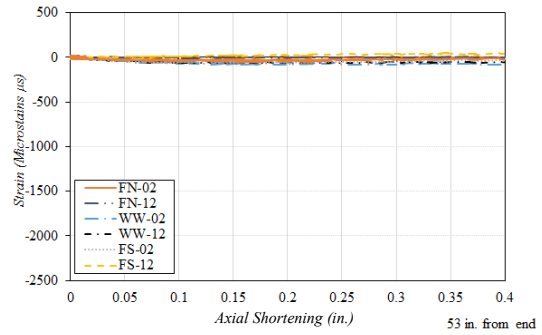


**Figure A.21** Deformation profile with respect to the pile length: (a) Horizontal profile, (b) Vertical profile

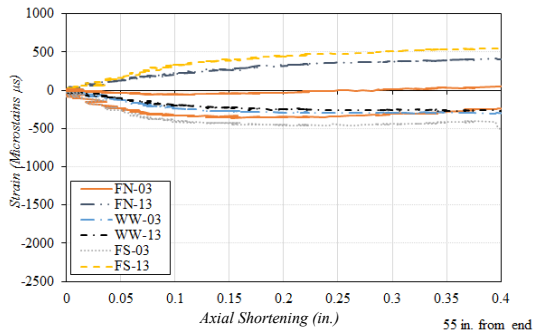
### A.12.2 Axial shortening-strain relation



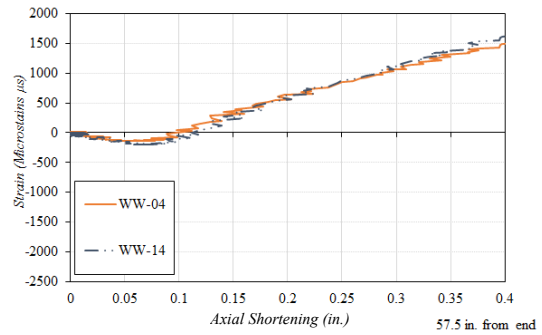
(a)



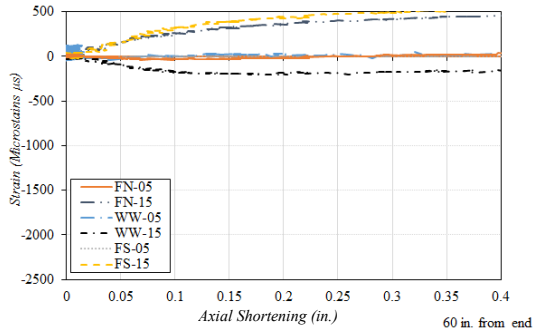
(b)



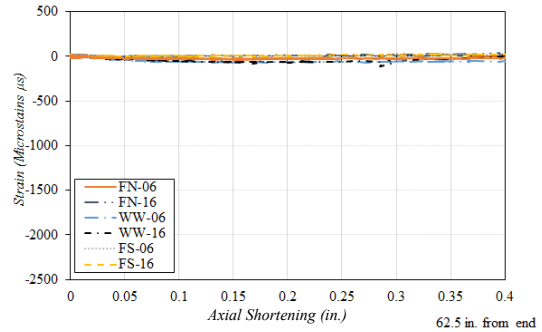
(c)



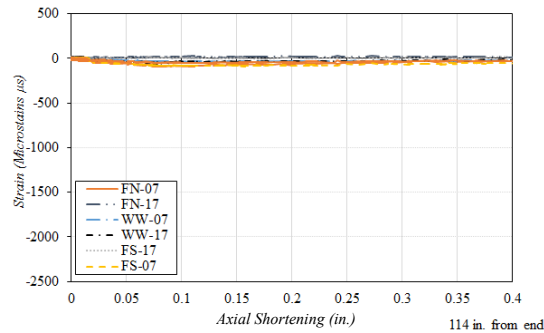
(d)



(e)



(f)



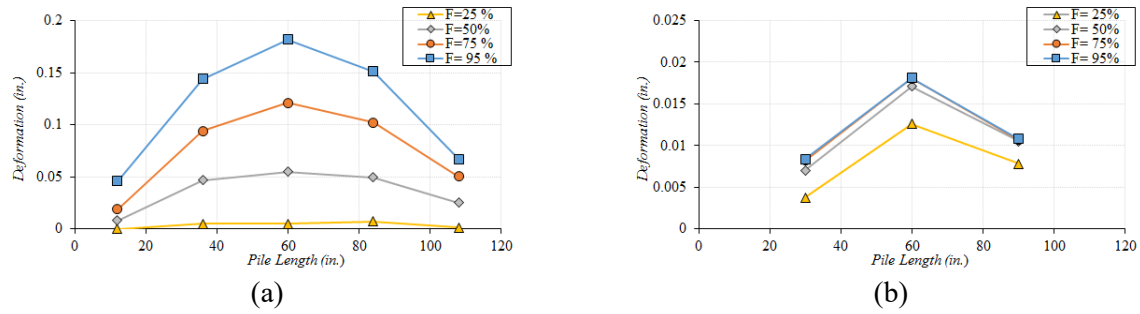
(g)

**Figure A.22** Axial shortening-steel strains in different position of pile: (a) 6in from edge, (b) 53in. from edge, (c) 55in. from edge, (d) 57.5in. from edge, (e) 60in. from edge, (f) 62.5 from edge, and (g) 114in. from edge

FN: Flange north FS: Flange south WW: Web west WE: Web east

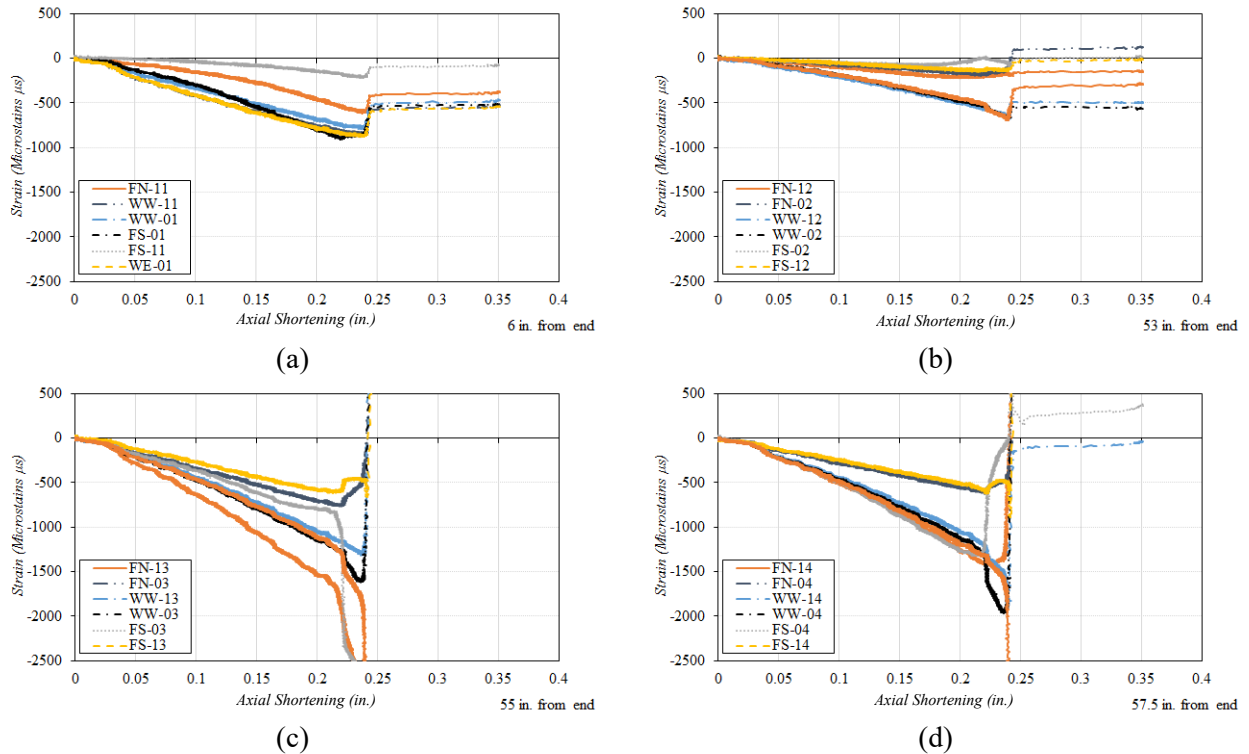
### A.13 W70-F50-10%. Pile

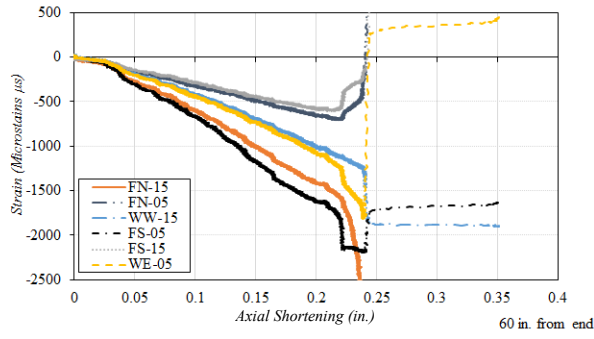
#### A.13.1 Profile of pile



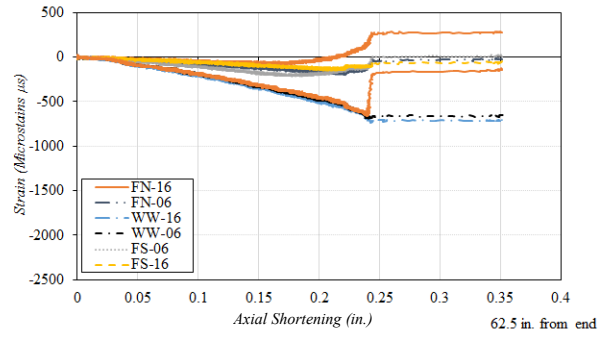
**Figure A.23** Deformation profile with respect to the pile length: (a) Horizontal profile, (b) Vertical profile

#### A.13.2 Axial shortening-strain relation

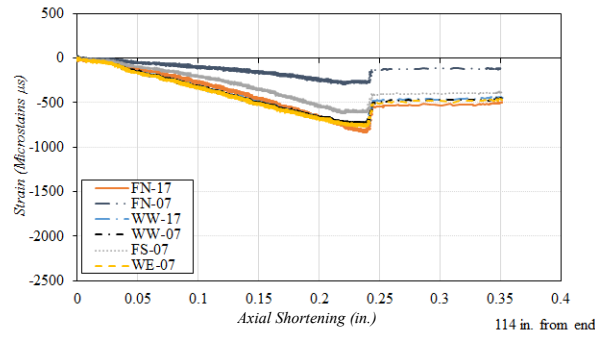




(e)



(f)



(g)

**Figure A.24** Axial shortening-steel strains in different position of pile: (a) 6in from edge, (b) 53in. from edge, (c) 55in. from edge, (d) 57.5in. from edge, (e) 60in. from edge, (f) 62.5 from edge, and (g) 114in. from edge

FN: Flange north FS: Flange south WW: Web west WE: Web east

## Appendix B Specimens Experimental Works and Preparation



**Figure B.1** Steel H-pile cleaning and strain gauges attaching

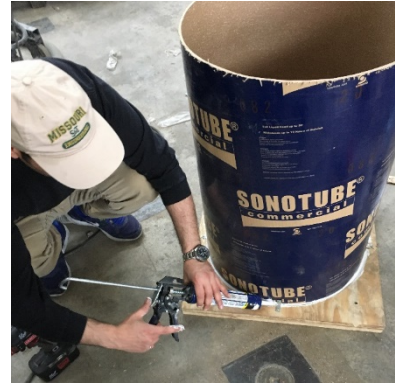
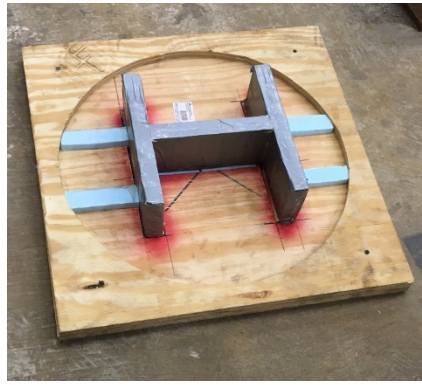


**Figure B.2** Form working



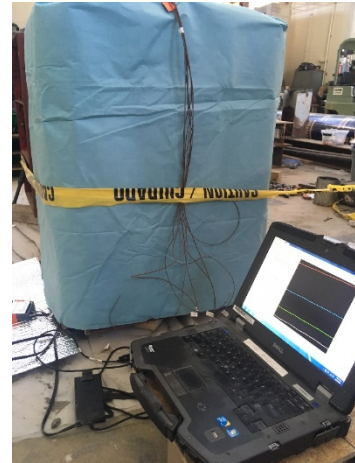
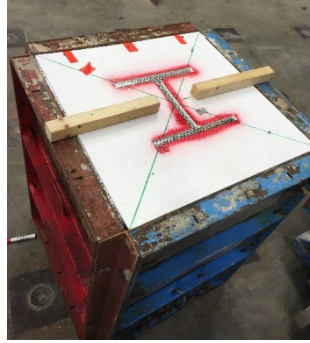


**Figure B.3** GT curing chamber manufacturing

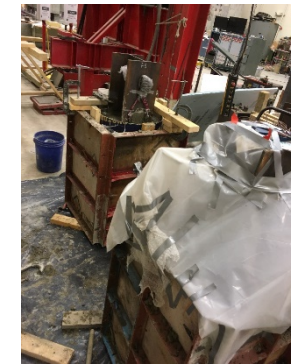


**Figure B.4** Specimens concrete mixing and Amb. curing



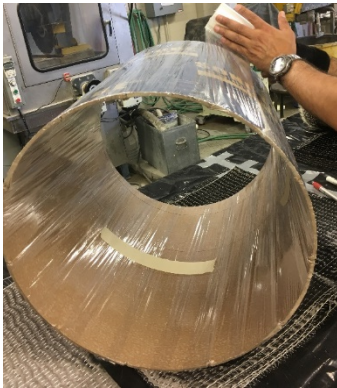


**Figure B.5** CFRP jacket (Fabric) works



**Figure B.6** CFRP jacket (Laminate) works



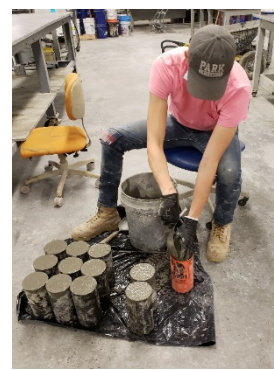
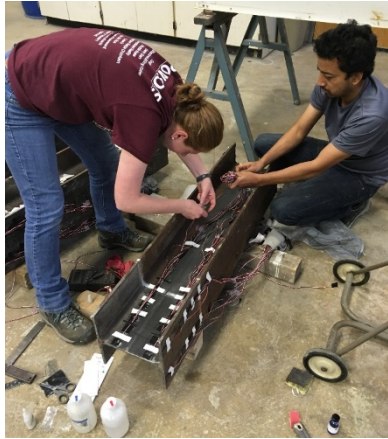


**Figure B.7** CFRP jacket + HS specimen concrete placing

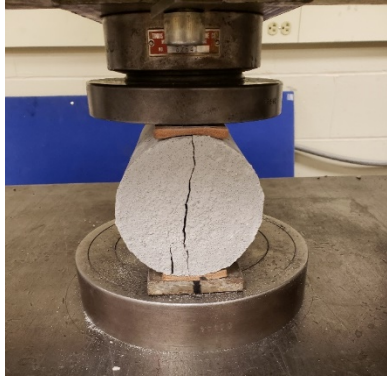


**Figure B.8** Specimen push-out testing





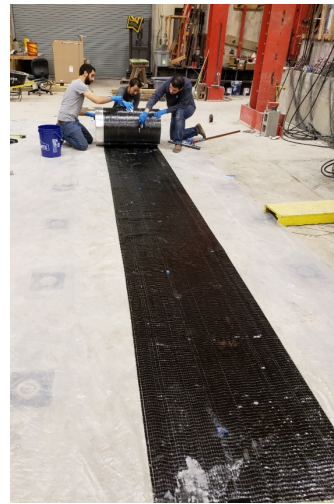






**Figure B.9** Stacking of the piles for storing



**Figure B.10** Milling the flanges to the reduced thickness



**Figure B.11** Milling the webs to the reduced thickness



**Figure B.12** Cleaning and painting the specimen with white water based paint





**Figure B.13** Trimming the rough edges of the specimens

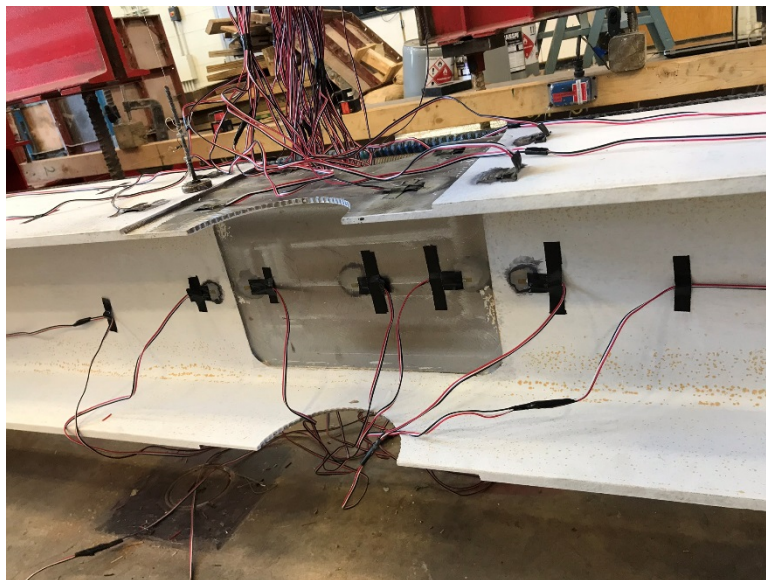


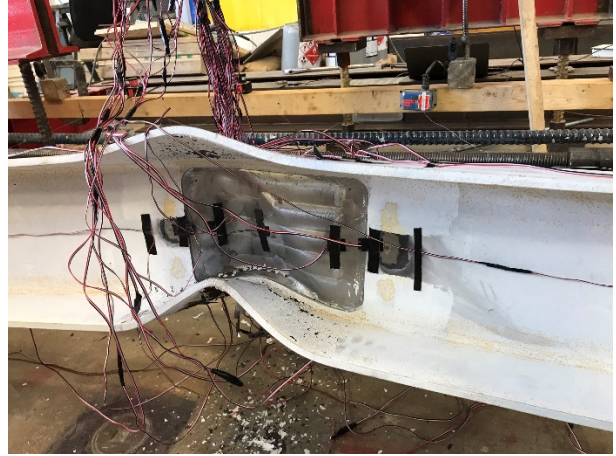
**Figure B.14** Attaching strain gauges to the expected points of failure



**Figure B.15** Installing the specimen in the testing setup



(a)

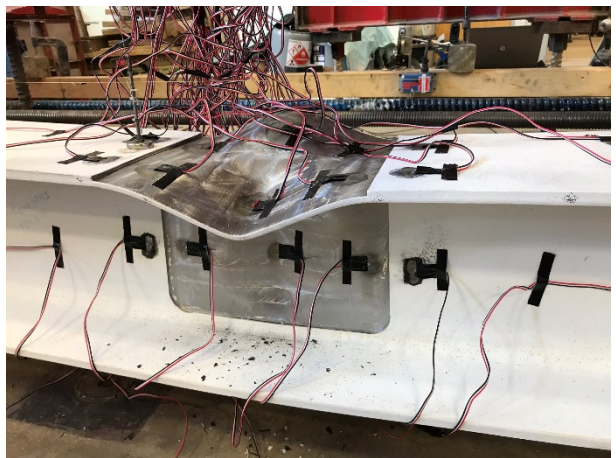


(b)

**Figure B.16** Local position of failure: (a) W00-F00, (b) W70-F00,



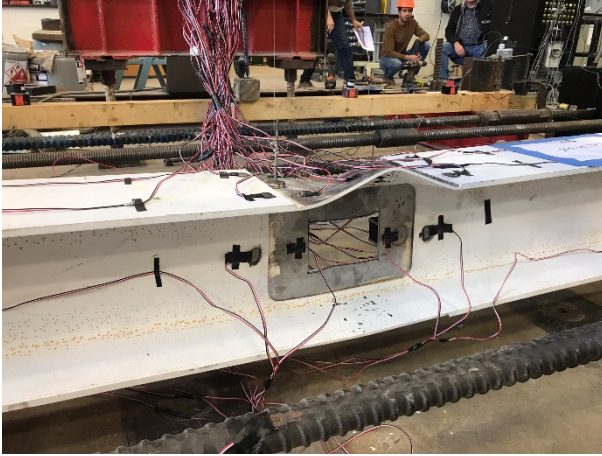
(a)



(b)

**Figure B.17** Local position of failure: (a) W70-F50, (b) W70-F50/0



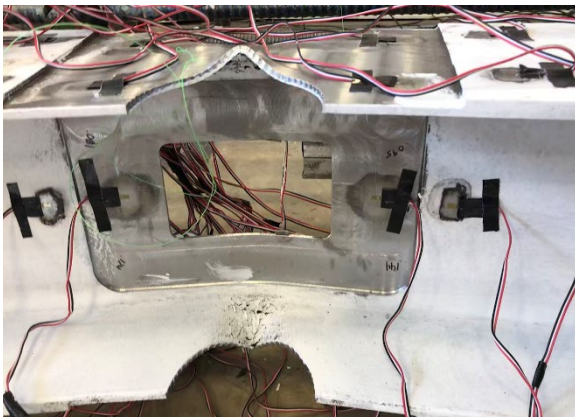


(a)

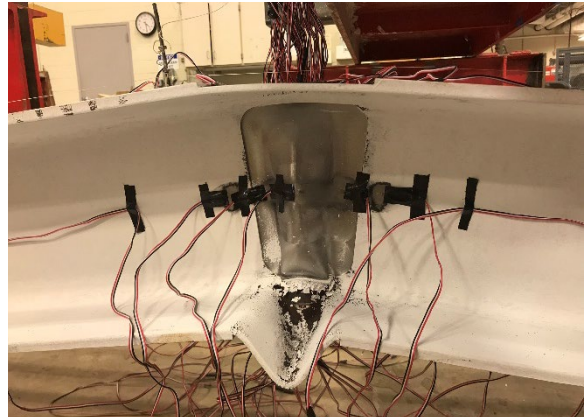


(b)

**Figure B.18** Local position of failure: (a) W70V-F50, (b) W70-F50C



(a)



(b)

**Figure B.19** Local position of failure: (a) W70V-F50C, (b) W70-F50-6in



(a)



(b)

**Figure B.20** Addition of stiffeners at the location of loading (a) stiffeners pattern (b) position of the stiffeners



(a)



(b)

**Figure B.21** Calibration of the used instrumentations (a) bolt of swivel plate (b) hydraulic jacks



(a)



(b)

**Figure B.22** Rail system for the loading beam (a) bottom track and roller (b) top roller